TUNING THE PROPERTIES OF MOLECULAR MAGNETS AND CONDUCTORS BASED ON LANTHANIDE AND TRANSITION METAL IONS BRIDGED BY TCNQ DERIVATIVES OR CYANOMETALLATE LIGANDS BY VARYING THE DIMENSIONALITY OF THE STRUCTURE AND METAL ION IDENTITY

A Dissertation

by

NAZARIO LOPEZ CRUZ

Submitted to the Office of Graduate Studies of
Texas A&M University
in partial fulfillment of the requirements for the degree of

DOCTOR OF PHILOSOPHY

May 2010

Major Subject: Chemistry

TUNING THE PROPERTIES OF MOLECULAR MAGNETS AND CONDUCTORS BASED ON LANTHANIDE AND TRANSITION METAL IONS BRIDGED BY TCNQ DERIVATIVES OR CYANOMETALLATE LIGANDS BY VARYING THE DIMENSIONALITY OF THE STRUCTURE AND METAL ION IDENTITY

A Dissertation

by

NAZARIO LOPEZ CRUZ

Submitted to the Office of Graduate Studies of
Texas A&M University
in partial fulfillment of the requirements for the degree of

DOCTOR OF PHILOSOPHY

Approved by:

Chair of Committee,	Kim R. Dunbar
Committee Members,	Donald J. Darensbourg
	François P. Gabbaï
	Winfried Teizer
Head of Department,	David H. Russell

May 2010

Major Subject: Chemistry

ABSTRACT

Tuning the Properties of Molecular Magnets and Conductors Based on Lanthanide and Transition Metal Ions Bridged by TCNQ Derivatives or Cyanometallate Ligands by Varying the Dimensionality of the Structure and Metal Ion Identity.

(May 2010)

Nazario Lopez Cruz, B. S., Universidad de Guadalajara; M. S., The University of Texas at El Paso

Chair of Advisory Committee: Dr. Kim R. Dunbar

Research in the fields of molecular conductors and magnets over the past four decades has involved collaborative efforts of chemists and physicists whose common goal is to design useful materials composed of molecular building blocks. Of particular interest are materials whose properties can be tuned by electronic or steric changes in the molecular sub-units. The research on TCNQ derivatives described in this thesis was inspired by the observation that, although a vast amount of research has been directed at understanding binary M/TCNQ$^{\bullet-}$ materials, analogous compounds based on substituted TCNQ acceptors are surprisingly scarce. Single crystals of a new structure type for the $M^{+}(TCNQ)^{\bullet-}$ binary family were isolated from reactions of two dihalogenated TCNQ derivatives with Cu^{I} ions, namely $Cu(TCNQX_2)$ (X = Cl, Br). The new 3-D compound $Cu(TCNQCl_2)$ exhibits the highest conductivity of the $M^{+}(TCNQ)^{\bullet-}$ series, despite the greater separation of $TCNQCl_2$ units as compared to other derivatives to date.

Compounds of lower dimensionality were also obtained, namely the 2-D $Cu(TCNQBr_2)(CH_3CN)$ and 1-D $Cu(TCNQI_2)(CH_3CN)_2$ phases. Several 2p-3d heterospin molecular magnets were synthesized. For example a "magnetic sponge" material based on a 2-D hexagonal framework of composition $\{[Mn_2(TCNQF_4)(CH_3OH)_{7.5}(H_2O)_{0.5}]\text{-}(TCNQF_4)_2\cdot 7.5CH_3OH\}_\infty$, as well as molecular magnets based on first row metal ions and $TCNQF_4$ ligands of composition $M^{II}(TCNQF_4)^{-\bullet}(TCNQF_4^{2-})_{0.5}(CH_3CN)$ (M = Mn, Co) were prepared. In addition, unprecedented isostructural 2-D frameworks based on combinations of first row metal ions with $TCNQBr_2$ radicals of composition $[M(TCNQBr_2)_2(H_2O)_2]_\infty$ (M = Mn, Zn) were synthesized.

Lanthanide chemistry is also described in this dissertation. A series of mononuclear Ln-$TCNQF_4$ heterospin complexes of composition $\{M^{III}[TCNQF_4]_2[H_2O]_{6\text{-}7}\}\cdot(TCNQF_4)(3H_2O)$ (M = La, Pr, Nd, Sm, Eu, Gd, Dy, Ho, Er and Yb) was obtained which exhibit remarkable properties. The Tb analogue exhibits an unprecedented subtle interplay between single molecule magnetic behavior and phonon bottleneck effect. Magnetic ordering was observed for the Sm analogue. A homologous series of 1-D materials based on alternating lanthanide ions and hexacyanometallates of formula $\{[Ln(tptz)(H_2O)_4Fe(CN)_6]\cdot 8H_2O\}_\infty$ (Ln = Pr, Nd, Sm, Eu, Gd, Tb) was obtained and a detailed magnetic study provided incontrovertible evidence that the $Sm^{III}\text{-}[Fe^{III}(CN)_6]^{3-}$ compound exhibits ferromagnetic and not antiferromagnetic coupling as had been reported for related 1-D chains.

DEDICATION

To my niece, Isabella

ACKNOWLEDGEMENTS

I am truly appreciative of Professor Kim R. Dunbar for her direction and assistance in helping me complete my doctorate studies. I learned from her the art that is involved in scientific research and in education. I am a better chemist and teacher because of everything I learned from her while pursing my goals. I will forever treasure the wisdom and discipline that I learned from her, and I will always be grateful for everything she did on my behalf. I always had a great time discussing science as well as having regular conversations with her. Professor Dunbar always gave me valuable advice and suggested experiments to increase the scope of my projects. I also would like to sincerely thank Professor Juan C. Noveron for his advice, support, and the opportunity to do graduate research work under his supervision during my master's studies. I also would like to sincerely thank Professor Carlos F. Jasso for his advice, support, and the opportunity to do undergraduate research work under his supervision.

I would like to acknowledge my committee members Professor Donald J. Darensbourg, Professor François P. Gabbaï, and Professor Winfried Teizer for the help and advice they have provided and the Texas A&M University Chemistry faculty members. Professor Hongcai Zhou provided assistance for thermogravimetric analysis and Dr. Wenjuan Zhuang directly assisted me during the measurements and was always very friendly. Furthermore, I would like to express my gratitude for Dr. Nattamai Bhuvanesh who I consulted with on the crystallographic work presented herein. I would

like to aknowledge Dr. Wolfgang Wernsdorfer from Institut Néel at Grenoble for the micro-SQUID measurements presented in this dissertation.

I also wish to acknowledge my fellow labmates in the Dunbar's research group. Dr. Hanhua Zhao helped me to get started in the lab on the synthesis of coordination compounds and characterization by single crystal X-ray diffraction. His support and advice made a big impact on my career. Professor Michael Shatruk helped me to develop writing skills and also introduced me to magnetism and crystallography. Dr. Andrey V. Prosvirin showed me how to perform magnetic measurements and Dr. Akira Ota instructed me on how to perform conductivity measurements. Dr. Abdellatif Chouai trained me in the synthesis of functionalized ligands. Dr. Helen T. Chifotides, Dr. Xinyi Wang, Professor José Ramón Galán-Mascarós and Dr. Barbara Gastel helped me to correct my manuscripts before giving them to Dr. Dunbar. I also would like to acknowledge Carolina Avendano, Dr. Daphne Aguirre, Dr. Alfredo Angeles-Boza, Edward Funck, Kristen Funck, Ian Giles, Dr. Ferdi Karadas, Sarah Lane, Codi Anne Sanders, Heather Southerland, Zhongyue Zhang, Amanda David, Bruno Pena Maceda, Mohamed Saber, Andrew Brown, Maryfer Ballesteros Rivas, Zhanyong Li, Dr. Matthew Hilfiger, and Michael Woodie for all the good times in the lab.

I would like to thank my friends outside the Dunbar group Mario F. Borunda, Alejandro Bugarin, Miguel A. Castañeda, Maria Duran Galvan, Francisco Escobedo, Sarah Flores, Roxanne M. Jenkins, Adriana I. Moncada, Oscar Ojeda, Diana Sepulveda, and Yolanda Vasquez for their friendship and advice.

Finally, I would like to express my sincerest appreciation for the people who are part of my family Margarita Lopez, Federico Lopez, Idania Romo and Isabella Lopez, without whose support and care, this would not have been possible. I especially thank my parents, Miguel Lopez Ruvalcaba and Maria Teresa Cruz Leal, whose dream this Ph. D. has been as much as it has been my own.

TABLE OF CONTENTS

CHAPTER Page

CHAPTER Page

CHAPTER Page

LIST OF FIGURES

FIGURE Page

FIGURE Page

FIGURE Page

FIGURE Page

FIGURE Page

FIGURE Page

FIGURE Page

FIGURE Page

FIGURE Page

FIGURE Page

FIGURE Page

FIGURE Page

FIGURE Page

FIGURE Page

FIGURE Page

LIST OF TABLES

TABLE Page

TABLE Page

CHAPTER I

INTRODUCTION: MOLECULAR CONDUCTORS AND MAGNETS

Background

Research in the fields of molecular conductors and magnets over the past four decades has involved collaborative efforts of chemists and physicists alike whose common goal is to design useful materials composed of molecular building blocks. Of particular interest are materials whose properties can be tuned by electronic or steric changes in the molecular sub-units. Both fields were initiated with ambitious aspirations of mimicking the performance of conventional conductors and magnets. Much progress to this end has been made as evidenced by the fact that there are three-dimensional molecular magnets with high ordering temperatures and large coercivities and molecular conductors whose properties span the entire range of possibilities, namely semiconductors, metals and superconductors.

Naturally occurring conductors and magnets such as copper and magnetite have been known for thousands of years, but the understanding of the physical phenomena did not develop until prominent physicists such as Franklin, Coulomb, Ampère, Faraday, and Maxwell contributed to the field in the eighteenth and nineteenth centuries. Their discoveries of charge conservation, forces between electric charges, the relationship between electricity and magnetism, and the unification of electricity and magnetism into a classical theory of electromagnetism led to great technological advances in the last

---

This dissertation follows the style of *Chemistry-A European Journal*.

century. Traditional conductors and magnets are based on simple materials which contain only one kind of metal atom, a combination of metals atoms (intermetallics), or combinations of metal ions bridged by atoms such as oxygen as in the case of magnetite.

Molecule-based magnets and conductors offer certain advantages as compared to traditional solid state materials; including the fact that: a) they can be synthesized at room temperature; b) they are less dense which reduces the mass of device components; c) new interesting physical phenomena can be observed which are difficult or impossible to obtain with conventional materials; d) they can more easily be fabricated into thin films at room temperature; and e) they are composed of building blocks that can be chemically altered to tune the properties of the material. Current trends in molecular conductors include: 1) the synthesis of conductors that behave as superconductors at higher temperatures;[1] 2) the control of phase transitions in order to use the materials in memory devices;[2] 3) the development of single component conductors;[3] 4) the realization of nonvolatile memory devices based on resistance change of the material in response to external stimuli such as an applied potential or light;[4] and 5) the development of methods to downscale to the nano-regime for applications in nanodevices.[5] In terms of trends in molecular magnets, these include 1) the synthesis of molecular magnets with high ordering temperature; 2) the pursuit of lower dimensional magnetic materials composed of discrete coordination complexes that behave as nanomagnets also known as single molecule magnets (SMMs) which have been found to have unusual physical behavior such as quantum tunneling of the magnetization and hysteresis at the molecular level.[6] Included in this goal are magnetic chains which

exhibit a slow relaxation of the magnetization similar to the SMMs and thus are named single chain magnets (SCMs);[7] 3) the design of materials with potential applications as sensors or switching memory devices due to the ability to control changes in their magnetic properties by external stimuli such as light, pressure, temperature, or amount of interstitial solvent molecules;[8] 4) the pursuit of multifunctional magnetic materials in which there is a coexistence of long range magnetic ordering with metallic conductivity, superconductivity, optical activity, ferroelectricity, or porosity;[9] 5) the development of new methods to deposit 3D molecular magnets, single molecule magnets[10] and single chain magnets on surfaces in order to fabricate devices; and 6) the incorporation of SMMs into single molecule devices for future use in quantum computing and spintronics.[11]

Molecular Conductors

The field of molecular conductors will be discussed first because its development predated the study of molecular magnets. It was first suggested by McCoy and Moore that molecules that behave as insulators could be combined with other insulator molecules to yield conducting materials via a charge transfer process.[12] Insulators are materials that have a large energy difference between the valence band and the conduction band and the electrons are essentially trapped in the valence band. Consequently only a small number of electrons are promoted to the conduction band and the material is poorly conducting because it has very few mobile electrons. The molecules of interest should be capable of existing as stable radical species in their reduced or oxidized forms in order to have unpaired electrons required for charge

transport. Several examples of common organic donors and acceptors used to obtain conducting materials are shown in Figure 1.1.

The first molecular semiconductor was synthesized by doping perylene, an insulating organic molecule, the result of which is a radical cation salt. Semiconductors are materials that have a smaller energy difference between the valence band and the conduction band as compared to insulators. Therefore, in semiconductors it is easier to promote electrons from the valence band into the conduction band and the conductivity is higher in comparison to insulators over a wide range of temperatures. The promotion of electrons from the valence band to the conduction band creates mobile charge carriers; electrons are moving in the conduction band and holes travel in the valence band. The decrease of temperature in semiconductors causes an increase of resistivity because the band gap energy stays the same over the whole temperature range but there are fewer electrons in the conduction band at lower temperatures (Figure 1.2).

Molecular Conductors Based on $M^+(TCNQ)^{\bullet-}$ Salts: Some of the earliest examples of materials with a transition from a semiconducting to an insulating state due to a phase transition include the family of $M^+(TCNQ)^{\bullet-}$ alkali salts. The semiconducting state has segregated columns of cations and evenly spaced TCNQ mono-reduced molecules within the stack of $M^+(TCNQ)^{\bullet-}$ alkali salts (Figure 1.3). The electrons travel along the TCNQ columns, thus these materials are considered to be 1D semiconductors, also known as 1D Mott insulators.

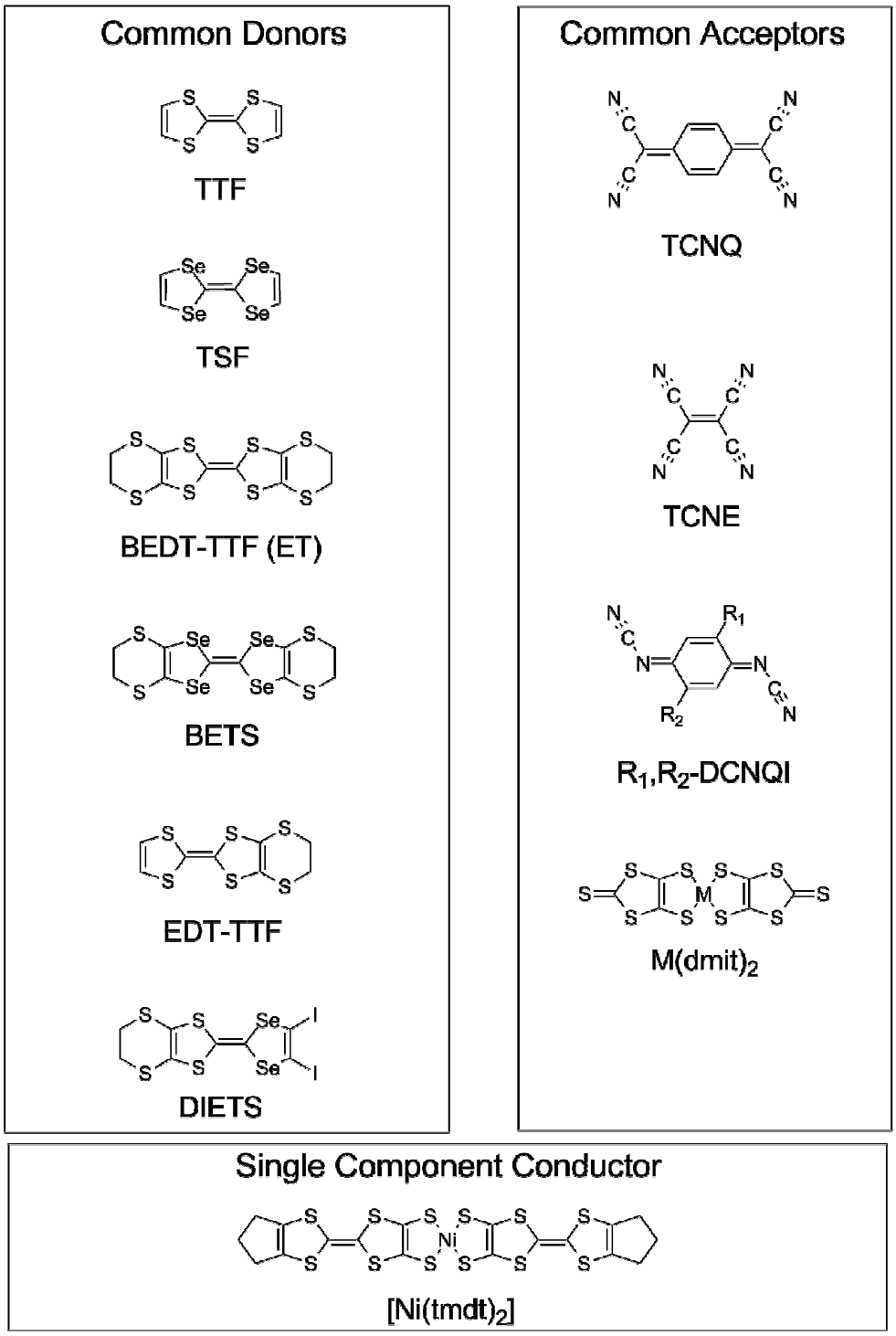

Figure 1.1 Common organic donors and acceptors used to obtain conducting materials and an example of a single component conductor.

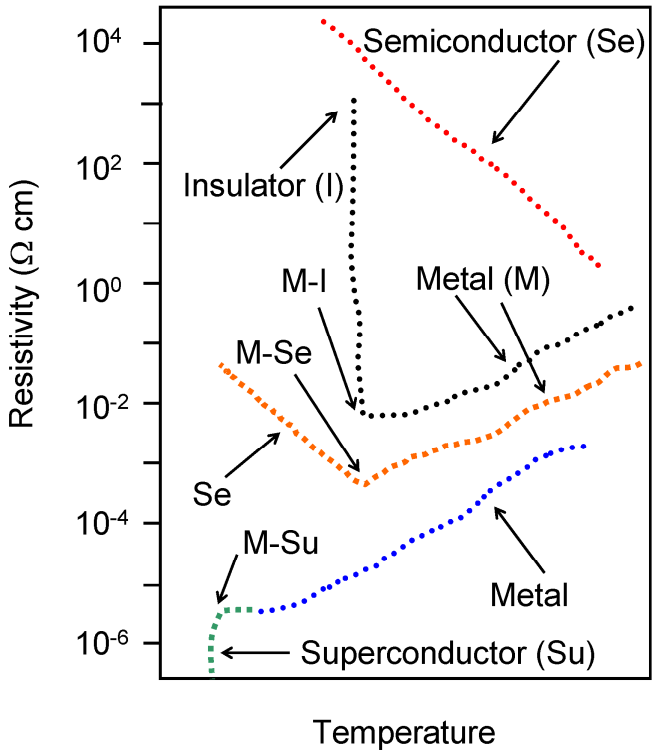

Figure 1.2 Temperature dependence of the resistivity for several conducting behaviors. Su = Superconductor, M = Metal, Se = Semiconductor, I = Insulator, M-I = Metal to insulator transition, M-Se = Metal to semiconductor transition, M-Su = Metal to superconductor transition.

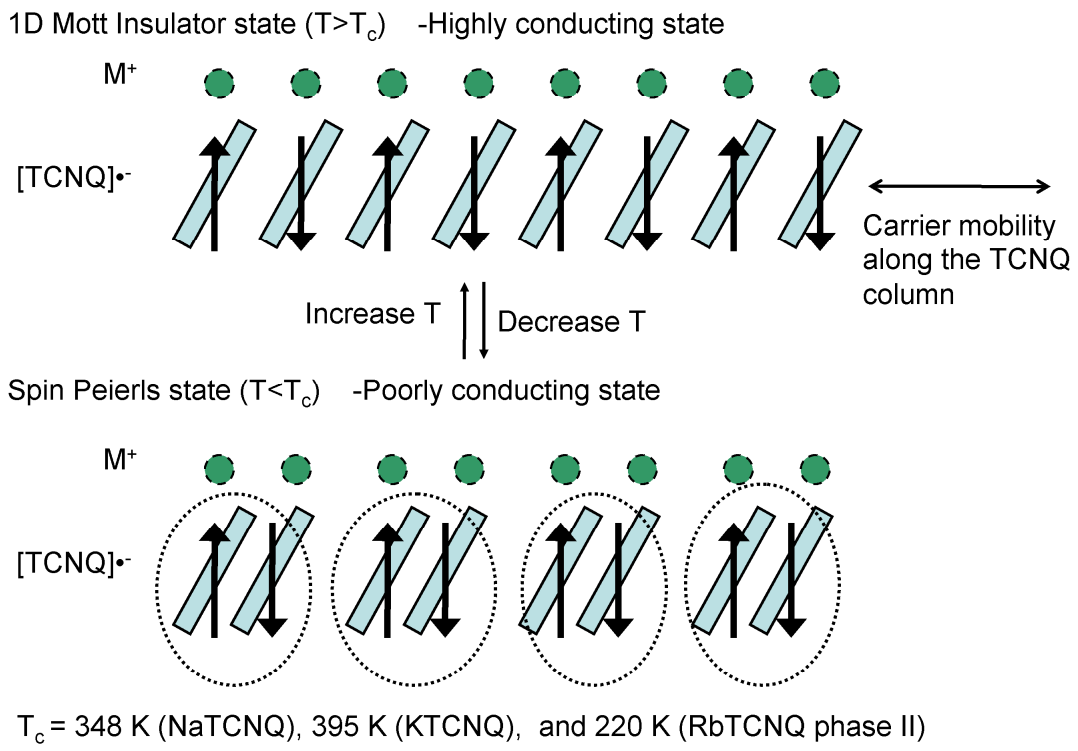

Figure 1.3 Schematic representation of the transition between a 1D Mott insulator and a spin Peierls state in a $M^+[TCNQ]^{\bullet-}$ material.

The TCNQ molecules undergo a dimerization within the stack at a particular temperature, resulting in an insulating phase composed of π-$(TCNQ^{\bullet-})_2$ dimers, which is referred to as the Peierls transition; T_c = 348 K (Na-TCNQ),[13] 395 K (K-TCNQ),[14] and 220 K (Rb-TCNQ phase II)[15] (Figure 1.3). Stabilization of the high temperature structure and therefore the stabilization of the Mott insulator state is a target goal for such materials. The transition is observed at high temperatures for the alkali metal salts of TCNQ because the interactions between the TCNQ radical anions and the cations is ionic and weak.

Molecular Conductors Based on $M^{+}(TCNQ)^{\bullet-}$ Metal Organic Frameworks: Semiconductors based on coordination framework solids such as Cu(TCNQ) and Ag(TCNQ) offer an advantage over the alkali metal salts of TCNQ because the coordination bonds maintain the ligands in a fixed position, thus preventing the dimerization that leads to a phase transition (Figure 1.3). The crystal structures of Cu(TCNQ) phase I reported by Dunbar and coworkers (Figure 1.4)[16] and Ag(TCNQ) reported by Shields (Figure 1.5)[17] adopt a common topology, which involves metal ions in a highly distorted tetrahedral environment with μ_4-TCNQ ligands arranged in segregated stacks of TCNQ along the short axis. The stacks contain $(TCNQ)^{\bullet-}$ radicals with a regular stacking distance of 3.2 Å for Cu(TCNQ) phase I and alternating short-long distances for Ag(TCNQ) in which there are 3.30 Å and 3.48 Å distances in one column, and 3.13 Å and 3.40 Å for another stack. The adjacent stacks of TCNQ are rotated by 90º with respect to each other (Figures 1.4 and 1.5).

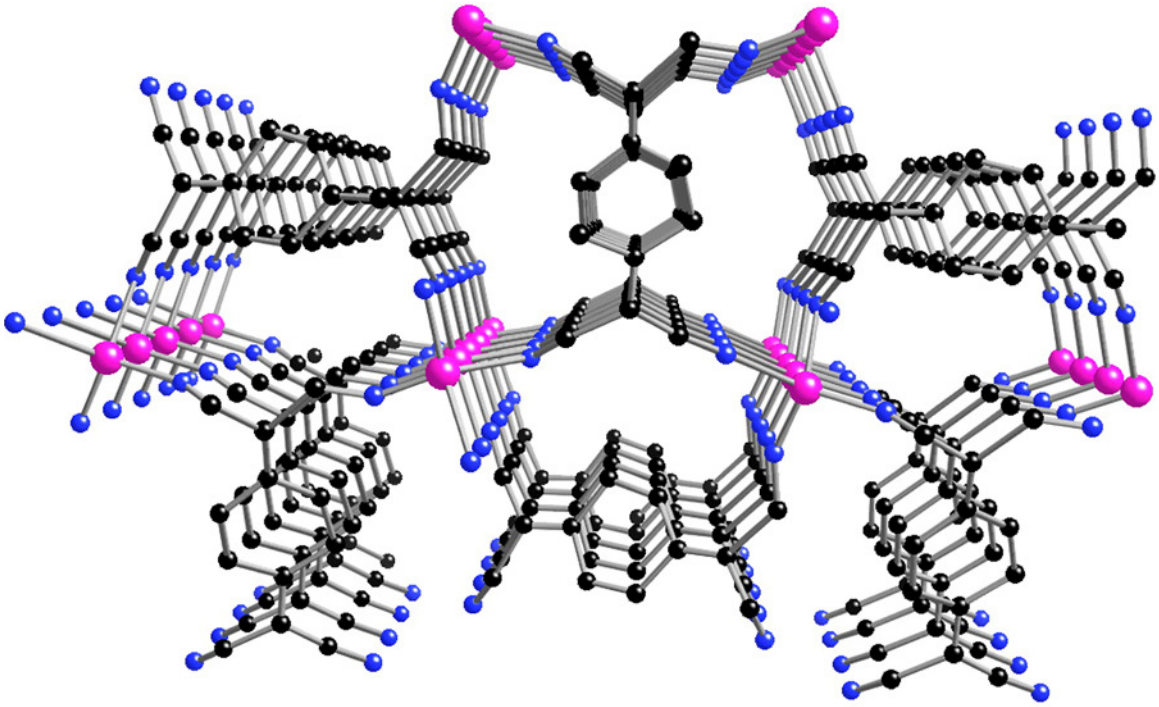

Figure 1.4 A perspective view of Cu(TCNQ) phase I. The hydrogen atoms are omitted for the sake of clarity. Cu = pink, N = blue, C = black.

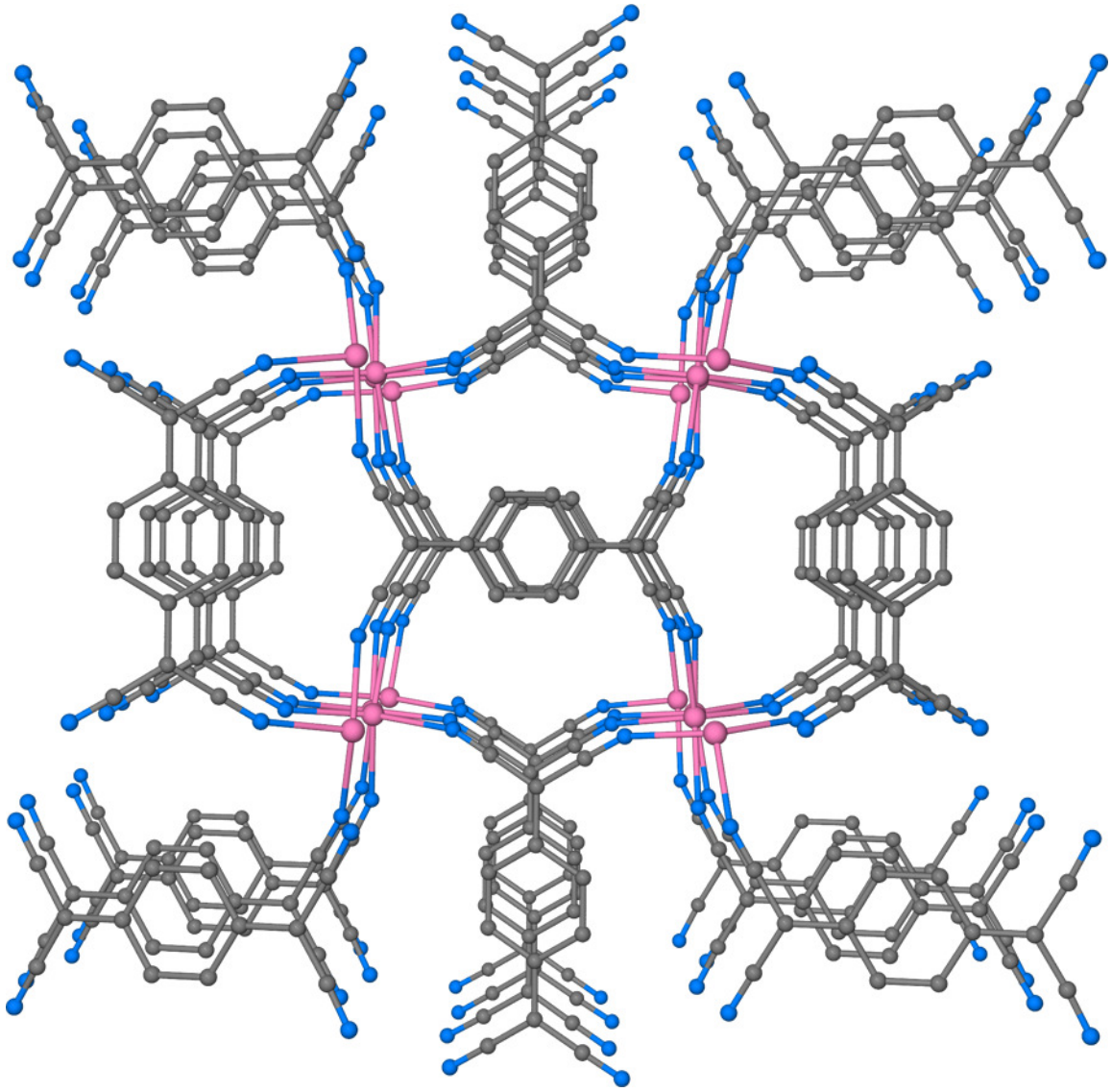

Figure 1.5 A perspective view of Ag(TCNQ) emphasizing the π-π stacking along the short axis. The hydrogen atoms are omitted for the sake of clarity. Ag = pink, N = blue, C = gray.

The high conductivity of Cu(TCNQ) phase I (2.5 x 10^{-1} Scm^{-1}) stems from the mono-reduced TCNQ units being arranged in columns with a regular stacking distance of 3.2 Å. The lower conductivity of Ag(TCNQ) (3.6 x 10^{-4} Scm^{-1}) can be correlated to the irregular and larger separation of the TCNQ units in comparison to Cu(TCNQ) phase I. Crystalline polymorphs were reported by Dunbar and coworkers for Cu(TCNQ); the kinetic phase Cu(TCNQ) phase I forms first and is converted into the thermodynamic phase Cu(TCNQ) phase II if phase I is left in contact with acetonitrile solutions.[16] Cu(TCNQ) phase II differs from phase I in that the TCNQ ligands are parallel to each other throughout the extended framework. There are two interpenetrating lattices in phase II but this situation does not bring the TCNQ groups into close contact; rather the TCNQ rings are "slipped" and no π-stacking occurs. Moreover, the closest distance between parallel TCNQ units in the same network is 6.8 Å (Figure 1.6).

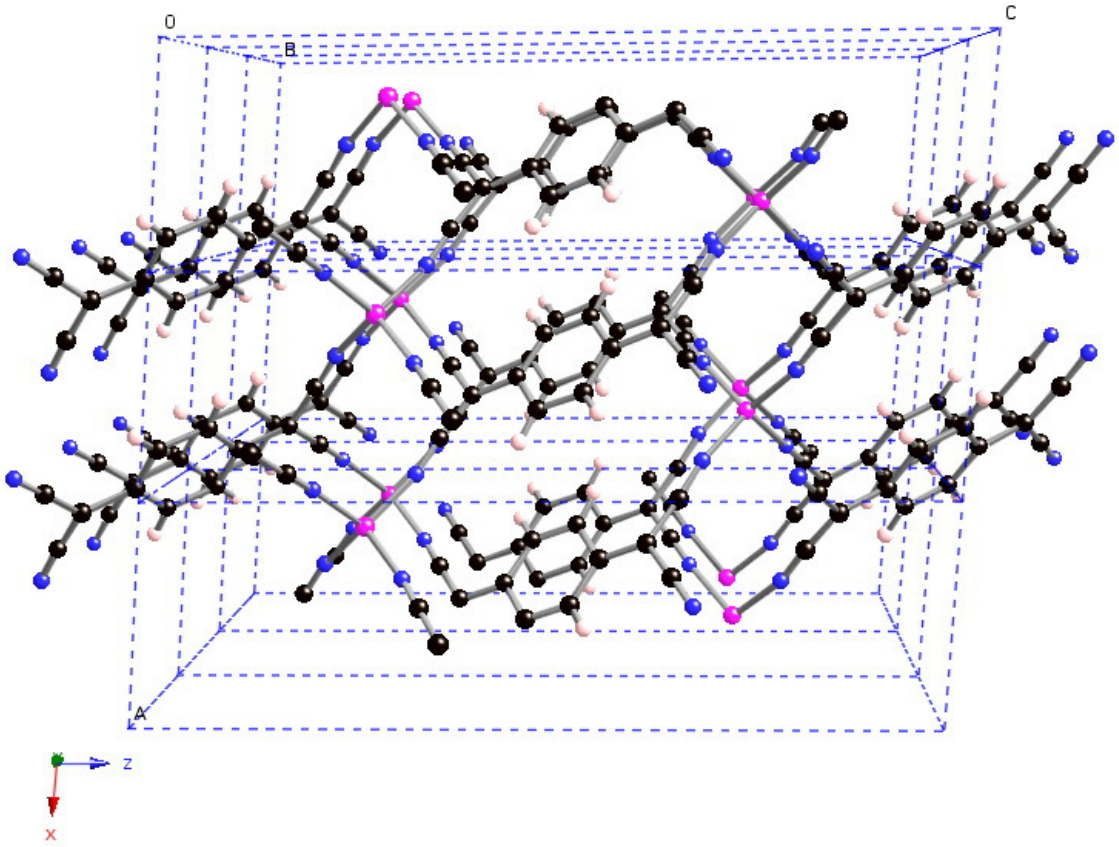

Figure 1.6 A perspective view of Cu(TCNQ) phase II, structure type B, in which the TCNQ···TCNQ interplanar distance is 6.8 Å and therefore there are no π interactions between TCNQ groups. Cu = pink, N = blue, C = gray, H = light pink.

Molecular Conductors Based on TTF Radical Cations: The interest in molecular conductors continued to grow, and from 1969 to 1972 the TTF (tetrathiafulvalene) molecule was synthesized by the groups of Coffen,[18] Wudl,[19] and Hünig;[20] this molecule is a excellent electron donor and its reactivity was tested with several organic acceptors (Figure 1.1). The combination of TTF and TCNQ resulted in the first purely organic charge transfer salt, $TTF^{\delta+}TCNQ^{\delta-}$ ($\delta \sim 0.59$), which exhibits metallic conductivity and a room temperature low resistivity of $\sim 10^{-3}$ Ωcm with a metal-to-insulator transition at ~ 50 K. The TTF-TCNQ material exhibits metallic conductivity due to the partially reduced units that are arranged in segregated columns with an even separation between the stacked units (Figure 1.7). The abrupt change of conductivity in TTF-TCNQ crystals is due to a Peierls transition.

As mentioned earlier, one of the most interesting aspects of the M(TCNQ) and TTF-TCNQ materials is their conduction pathway. Both types of conductors consist of segregated columns of anions and cations and the electrons can only travel within the column leading to 1D conductivity, which was unprecedented at the time of their discovery; all previously known conventional conductors were of the 3D type. The observation of anisotropic conductivity captured the attention of many physicists who proceeded to study this phenomenon as well as chemists who sought to prepare new types of 1D materials with unusual properties.

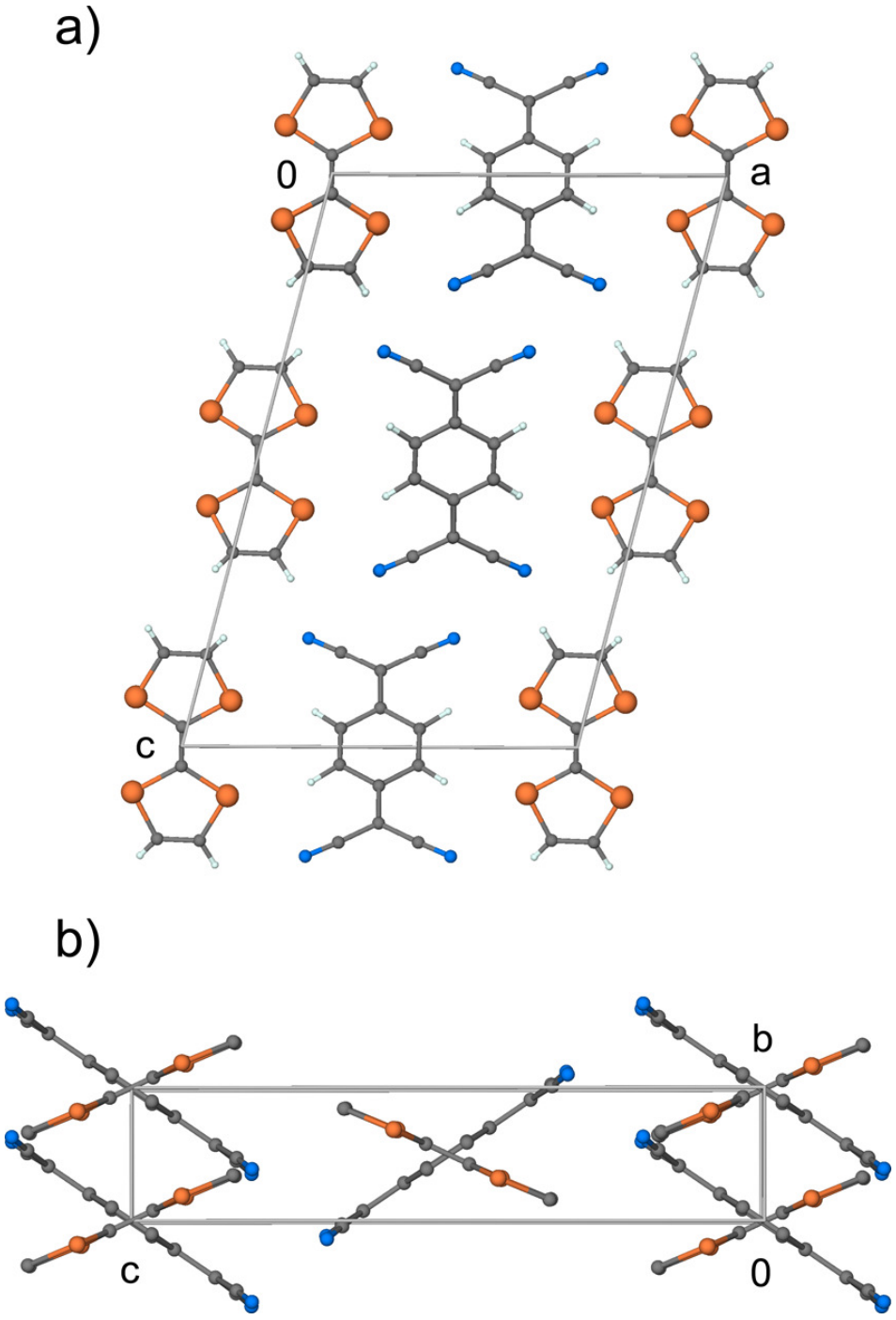

Figure 1.7 Packing diagram of TTF-TCNQ viewed along the *b* axis (a), and along the *a* axis (b) depicting the stacking of segregated donor acceptor columns. S = orange, N = blue, C = gray, H = white.

In a classical metal, such as copper, the conduction electrons are shared by all the metal atoms. The metallic state is a result of the fact that electrons occupy the conduction band and therefore the conductivity is much higher than that of semiconductors. By comparison, the metallic conductivity of TTF-TCNQ is due to two factors: 1) a small on-site electron-electron repulsion because there is only partial charge transfer, thus electrons can hop to the next molecule within the column with lower probabilities to encounter another electron already residing at the new location and 2) a good overlap of the TTF units due to favorable sulfur···sulfur contacts along the stack. Physicists made the following predictions as to how the conducting properties of these materials could be enhanced: a) by using larger molecules with more conjugated bonds which should lead to a smaller onsite electron-electron repulsion; b) by preparing derivatives of the molecules with better overlaps in the columns which could be achieved if more sulfur atoms were included in the molecules to increase the number of sulfur···sulfur contacts in the donor stack; c) by replacing sulfur atoms in the TTF molecule with more polarizable selenium atoms which would also lead to a better overlap of the molecules in the column and thus higher conductivity and d) by circumventing the Peierls dimerized state by using molecules with intermolecular interactions between units from adjacent columns such as hydrogen bonding, metal coordination bonds, or sulfur···sulfur contacts. By following these rules of thumb chemists proceeded to synthesize extended TTF derivatives such as BEDT-TTF (ET) (bis(ethylenedithio)-tetrathiafulvalene) and EDT-TTF (ethylenedithio-tetrathiafulvalene) which are examples of widely used symmetric and asymmetric extended versions of

TTF respectively (Figure 1.1). In fact, the family of ET hybrid organic/inorganic salts comprises the largest number of molecular superconductors with more than one hundred reports having appeared by 2007.[21] The synthesis of TTF derivatives was extended to include selenium based analogues TSF (tetraselenafulvalene) and mixed selenium sulfur molecules such as BEDT-TSF (BEDT-TSF = BETS = bis(ethylenedithio)tetraselenafulvalene) and DIETS (diiodo(ethylenedithio)diselenadithiafulvalene) (Figure 1.1). The enormous efforts put forth in this vein were rapidly rewarded as exemplified by the exciting report in 1980 by Jérome and coworkers on the unprecedented superconductivity behavior of the organic-inorganic hybrid salt $(TMTSF)_2PF_6$ (TMTSF = (tetramethyl)-tetraselenafulvalene) under pressure.[22] The resistivity of a metal decreases by decreasing the temperature (Figure 1.2), due to less lattice vibrations interfering with the movement of electrons. On rare occasions, a zero resistivity state, namely the superconducting state, can be achieved and the electrons can freely move below the transition temperature (Figure 1.2). The observation of superconductivity is unusual because the zero resistivity state cannot be reached if there are impurities in the material or if there are imperfections (defects) in the lattice.

In terms of comparison, metallic conductivity is rarely observed for TCNQ charge-transfer salts because the ligand is typically present as the mono-reduced species; a few examples of those materials that do exhibit metallic behavior are TMTSF(TCNQ), $TSF{\cdot}Et_2(TCNQ)$,[23] $TTT(TCNQ)_2$ (TTT = tetrathiotetracene), and $TSeT(TCNQ)_2$ (TSeT = tetraselenotetracene).[24] The strategy of tuning the conducting properties by ligand

design was applied to TCNQ materials and some examples of superconductors under pressure were reported, namely $(BETS)_2(TCNQX_2)$ (X = Cl, Br).[25]

Molecular Conductors Based on DCNQI Polynitriles: The synthesis of TCNQ derivatives is tedious which, arguably, has stymied the development of new materials based on substituted analogs. A new venue for the field was opened up by Hünig who set out to prepare a ligand analogous to TCNQ that could be easily derivatized. In 1984, Hünig reported a clever one-step synthesis of DCNQI (dicyanoquinonediimine, see Figure 1.1) and its derivatives and initiated investigations into the chemistry of these polynitrile electron acceptors.[26] Hünig prepared *N,N′*-Dicyano-1,4-naphthoquinonediimine charge transfer salts with TTF which, similarly to TTF-TCNQ, behaves as a metal from room temperature to 140 K below which temperature the behavior becomes semiconducting.[27] Extrapolation of the use of the DCNQI acceptors to metal ion coordination chemistry by the Hünig and Kobayashi groups led to the syntheses of materials of general formula $M(R_1,R_2\text{-DCNQI})_2$ (M = Cu, Ag) which are among the most studied series of conducting coordination compounds.[28] In particular, studies performed on the copper compounds revealed that their high metallic conductivity is due to the existence of partially reduced units arranged in segregated columns with an even separation between the stacked units as well as to efficient overlap between the d orbitals on the metal and the p orbitals of the ligands, the consequence of which is high charge mobility through the copper ions in addition to the typical charge transport through the stacks observed in the usual $M^{+}TCNQ^{\bullet -}$ materials (Figure 1.8).[29-35]

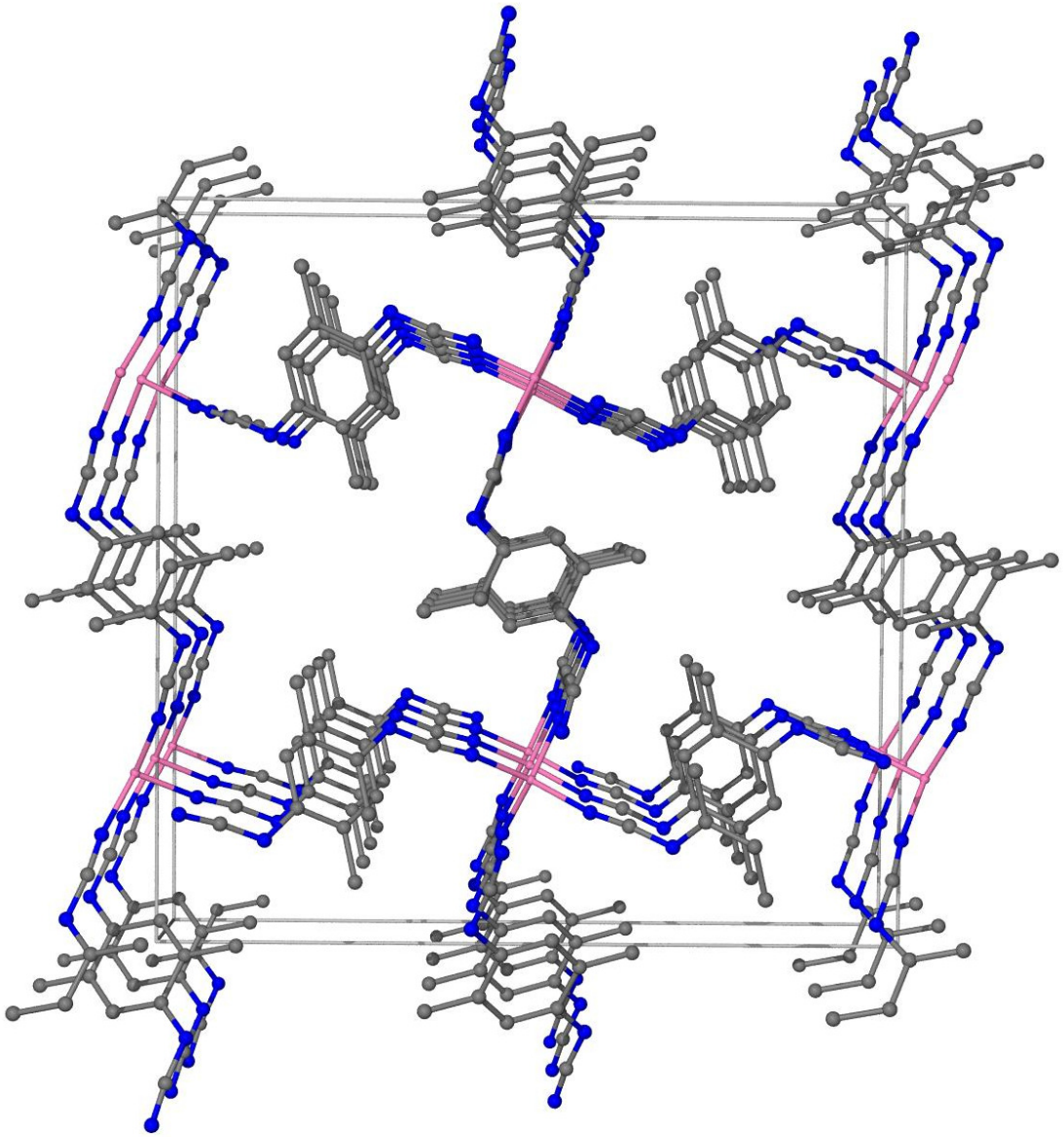

Figure 1.8 A perspective view of $Cu(DM\text{-}DCNQI)_2$ emphasizing the π-π stacking of the polynitrile ligand. The hydrogen atoms are omitted for the sake of clarity. Cu = pink, N = blue, C = gray.

The coordination polymer $Cu(DM\text{-}DCNQI)_2$, (DM-DCNQI = dimethyl-*N*,*N*′-dicyanoquinonediimine) was identified as the most conducting compound of the series due to improved overlap of the metal and ligand orbitals owing to the degree of compression of the copper tetrahedron which is actually observed for the entire series. The ligand design approach played a major role in the $Cu(R_1,R_2\text{-}DCNQI)_2$ isostructural series because steric effects of the R_1 and R_2 substituents leads to variations in the Cu-N angles and helps to tune the degree of compression of the copper tetrahedron; the result is variation in the conducting properties of the coordination polymer.

In addition to the aforementioned cases, there are only a handful of other conductors based on structurally characterized coordination polymers, the aforementioned Cu(TCNQ) phase I (Figure 1.4) by Dunbar,[16] Ag(TCNQ) (Figure 1.5) by Shields,[17] and $M(2,5\text{-}R_1,R_2\text{-}DCNQI)_2$ (M = Cu, Ag; R = CH_3, OCH_3, Cl, Br) by Hünig and Kobayashi, among which $M(2,5\text{-}R_1,R_2\text{-}DCNQI)_2$ is the only series in the literature thus far wherein the ligand substituent approach has been employed.

Single Component Conductors: Thus far, only examples of two component molecular conductors have been described, but it is important to mention that fascinating one-component conductors of a coordination complex have been reported by Kobayashi and coworkers. In particular $Ni(tmdt)_2$ (tmdt = trimethylenetetrathiafulvalenedithiolate) is a metal at room temperature and remains metallic until 0.6 K (Figure 1.9). The single crystals of $Ni(tmdt)_2$ exhibit 3D metallic conductivity due to 3D intermolecular interactions in the solid state.[36]

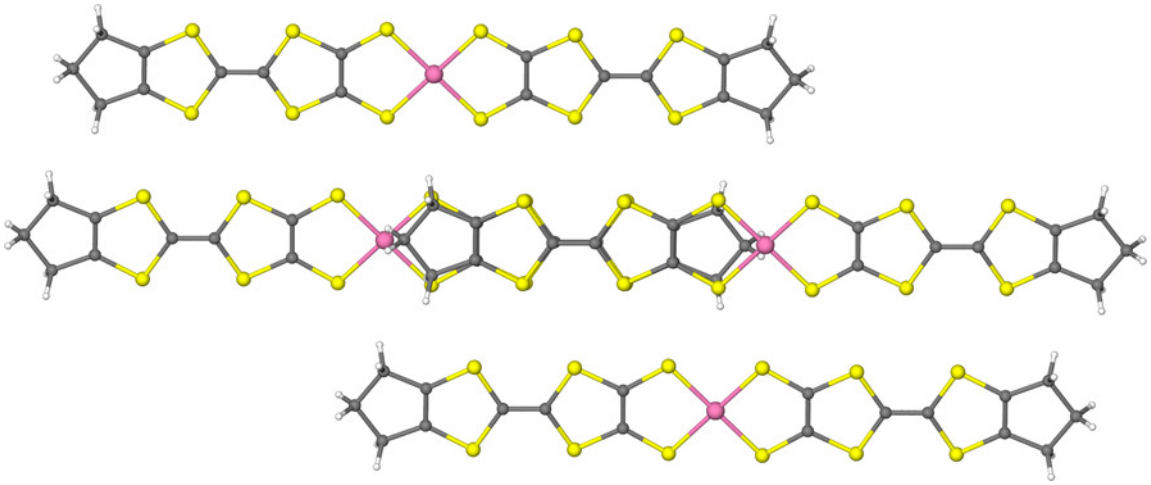

Figure 1.9 A view showing the stacking interactions, along with intra- and inter-stack S···S contacts that lead to metallic conductivity. Ni = pink, S = yellow, C = gray, H = white.

Molecular Magnets

Molecular Magnets followed a similar approach as the aforementioned molecular conductors in terms of crossing into new scientific territory. Traditional magnets based on metal atoms have unpaired electrons on the metal centers that interact with the unpaired electrons of neighboring metal atoms through atomic orbital overlaps. In metal oxide magnets, overlap with the orbitals of oxygen leads to exchange interactions between neighboring metal ions which often leads to magnetic ordering. In principle, materials composed of interacting paramagnetic metal ions can have one of three ground states: (a) a ferromagnetic situation wherein there are ferromagnetic interactions between all the paramagnetic centers with all the spins aligned parallel to each other ($\cdots\uparrow_a\cdots\uparrow_b\cdots$), (b) a ferrimagnetic situation wherein there are antiferromagnetic interactions between adjacent paramagnetic units of different spin states with adjacent spins being aligned antiparallel to each other ($\cdots\uparrow_a\cdots\downarrow_b\cdots$, $a \neq b$, $S_{total} \neq 0$) or (c) a nonmagnetic state when the interactions are antiferromagnetic and the units are of the same spin state ($\cdots\uparrow_a\cdots\downarrow_b\cdots$, $a = b$, $S_{total} = 0$). The temperature dependence of the product of the molar magnetic susceptibility (χ) and the temperature (χT) gives a indication of the interactions between paramagnetic centers: a) in the ferromagnetic case the χT value increases when the temperature is decreased, b) in the antiferromagnetic case the χT value decreases when the temperature is decreased, c) in the paramagnetic case the χT value remains constant at all temperatures, and d) in the diamagnetic case the χT value is negative at all temperatures (Figure 1.10).

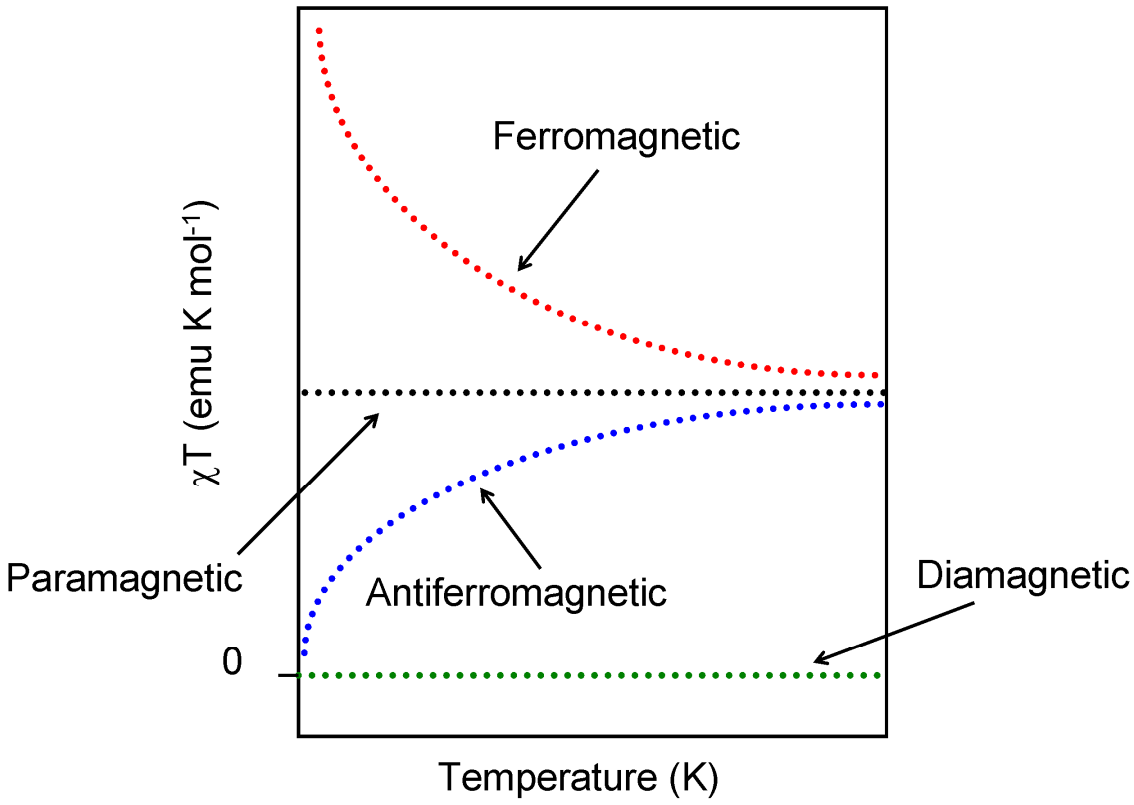

Figure 1.10 Temperature dependence of the χT for several magnetic interactions.

The original main objective of research in molecular magnets was to obtain coordination polymers that exhibit long range magnetic ordering based on paramagnetic metal ions connected by ligands that can engender a strong magnetic communication between the metal centers. Early progress in the field of molecular magnets can be attributed to the pioneer studies performed on Prussian blue by Lewis and coworkers at Bell Labs in 1956 which indicated that such materials are ferromagnets at very low temperatures.[37] The first ferromagnet composed of a molecule, $Fe(diEt\text{-}DTC)_2Cl$ (diEt-DTC = *N*,*N*-diethyldithiocarbamato), was characterized in 1967 by Merritt and coworkers at Bell Labs in 1967; crystals of the molecule exhibit a Curie temperature T_c of 2.5 K.[38] The observation of magnetic ordering for a mononuclear complex was quite surprising and the finding motivated scientists to develop more paramagnetic molecular building blocks that could be used for the realization of additional examples of molecular magnets. The field has evolved since these early examples with a remarkable growth over the past decade due, in part, to the discovery of high-temperature molecule-based magnets,[39] multiproperty magnetic materials[8,40] and single molecule magnets (SMMs).[41]

Magnetic Properties of Materials with Interactions Between TCNX Units (X = Q, E): Early studies of the TCNQ radical anion salts $Cs_2(TCNQ)_3$, $[(C_2H_5)_3NH](TCNQ)_2$, and $[(C_6H_5)_3AsCH_3](TCNQ)_2$ indicated that the magnetic susceptibility is drastically reduced below the Peierls transition and that there is also a strong antiferromagnetic interaction which correlates to the π-dimerization of TCNQ units observed in crystal structures obtained at temperatures below the transition.[42] The organic radicals of TCNX (X = E, Q) can also pair their extra electrons forming a σ bond, in fact σ dimers are by

now common in the literature; the $(TCNX\text{-}TCNX)^{2-}$ units often lead to 2D or 3D frameworks but the magnetic coupling between paramagnetic metal center is negligible because the bridging group is now a large diamagnetic ligand.[39g,43] Another situation that can arise is the formation of the doubly reduced $[TCNX]^{2-}$ dianion by disportionation of interacting TCNX radicals, which is also a diamagnetic ligand, but this dianion is rarely observed in structurally characterized materials.[44-48]

Molecular Magnets Based on TCNE: The first charge transfer molecular magnet was discovered by Miller and coworkers. The material is composed of mixed stacks of $[M(Cp)_2^*][TCNE]$ (M = Mn, Fe; TCNE = tetracyanoethylene (Figure 1.11)) in a $D^+\cdots A^-\cdots D^+\cdots A^-$ array where $D^+ = [M(Cp)_2^*]^{\bullet+}$ and $A^- = [TCNE]^{\bullet-}$. Such materials exhibit ferromagnetic long range ordering at 4.8 K and 8.8 K for the Fe and Mn analogues respectively. It is remarkable that there is no need for a continuous coordination framework in order to observe magnetic ordering, and, in this case, the supramolecular interactions between paramagnetic $[TCNE]^{\bullet-}$ radicals and paramagnetic $[M(Cp)_2^*]^{\bullet+}$ cations is sufficiently strong to lead to ordering.[49] This result and the other aforementioned findings represent an important backdrop for the development of the field which rapidly gathered momentum starting in the 1980's.

Another notable discovery is the amorphous molecule-based magnet of composition $[V(TCNE)_x]\cdot zCH_2Cl_2$ ($x \approx 2$; $z \approx 0.5$)[24] which has a ferromagnetic ordering temperature (T_c) of approximately 400 K, the first high-temperature magnet based on a polynitrile ligand.

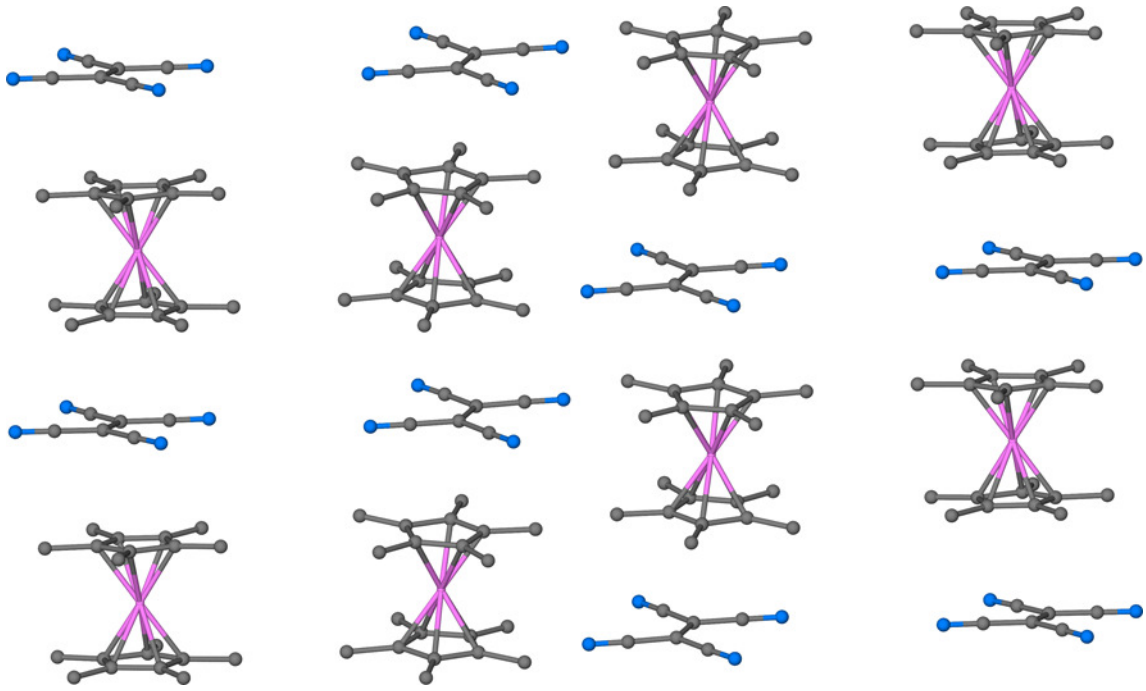

Figure 1.11 A view of $[Fe(Cp)_2^*][TCNE]$ depicting the stacking of mixed donor acceptor columns. The hydrogen atoms are omitted for the sake of clarity. Fe = pink, N = blue, C = gray.

Studies on the $M(TCNE)_2 \cdot xCH_2Cl_2$ (M = Mn, Fe, Co, Ni; x : 0.4-1.1) family of compounds reported by Miller and coworkers indicate that the products tend to be amorphous with only the Fe analogue being partially crystalline. Even in the absence of structural information, these materials are interesting due to their high T_c's: 107 K (Mn), 121 K (Fe), 44 K (Co), and 44 K (Ni).[50]

More recently, the structure of two high temperature magnetic materials with varying dimensionality, namely the 2D $([Fe^{II}(TCNE^{\bullet-})(CH_3CN)]^+[Fe^{III}Cl_4]^-$ (T_c = 90 K)[39f] (Figure 1.12) and the 3D material $[Fe^{II}(TCNE)(\sigma\text{-TCNE-TCNE})_{0.5}] \cdot zCH_2Cl_2$ ($T_c \approx 100$ K) (Figure 1.13),[39g] were determined by high-resolution synchrotron powder diffraction data, a necessity that underscores the difficulty in obtaining suitably large crystals due to the insolubility of the products.

Of particular relevance to the topic of this thesis, the isolation of crystalline binary metal/TCNX (X = E or Q) phases is a challenge that has only been met in a few cases. In fact, even after four decades of studies on the coordination chemistry of TCNX, the structure of $M(TCNX)_2$ binary magnets remains unknown. The TCNX ligands exhibit a variety of binding modes including η_1, μ_2, μ_3, and μ_4, which leads to amorphous materials if several binding modes are randomly distributed in the repeat lattice. The simultaneous formation of different products is also possible, either in the amorphous or crystalline state. The only known structures, to date, of binary phases are the alkali metal semiconductors salts M(TCNQ) (M = Na, K, Rb), $M_2(TCNQ)_3$ (M = Rb, Cs), and the semiconducting coordination polymers of M(TCNQ) (M = Cu, Ag) and the tetra-fluoro derivative $Ag(TCNQF_4)$.[51]

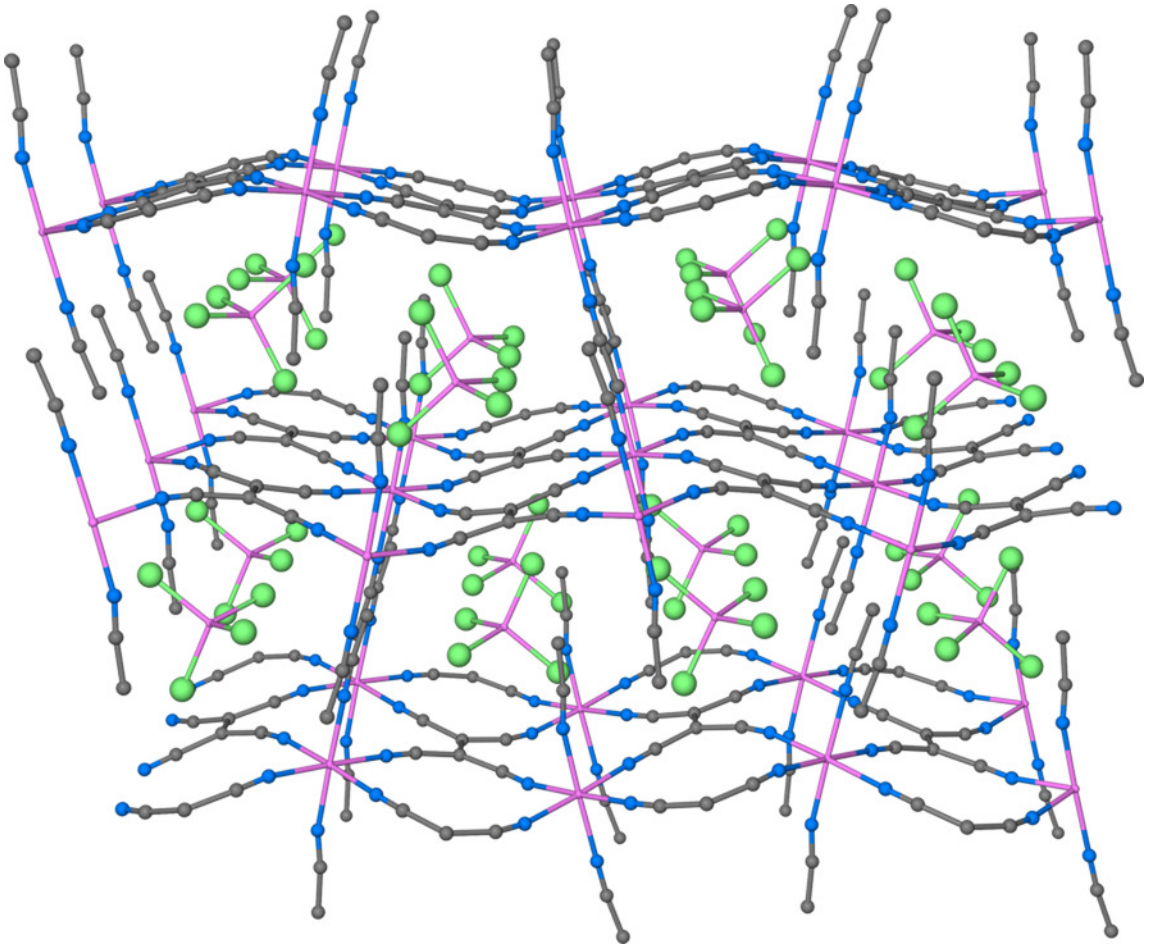

Figure 1.12 A perspective view of $[Fe^{II}(TCNE^{\bullet-})(CH_3CN)]^+[Fe^{III}Cl_4]^-$ depicting the 2D layer. The hydrogen atoms are omitted for the sake of clarity. Fe = pink, Cl = green, N = blue, C = gray.

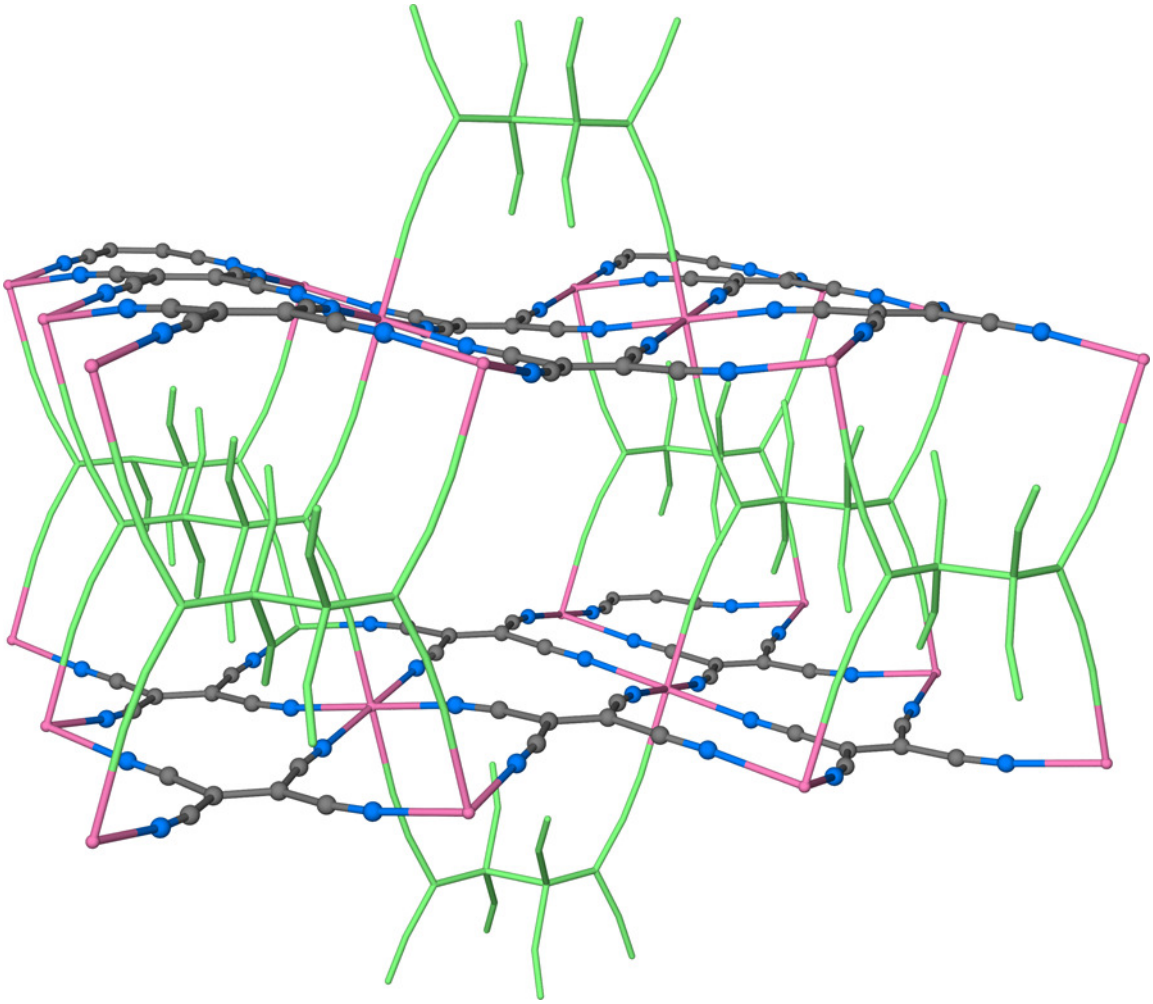

Figure 1.13 A perspective view of $[Fe^{II}(TCNE)(\sigma\text{-TCNE-TCNE})_{0.5}]\cdot z CH_2Cl_2$ depicting the 3D framework. The interstitial solvent molecules are omitted for the sake of clarity. Fe = pink, N = blue, C = gray, σ-TCNE-TCNE = green.

Molecular Magnets Based on 3d Metals and TCNQ: Studies by Dunbar and coworkers[52] and later by Miller and coworkers[53] on binary $M(TCNQ)_2$ materials revealed that the products are crystalline but that the crystals are very small which leads to broad features in the X-Ray powder diffraction pattern. In these cases, the structures could not be solved by fitting the diffraction pattern. The $M(TCNQ)_2$ series is of high interest because the compounds exhibit ferrimagnetic ordering with T_c values of 44 K, 28 K, 7 K, and 24 K for Mn, Fe, Co, and Ni respectively. Although these are lower ordering temperatures as compared to the $M(TCNE)_2 \cdot xCH_2Cl_2$ family, the behavior is nevertheless interesting and structure/property relationship would be of great value in understanding how TCNQ radical anions can be used to make magnets.

Molecular Magnets Based on Metal Ions, TCNQ and Co-ligands: In an effort to obtain valuable structural information, various research groups have opted to study lower dimensionality TCNX coordination compounds in hopes of obtaining crystalline materials that are amenable to structural characterization by conventional single crystal X-ray diffraction techniques. Subsequent correlation of the parameters such as the magnetic coupling constants and g values to the structure is an important exercise. The co-ligands used range from coordinated solvent to mono-, bi-, tri-, tetra-, and pentadentate units, with the resulting coordination polymers with TCNQ ligands exhibiting dimensionality ranging from discrete clusters,[54] 1D,[55] 2D,[39e,56] and 3D architectures.[39i]

Molecular Magnets Based on Metal-Metal Bonded Units and TCNQ: The coordination chemistry of dinuclear complexes and TCNQ has been explored with the motivation of obtaining heterospin extended networks. The first complex in this vein is the donor-acceptor complex reported by Dunbar and coworkers formed upon combination of neutral TCNQ and $Re_2^{II,II}$ units, namely $[Re_2Cl_4(dppm)_2]_2(trans\text{-}\mu_2\text{-}TCNQ)$. The dimer-of-dimers is a paramagnetic coordination compound with unpaired electrons in both the Re_2 moieties and also the TCNQ molecule.[57] There is also electronic delocalization in this 2:1 donor acceptor complex with the following resonance forms being operative: $Re_2^{II,II}\text{-}(TCNQ)^{-1}\text{-}Re_2^{II,III}$, $Re_2^{II,II}\text{-}(TCNQ)^{0}\text{-}Re_2^{II,II}$, and $Re_2^{II,III}\text{-}(TCNQ)^{-1}\text{-}Re_2^{II,II}$. The combination of high electronic delocalization and strong magnetic interactions could potentially lead to molecular conducting/magnetic materials, which is highly desirable. The use of other dimetal complexes in combination with TCNQ and its derivatives resulted in higher dimensionality coordination polymers with a variety of magnetic properties. Dunbar and coworkers obtained 1D ladders of composition $M_2(O_2CCF_3)_4(\mu_4\text{-}TCNQ)_{0.5}$ (M = Mo, Ru) upon combination of neutral TCNQ and $M_2^{II,II}$ units, which exhibited a negligible degree of charge transfer for the Mo_2 analogue.[55a,c] In the case of the Ru_2 analogue there is a small degree of charge transfer and the $TCNQ^{\delta-}$ units are partially reduced (δ = 0.15-0.20). The same Ru_2 paddlewheel complex in combination with TCNQ leads to 2D hexagonal networks which are polymorphs of the 1D chains because the same ratio of 1:2 TCNQ:Ru_2 is obtained for both topologies. The 2D hexagonal network was also obtained for the Rh_2 complex, with general composition of $M_2(O_2CCF_3)_4(\mu_4\text{-}TCNQ)_{0.5}$ (M = Ru, Rh). Both

compounds exhibit partial charge transfer with δ values of -0.42 and -0.63 for Ru_2 and Rh_2 containing compounds respectively. The Ru_2 analogue exhibits a strong antiferromagnetic interaction between Ru_2 units through the TCNQ bridges.

The use of TCNQ is attractive in this case because the electron accepting ability can be enhanced by using TCNQ derivatives with electron withdrawing groups on the quinoid ring. We recently reported, in collaboration with Miyasaka at Tohoku University, a 2D diruthenium-$TCNQF_4$ metamagnet of composition $\{[\{Ru_2(O_2CCF_3)_4\}_2TCNQF_4]\cdot 3(p\text{-xylene})\}_\infty$ which exhibits full electron transfer to the $TCNQF_4$ ligand and also long range magnetic ordering at 95 K (Figure 1.14).[73] More recently, a 3D diruthenium-BTDA-TCNQ ferromagnet of composition $\{[\{Ru_2(O_2CPh\text{-}m\text{-}F)_4\}_2(BTDA\text{-}TCNQ)]\}_\infty$ (*m*-F-$PhCO_2^-$ = *m*-fluorobenzoate, BTDA-TCNQ = bis(1,2,5-thia-diazolo)tetracyanoquino-dimethane)) was reported with a T_c = 107 K (Figure 1.15).[76] The BTDA-TCNQ units are slightly more reduced that the monoanion form with charges ranging from -1.1 to -1.4. The latter two compounds emphasize the influence of dimensionality on the transition temperatures.

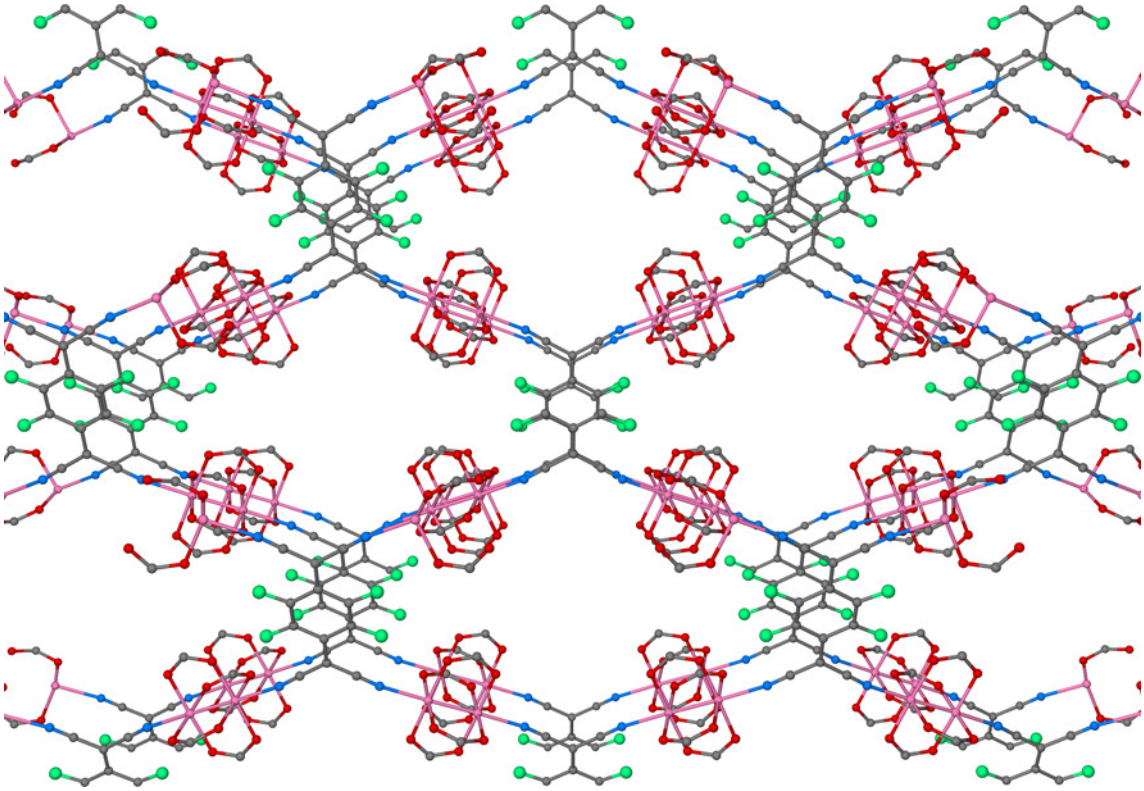

Figure 1.14 A perspective view of $\{[\{Ru_2(O_2CCF_3)_4\}_2TCNQF_4]\cdot 3(p\text{-xylene})\}_\infty$ depicting the 2D layer architecture. The interstitial solvent molecules and CF_3 groups are omitted for the sake of clarity. Ru = pink, F = green, O = red, N = blue, C = gray.

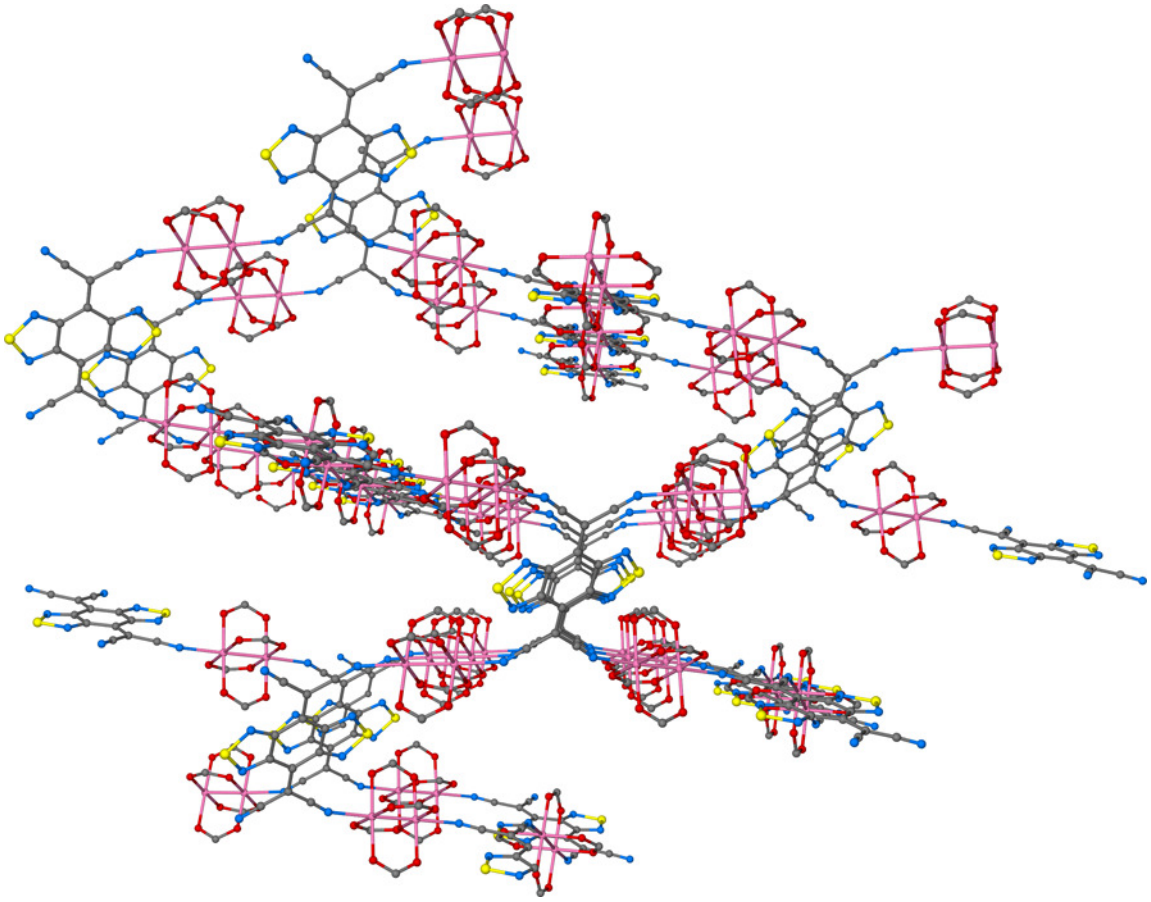

Figure 1.15 A perspective view of $\{[\{Ru_2(O_2CPh\text{-}m\text{-}F)_4\}_2(BTDA\text{-}TCNQ)]\}_\infty$ depicting the 3D framework. The interstitial Ph-*m*-F groups are omitted for the sake of clarity. Ru = pink, S = yellow, O = red, N = blue, C = gray.

Molecular Magnets Based on Prussian Blue Analogues: Prussian blue analogues are another important family of molecular magnets;[58] some of the notable examples of high temperature molecular magnets include $Cr^{II}_3[Cr^{III}(CN)_6]_2\cdot 10H_2O$ (T_N = 240 K), $\{Cs_{0.75}[Cr^{II}_{1.125}[Cr^{III}_{1.00}(CN)_6]_2\cdot 5H_2O\}$ (T_N = 190 K)[39b] and $V^{II}_{0.42}[V^{II}_{0.58}[Cr^{III}(CN)_6]_{0.86}\cdot 2.8H_2O$ (T_N = 315 K)[59] reported by Verdaguer and coworkers as well as $Cs_2Mn^{II}[V^{II}(CN)_6]$ (T_N = 125 K), and $(Et_4N)_{0.5}Mn_{1.25}[V(CN)_5]\cdot 2H_2O$ (T_N = 230 K) reported by Girolami and coworkers.[39c] Verdaguer recently reported additional mixed V/Cr Prussian blue analogues with magnetic orderings above room temperature; these materials have complex formulae that include alkali metal cations: $(TBA)_{0.02}K_{0.48}V[Cr(CN)_6]_{0.84}\cdot(TBAI)_{0.17}2.35H_2O$ (T_N = 360 K), $(TBA)_{0.08}Rb_{0.44}V[Cr(CN)_6]_{0.84}\cdot(TBAI)_{0.01}3.3H_2O\cdot 0.7EtOH$ (T_N = 346 K), and $(TBA)_{0.09}Cs_{0.4}V[Cr(CN)_6]_{0.83}\cdot(TBAI)_{0.015}5H_2O\cdot 0.85EtOH$ (T_N = 340 K).[39i] The family of high temperature Prussian blue-like analogues has been extended to the octacyanoniobate building block material as well. The material $K_{0.10}V^{II}_{0.54}[V^{III}_{1.24}[Nb^{IV}(CN)_8]\cdot(SO_4)_{0.45}\cdot 6.8H_2O$ was recently prepared by Ohkoshi and coworkers and exhibits antiferromagnetic interactions with an ordering temperature T_N = 138 K.[39j]

Single Molecule Magnets (SMMs)

During the course of research in the area of discrete molecular oxide containing clusters, an extraordinary finding was made, namely that molecules can exhibit hysteresis reminiscent of bulk magnets. These compounds became known as Single Molecule Magnets (SMMs). The most studied, and also the first example of an SMM, is the so-called "Mn_{12} acetate" cluster. The Mn_{12} molecule $[Mn_{12}O_{12}(OOCH_3)_{16}(H_2O)_4]\cdot 4H_2O\cdot 2CH_3COOH$ with an S=10 ground state, was first structurally characterized by Lis in 1980,[60] but the unusual SMM behavior was not recognized until further magnetic studies were performed independently by Gatteschi's and the collaborative groups of Chiristou and Hendrickson in the early 1990's (Figure 1.16).[41a-d] The magnetic hysteresis observed for crystals and frozen solutions of Mn_{12} originates from the cluster itself due to the presence of an energy barrier (U) in SMMs that separates the +S and –S ground states with the barrier height being dependent on the magnitude of the axial ZFS parameter $-D_z$. The energy barrier (U) is related to the ground spin state (S) and the negative zero-field splitting term (D) of the molecule by $S^2|D|$ and $(S^2\text{-}1/4)|D|$ for integer and half integer S values respectively. For the recording of the hysteresis loop the sample is magnetized until the M_s saturation point (S_{total} = 10 for Mn_{12}) and the material remains magnetized even after removing the field if the temperature is kept below the blocking temperature because the energy in the material is not sufficient to overcome the energy barrier.

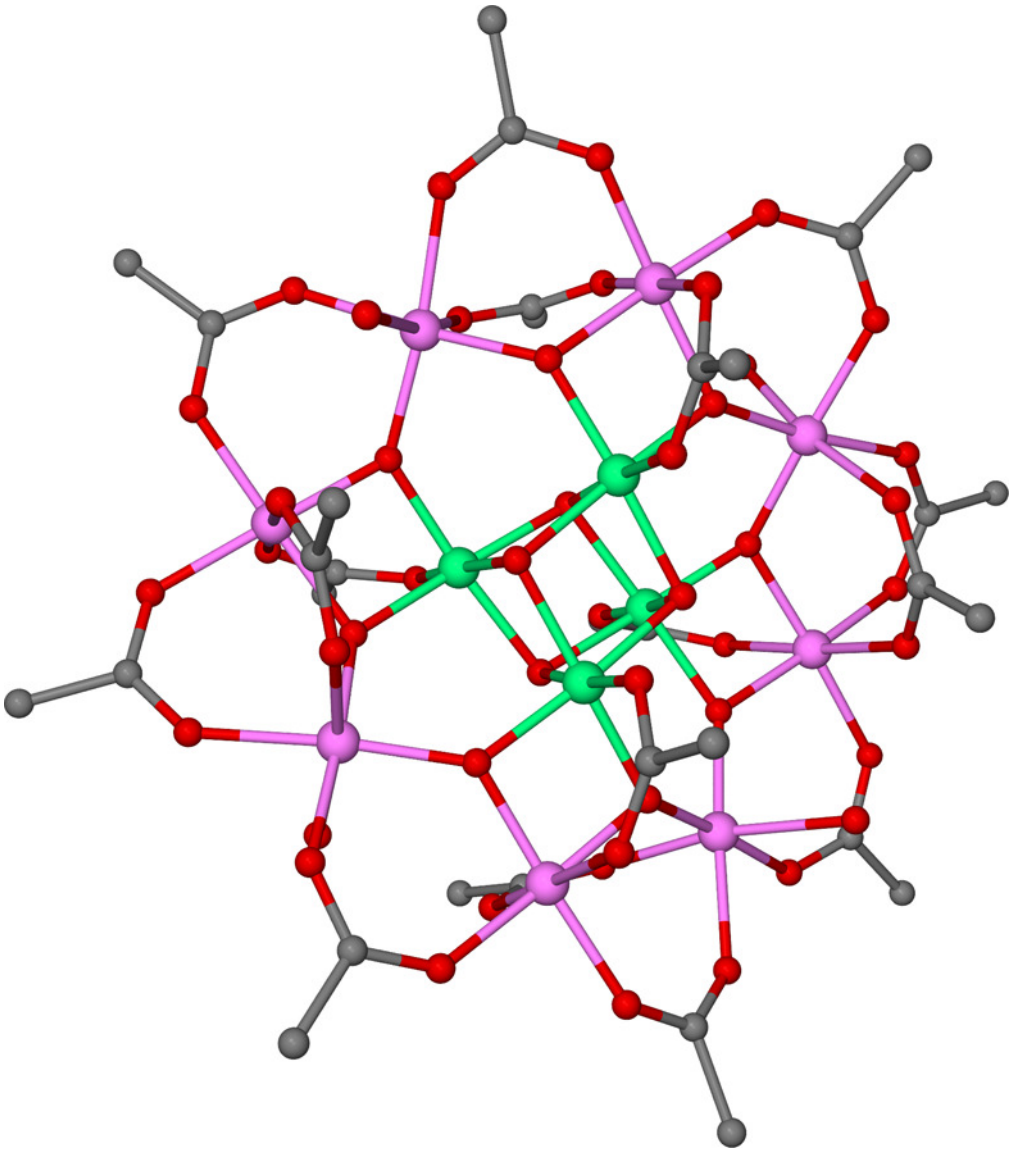

Figure 1.16 The structure of $[Mn_{12}O_{12}(OOCH_3)_{16}(H_2O)_4]\cdot 4H_2O\cdot 2CH_3COOH$ (Mn12 acetate). The interstitial solvent molecules and hydrogen atoms are omitted for the sake of clarity. Mn^{III} = pink, Mn^{IV} = green, O = red, C = gray.

The opposite state can be obtained if the magnetic field is reversed thereby passing through a field where the magnetization is lost (coercive field) until saturation $-M_s$ is reached ($S_{total} = -10$ for Mn_{12}); again the sample remains magnetized if the temperature is below the blocking temperature. The Mn_{12} SMM family has been discussed as a proof-of-concept for the potential use of molecules in binary memory devices due to their magnetic bistability.

In principle, a single cluster can be magnetized "up" ($S_{total} = 10$, 1 state), erased by applying the coercive field, magnetized "down" ($S_{total} = 10$, 0 state), erased again and rewrite either 1 or 0 states (Figure 1.17). The goal is to have binary information stored in the smallest space possible, thus small molecules are a reasonable alternative to the conventional data storage in magnetic nanoparticles which cannot be reduced to very small sizes because the magnetization is lost after a critical particle size. Single molecule magnets are nanosized objects and, at such dimensions, quantum events become important. Indeed, quantum tunneling has been observed for SMMs, an event that involves a short cut through the energy barrier (U) instead of following the usual pathway which is to traverse the barrier of the double well potential. Quantum tunneling is a drawback for the proposed data storage applications because the tunneling causes the reversal of the magnetization without the need of overcoming the energy barrier that separates the aforementioned ground states, thus data is lost during this event.[61]

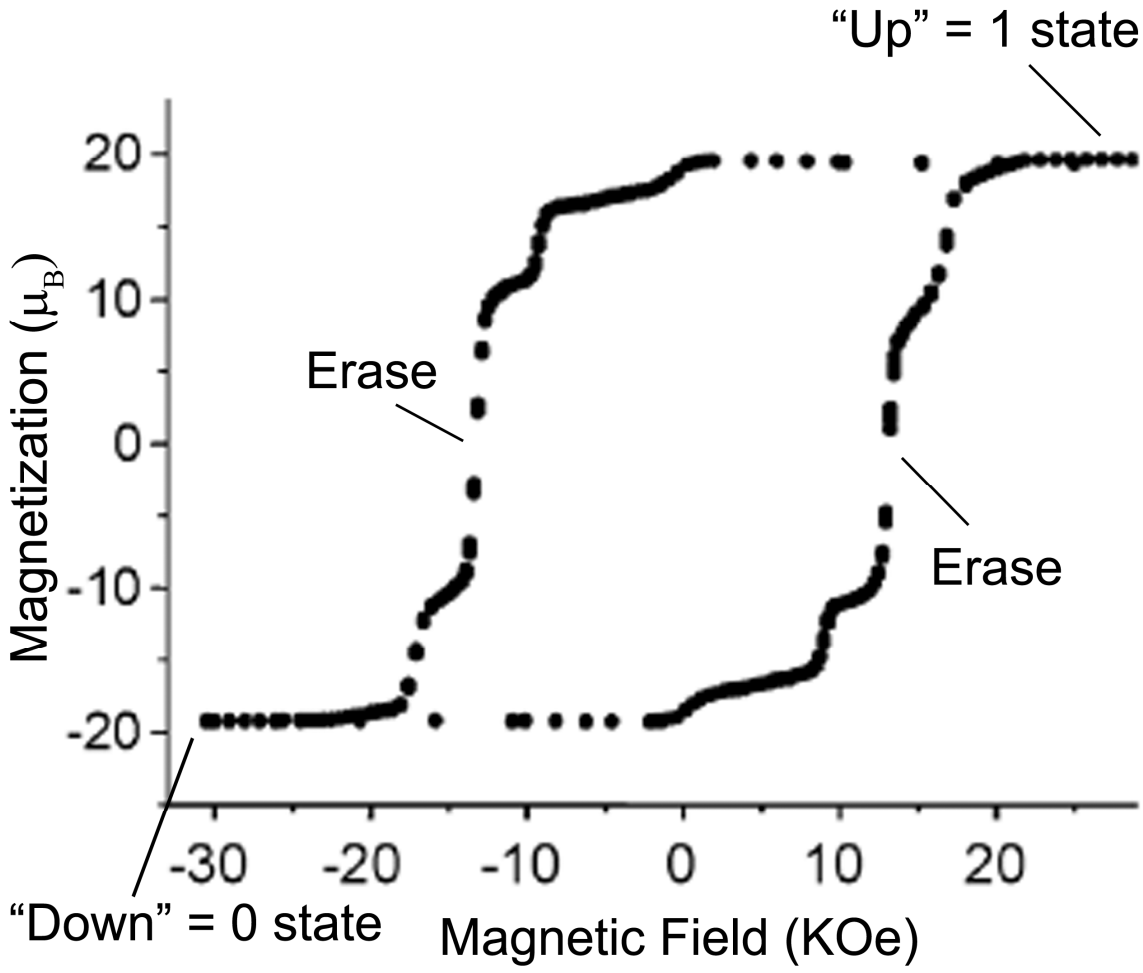

Figure 1.17 Magnetization hysteresis loop for a single crystal of Mn12 acetate with the field parallel to the tetragonal axis measured at 1.9 K.[61] The magnetic bistability can in principle be used for binary data storage, the 0 and 1 states are indicated along with the coercivity field needed to erase, demagnetize, the SMM.

Studies performed on the Mn_{12} compound indicate that the cluster loses its SMM behavior upon deposition on gold surfaces due to distortions of coordination bonds of the metal core and reduction of the cluster by gold. In another such study Sessoli and coworkers deposited a sulphur-functionalized derivative of an Fe_4 SMM, $[Fe_4(L)_2(dpm)_6]$ (H_3L = 11-(acetylthio)-2,2-bis(hydroxymethyl)undecan-1-ol, and Hdpm = dipivaloylmethane), on a gold surface. The SMM behavior was retained due to the redox stability and robust nature of the Fe_4 cluster.[41i]

Quantum Computing and Spintronics on SMMs: Due to the aforementioned findings, there is a growing excitement in molecular nanomagnets for their use in data storage devices.[62,41g] An approach to advances in computing that is receiving enormous attention is based on the manipulation of both spin and electronic degrees of freedom. The field, dubbed "spintronics",[63,64] encompasses a range of novel applications for magnetic materials, but one of the most intriguing ideas that is rapidly gaining credibility in terms of future viability is that the superposition of quantum spin states can be used to perform computations. This concept was first proposed in 1994 by Shor who outlined an algorithm for factorizing numbers with a quantum computer that would be much faster than a classical computer.[65] Three years later, in 1997, Grover published an algorithm for fast database searching with a quantum computer.[66] In support of the hypothesis that molecules hold promise in these applications is the work of Leuenberger and Loss who proposed in 2001 that the Grover algorithm could be applied to a single molecule of Mn_{12} acetate.[67] Theory in the area continues to expand at a rapid pace.[68-71]

Non Volatile Memory Devices

A great deal of current scientific research is being directed at the synthesis and fabrication of nanoscale materials for new types of electronic and magnetic devices. Pressure to reduce the size and improve response times of electronic components has always existed in information technology, but as we approach the miniaturization limits of traditional charge storage estimated to occur by 2016[72] the global quest for faster and more efficient data storage and processing is heightening.[73] One strategy that is being explored for the development of new device components is the pursuit of materials whose bistability is induced by a resistance change rather than current flow. Such "non-volatile" memory devices are capable of operating at increased speeds and they require less energy.

Specifically, with respect to one of the main goals of molecular devices, is the fact that gigantic non-linear response or switching phenomena of materials has been observed in molecule-based organic-containing materials in response to short pulses of low-power external stimuli. Materials are being vigorously pursued that respond to the application of an electric field, light, pressure, or temperature as the basis for electronic devices with ultra-fast operating speeds.[8] For example, spin-crossover complexes such as (Fe(picolylamine)$_3$Cl$_2$(C_2H_5OH)),[74,75] neutral-ionic transition systems represented by (TTF-Chloranil),[76-78] the metallo-organic conductor Cu(DM-DCNQI)$_2$,[28b-35] and the salt (EDO-TTF)$_2$$PF_6$,[79,80] EDO-TTF = ethylendioxy-tetrathiafulvalene, constitute significant examples of simple organic-containing materials that exhibit non-linear phenomena. These materials provide compelling evidence for the contention that molecular solids

may eventually be useful in device applications. In terms of electric field induced behavior, one of the most intensively studied examples is Cu(TCNQ) phase I, described earlier, which exhibits reversible switching from a high resistive state to a conducting state promoted by the application of an electric field or upon irradiation.[81,82]

Coexistence of Conductivity and Magnetism in Molecular Materials

The coexistence of magnetism and conductivity in molecular materials has been observed for a number of systems,[9] for example paramagnetic anions of different volumes combined with partially oxidized TTF and its derivatives exhibit conducting properties ranging from insulators,[83-85] semiconductors,[86-89] metallic conductors,[90-92] to superconductors.[93] Another variation involves materials with antiferromagnetic interactions between paramagnetic units, the results of which are insulators,[94,95] semiconductors,[96-98] metallic conductors[99-101] and superconductors.[102,103] The co-existence of ferromagnetic ordering and metallic conductivity is the most interesting and scare phenomenon; such materials are all based on combinations of charge-transfer salts of TTF derivatives and bimetallic oxalate-bridged anions as reported by Coronado and coworkers (Figure 1.18).[104-107]

Another interesting group of hybrid materials are those in which SMM behavior is combined with conducting properties. The only two examples of such hybrid materials were recently reported by Yamashita and coworkers who combined $[Mn_4]^{4+}$ SMM clusters with platinum maleonitriledithiolate anions which led to a semiconducting SMM material.[108]

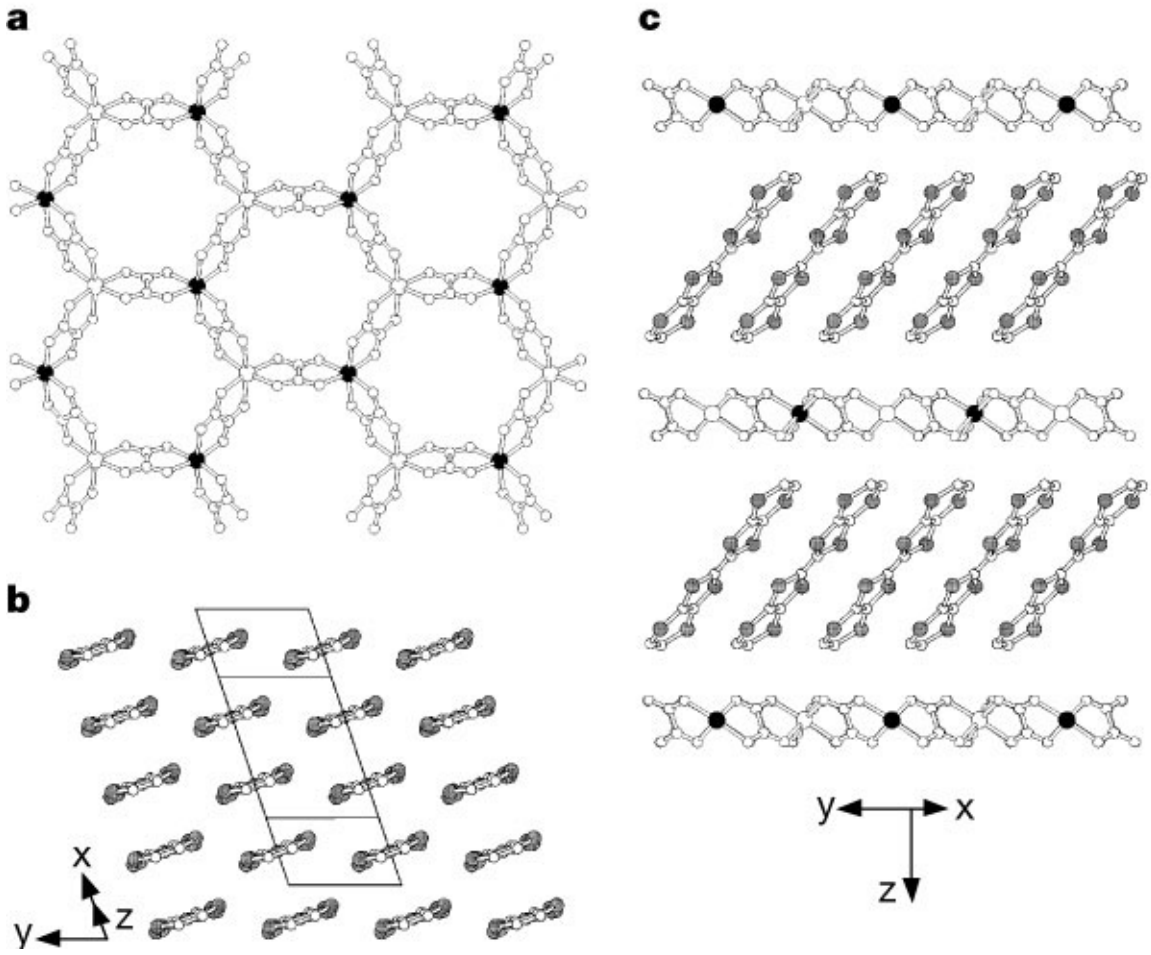

Figure 1.18 Structures of the hybrid material and the two sublattices. a) View of the $[M^{II}M^{III}(C_2O_4)_3]^-$ bimetallic layers. Filled and open circles in the vertices of the hexagons represent the two types of metals. b) Structure of the organic layer, showing the b packing of the BEDT-TTF molecules. c) Representation of the hybrid structure along the c axis, showing the alternating organic/inorganic layers.[104]

The same group also reported similar hybrid materials based on $[Mn_2]^{2+}$ SMMs and $[Ni(dmit)_2]^{0.29-}$ units with semiconducting properties arising from the $[Ni(dmit)_2]$ stacks (dmit = 2-thioxo-1,3-dithiole-4,5-dithiolate, see figure 1.1).[109]

CHAPTER II

SYNTHESES AND PHYSICAL PROPERTIES OF MOLECULAR CONDUCTORS BASED ON Cu(I) IONS AND DISUBSTITUTED TCNQ DERIVATIVES: TUNING THE CONDUCTING PROPERTIES BY LIGAND DESIGN*

Introduction

Organic acceptor molecules such as TCNE, TCNQ and DCNQI occupy a central position in the development of the field of molecular materials (Figure 1.1).[110] Apart from the purely organic research involving these molecules that began in the 1960's, research in the last twenty years from our group and others has demonstrated that metal complexes of organocyanide radicals exhibit fascinating magnetic and conducting properties.[16,39e,h,,43b,51,52,55-57,111-126] The TCNQ molecule is particularly versatile for magnet and conductor applications for a variety of reasons: (a) it is quite stable in the radical anion form, (b) it can exist in a partially reduced form in columnar arrangements that allow for electrons to travel over long distances with small electron-electron repulsions which leads, in some cases to metallic behavior and (c) the redox behavior and properties of materials based on TCNQ can be tuned by altering the substituents on the ring. Since the discovery of TCNQ nearly 50 years ago, [127] the chemistry of this

---

* Reprinted in part with permission from *Advanced Materials,* N. Lopez, H. Zhao, A. Ota, A. V. Prosvirin, E. W. Reinheimer, K. R. Dunbar, "*Unprecedented Binary Semiconductors Based on TCNQ: Single Crystal X-ray Studies and Physical Properties of Cu(TCNQX$_2$) X = Cl, Br*," **2010**, *22*, 986-989.

organic acceptor has spawned a host of compounds with promising properties. In fact, one of the most important findings in the history of molecular metals is the discovery of TTF-TCNQ which is the first organic charge transfer salt to exhibit metallic conductivity. [128]

In terms of the use of the TCNQ anion as an inner sphere group (i.e., a ligand) one of the first examples is Cu(TCNQ) reported in 1962.[42b] This material exhibits remarkable electronic properties and remains one of the most studied, and controversial, TCNQ compounds in the history of the field. Beginning in 1979,[48,49] and for the next 20 years, researchers prepared devices based on micron size Cu(TCNQ) layers sandwiched between a copper and a top electrode, typically Al. The device responds to a threshold potential by becoming conducting, a state that persists until the reverse potential reverts it back to an initial, poorly conducting, state. These Cu(TCNQ) devices were studied for many years without knowledge of the purity or structural data despite the fact that the properties were not reproducible from one laboratory to another - a hint that something was definitely awry. This situation stymied research in the area with the result being a decrease in activity surrounding TCNQ switching materials. Our report of the two different crystal forms and their X-ray structures in 1999, however, offered new hope that these insoluble materials were not impossible to characterize.[59] In the last ten years, there has been a renewed interest in Cu(TCNQ), especially in devices, because researchers now realize that the diffraction patterns of pure films or nanocrystals that undergo switching matches the XRD of what we reported as the kinetic phase (or Phase

I) of Cu(TCNQ). This case study epitomizes the peril in attempting to understand and tailor molecular materials in the absence of structural information.

The proposed mechanisms of the resistance change, switching effect, of the thin film of Cu-TCNQ are categorized into the following three groups: 1) The switching is postulated to occur by the electric field induced phase transition of Cu-TCNQ ($[Cu^{+}\text{-}TCNQ^{\bullet -}]_n$ "off state" $\rightarrow$ $[Cu^0]_x + [TCNQ^0]_x + [Cu^{+}\text{-}TCNQ^{-}]_{n-x}$ "on state");[81] 2) The switching is postulated to occur in the aluminum oxide layer between Cu-TCNQ film and Al electrode, and Cu-TCNQ assists the change in the oxide layer;[129] and 3) Cu metal filament forms a short circuit through the Cu-TCNQ thin film by the electrochemical reaction upon switching.[130]

From the aforementioned discussion, it is clear that Cu(TCNQ) is an excellent candidate for non-volatile memory due to its reversible switching from a high resistive state to a conducting state promoted by the application of an electric field or upon irradiation.[81,82] The promise for commercial applications is sufficiently high such that researchers have fabricated devices with nanowires, nanorods and nanoribbons of Cu(TCNQ) as well as Ag(TCNQ).[4,131-135] The extraordinary properties observed for Cu(TCNQ) have spurred the exploration of numerous strategies to obtain crystalline phases of Cu(TCNQ); these efforts include spontaneous electrolysis,[136] reduction of TCNQ with CuI,[16] vapor deposition of TCNQ on Cu,[137] photocrystallization,[138] electrocrystallization,[139] physical chemical vapor combined deposition and vacuum co-deposition.[140] The only known instance wherein crystals sufficiently large for single crystal data collection were obtained is the work from our laboratories a number of years

ago which led to the determination of marginal single-crystal X-ray data obtained on very tiny crystals of Cu(TCNQ). During the course of our studies, we discovered the previously unrecognized existence of polymorphism in Cu(TCNQ). The materials, which we dubbed phase I and phase II, exhibit marked differences involving not only the arrangements of TCNQ ligands but the infrared spectral, conducting and magnetic properties as well.[16] It was noted in this study that Cu(TCNQ) phase I (Figure 1.4) and the only other previously analog that had been structurally characterized, namely Ag(TCNQ) (Figure 1.5),[17] adopt a common structure, referred to hereafter as type-A which involves metal ions in a highly distorted tetrahedral environment with μ_4-TCNQ ligands arranged in segregated stacks of TCNQ along the short axis; the adjacent stacks of TCNQ are rotated by 90º with respect to each other (Figures 1.4 and 1.5). Cu(TCNQ) phase II, defined as structure type-B, differs from phase I in that the TCNQ ligands are parallel to each other throughout the extended framework. There are two interpenetrating lattices in phase II but this situation does not bring the TCNQ groups to close contacts; the TCNQ rings are "slipped" and no π-stacking occurs. Moreover, the closest distance between parallel TCNQ units in the same network is 6.8 Å (Figure 1.6). The types of overlap between TCNQ molecules are shown in Figure 2.1.

Although a vast amount of research has been directed at understanding the Cu(TCNQ) system, analogous materials based on TCNQ derivatives are surprisingly scarce.[141] Given this situation, we recently initiated a broad survey of binary metal-containing TCNQ derivatives in order to probe the steric and electronic influences of the substituent on the structure and properties of these materials.

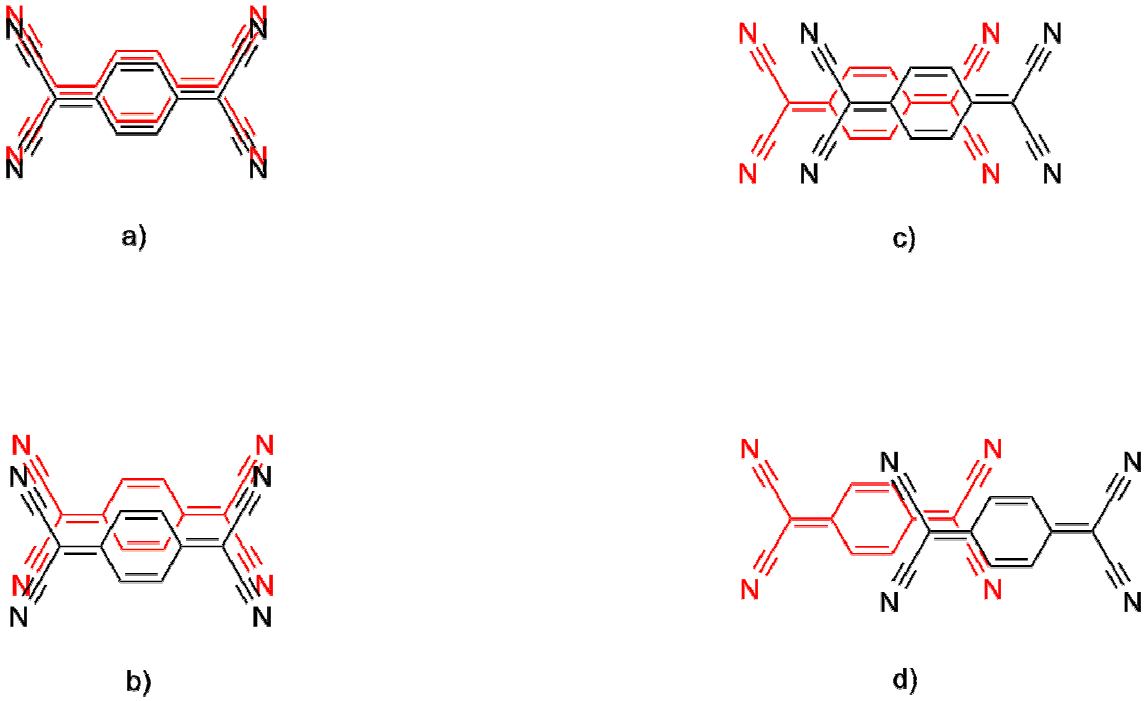

Figure 2.1 Types of overlap for adjacent TCNQ molecules: a) eclipsed ring-over-ring, b) ring-over-ring slipped along the transverse axis, c) ring-over-external bond, and d) external bond-over-external bond.

Results and Discussion

Herein we report the preparation and structural determination of large high-quality crystals of two new isostructural semiconductors based on Cu^{I} ions. The materials are $Cu(TCNQCl_2)$ and $Cu(TCNQBr_2)$ ($TCNQCl_2$ = 2,5-dichloro-7,7,8,8-tetracyanoquinodimethane; $TCNQBr_2$ = 2,5-dibromo-7,7,8,8-tetracyanoquinodimethane).

During the course of these studies a second product was identified by single crystal diffraction studies and found to be the solvated material $Cu(TCNQBr_2)(CH_3CN)$, which contains an acetonitrile molecule in the coordination sphere of the Cu^{I} ions. Related studies of the coordination chemistry of Cu^{I} ions and $TCNQI_2$ (2,5-diiodo-7,7,8,8-tetracyanoquinodimethane) resulted in the isolation of single crystals which include two acetonitrile molecules in the coordination sphere of copper ions, namely $Cu(TCNQI_2)(CH_3CN)_2$. The conductivity of compound $Cu(TCNQCl_2)$ is the highest in the family of 1:1 M^{+}:$(TCNQ)^{\bullet-}$ salts whereas the conductivity of $Cu(TCNQBr_2)$ is comparable to that of Cu(TCNQ) phase I. The three-dimensional architecture of the Cu^{I} ions coordinated to the μ_4-$TCNQX_2$ ligands in $Cu(TCNQCl_2)$ and $Cu(TCNQBr_2)$ is unprecedented among the widely studied Cu(TCNQ) and Ag(TCNQ) compounds and derivatives. Single crystals of all the compounds were obtained by slow diffusion of acetonitrile solutions of CuI and the respective $TCNQX_2$ derivative (X = Cl, Br, I), in a manner akin to the method used to prepare Cu(TCNQ) phase I.[16]

Crystal Structures of Compounds Cu(TCNQX$_2$) (X = Cl, Br): Compounds Cu(TCNQX$_2$) (X = Cl, Br) are isostructural and crystallize in the monoclinic space group C2/c (Table 2.1). The X-ray crystal structures of Cu(TCNQCl$_2$) and Cu(TCNQBr$_2$) at 110 K revealed that as in the case of both phases of Cu(TCNQ), they also crystallize as 3-D frameworks with Cu^I ions coordinated to four different μ_4-$[TCNQX_2]^{\bullet-}$ anions (Figure 2.2). The Cu^I ions are in a highly distorted tetrahedral environment as evidenced by the N-Cu-N angles of Cu(TCNQCl$_2$): 94.73°, 101.77°, 130.89°, and 139.68°; and of Cu(TCNQBr$_2$): 93.21°, 103.32°, 130.81° and 139.77°. The TCNQX$_2$ units are arranged in columnar stacks that propagate along the b axis, with regular TCNQX$_2$•••TCNQX$_2$ stacking distances of 3.300 Å for Cu(TCNQCl$_2$), and 3.372 Å for Cu(TCNQBr$_2$) - significantly longer than the ~3.24 Å observed in the structure of Cu(TCNQ) type-A (Figure 1.4). There is no rotation of TCNQX$_2$ molecules throughout the stacks, consequently the halogen groups lie directly on top of each other for all stacked TCNQX$_2$ groups (Figure 2.2). Given this situation, the TCNQX$_2$•••TCNQX$_2$ distances in the columns are determined by the steric influence of the halogen substituent. The TCNQX$_2$ ligands within a stack are slipped in a ring-over-ring conformation (Figures 2.1b and 2.3). It is important to note that, the X···X distances (Cu(TCNQCl$_2$): Cl···Cl = 3.53 Å, Cu(TCNQBr$_2$): Br···Br = 3.68 Å) in the columns are shorter than the sum of the halogen van der Waals radii (Cl···Cl = 3.60 Å, and Br···Br = 3.80 Å),[142] and that the TCNQX$_2$ ligands are sufficiently close to be engaged in π-π interactions.

Table 2.1 Crystallographic data for the Cu/$TCNQX_2$ coordination compounds.

Compound	$Cu(TCNQCl_2)$	$Cu(TCNQBr_2)$	$Cu(TCNQBr_2)(CH_3CN)$	$Cu(TCNQI_2)(CH_3CN)_2$
Formula	$C_{12}H_2N_4Cl_2Cu$	$C_{12}H_2N_4Br_2Cu$	$C_{14}H_5N_5Br_2Cu$	$C_{16}H_8N_6I_2Cu$
F_w [g mol^{-1}]	336.62	425.53	466.58	601.63
Crystal system	monoclinic	monoclinic	triclinic	monoclinic
Space group	C2/c	C2/c	P-1	C2/c
a [Å]	22.29(1)	22.129(5)	4.1092(8)	20.156(4)
b [Å]	3.534(2)	3.6781(8)	16.653(3)	4.6543(9)
c [Å]	13.657(9)	13.749(3)	20.839(4)	19.747(4)
α [°]	90	90	89.89(3)	90
β [°]	90.59(2)	90.036(4)	90.00(3)	96.668(2)
γ [°]	90	90	82.91(3)	90
V [$Å^3$]	1076(1)	1119.0(4)	1415.1(5)	1840.0(6)
Z	4	4	2	4
ρ_{calc} [g cm^{-3}]	2.078	2.526	2.059	2.172
μ ($Mo_{K\alpha}$) [mm^{-1}]	2.510	9.078	7.186	4.554
Reflections collected	4450	5865	9745	5675
Unique reflections	1324	1330	3780	1522
Reflections with $I > 2\sigma(I)$	1273	1182	1285	1103
parameters	87	87	209	115
R(int)	0.0258	0.0393	0.2425	0.0577
$R1$[a]	0.0218	0.0242	0.1891	0.0336
$wR2$[b]	0.0595	0.0622	0.4624	0.0772
GOF	1.078	1.060	1.169	0.963

[a] $R1 = \Sigma||F_o| - |F_c||\Sigma|F_o|$. [b] $wR2 = [\Sigma[w(F_o^2 - F_c^2)^2]/\Sigma[w(F_o^2)^2]]^{1/2}$.

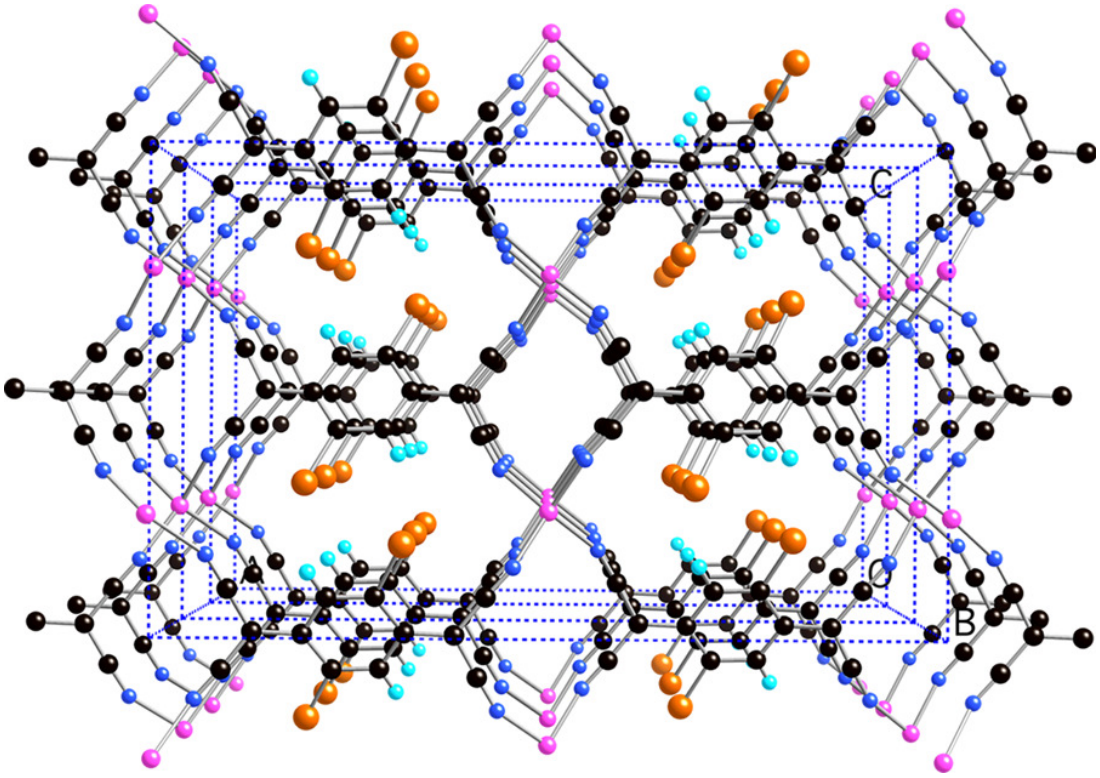

Figure 2.2 A perspective view of Cu(TCNQBr$_2$) emphasizing μ_4-[TCNQBr$_2$] binding mode and the π-π stacking along the short axis (b axis). Color code: Cu = pink, C = black, N = blue, Br = orange, H = light blue.

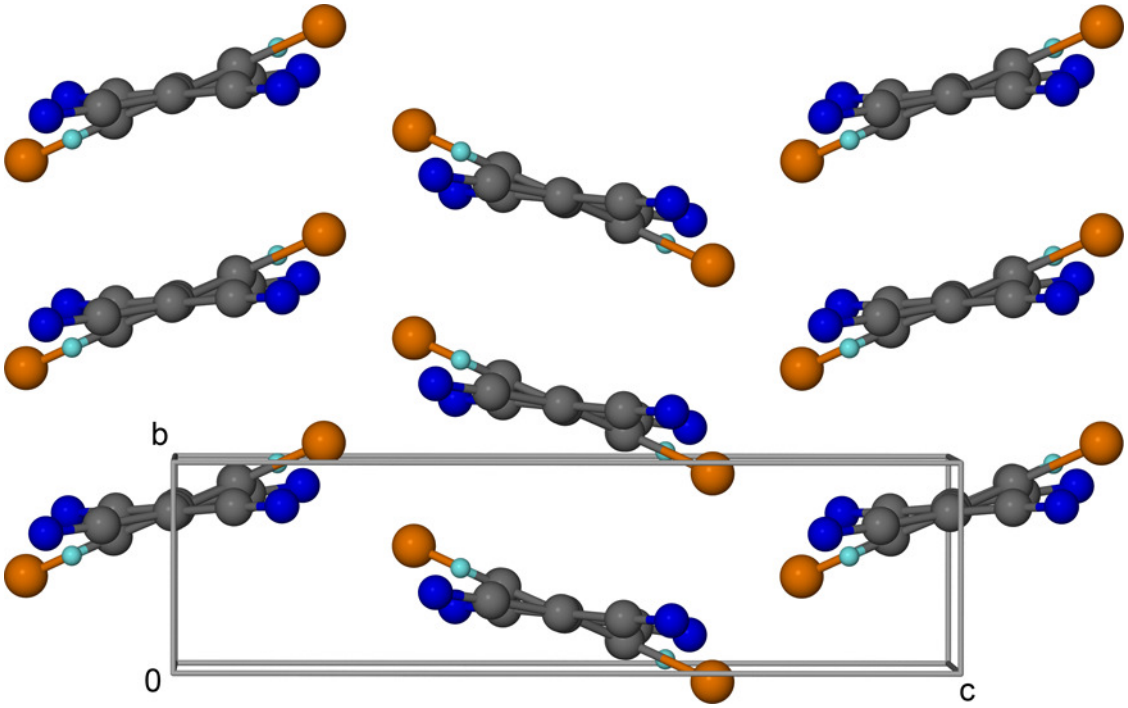

Figure 2.3 Packing diagram parallel to the *bc* plane depicting π-π stacking interactions in the crystal structure of Cu(TCNQBr$_2$), and emphasizing that the TCNQBr$_2$ ligands within a stack are slipped in a ring-over-ring conformation. The copper ions are omitted for the sake of clarity. Color code: C = gray, N = blue, Br = orange, H = light blue.

For quinone rings to be considered as exhibiting appreciable π contacts, the distances are required to be less than the sum of C···C van der Waals radii (3.40 Å). The adjacent $TCNQX_2$ stacks are parallel to each other, as in the case of Cu(TCNQ) Phase II (structure type B), but in an unprecedented arrangement that we label as structure type-C.[16] The most notable differences are that in Cu(TCNQ) Phase II the copper ions are in a regular tetrahedral environment which leads to an open framework with sufficient space for a second network to interpenetrate, whereas in $Cu(TCNQX_2)$ the compressed tetrahedron maintains a tightly packed framework and thus no interpenetration is observed. Close contacts exist for $Cu(TCNQCl_2)$ and $Cu(TCNQBr_2)$ between $TCNQX_2$ molecules in adjacent stacks, in particular, the H···X ($Cu(TCNQCl_2)$: 2.83 Å, and $Cu(TCNQBr_2)$: 2.85 Å) interactions are much less than the sum of the van der Waals radii (H···Cl: 3.10 Å, and H···Br: 3.20 Å) (Figure 2.4 and Table 2.2).

It should be pointed out at this point that the X-ray powder diffraction pattern of the slow diffusion reaction of Cu^I ions with $TCNQCl_2$ and $TCNQBr_2$ contained extra peaks in addition to the simulated powder pattern for the isostructural 3-D framework. Upon observation under the optical microscope, we observed large blocks, long needles and short thin needles from the same crystallization cell. The collection of short sequence of frames indicated that the large block and needles were the same material, but the very thin needles had different unit cell parameters and a very weak diffraction signal. A full data collection on the poorly diffracting small needles was used for the crystallography studies. Although the refinement of the crystal was not suitable, the framework was able to be discerned and the details will be discussed here.

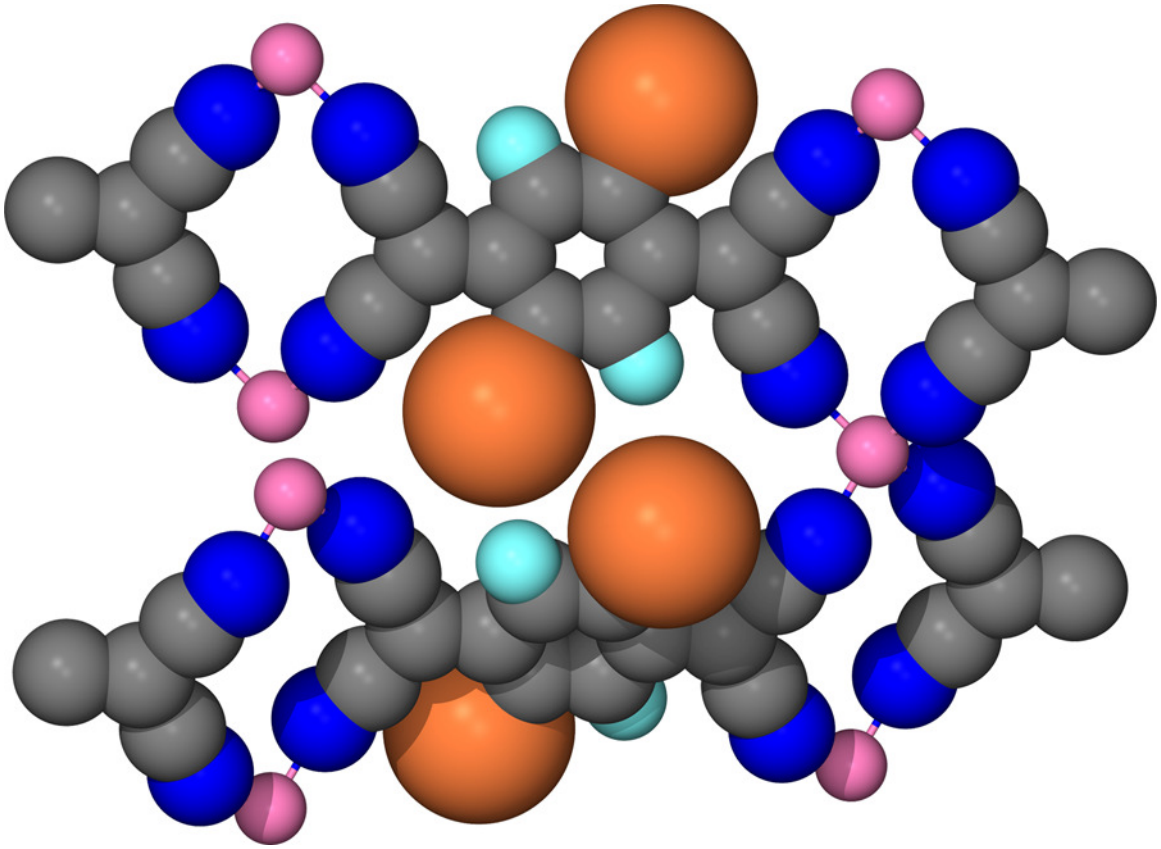

Figure 2.4 Space-filling representation of $Cu(TCNQBr_2)$, showing the H···Br interaction. Color code: Cu = pink, C = gray, N = blue, Br = orange, H = light blue.

Table 2.2 Crystallographic parameters of several conducting MOFs

Compound	Stacking distance	X···X distance	van der Waals radii	H···X distance	van der Waals radii	α_1[a]	α_2[a]
$Cu(TCNQCl_2)$	3.30	Cl···Cl 3.54	Cl···Cl 3.60	2.83	H···Cl 3.10	139.7	130.9
$Cu(TCNQBr_2)$	3.37	Br···Br 3.68	Br···Br 3.80	2.85	H···Br 3.20	139.8	130.8
CuTCNQ type-A	3.24	-	C···C 3.40	H···H 3.24	H···H 2.60	142	142
$Cu(DMDCNQI)_2$	3.21	-	C···C 3.40	H···H 3.21	H···H 2.60	126.3	126.3

[a]: α_1 and α_2 are N-Cu-N angles of the compressed tetrahedron

Crystal Structure of $Cu(TCNQBr_2)(CH_3CN)$: The X-ray crystal structure of $Cu(TCNQBr_2)(CH_3CN)$ at 110 K revealed that it crystallizes as a 2-D framework with Cu^I ions coordinated to three different μ_3-$[TCNQBr_2]^{\bullet-}$ anions and one acetonitrile molecule (Figure 2.5). The Cu^I ions are in a nearly regular tetrahedral environment as evidenced by the N-Cu-N angles of 99.74°, 102.84°, 113.06°, and 125.84°. The $TCNQBr_2$ units are arranged in columnar stacks that propagate along the a axis, with several $TCNQBr_2$•••$TCNQBr_2$ stacking distances of 3.42 Å, and 3.51 Å - much longer than the ~3.24 Å observed in the structure of Cu(TCNQ) type-A (Figure 1.4). Therefore, the $TCNQBr_2$ ligands are only weakly engaged in π-π interactions at a stacking distance of 3.42 Å. The TCNQ ligands within a stack are slipped in a ring-over-external bond conformation (Figure 2.1c). Rings of four alternating Cu ions and four $TCNQBr_2$ units are formed in the 2-D layer (Figure 2.5). Close contacts exist for $Cu(TCNQBr_2)(CH_3CN)$ between $TCNQBr_2$ and acetonitrile molecules from adjacent frameworks, in particular, the H···Br of 2.89 Å, and 2.97 Å interactions are much less than the sum of the van der Waals radii (H···Br: 3.20 Å). It is noted that the H···Br interactions between $TCNQBr_2$ molecules observed in the $Cu(TCNQX_2)$ (X = Cl, Br) 3-D frameworks are not observed in this case.

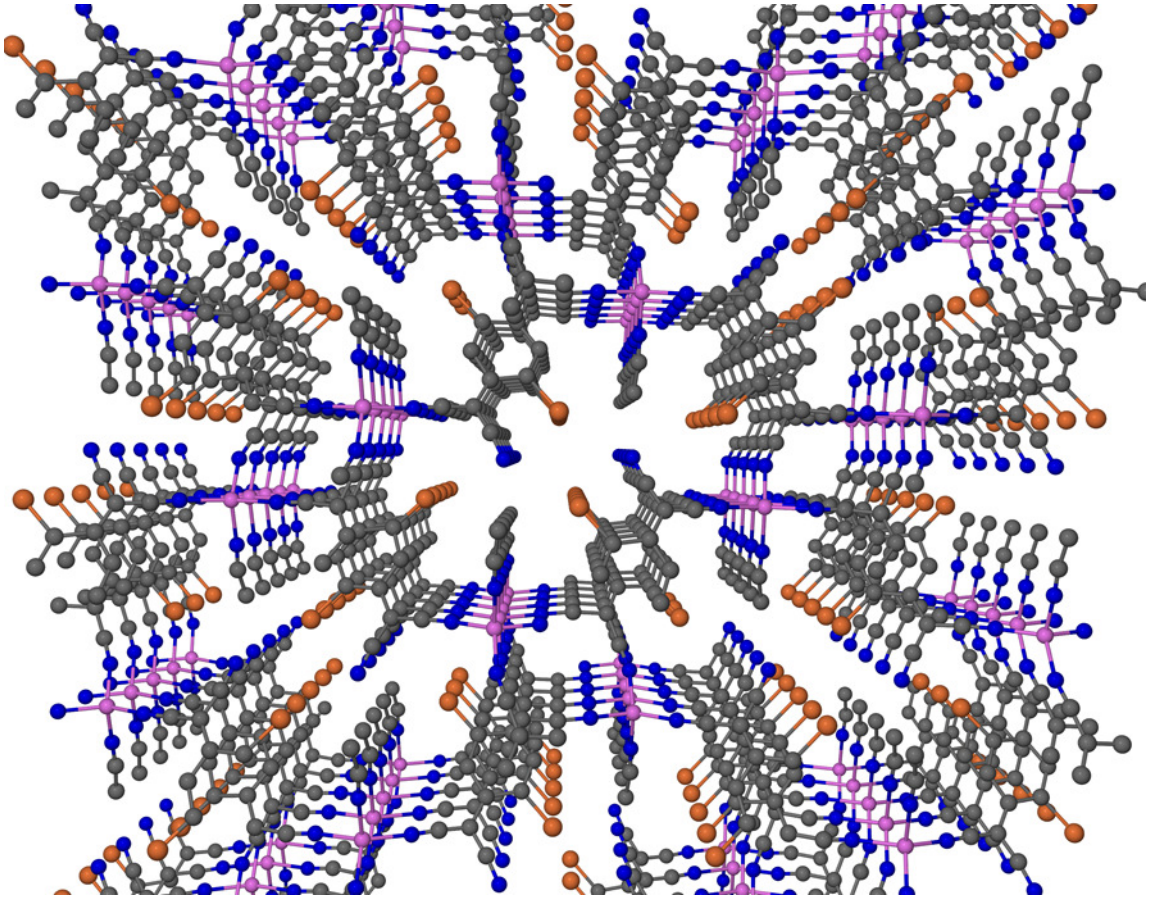

Figure 2.5 A perspective view of $Cu(TCNQBr_2)(CH_3CN)$ emphasizing the μ_3-$[TCNQBr_2]$ binding mode and the stacking along the short axis. The hydrogen atoms are omitted for the sake of clarity. Color code: Cu = pink, C = gray, N = blue, Br = orange, H = light blue.

Crystal Structure of $Cu(TCNQI_2)(CH_3CN)$: The X-ray crystal structure of $Cu(TCNQI_2)(CH_3CN)_2$ at 110 K revealed that it crystallizes as a 1-D zigzag chain with Cu^I ions coordinated to two different trans μ_2- $[TCNQI_2]^{\bullet-}$ anions and two acetonitrile molecules (Figures 2.6 and 2.7). The Cu^I ions are in a nearly regular tetrahedral environment as evidenced by the N-Cu-N angles of 103.51°, 111.48°, 113.15°, and 114.02°. The $TCNQI_2$ units are arranged in columnar stacks that propagate along the b axis, with $TCNQI_2$•••$TCNQI_2$ stacking distances of 3.476 Å **-** much longer than the ~3.24 Å distance observed in the structure of Cu(TCNQ) type-A (Figure 1.4). Therefore, the $TCNQI_2$ ligands are not engaged in considerable π-π interactions. The $TCNQI_2$ ligands within a stack are slipped in a ring-over-external bond conformation (Figures 2.1c and 2.8). Close contacts are present for $Cu(TCNQI_2)(CH_3CN)_2$ between $TCNQI_2$ and acetonitrile molecules from adjacent chains, in particular, the H···I interactions of 3.23 Å are slightly less than the sum of the van der Waals radii (H···I: 3.30 Å) (Figure 2.7).

At this point it is interesting to note that in all of these structures which range from 1- to 3-D in dimensionality that the halogen groups lie directly on top of each other for all stacked $TCNQX_2$ groups. The halogen···halogen distances in the case of $Cu(TCNQBr_2)(CH_3CN)$ (Br···Br: 4.11 Å) and $Cu(TCNQI_2)(CH_3CN)_2$ (I···I: 4.65 Å), however, are much longer than the sum of the van der Waals radii (Br···Br: 3.80 Å, I···I: 4.00 Å), thus there are not significant interactions between these group, in contrast to the considerable X···X interactions observed for $Cu(TCNQX_2)$ (X = Cl, Br) 3-D frameworks (Cl···Cl: 3.54 Å, Br···Br: 3.68 Å) (Table 2.2).

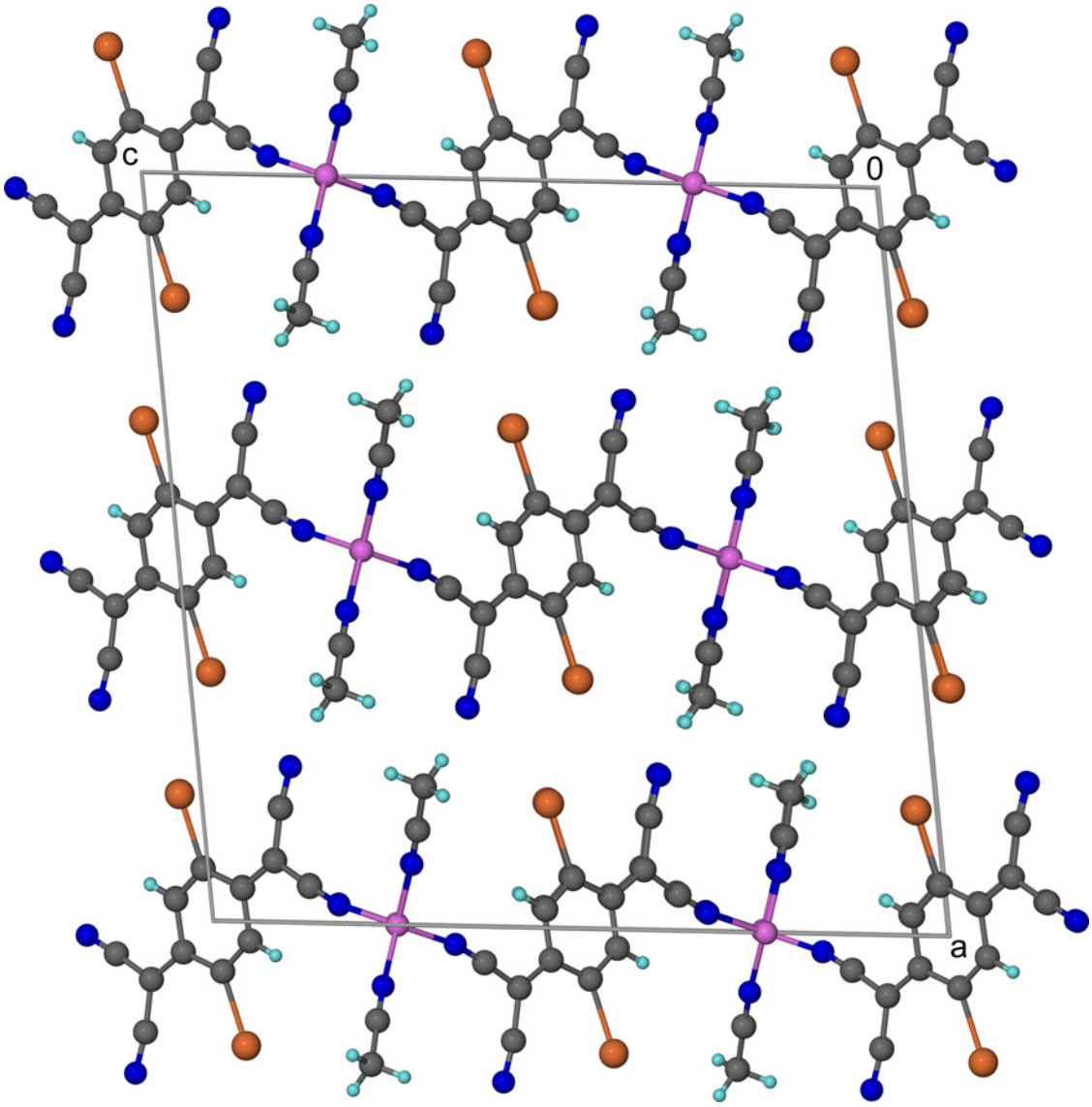

Figure 2.6 Packing diagram of $Cu(TCNQI_2)(CH_3CN)_2$ along the *b* axis emphasizing the trans μ_2-$[TCNQI_2]$ binding mode of the ligand. Color code: Cu = pink, C = gray, N = blue, I = orange, H = light blue.

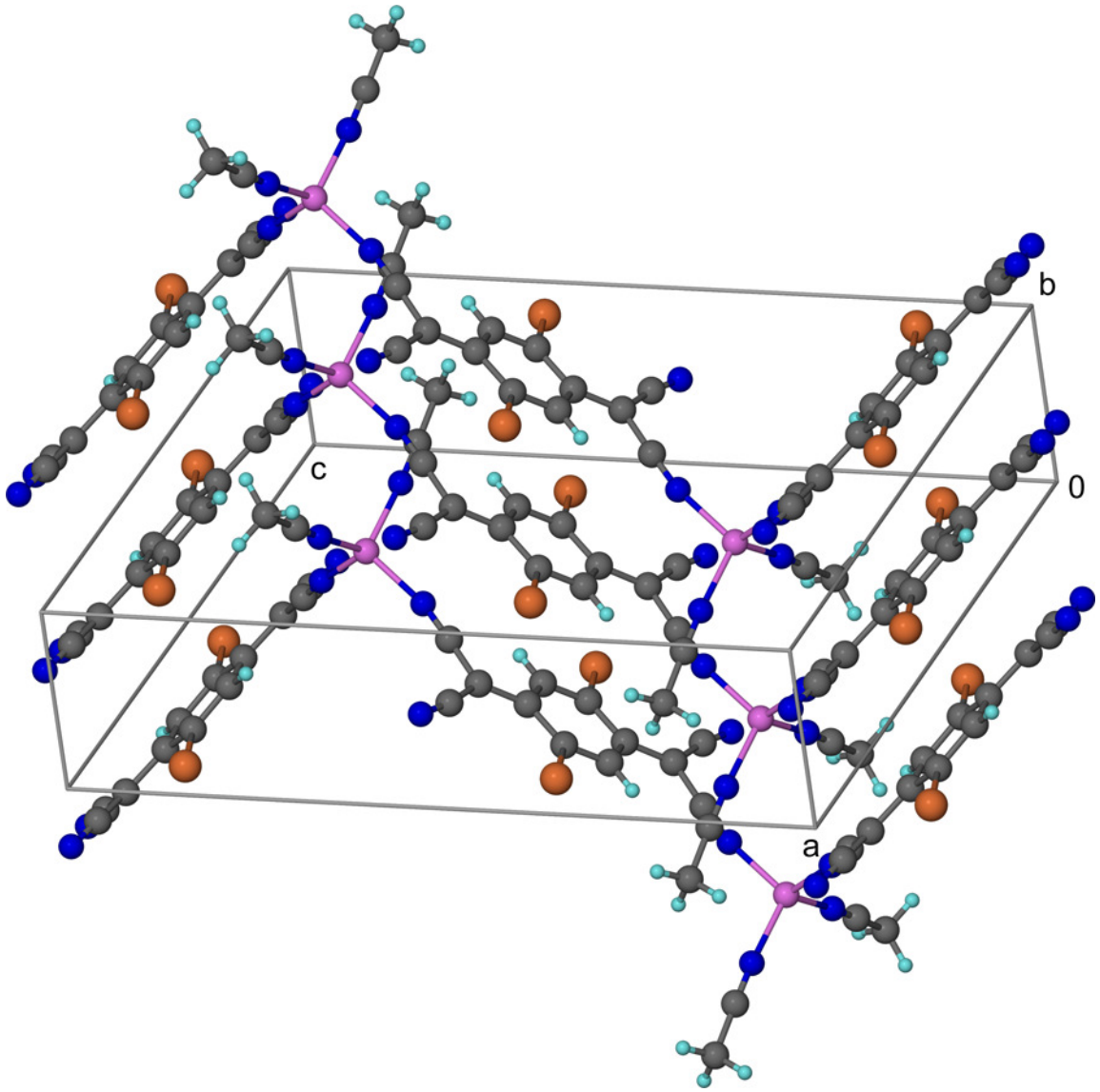

Figure 2.7 Packing diagram of $Cu(TCNQI_2)(CH_3CN)_2$ emphasizing the 1-D zigzag chain packing arrangement. Color code: Cu = pink, C = gray, N = blue, I = orange, H = light blue.

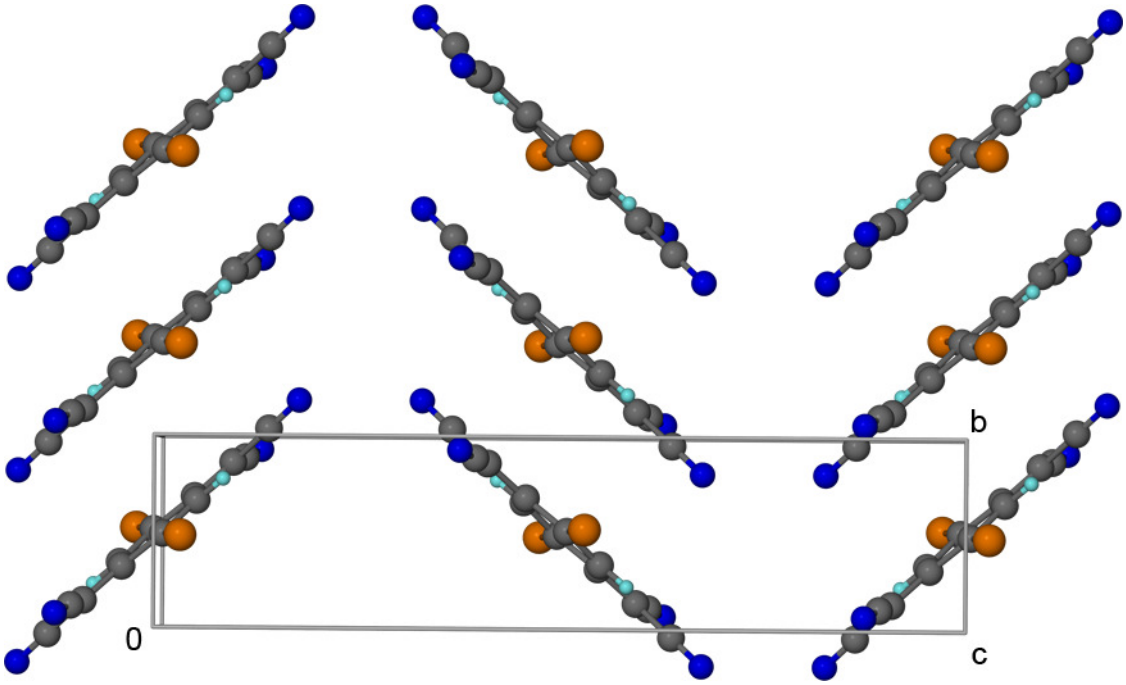

Figure 2.8 Packing diagram parallel to the *bc* plane depicting stacking interactions in the crystal structure of $Cu(TCNQI_2)(CH_3CN)_2$ which emphasizes that the $TCNQI_2$ ligands within a stack are slipped in a ring-over-external bond conformation. The copper ions are omitted for the sake of clarity. Color code: C = gray, N = blue, I = orange, H = light blue.

Conversion of $Cu(TCNQX_2)$ Into $Cu(TCNQX_2)(CH_3CN)$ Monitored by Powder X-ray Diffraction Studies: The observation by single crystal X-Ray diffraction of two products in the $TCNQBr_2$ studies, namely $Cu(TCNQX_2)$ and $Cu(TCNQX_2)(CH_3CN)$, led us to perform powder X-ray diffraction (XRD) studies in order to follow the interconversion of these materials. Powder XRD patterns of bulk reactions between $[Cu(CH_3CN)_4](BF_4)$ and $Li(TCNQX_2)$ (X = Cl, Br) in a 1:1 ratio in acetonitrile were monitored periodically by collecting data on the dark green powder that formed essentially instantaneously. The reactions with $TCNQBr_2$ were focused upon because more material was available in the exploratory stage of the project and also because the chemistry is similar for both ligands. The diffraction pattern of samples taken after 10, 30 minutes and 1 hour are basically identical and match the simulated patterns of the $Cu(TCNQBr_2)$ crystal structure along with additional diffraction peaks corresponding to an unidentified product (Figure 2.9). The diffraction pattern of samples measured after 1 day matched the simulated patterns of the $Cu(TCNQBr_2)(CH_3CN)$ crystal structure along with additional diffraction peaks corresponding to an unidentified product (Figure 2.10). Thus, by this method none of the products could be obtained in a pure form although $Cu(TCNQBr_2)(CH_3CN)$ is the dominant product in the sample after 1 day of reaction.

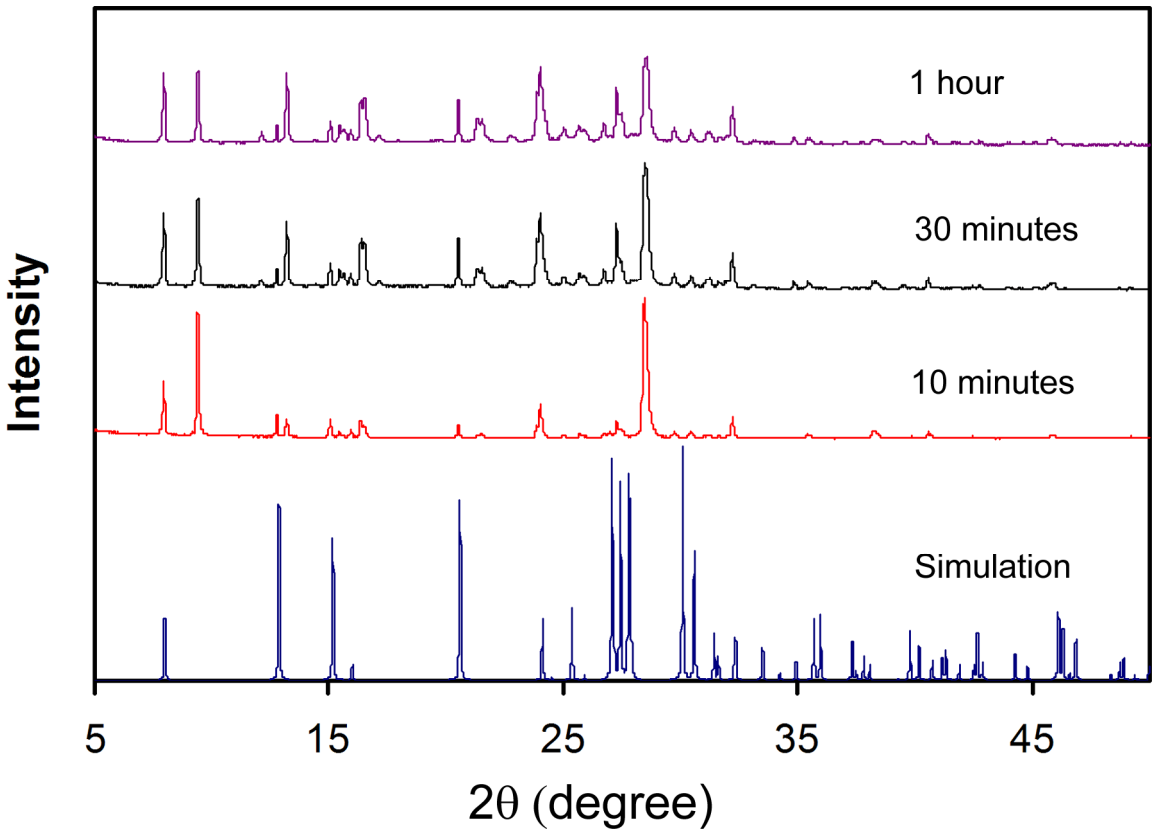

Figure 2.9 XRD powder patterns obtained from bulk syntheses between $[Cu(CH_3CN)_4](BF_4)$ and $Li(TCNQBr_2)$ in a 1:1 ratio in acetonitrile; XRD powder pattern of $Cu(TCNQBr_2)$ simulated (blue).

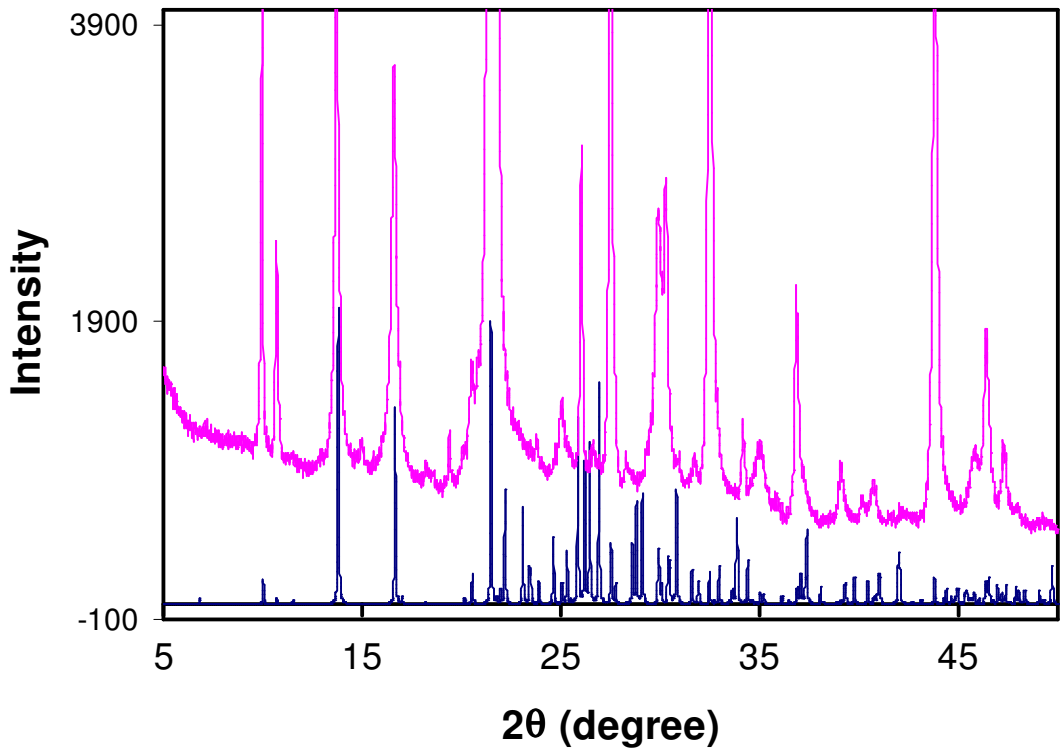

Figure 2.10 Experimental XRD powder pattern obtained from the bulk reaction between $[Cu(CH_3CN)_4](BF_4)$ and $Li(TCNQBr_2)$ in a 1:1 ratio in acetonitrile after 1day (pink); XRD powder pattern of $Cu(TCNQBr_2)(CH_3CN)$ simulated (blue).

At this point, a methanol/acetonitrile mixed solvent system was tried because we had observed that the use of methanol for slow diffusion reactions of CuI and neutral $TCNQBr_2$ slowed down the reaction considerably. The bulk reactions in methanol/acetonitrile mixed solvents appeared to proceed in the same manner as when pure acetonitrile was used, namely similar powder patterns corresponding to $Cu(TCNQBr_2)$ and an the unidentified crystalline product were obtained. It turns out, however that reactions performed in a Cu: $Li(TCNQBr_2)$ ratio of 1:1.5 result in pure $Cu(TCNQBr_2)$, which does not transform into another product even after standing in acetonitrile for 12 hours (Figure 2.11). The same conditions were used for reactions involving $TCNQCl_2$ and pure $Cu(TCNQCl_2)$ was also obtained (Figure 2.12).

It is speculated that the unidentified product may have acetonitrile bound to the copper ions because it does not form in an excess of $TCNQX_2$. In addition, the XRD pattern of the products from slow diffusion reactions of CuI and neutral $TCNQI_2$ also indicate the existence of other products in addition to $Cu(TCNQI_2)(CH_3CN)_2$ which form small blocks. There are also small needle crystals, which are most likely another phase, but structural determination was not possible because the small needles diffracted poorly and are badly twinned.

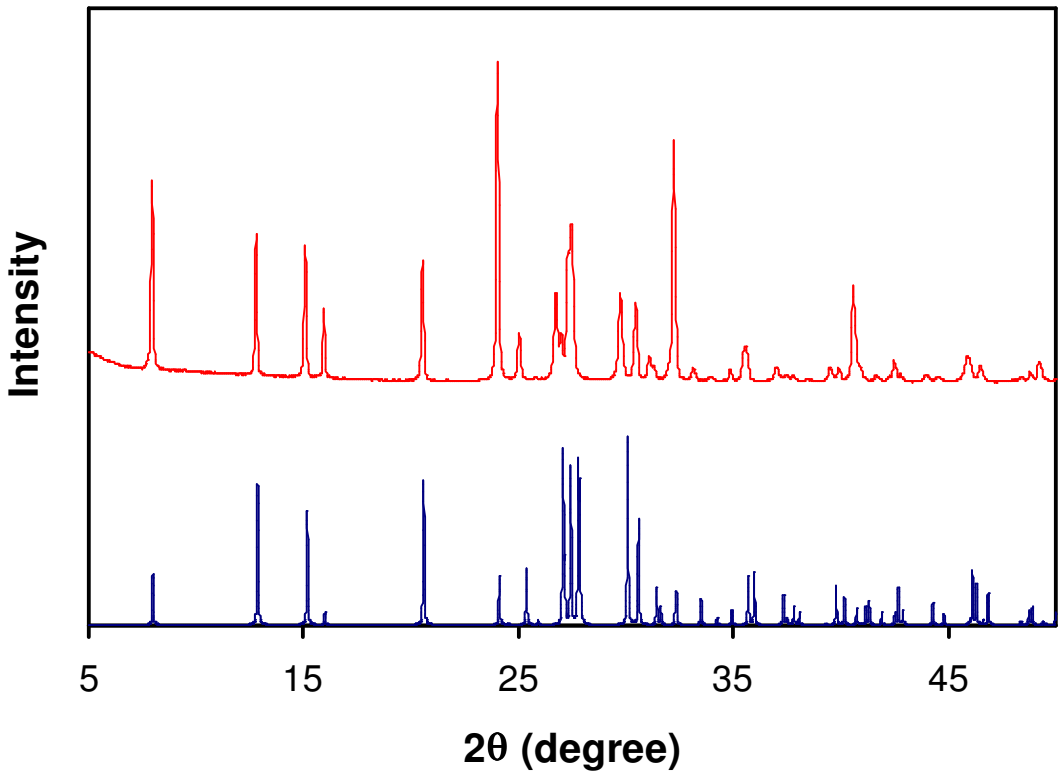

Figure 2.11 XRD powder pattern of Cu(TCNQBr$_2$), obtained from a bulk reaction in a mixture of methanol/acetonitrile solvents (red); XRD powder pattern of Cu(TCNQBr$_2$) simulated (blue).

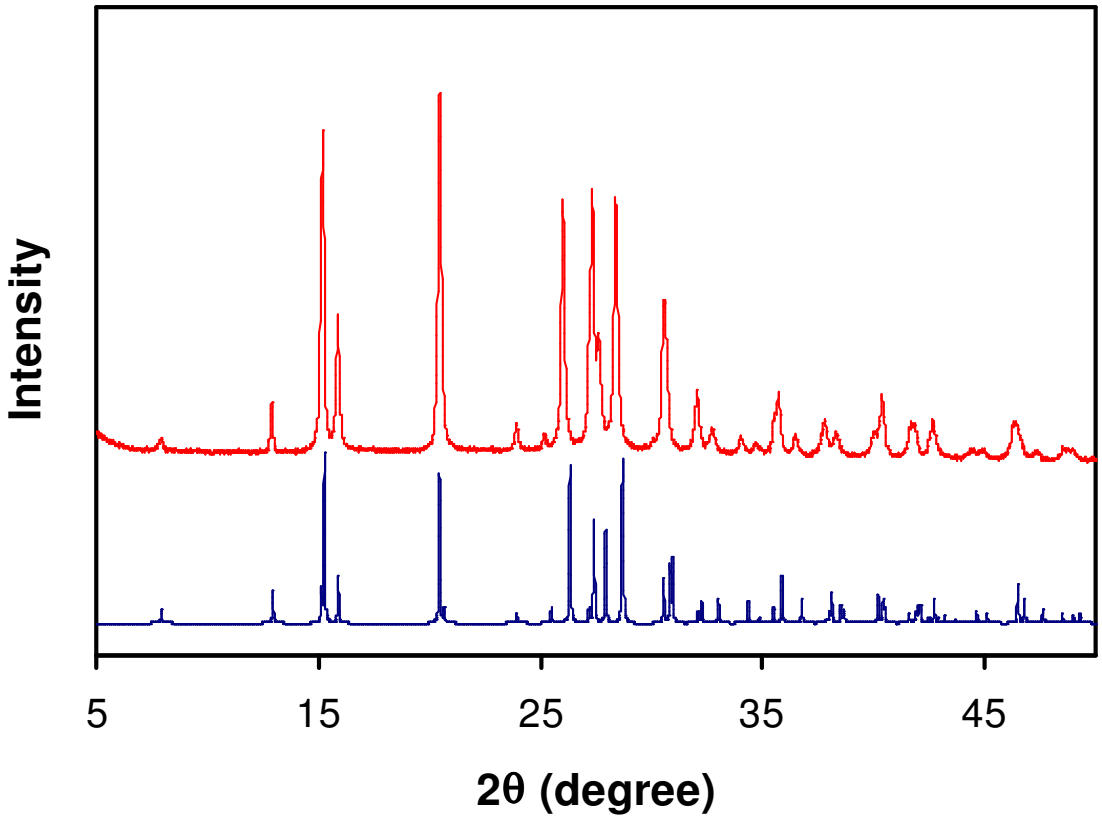

Figure 2.12 XRD powder pattern of $Cu(TCNQCl_2)$, obtained from a bulk synthesis in a mixture of methanol/acetonitrile solvents (red); XRD powder pattern of $Cu(TCNQCl_2)$ simulated (blue).

Cu(TCNQBr$_2$) Film Growth Studies, Powder X-ray Diffraction and Scanning Electron Microscopy Studies of Cu(TCNQBr$_2$) Films Prepared on Cu Substrates: Cu(TCNQ) films grown on Cu foil surfaces in acetonitrile have been widely investigated as a general method for obtaining nonvolatile memory devices. The reaction is a corrosion process in which the copper metal placed in an acetonitrile solution of TCNQ reduces the TCNQ in-situ and at the same time releases Cu^I ions that coordinate to the monoreduced TCNQ ligand causing an epitaxial growth of small parallelepiped crystals, typically ranging from the nano to the micron scale. Our group reported that Cu(TCNQ) films grown on Cu foil surfaces at short reaction times (6 hours at room tempertature) are composed of Cu(TCNQ) phase I, which, at longer reaction times, transforms into Cu(TCNQ) phase II (46 hours at room temperature); after 76 hours the film is mainly composed of phase II.[16] The transformation is accelerated by heating to 80 °C and after just one hour the film is composed of Cu(TCNQ) phase II. The phase transformation was monitored by powder X-ray diffraction studies and it was observed that the morphology changes from needles corresponding to phase I to platelets corresponding to phase II as observed by Scanning Electron Microscopy (SEM).

Since the new Cu(TCNQX$_2$) compounds may also be potentially useful for nonvolatile memory devices, it is important to investigate changes in film composition as a function of reaction time. Consequently, powder XRD patterns of the Cu(TCNQBr$_2$) films were monitored periodically by removing one of the pieces of copper sheet from the TCNQBr$_2$ solution in acetonitrile at 60°C and collecting an X-ray powder pattern on the resulting material. The diffraction pattern of films grown after 5,

10 and 30 minutes did not match the simulated patterns of either $Cu(TCNQBr_2)$ or $Cu(TCNQBr_2)(CH_3CN)$ crystals structures. The SEM data indicate that such samples are mainly composed of blocks with dimensions ranging from two to ten microns after five minutes of dipping time (Figure 2.13a). After ten minutes there are some needles present but the majority of the sample is still composed of blocks (Figure 2.13b). The blocks are ~50 microns long after dipping for 30 minutes and more needles were observed (Figure 2.13c). The needles continue to grow and replace the platelets as evidenced from samples grown for 1 hour (Figure 2.13d) and the diffraction pattern matches that of the $Cu(TCNQBr_2)$ crystal structure. After 5 hours of reaction, the powder XRD contains features attributed to $Cu(TCNQBr_2)(CH_3CN)$, therefore it was determined that reactions at 1 hour at 60 ºC are the optimal conditions to grow thin films of micron-sized parallelepipeds of $Cu(TCNQBr_2)$ (Figure 2.13d) by spontaneous electrolysis of Cu foil with neutral $TCNQBr_2$ in acetonitrile. The anisotropic shape of the crystals indicates that they grow along the short axis, similar to the nanowires, nanorods and nanoribbons reported for Cu(TCNQ) Phase I.[4,132,133] It seems reasonable, therefore, to expect that one could assemble nanodevices based on nanowires, nanorods and nanoribbons of $Cu(TCNQX_2)$ using the techniques reported for Cu(TCNQ).[4,132,133] The presence of $Cu(TCNQBr_2)$ in the film was confirmed by X-ray powder diffraction (Figure 2.14). It is noted that the color of the films remained constant during the reaction and there were no other visible changes in the film with the exception of its thickness. Face indexing of a large parallelepiped single crystal of $Cu(TCNQBr_2)$ indicates that the crystal grows along the short axis involving the stacking interactions (Figure 2.15).

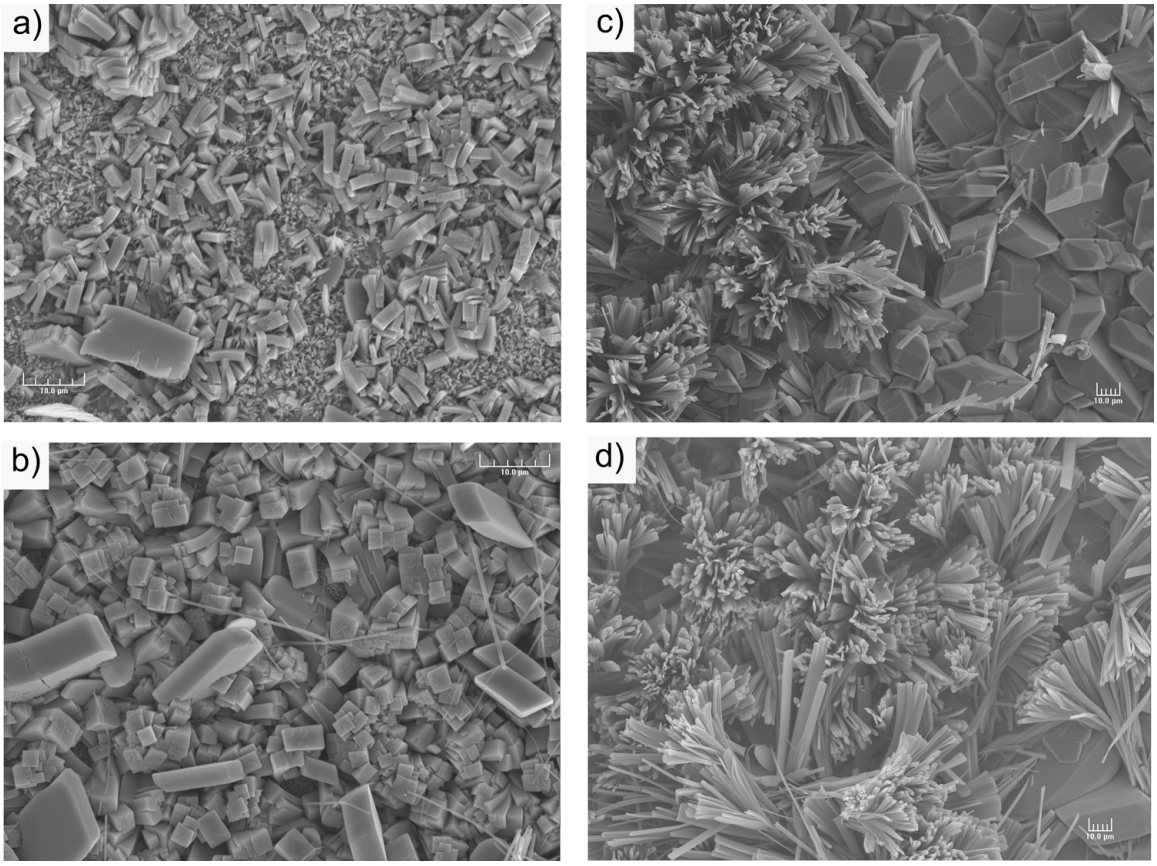

Figure 2.13 Scanning electron micrographs of films grown on copper in acetonitrile at 60°C in the presence of $TCNQBr_2$ for (a) 5 minutes (b) 10 minutes (c) 30 minutes and (d) 1 hour.

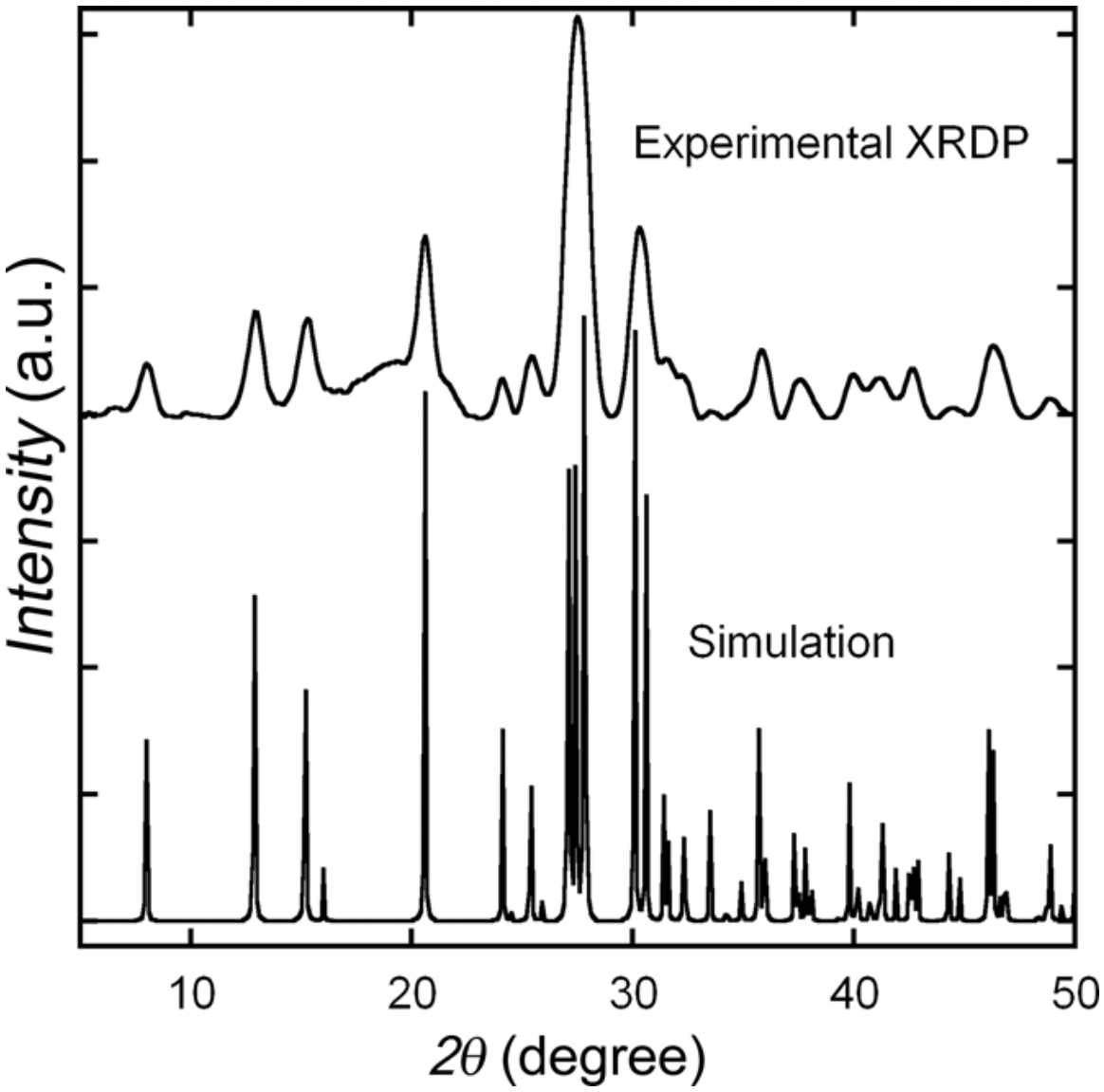

Figure 2.14 Experimental XRD powder pattern of films of Cu(TCNQBr$_2$) grown on copper foil in acetonitrile at 60°C for 1 h (top); XRD powder pattern of Cu(TCNQBr$_2$) simulated (bottom).

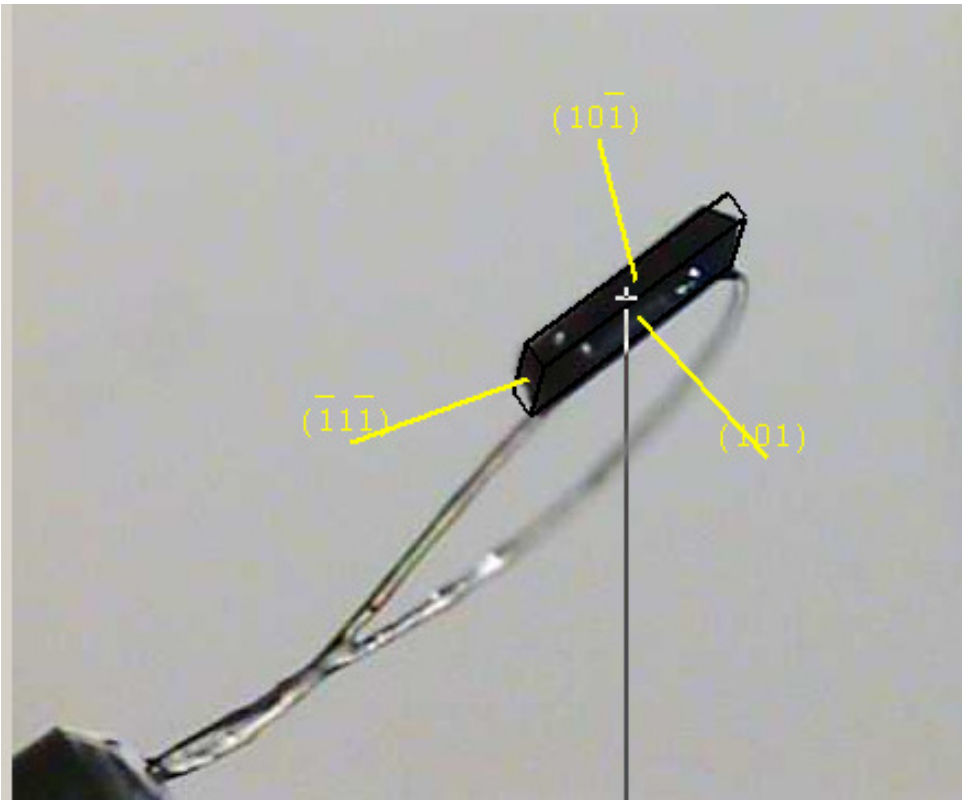

Figure 2.15 Face indexing of a large parallelepiped single crystal of Cu(TCNQCl_2), which indicates that the crystal grows along the short axis (axis b).

Infrared Spectroscopic Studies: Infrared spectral data revealed two ν_{CN} stretching modes for $Cu(TCNQBr_2)$ (2189 and 2165 cm^{-1}) and $Cu(TCNQCl_2)$ (2191 and 2157 cm^{-1}); these occur at lower energies than the corresponding stretches of neutral $TCNQCl_2$ (2224 cm^{-1}) and $TCNQBr_2$ (2218 cm^{-1}) respectively, as expected for $[TCNQX_2]^{-\bullet}$ radical anions.

X-ray Photoelectron Spectroscopy (XPS) Studies: X-ray Photoelectron Spectroscopy (XPS) studies were conducted in order to probe the oxidation state of Cu in the $TCNQX_2$ coordination environments (Figure 2.16). The XPS data for $Cu(TCNQBr_2)$ and $Cu(TCNQCl_2)$ revealed characteristic binding energies for Cu(I) $2p_{1/2}$ ($Cu(TCNQBr_2)$: 951.4 eV; $Cu(TCNQCl_2)$: 951.2 eV) and $2p_{3/2}$ ($Cu(TCNQBr_2)$: 931.4 eV; $Cu(TCNQCl_2)$: 931.3 eV) which are in the range of reported values for Cu(TCNQ) type-A: $2p_{1/2}$ (951.0-951.9 eV) and $2p_{3/2}$ (931.2-932.0 eV).[16]

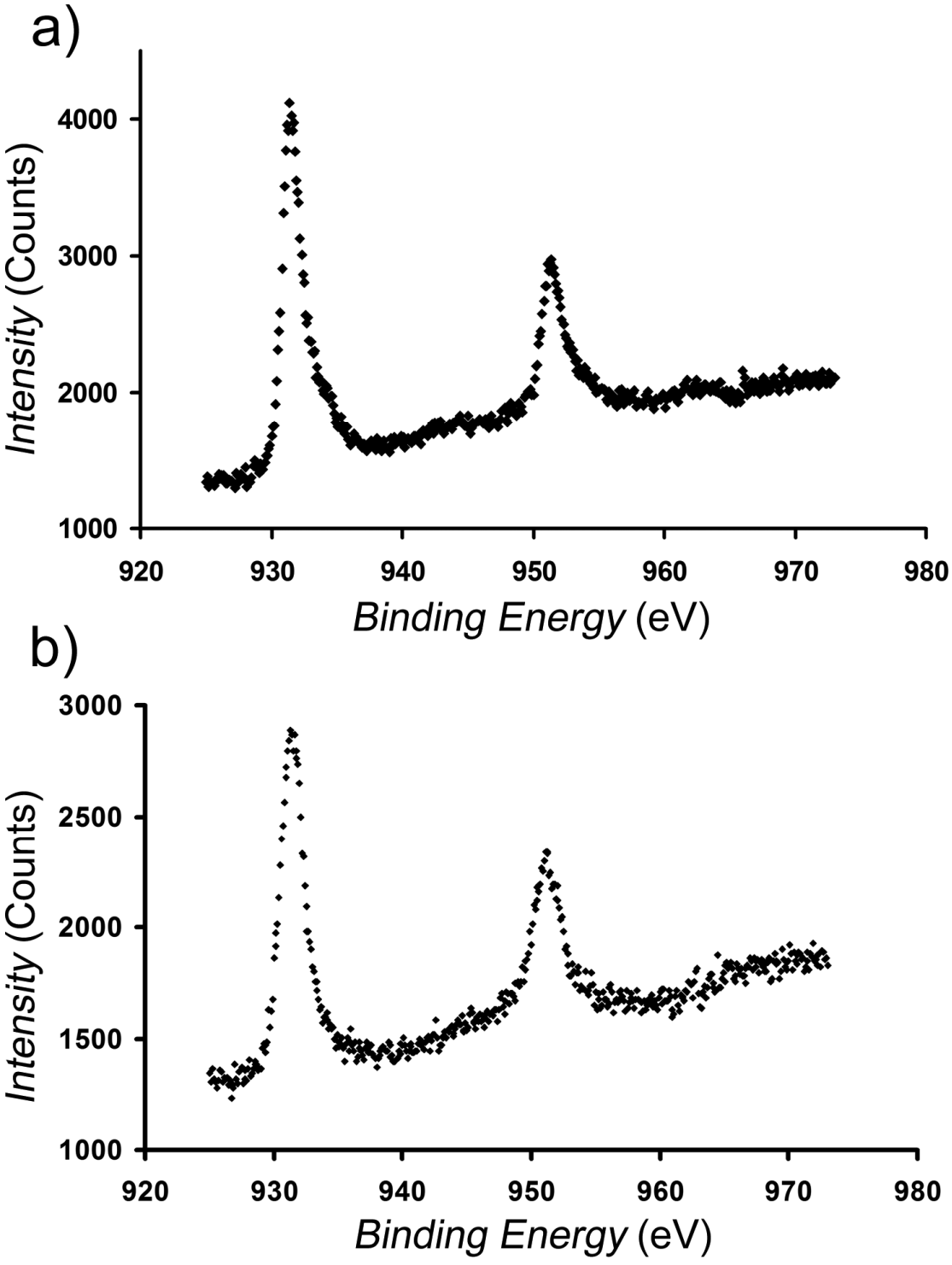

Figure 2.16 XPS data in the Cu $2p_{3/2}$ and $2p_{1/2}$ regions for $Cu(TCNQCl_2)$ (a) and $Cu(TCNQBr_2)$ (b).

Moreover, the single feature observed for the N1s orbitals ($Cu(TCNQBr_2)$: 398.7 eV; $Cu(TCNQCl_2)$: 399.0 eV) indicates that there is only one type of $TCNQX_2$ binding mode (Figure 2.17); such values are also in the range of those reported for Cu(TCNQ) (398.1-398.7 eV).[16,143]

Based on the collective aforementioned evidence from X-ray crystallography as well as IR and XPS spectroscopy, $Cu(TCNQBr_2)$ and $Cu(TCNQCl_2)$ are assigned as being composed of Cu^{I} ions and $[TCNQX_2]^{\bullet-}$ radical anions as was concluded in earlier studies for pure crystalline samples of Cu(TCNQ) type-A and –B.

Conductivity Studies: Conductivity measurements were performed on single crystals by the standard four-probe method. All compounds behave as semiconductors (Figure 2.18). At room temperature $Cu(TCNQCl_2)$ and $Cu(TCNQBr_2)$ exhibit conductivity values of 1.15 Scm^{-1} and 2.7 x 10^{-1} Scm^{-1} with activation energies of 0.032 eV (300 - 238 K) and 0.050 eV (236 - 100 K) for $Cu(TCNQCl_2)$; in the case of $Cu(TCNQBr_2)$ the activation energies are 0.036 eV (300 - 228 K) and 0.084 eV (225 - 150 K). The unexpectedly higher conductivity of $Cu(TCNQCl_2)$ compared to Cu(TCNQ) type-A is attributed to the compression of the copper tetrahedron which causes a mixing of 3d-pπ orbitals, thereby leading to the participation of the copper ions in the charge-carrier transport. This rationale is a well-accepted one for the, albeit much more highly conducting, $Cu(DCNQI)_2$ family.[28]

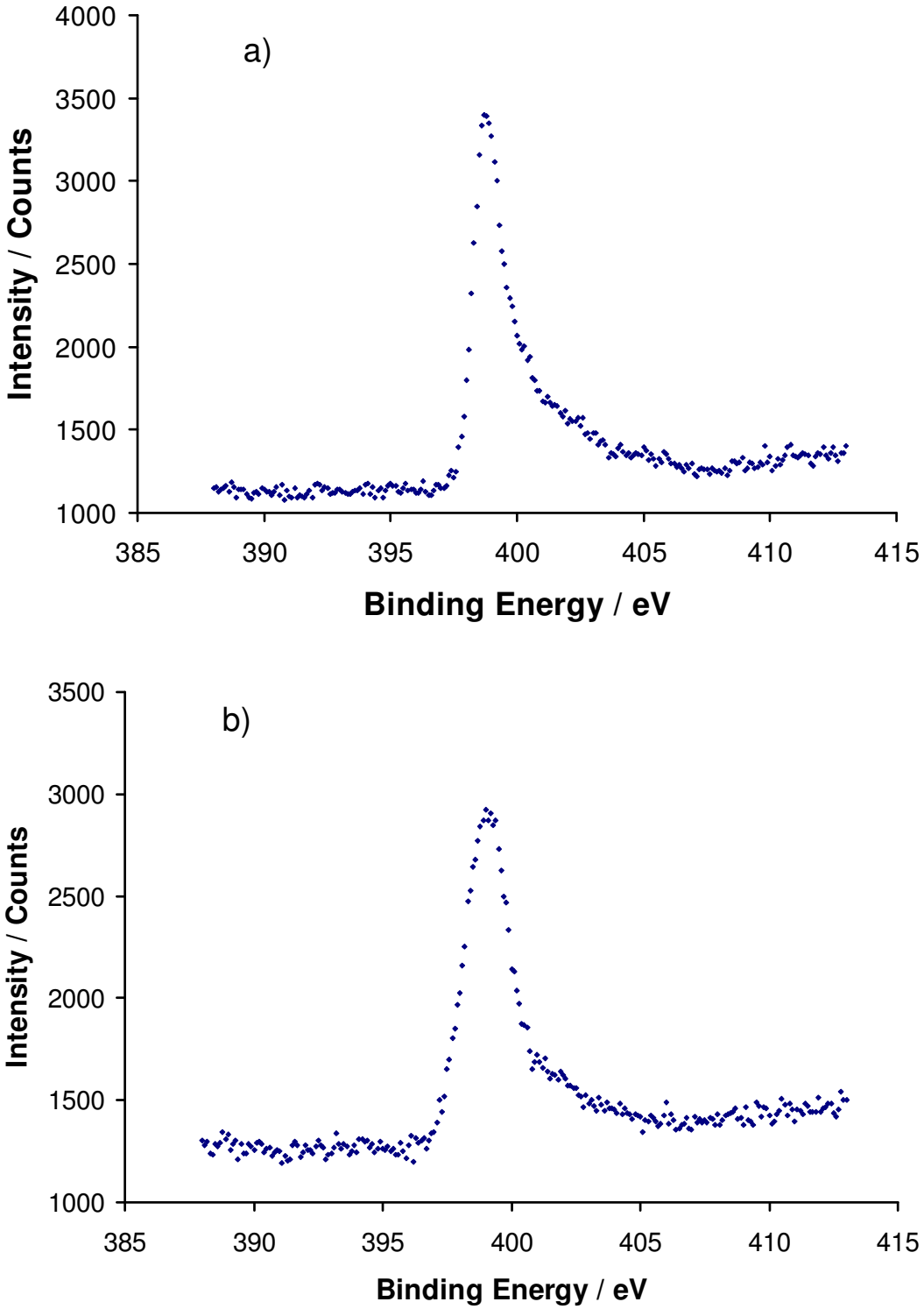

Figure 2.17 XPS data in the N1s region for (a) $Cu(TCNQCl_2)$ and (b) $Cu(TCNQBr_2)$.

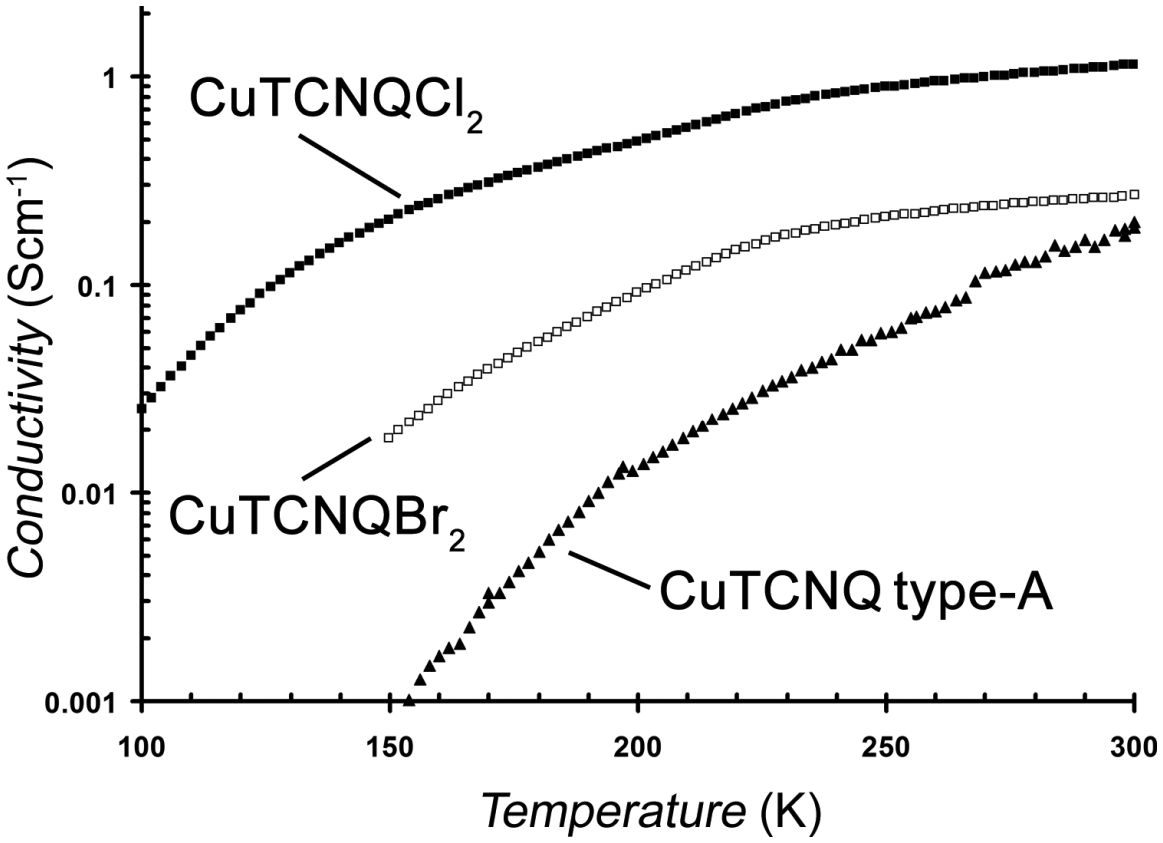

Figure 2.18 (a) Temperature dependence of the single crystal conductivity data for $Cu(TCNQCl_2)$: ■, $Cu(TCNQBr_2)$: □, and Cu(TCNQ) Phase I, type-A: ▲.

The lower conductivity of $Cu(TCNQBr_2)$ as compared to $Cu(TCNQCl_2)$ is attributed to the greater distance between adjacent $TCNQBr_2$ units (3.37 Å) in the stacks as compared to the corresponding $TCNQCl_2$ phase (3.30 Å) in $Cu(TCNQCl_2)$. The conductivity of $Cu(TCNQBr_2)$ at room temperature is comparable to that of Cu(TCNQ) type-A (2.0×10^{-1} Scm^{-1}) despite the fact that the distance between $TCNQX_2$ units is much greater in $Cu(TCNQBr_2)$.[16] Of additional note is the fact that the activation energies for $Cu(TCNQCl_2)$ and $Cu(TCNQBr_2)$ are less than that of Cu(TCNQ) type-A (0.137 eV from 300 to 150 K), presumably due to a higher degree of charge carrier transport through the copper ions and $TCNQX_2$ units.

Conclusions

In summary, large single crystals of $Cu(TCNQCl_2)$ and $Cu(TCNQBr_2)$ were prepared and found to exhibit a new structural motif for the $M^I(TCNQ)$ family. Importantly, $Cu(TCNQCl_2)$ exhibits the highest reported conductivity in the 1:1 $M^+:(TCNQ)^{\bullet -}$ family of salts in spite of the greater separation between $TCNQCl_2$ acceptor units in the stacks. Moreover, the conductivity of $Cu(TCNQBr_2)$ is comparable to that of Cu(TCNQ) type-A, in spite of the fact that $TCNQBr_2$ units in $Cu(TCNQBr_2)$ exhibit a greater separation than the TCNQ units in the original compound. We attribute the unexpectedly high conductivity of both compounds as being due to the fact that charge transport is not only through the 1-D stacks as is typically the case for Mott insulators; it is postulated that the conductivity is enhanced by $p\pi$-3d mixing caused by a compression of the tetrahedral environment of Cu(I). The result is a conducting pathway through the copper ions in two

dimensions. We interpret the present findings as an excellent sign that numerous other binary derivatives of metal ions with TCNQ ligands may be accessible whose structures and properties can be tuned by substituents with specific steric and electronic effects. Such flexibility, combined with ease of fabrication of nano-phases, is highly desirable for applications in non-volatile memory devices. Under certain reaction conditions, we also observed that the acetonitrile molecules compete with $TCNQX_2$ molecules for binding to the Cu^I ions, the result of which is lower dimensionality coordination polymers.

Experimental Section

Synthesis*:* The acceptor molecules $TCNQCl_2$ and $TCNQBr_2$ were obtained from an adaptation of the reported procedure for $TCNQCF_3$.[144] The starting materials 1,4-diiodo-2,5dichlorobenzene and 1,4-diiodo-2,5dibromorobenzene were obtained from the method reported for iodination of benzene.[145]

Preparation of Cu($TCNQBr_2$) Films*:* Copper foil (1cm^2 area) was treated with 1M HCl, rinsed with acetone followed by ethanol, and dried *in vacuo*. The clean copper foil was then immersed in a 20 mL solution of acetonitrile containing 20 mg of $TCNQBr_2$ at 60°C. A dark purple film was observed to form essentially instantaneously. The foil was removed after 1 h, rinsed with cold acetonitrile, and dried *in vacuo*.

Preparation of Single Crystals of Cu($TCNQCl_2$): Large dark blue single crystals were obtained after one week by slow diffusion of $TCNQCl_2$ (32 mg, 0.12 mmol) in 10 mL of acetonitrile into a saturated solution of CuI in 10 mL of acetonitrile; yield 22 mg (56%).

Bulk Preparation of Cu(TCNQCl$_2$): The reactions were performed in a mixture of solvents (26% acetonitrile, 74% methanol). Dark green microcrystals were obtained after adding a dark green solution of LiTCNQCl$_2$ (23 mg, 0.081 mmol) in 5 ml of an acetonitrile/methanol mixture to a colorless solution of [Cu(CH$_3$CN)$_4$](BF$_4$) (17 mg, 0.054 mmol) in 2.5 ml of an acetonitrile/methanol mixture. The dark green suspension was stirred for 1 h and then left to stand overnight under a stream of nitrogen. The dark green product was collected by filtration and washed three times with 7 mL aliquots of methanol, and finally dried under a reduced pressure; yield 16 mg (88%); IR (Nujol): ν CN = 2189 (m) and 2165 cm^{-1} (m); Anal. calcd for $C_{12}H_2N_4Cl_2Cu_1$: C 42.82, H 0.60, N 16.64; found: C 42.99, H 0.64, N 16.62.

Preparation of Single Crystals of Cu(TCNQBr$_2$): Analogous experimental conditions to those described for Cu(TCNQCl$_2$) were used for the preparation of large single crystals of Cu(TCNQBr$_2$); yield = 38%.

Bulk Preparation of Cu(TCNQBr$_2$): Analogous experimental conditions as those described for Cu(TCNQCl$_2$) were used for the preparation of Cu(TCNQBr$_2$) microcrystals; yield 10 mg (44%); IR (Nujol): ν CN = 2191 (s), 2157 cm^{-1} (s); Anal. calcd for $C_{12}H_2N_4Br_2Cu_1$: C 33.87, H 0.47, N 13.17; found: C 33.58, H 0.26, N 12.93.

Preparation of Single Crystals of Cu(TCNQBr$_2$)(CH$_3$CN): Analogous experimental conditions to those described for Cu(TCNQCl$_2$) were used for the preparation of small single crystals of Cu(TCNQBr$_2$)(CH$_3$CN) which co-crystallize with Cu(TCNQBr$_2$).

Preparation of Single Crystals of $Cu(TCNQI_2)(CH_3CN)_2$: Analogous experimental conditions to those described for $Cu(TCNQCl_2)$ were used for the preparation of small single crystals of $Cu(TCNQI_2)(CH_3CN)_2$.

X-ray Crystallography. General Procedures: In a typical experiment, a crystal selected for study was suspended in polybutene oil (Aldrich) and mounted on a cryoloop, which was placed in an N_2 cold stream. Single-crystal X-ray data were collected at 110 K on a Bruker SMART 1000 diffractometer equipped with a CCD detector for $Cu(TCNQX_2)$ (X = Cl, Br) and $Cu(TCNQI_2)(CH_3CN)_2$. Data for $Cu(TCNQX_2)(CH_3CN)$ were collected on a Bruker D8 GADDS X-ray diffractometer also operating at 110 K. The data sets were integrated with the Bruker SAINT[146] software package. The absorption correction (SADABS)[147] was based on fitting a function to the empirical transmission surface as sampled by multiple equivalent measurements. Solution and refinement of the crystal structures was carried out using the SHELX[148] suite of programs and the graphical interface X-SEED.[149] Preliminary indexing of the data sets established similar monoclinic unit cells for $Cu(TCNQX_2)$ (X = Cl, Br) and systematic extinctions indicated the space group C2/c (No. 15). Preliminary indexing of the data sets established a triclinic unit cell for $Cu(TCNQX_2)(CH_3CN)$ and systematic extinctions indicated the space group *P*-1 (No. 2). Preliminary indexing of the data sets established a monoclinic unit cell for $Cu(TCNQI_2)(CH_3CN)_2$ and systematic extinctions indicated the space group C2/c (No. 15). All of the structures were solved by direct methods that resolved the positions of the metal atoms and most of the C, N and X atoms (X = Cl, Br, I). The remaining non-hydrogen atoms were located by alternating

cycles of least-squares refinements and difference Fourier maps. Hydrogen atoms were placed at calculated positions. CCDC-719038 ($Cu(TCNQCl_2)$) and CCDC-648454 ($Cu(TCNQBr_2)$) contain the supplementary crystallographic data for this chapter. These data can be obtained free of charge from The Cambridge Crystallographic Data Centre via www.ccdc.cam.ac.uk/data_request/cif.

CHAPTER III

HETEROSPIN MOLECULAR MAGNETS BASED ON FIRST ROW TRANSITION METAL IONS AND TCNQ DERIVATIVES*

Introduction

Compounds that contain cyanide bridges have contributed to rapid growth of molecular magnetism over the past decade;[150a] these materials include those based on organocyanide ligands such as 7,7,8,8-tetracyano-quinodimethane (TCNQ) that form complexes with metal ions that exhibit interesting magnetic[52,53] and electronic properties.[81,16] The coordination chemistry of TCNQ is diverse,[110] as illustrated by the formation of 0-D complexes,[54a,b] 1-D chains,[44,55] 2-D[39e,56] and 3-D frameworks.[17,16,45,51] The use of capping ligands that limit the growth of extended structures has led a variety of compounds with interesting properties as illustrated by the examples of the mononuclear spin crossover complex $[Fe^{II}(abpt)_2(TCNQ^{-\bullet})_2]$ (abpt = 4-amino-3,5-bis(pyridin-2-yl)-1,2,4-triazole),[54a] the single-chain magnet $\{[Mn^{III}(5\text{-TMAMsaltmen})(\mu\text{-}TCNQ^{-\bullet})](ClO_4)_2\}_\infty$ (5-TMAMsaltmen = N,N′-(1,1,2,2-tetramethyl-ethylene)bis(5-trimethylammoniomethyl-salicylideneiminato)),[55b] and a variety 2-D networks with $[M_2(O_2CCF_3)_4]^+$ (M = Ru, Rh)[56a]

---

*Reprinted in part with permission from *Chemical Communications*, N. Lopez, H. Zhao, A. V. Prosvirin, A. Chouai, M. Shatruk, K. R. Dunbar, "*Conversion of a Porous Material Based on a Mn^{II}-$TCNQF_4$ Honeycomb Net to a Molecular Magnet Upon Desolvation*," **2007**, 4611-4613. Copyright 2007 by The Royal Society of Chemistry.

paddlewheel complexes. If the metal complexes used in the chemistry consist of unprotected metal ions (those with all labile ligands), extended coordination frameworks are formed. In this vein, we and others have explored the μ_4-TCNQ binding mode in 3-D networks with mono-valent metal ions such as Cu(I).[16] Along with these studies, we have also explored the coordination chemistry of the tetrafluoro derivative of TCNQ, 2,3,5,6-tetrafluoro-7,7,8,8-tetracyanoquinodimethane ($TCNQF_4$), (Figure 3.1a), efforts that led to the isolation of 3-D architectures based on μ_4-$TCNQF_4$ coordinated to Ag(I)[51] and 2-D frameworks in the case of the $[Ru_2(O_2CCF_3)_4]^+$ [39e] paddlewheel precursor. Of particular interest is the fact that the metamagnet of composition $\{[\{Ru_2(O_2CCF_3)_4\}_2TCNQF_4]\cdot 3(p\text{-xylene})\}_\infty$, prepared in collaboration with the Miyasaka group, exhibits long range magnetic ordering at 95 K (Figure 1.14).[39e]

Of direct relevance to the topic of understanding the magnetic properties of TCNQ materials is the fact that the chemistry of first row transition metal ions ions with substituted TCNQ derivatives is a relatively unexplored topic with the only report being the series $V(TCNQX_2)\cdot zCH_2Cl_2$ (z ~ 1.38-0.02; X = H, Br, Me, Et, i-Pr, OMe, OEt, and OPh) reported by Miller and coworkers.[151] Given the simplicity of these binary materials and their superior properties as compared to many other molecule-based materials, it is of considerable interest to obtain additional examples with other first row transition metals and to establish structure/magnetic property relationships. Herein we present the syntheses and characterization, including magnetic studies for a series of heterospin molecules composed of first row metal ions and radicals of TCNQ derivatives.

Results and Discussion

Synthesis: Methanol solutions of $[Mn(CH_3CN)_4(BF_4)_2]$ and $Li(TCNQF_4)$ were layered in a 1:1 ratio, and after slow diffusion over the period of two weeks, dark blue crystals of the product $\{[Mn_2(TCNQF_4)(CH_3OH)_{7.5}\ (H_2O)_{0.5}](TCNQF_4)_2 \cdot 7.5CH_3OH\}_\infty$, **1⊃7.5CH$_3$OH** were harvested. In another effort, the method previously developed in our laboratories.[52] for preparing $M^{II}(TCNQ)_2$ magnets was extended to the preparation of M/$TCNQF_4$ binary phases. The bulk reaction of fully solvated precursors $[M^{II}(CH_3CN)_6](BF_4)_2$ and $TBA(TCNQF_4)$ in acetonitrile leads to materials of composition $M^{II}(TCNQF_4)^{-\bullet}(TCNQF_4^{2-})_{0.5}(CH_3CN)$ (M = Mn, Co). In related studies, reactions between zero-valent metals and neutral $TCNQBr_2$ in acetonitrile lead to spontaneous electron transfer to yield isostructural compounds of formula $[M^{II}(TCNQBr_2)_2(H_2O)_2]_\infty$ (M = Mn and Zn; $TCNQBr_2$ = 2,5-dibromo-7,7,8,8-tetracyanoquinodimethane).

Structure of $\{[Mn_2(TCNQF_4)(CH_3OH)_{7.5}\ (H_2O)_{0.5}](TCNQF_4)_2 \cdot 7.5CH_3OH\}_\infty$: Compound **1⊃7.5CH$_3$OH** crystallizes in the monoclinic space group $P2_1/c$ (Table 3.1). An X-ray structural determination revealed that **1⊃7.5CH$_3$OH** crystallizes as a 2-D distorted hexagonal network in which one type of $TCNQF_4$ unit is coordinated via all four cyano groups to Mn^{II} ions (Figure 3.1b) and each Mn^{II} ion is bound to two different $TCNQF_4$ molecules in axial positions.

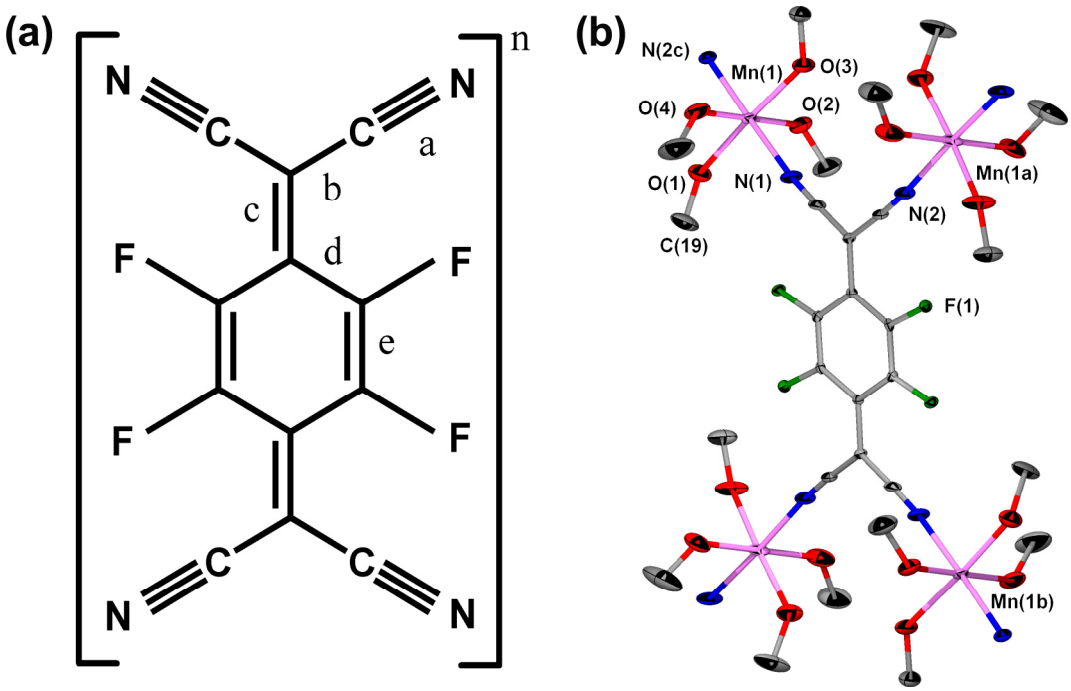

Figure 3.1 (a) $TCNQF_4$ (n = charge). (b) A fragment of the honeycomb net in the crystal structure of **1**⊃7.5CH_3OH showing a μ_4-$TCNQF_4$ ligand coordinated to four Mn^{II} ions. Hydrogen atoms are omitted for the sake of clarity. Mn = pink, C = gray, N = blue, O = red, F = green. Bond angles: O3-Mn1-O4 94.5(1), O3-Mn1-N1 86.5(1), O4-Mn1-N1 89.4(1), O3-Mn1-O2 86.1(1), N1-Mn1-O2 90.8(1), O3-Mn1-N2c 91.5(1), O4-Mn1-N2c 89.4(1), O2-Mn1-N2c 90.4(1)°.

Table 3.1 Crystallographic data for 3d/TCNQX MOFs X = F_4, Br_2.

Compound	**1⊃7.5CH_3OH**	**[Mn(TCNQBr_2)$_2$(H_2O)$_2$]$_\infty$**	**[Zn(TCNQBr_2)$_2$(H_2O)$_2$]$_\infty$**
Formula	$C_{51}H_{60}F_{12}N_{12}O_{15.5}Mn_2$	$C_{24}H_8Br_4N_8O_2Mn$	$C_{24}H_8Br_4N_8O_2Zn$
F_w [g mol^{-1}]	1426.28	814.96	825.39
Crystal size [mm^3]	0.26 x 0.24 x 0.12	0.21 x 0.05 x 0.03	0.34 x 0.14 x 0.05
Crystal system	monoclinic	monoclinic	monoclinic
Space group	$P2_1/c$	$C2/c$	$C2/c$
a [Å]	9.538(2)	24.489(5)	24.180(5)
b [Å]	14.957(3)	7.966(2)	7.945(2)
c [Å]	23.021(4)	13.383(3)	13.343(3)
β [°]	91.399(3)	100.88(3)	101.21(3)
V [$Å^3$]	3283(1)	2563.8(9)	2514.5(9)
Z	2	4	4
ρ_{calc} [g cm^{-3}]	1.468	2.111	2.180
μ ($Mo_{K\alpha}$) [mm^{-1}]	0.490	6.790	7.375
Reflections collected	28532	9213	13902
Unique reflections	7962	1850	3007
Reflections with I >2σ(I)	5097	1546	2821
parameters	486	186	178
R(int)	0.0744	0.0578	0.0322
$R1$[a]	0.0768	0.0369	0.0186
$wR2$[b]	0.1605	0.1109	0.0524
GOF	1.046	1.166	1.012

[a] $R1 = \Sigma||F_o| - |F_c||\Sigma|F_o|$. [b] $wR2 = [\Sigma[w(F_o^2 - F_c^2)^2]/\Sigma[w(F_o^2)^2]]^{1/2}$.

Four methanol molecules in the equatorial sites complete the coordination sphere of each metal ion. The Mn^{II} ions are in an octahedral environment with angles that deviate slightly from the ideal value of 90° (94.35°, 90.49°, 89.00°, 86.17° for O-Mn-O angles from methanol molecules and 89.38°, 90.82° for O-Mn-N angles for the methanol and $TCNQF_4$ ligands). The bond distances Mn-N (2.18 Å and 2.19 Å) and Mn-O (2.15 Å, 2.17 Å, 2.19 Å) are in the typical ranges. The center of each μ_4-bridging $TCNQF_4$ coincides with an inversion center that relates the diagonal Mn^{II} ions bound through the $TCNQF_4$ ligand. The 2-D honeycomb-like net consists of eight-membered rings of alternating Mn^{II} ions and $TCNQF_4$ ligands (Figure 3.2a). Within each ring, two of the $TCNQF_4$ linkers form a five-atom bridge between metal centers whereas the others create a ten-atom bridge; the result is a large opening with metal-metal separations of Mn1-Mn1a 7.480 and Mn1a-Mn1b 11.515 Å (Figure 3.1b). The longest Mn-Mn separation across the center of the eight-membered ring composed of four alternating manganese ions and four $TNQF_4$ ligands is 13.929 Å.

The 2-D net in **1⊃7.5CH$_3$OH** is topologically identical to that found in $\{[M_2(O_2CCF_3)_4]_2(TCNQ)\cdot 3(C_7H_8)\}_\infty$ (M = Ru, Rh).[56a] The latter structures contain partially reduced μ_4-$TCNQ^{\delta-}$, with δ = –0.42 and –0.63, respectively. The μ_4-TCNQ linkers are σ-bonded to the axial positions of the dimetal units in a similar fashion to the binding of μ_4-$TCNQF_4$ to the axial positions of octahedral Mn^{II} ions in **1⊃7.5CH$_3$OH**.

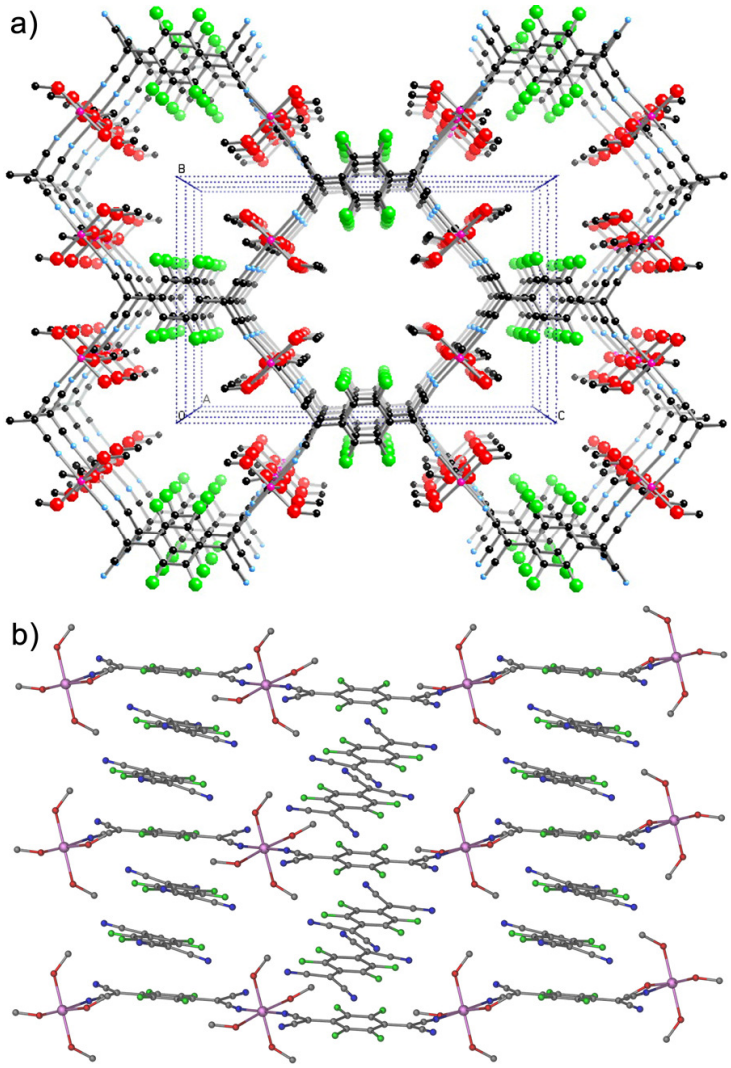

Figure 3.2 (a) Crystal structure of **1⊃7.5CH$_3$OH** viewed down the *a* axis emphasizing the 2-D framework and the μ_4-TCNQF$_4$ binding mode. The interstitial methanol molecules and uncoordinated TCNQF$_4$ units are omitted for the sake of clarity. Mn = pink, C = black, N = blue, O = red, F = green. (b) A view showing π–π stacking interactions in the crystal structure of **1⊃7.5CH$_3$OH**, the interstitial methanol molecules and hydrogen atoms are omitted for the sake of clarity. Mn = pink, C = gray, N = blue, O = red, F = green.

In addition to the coordinated $TCNQF_4$ molecules, the structure contains uncoordinated $TCNQF_4$ units. A pair of these molecules resides between μ_4-$TCNQF_4$ ligands of the consecutive layers, creating 1-D π–π stacks along the *a* axis (Figure 3.2b). The interplanar distances are 3.03 Å between uncoordinated $TCNQF_4$ units and 3.24 Å between the uncoordinated $TCNQF_4$ and μ_4-$TCNQF_4$. Thus, the uncoordinated $TCNQF_4$ units are present as π-dimers in a slipped ring-over-ring conformation (Figure 2.1b). It is also interesting to note that the uncoordinated···coordinated $TCNQF_4$ units stack in an unusual arrangement, namely a slipped-rotated ring-over-ring conformation (Figure 3.3). The structure contains large channels that run parallel to the *a* axis and are occupied by methanol molecules.

The molecules are connected by hydrogen bonds which generate a second shell that surrounds the 2-D coordination framework. The methanol molecules of the 2-D coordination network interact with uncoordinated $TCNQF_4$ units (O···N = 2.75 Å and 2.85 Å) and interstitial methanol molecules (O···O = 2.63 Å, 2.72 Å, 2.81 Å, and 2.94 Å). There are also hydrogen bonds between individual interstitial methanol molecules (O···O = 2.61 Å) and between uncoordinated $TCNQF_4$ units and interstitial methanol molecules (O···N = 2.83 Å). The uncoordinated $TCNQF_4$ units are hydrogen bonded to three different methanol molecules: there is a trans-μ_2 binding mode to two coordinated methanol molecules for an overall μ_3 binding mode due to the interaction with an additional uncoordinated methanol molecule.

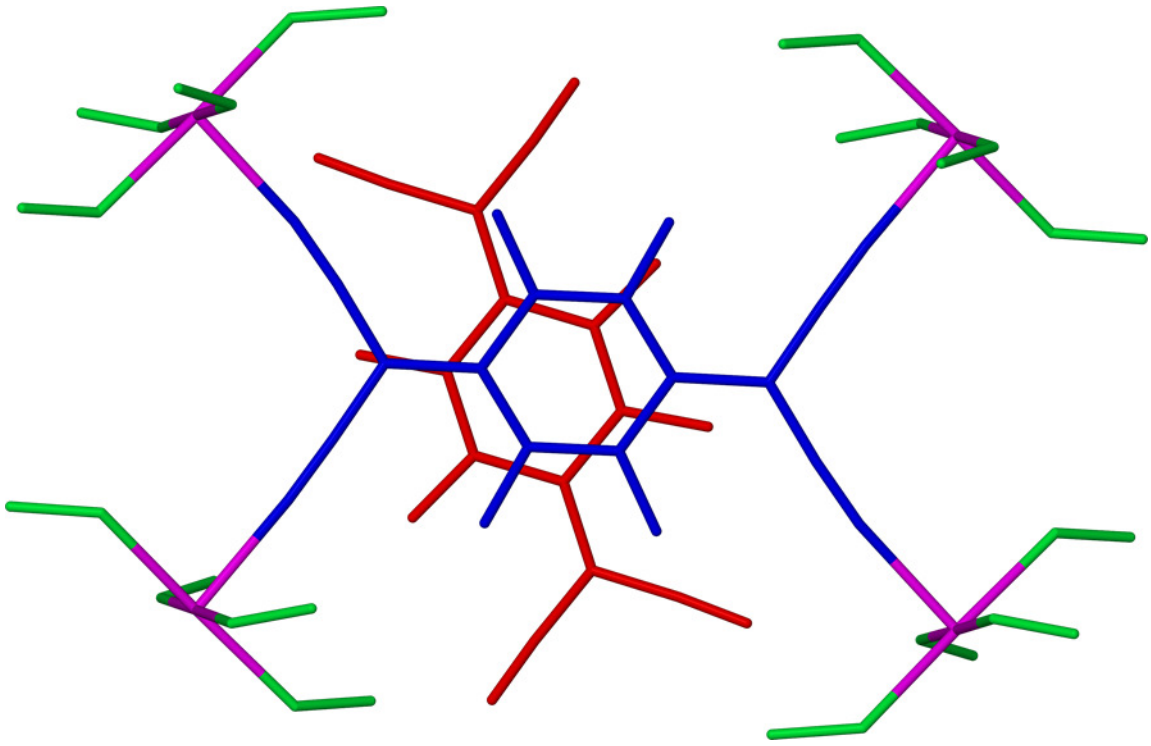

Figure 3.3 Crystal structure of **1⊃7.5CH$_3$OH** viewed down the *a* axis emphasizing the slipped-rotated ring-over-ring conformation of μ_4-TCNQF$_4$ and uncoordinated TCNQF$_4$. The interstitial methanol molecules and hydrogen atoms are omitted for the sake of clarity. Mn = pink, μ_4-TCNQF$_4$ = blue, uncoordinated TCNQF$_4$ = red, coordinated methanol = green.

The charge ρ of each independent $TCNQF_4$ unit in **1⊃7.5CH_3OH** was estimated from the Kistenmacher relationship, ρ = A[c/(b + d)] + B (A = –46.729 and B = 22.308; A and B are determined from neutral $TCNQF_4$ (ρ = 0)[152] and (n-Bu_4N)$TCNQF_4$ (ρ = –1)[51]). The values of c, b, and d are the $TCNQF_4$ bond lengths (Figure 3.1a). The calculated values support the assignment of the bridging units as doubly reduced $[TCNQF_4]^{2-}$ ligands (ρ = –2.09), and the uncoordinated molecules as singly reduced $[TCNQF_4]^{-\bullet}$ radical anions (ρ = –0.99).

Structure of $[M(TCNQBr_2)_2(H_2O)_2]_\infty$ (M = Mn, Zn): Neutral $TCNQBr_2$ and chips of manganese or zinc were immersed in acetonitrile. After two weeks, dark purple crystals of the product $[M(TCNQBr_2)_2(H_2O)_2]_\infty$ (M = Mn, Zn) were harvested. An X-ray structural determination revealed that $[M(TCNQBr_2)_2(H_2O)_2]_\infty$ crystallizes as a 2-D double layer network, in which $TCNQBr_2$ units are coordinated via two cyano groups to M^{II} ions in a trans-μ_2 fashion (Figure 3.4) and each M^{II} ion is bound to four different $TCNQBr_2$ molecules in equatorial positions. Two water molecules in the axial sites complete the coordination sphere of each metal ion. The 2-D net consists of eight-membered rings of alternating Mn^{II} ions and $TCNQBr_2$ ligands (Figure 3.4), which form a zig-zag double layer. Within each ring, two of the $TCNQBr_2$ linkers line the top part of the layer and the other two are located along the bottom of the layer. The interdigitation of the 2-D layers leads to a framework without large pores, in contrast to the case of **1⊃7.5CH_3OH** which has an essentially flat 2-D framework.

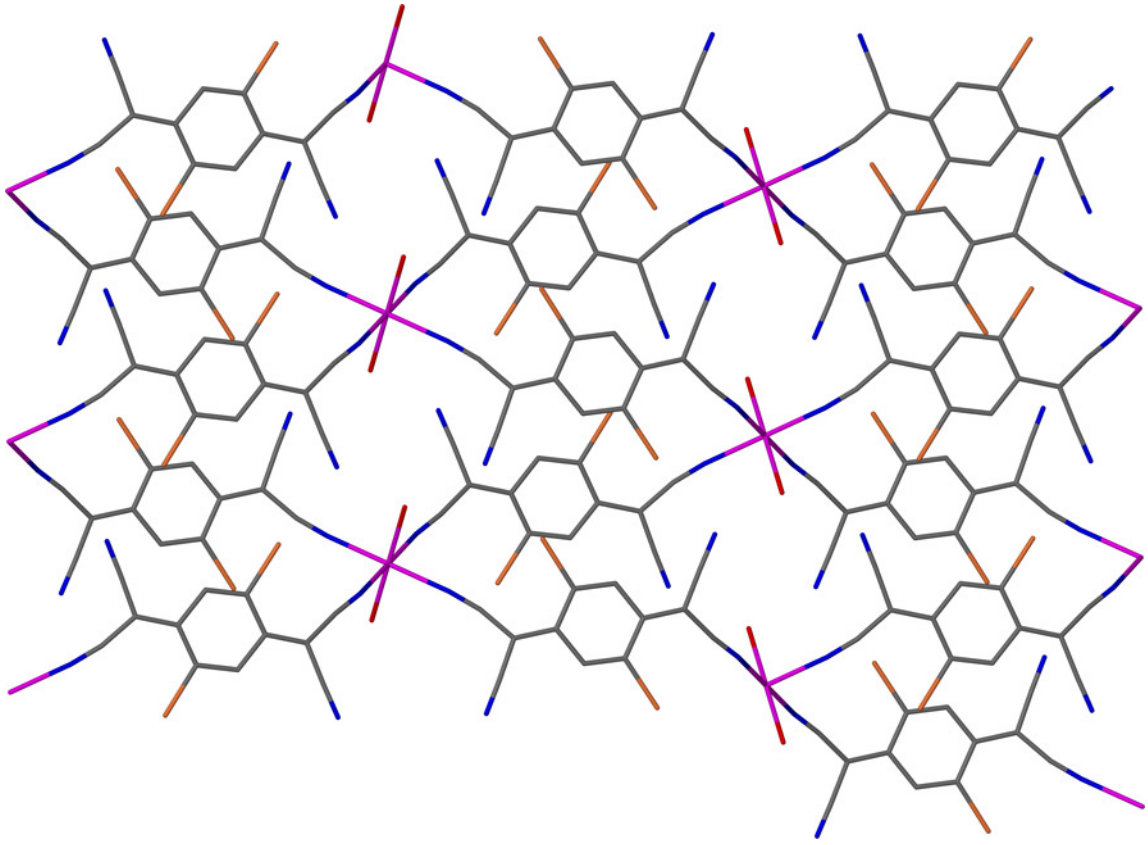

Figure 3.4 A perspective view of $[Mn(TCNQBr_2)_2(H_2O)_2]_\infty$ emphasizing the trans-μ_2-[$TCNQBr_2$] binding mode. The hydrogen atoms are omitted for the sake of clarity. Color code: Mn = pink, C = gray, N = blue, Br = orange, O = red.

There are no π-π contacts within the 2-D framework of $[M(TCNQBr_2)_2(H_2O)_2]_\infty$ because the trans-μ_2 binding mode prevents the $TCNQBr_2$ from forming stacks within the same framework. The closest lateral C···C distance between $TCNQBr_2$ groups from the top and bottom of the double layer is 3.714 Å and the interplanar distance within the double layer is 3.43 Å. There are strong interlayer π-π interactions, however, with an interplanar distance of 3.11 Å with slipped $TCNQBr_2$ groups in a ring-over-external-bond conformation (Figures 2.1c and 3.5).

This particular architecture is unprecedented; in the the case of the 2-D material $[Mn(TCNQ)_2(H_2O)_2]_\infty$ the binding mode is syn-μ_2 which causes strong intralayer π-π interactions (3.1 Å) with slipped TCNQ groups in a ring-over-ring conformation with weak interlayer π-π interactions (3.6 Å).[117] In the case of $[Mn(TCNQBr_2)_2(H_2O)_2]_\infty$ there are hydrogen bonds within the double layer between dangling CN groups of $TCNQBr_2$ units and coordinated water molecules with N···O distances of 2.99 Å and 3.05 Å. There are no interlayer hydrogen bonds. The H···Br contacts between $TCNQBr_2$ units residing in the same plane of the double layer are weak with H···Br distances of 3.26 Å, which are slightly longer than the sum of the van der Waals radii (H···Br: 3.20 Å). There are no interlayer H···Br interactions with the closest contacts being much longer that the van der Waals radii (O···Br distances between interlayer neighboring $TCNQBr_2$ and coordinated water molecules are 3.86 Å and H···Br distances between interlayer neighboring $TCNQBr_2$ units are 4.52 Å.)

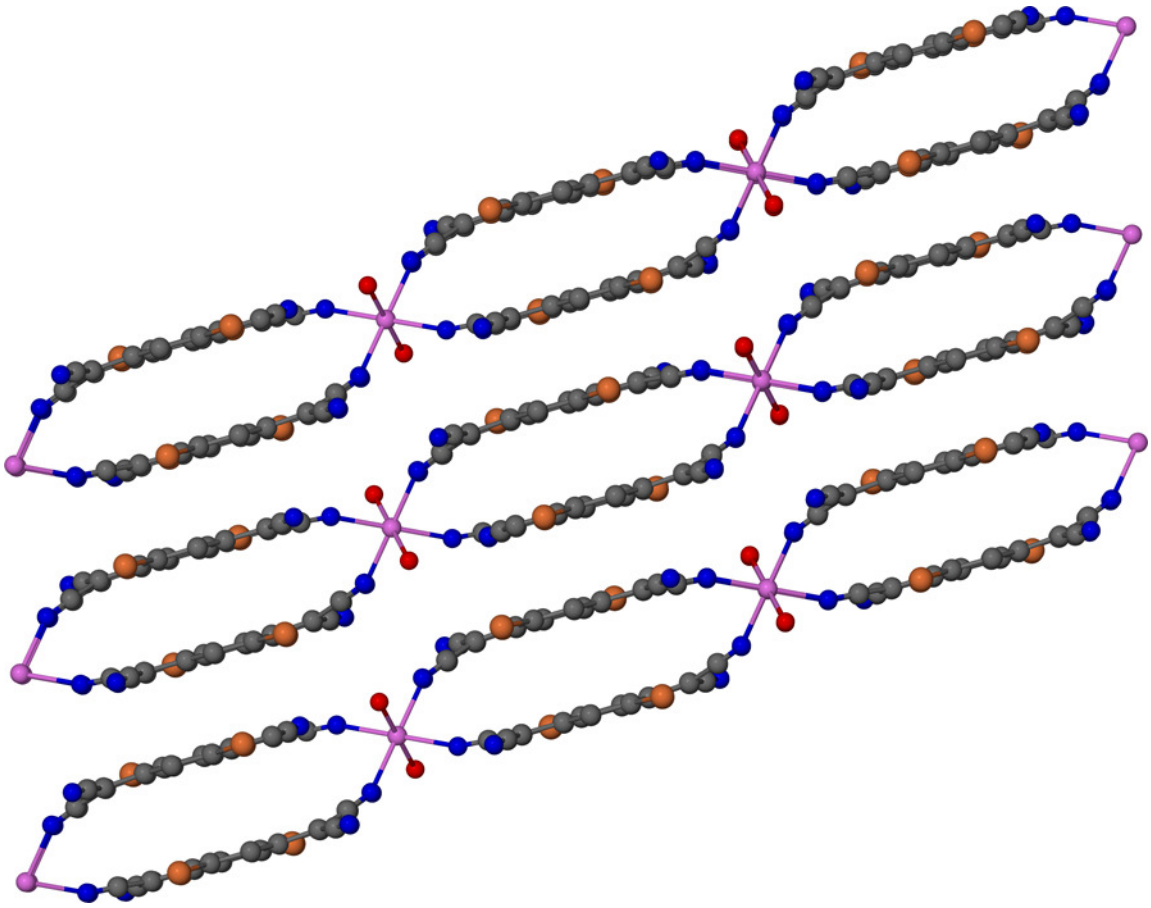

Figure 3.5 Packing diagram parallel to the *ac* plane depicting π-π stacking interactions in the structure of $[Mn(TCNQBr_2)_2(H_2O)_2]_\infty$ that emphasizes the fact that the $TCNQBr_2$ ligands within a stack are slipped in a ring-over-external-bond conformation. The hydrogen atoms are omitted for the sake of clarity. Color code: Mn, pink, C = gray, N = blue, Br = orange, H = light blue.

Infrared Spectroscopy: Infrared (IR) spectroscopy is also useful for assigning the oxidation state of TCNQ in its compounds.[153,46b] The IR spectrum of **1⊃7.5CH$_3$OH** exhibits three ν(CN) stretching modes at 2211, 2202, and 2161 cm^{-1}, all of which occur at lower frequencies than the corresponding features of neutral $TCNQF_4$ (2227 cm^{-1}). The absorptions at 2211 and 2202 cm^{-1} are in accord with the presence of the $[TCNQF_4]^{-\bullet}$ radical anion, whereas the stretch at 2161 cm^{-1} is evidence for the presence of the $[TCNQF_4]^{2-}$ dianion, as indicated by the similarity to the previously reported data for the doubly reduced species (2167 cm^{-1}).[46b] Therefore, as established by the structural and IR data, the present compound consists of an unusual combination of the cationic 2-D layer $\{[(Mn^{II})_2(\mu_4\text{-}[TCNQF_4]^{2-})(CH_3OH)_{7.5}(H_2O)_{0.5}]^{2+}\}_\infty$ co-crystallized with the radical anion $[TCNQF_4]^{-\bullet}$ (Figure 3.2b). It should be mentioned that there is no evidence of the presence of the dianion in the starting material, $Li(TCNQF_4)$, based on the IR data that revealed only a ν(CN) stretch at 2198 cm^{-1} which corresponds to the radical anion. Clearly the dianion was generated by disproportionation of the radical $[TCNQF_4]^{-\bullet}$, as previously observed by others.[45,154]

In general, instances of fully characterized $[TCNQF_x]^{2-}$ dianions (x = 0–4) are rare. Previously reported structurally characterized examples include the charge-transfer salts $([Cp^*_2M]^{+\bullet})_2[TCNQF_x]^{2-}$ (M = Co, Fe; x = 0, 4), discrete complexes $([Cp_2V]^{+\bullet})_2[TCNQ]^{2-}$ [46] $[B(C_6F_5)_3]_2$ and $\{[Cp_2V]^{2+}[TCNQ]^{2-}[B(C_6F_5)_3]_2\}_2$,[47] an infinite chain $[Mn^{III}(salen)(TCNQ^{2-})_{0.5}][Mn^{III}(salen)(TCNQ^{2-})_{0.5}\ (CH_3OH)]$,[44] and 3-D frameworks of composition $\{[Zn^{II}(\mu_4\text{-}TCNQ^{2-})bpy]\}_\infty$ [45] and $(Ph_3PMe)_2[Cd_2(TCNQ)_3]$.[48] Thus, according

to our knowledge μ_4-coordination of $[TCNQF_4]^{2-}$ dianion is unprecedented, moreover the coexistence of radicals and dianions of TCNQ has not been previously noted.

The IR spectrum of $Mn(TCNQF_4)^{-\bullet}(TCNQF_4^{-2})_{0.5}(CH_3CN)$ exhibits three ν(CN) stretching modes at 2205, 2170, and 2083 cm^{-1} all of which occur at lower frequencies than the corresponding features of neutral $TCNQF_4$ (2227 cm^{-1}). The absorption at 2205 is in accord with the presence of the $[TCNQF_4]^{-\bullet}$ radical anion, and the absorptions at 2170 cm^{-1} and 2083 cm^{-1} indicate the presence of the dianion.

The IR spectrum of $Co(TCNQF_4)^{-\bullet}(TCNQF_4^{-2})_{0.5}(CH_3CN)$ exhibits three ν(CN) stretching modes at 2207, 2134, and 2060 cm^{-1} all of which occur at lower frequencies than the corresponding features of neutral $TCNQF_4$ (2227 cm^{-1}). The absorption at 2207 is in accord with the presence of the $[TCNQF_4]^{-\bullet}$ radical anion, and the absorptions at 2134 cm^{-1} and 2060 cm^{-1} indicate the presence of the dianion.

The IR spectrum of $[Mn(TCNQBr_2)_2(H_2O)_2]_\infty$ exhibits two ν(CN) stretching modes at 2195, 2168 cm^{-1} all of which occur at lower frequencies than the corresponding features of neutral $TCNQBr_2$ (2218 cm^{-1}). Both absorptions at 2195 and 2168 cm^{-1} are in accord with the presence of the $[TCNQBr_2]^{-\bullet}$ radical anion because they are close to the stretch for $Li(TCNQBr_2)$ (2196 cm^{-1}).

Direct-current Magnetic Susceptibility Measurements: Measurements were performed at 1000 Oe from 1.8 to 300 K with the use of a SQUID magnetometer. To prevent the loss of interstitial solvent, magnetic susceptibility measurements of **1⊃7.5CH$_3$OH** were performed on a sample covered with methanol in a sealed tube. The value of χT for **1⊃7.5CH$_3$OH** at 300 K is 9.5 $emu \cdot mol^{-1} \cdot K$, which corresponds to the

expected spin-only value for two non-interacting Mn^{II} ions (S = 5/2, g = 2.0) and two $[TCNQF_4]^{-\bullet}$ radicals (S = 1/2, g = 2.0). As the temperature is lowered, the χT value decreases smoothly, indicating the presence of a weak antiferromagnetic interaction. The data were fitted to the Curie-Weiss law with parameters θ = –1.7 K and C = 9.5 emu·mol^{-1}·K, values which indicate that the magnetic coupling between Mn^{II} ions propagated by the $[TCNQ]^{2-}$ dianions is, as expected, very weak (Figure 3.6).

Next, the polycrystalline sample was filtered and dried *in vacuo* for 4 h. The magnetic behavior of this dry sample (**1a**) was found to be remarkably different. When the temperature is decreased, the χT value gradually increases from 9.5 emu·mol^{-1}·K at 300 K to a maximum of 18 emu·mol^{-1}·K at ~11 K (Figure 3.7), which indicates the presence of ferromagnetic interactions. Below 10 K, χT abruptly decreases, suggesting the possibility of a magnetic phase transition. The magnetic susceptibility of **1a** was fitted to a Heisenberg chain model. The fitting leads to the following parameters: $J_{intrachain}$ = +2.18 cm^{-1}, g = 2.00 and $J_{interchain}$ = -0.32 cm^{-1}, g = 2.00 (Figure 3.6). The model indicates that there are ferromagnetic interactions within the Mn chain and antiferromagnetic interactions between neighboring chains. In one possible scenario, the chains could be composed of Mn^{II} ions connected by $[TCNQF_4]^{\bullet-}$ radicals in a cis-μ_2 binding mode which establish ferromagnetic interactions with the $[TCNQF_4]^{2-}$ promoting antiferromagnetic interactions between neighboring chains. Evidence for the phase transition was obtained by AC susceptibility and field-cooled (FC) - zero-field-cooled (ZFC) magnetization measurements.

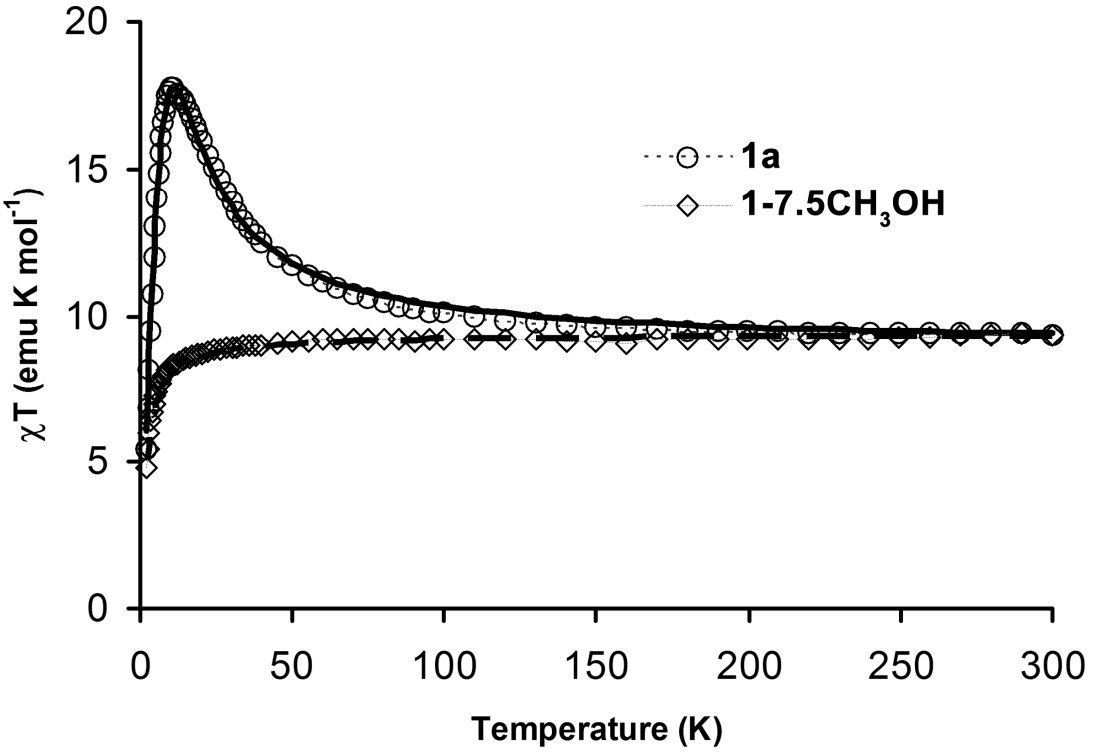

Figure 3.6 Temperature dependence of the χT product for **1**⊃7.5CH_3OH and **1a** (dry sample). The discontinuous black line is the best fit to the Curie-Weiss law for **1**⊃7.5CH_3OH. The continuous black line is the best fit to a Heisenberg chain model for **1a**. The fitting leads to the following parameters: $J_{intrachain}$ = +2.18 cm^{-1}, g = 2.00 and $J_{interchain}$ = -0.32 cm^{-1}, g = 2.00.

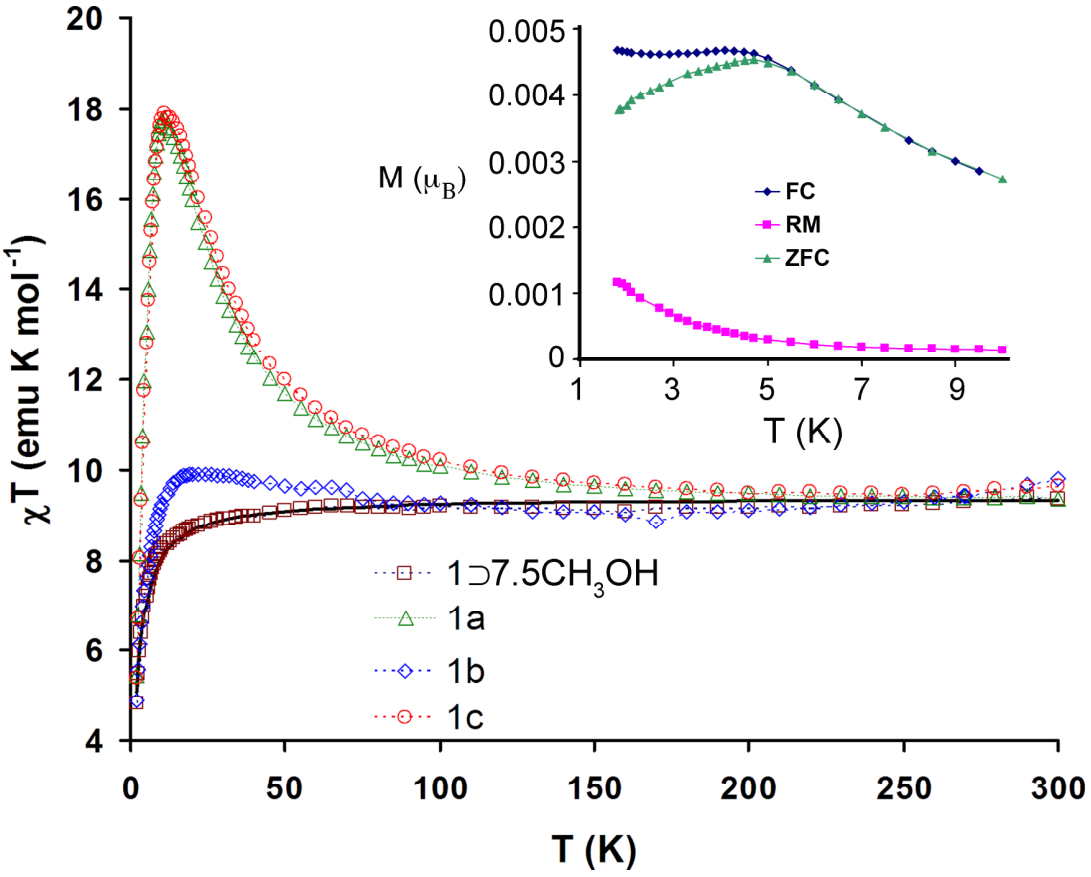

Figure 3.7 Temperature dependence of the χT product for **1**⊃7.5CH_3OH and **1a-c**. **1a** = dry sample, **1b** = resolvated sample, **1c** = sample dried for a second time. The solid black line is the best fit to the Curie-Weiss law for **1**⊃7.5CH_3OH. Inset: FC and ZFC curves for **1a**.

FC and ZFC dependences coincide down to T_c = 5 K (Figure 3.7, inset), below which temperature they diverge, suggesting spin-glass behavior. Hysteresis was observed for **1a** at 1.8 K with coercivity of ~100 Oe and remnant magnetization of 0.06 μ_B (Figure 3.8).

The dry sample **1a** was then immersed in methanol for 12 h resulting in sample **1b**. The magnetic susceptibility of **1b** was obtained on a sample covered with methanol in a sealed tube. The DC χT values of **1b** at low temperatures are considerably decreased from those observed for **1a**, but did not completely revert to the values observed for **1⊃7.5CH$_3$OH** (Figure 3.7). Thus, the short-range ferromagnetic interactions are now much weaker than those observed in **1a**. Sample **1b** was filtered and once again dried *in vacuo* for 4 h. The obtained dry sample (**1c**) again showed an increase in the χT values below 150 K (Figure 3.7), resembling the behavior observed for **1a**.

Reversible changes in magnetic properties upon desolvation-resolvation of coordination frameworks have been observed in several cases, and the term “magnetic sponges” was proposed for such materials.[155]

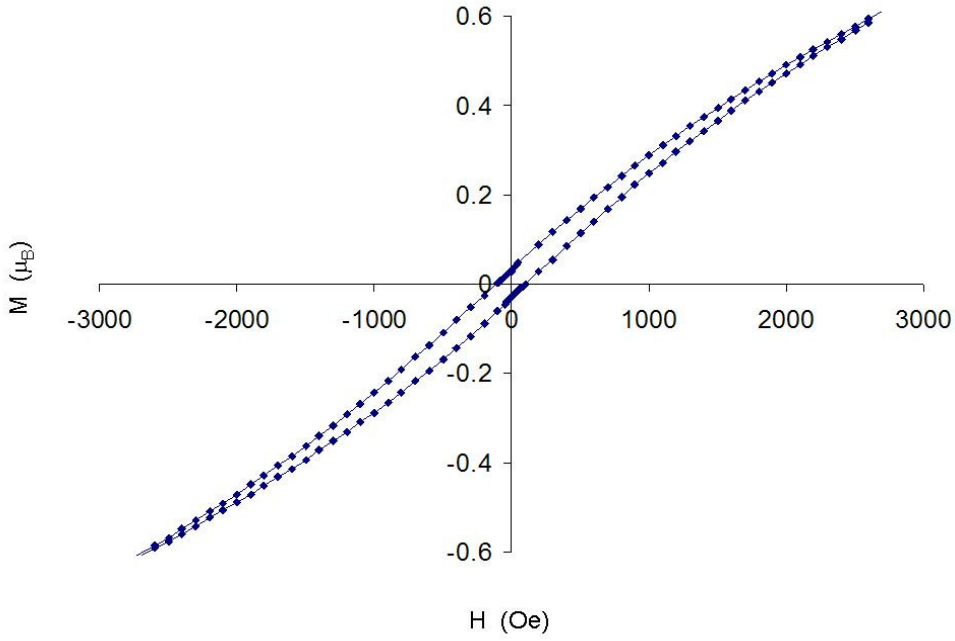

Figure 3.8 Hysteresis loop for **1a** at 1.8K.

The value of χT for $Mn(TCNQF_4)^{-\bullet}(TCNQF_4^{-2})_{0.5}(CH_3CN)$ at 300 K is 5.29 emu·mol^{-1}·K, which corresponds to the expected spin-only value for one non-interacting Mn^{II} ion (S = 5/2, g = 2.12) and one $[TCNQF_4]^{-\bullet}$ radical (S = 1/2, g = 2.0) χT_{calc} = 5.29 emu·mol^{-1}·K. As the temperature is lowered, the χT value increases smoothly until reaching 70 K, indicating the presence of ferromagnetic interactions. The χT value increases rapidly starting at 70 K and reaches a maximum of 12.61 emu·mol^{-1}·K at 13 K, after such temperature the χT value decreases rapidly reaching 3.07 emu·mol^{-1}·K at 2 K (Figure 3.9). The data were fitted to the Curie-Weiss law with parameters θ = +17 K and C = 4.9 emu·mol^{-1}·K; such values indicate the presence of ferromagnetic interactions. No hysteresis loop was observed for the magnetization versus field measurements. The zero-field-cooled (ZFC) versus field-cooled (FC) magnetization data shows a bifurcation at 6.5 K (Figure 3.10), which is indicative of a magnetic phase transition at that temperature.

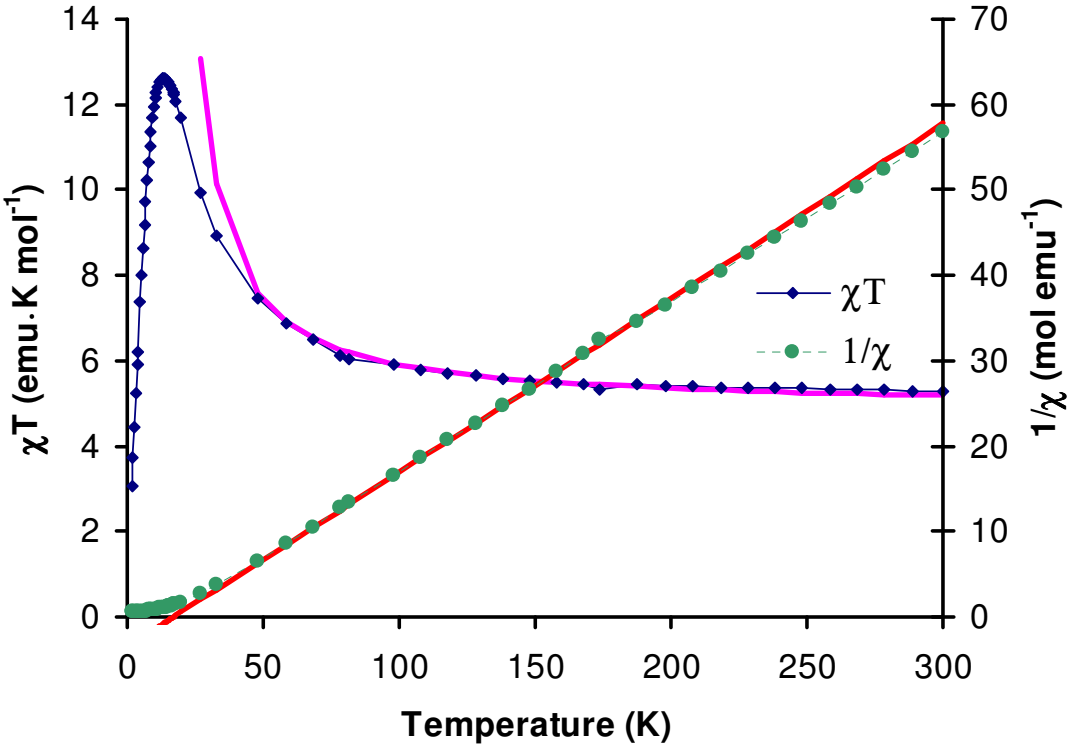

Figure 3.9 Temperature dependence of the χT product for $Mn(TCNQF_4)^{\bullet-}(TCNQF_4^{-2})_{0.5}(CH_3CN)$. The purple line is the best fit to the Curie-Weiss law with parameters θ = +17 K and C = 4.9 emu·mol^{-1}·K.

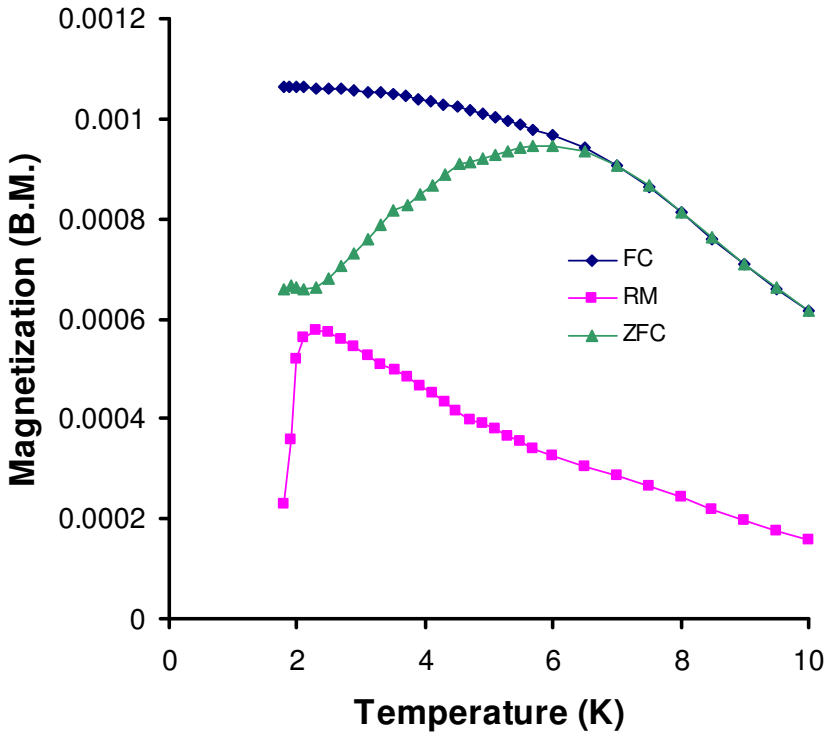

Figure 3.10 Field-cooled (FC), zero-field-cooled (ZFC) and remanent magnetization (RM) of the $Mn(TCNQF_4)^{-\bullet}(TCNQF_4^{-2})_{0.5}(CH_3CN)$ complex.

The value of χT for $Co(TCNQF_4)^{-\bullet}(TCNQF_4^{-2})_{0.5}(CH_3CN)$ at 300 K is 3.00 emu·mol^{-1}·K, which is close to the expected spin-only value for one non-interacting Co^{II} ion (S = 3/2, g = 2.37) and one $[TCNQF_4]^{\bullet}$ radical (S = 1/2, g = 2.0) χT_{calc} = 3.01 emu·mol^{-1}·K. As the temperature is lowered, the χT value decreases smoothly until reaching 2.07 emu·mol^{-1}·K at 26 K, indicating the presence of antiferromagnetic interactions. The χT value increases from 26 K to reach a maximum of 2.11 emu·mol^{-1}·K at 16 K followed by a decrease until reaching the value of 0.72 emu·mol^{-1}·K at 2K. (Figure 3.11). The data were fitted to the Curie-Weiss law with parameters θ = -28 K and C = 4.13 emu·mol^{-1}·K; these values indicate the presence of antiferromagnetic interactions. A hysteresis loop was observed for the magnetization versus field measurement with a coercive field of 600 Oe and a remnant magnetization of 0.0025 μ_B (Figure 3.12). The zero-field-cooled (ZFC) versus field-cooled (FC) magnetization data shows a bifurcation at 11.4 K (Figure 3.13), which is indicative of a magnetic phase transition.

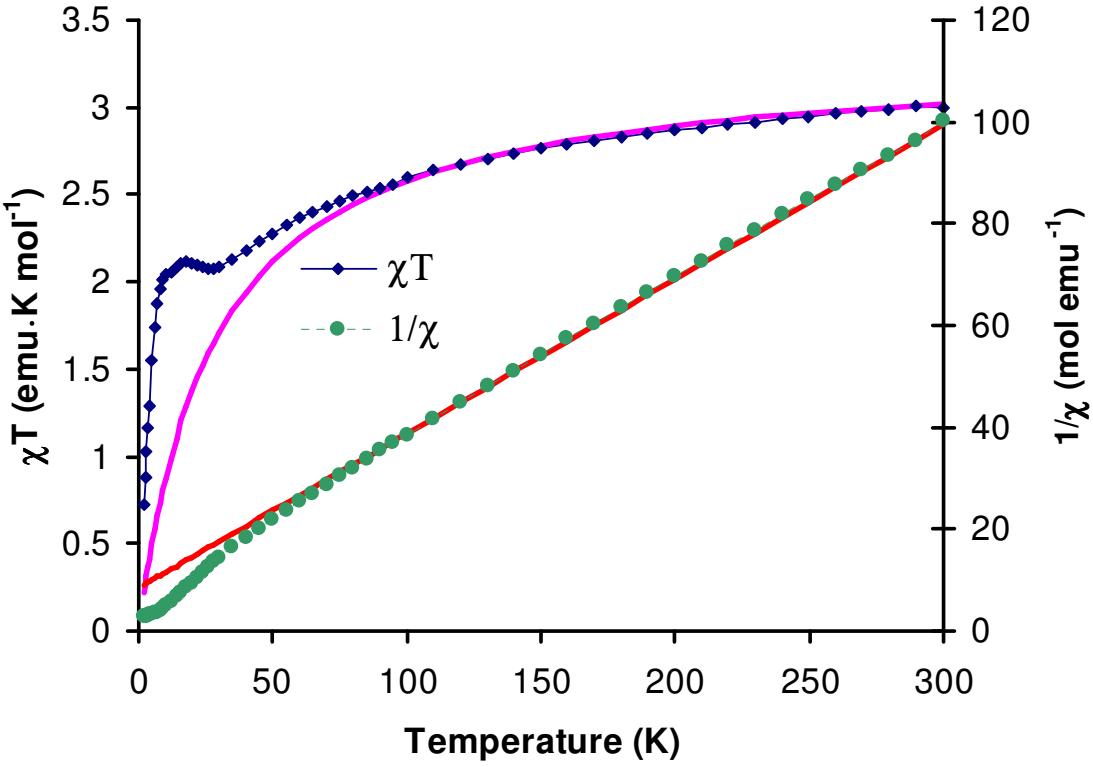

Figure 3.11 Temperature dependence of the χT product for $Co(TCNQF_4)^{-\bullet}(TCNQF_4^{-2})_{0.5}(CH_3CN)$. The purple line is the best fit to the Curie-Weiss law with parameters θ = -28 K and C = 4.13 emu·mol^{-1}·K.

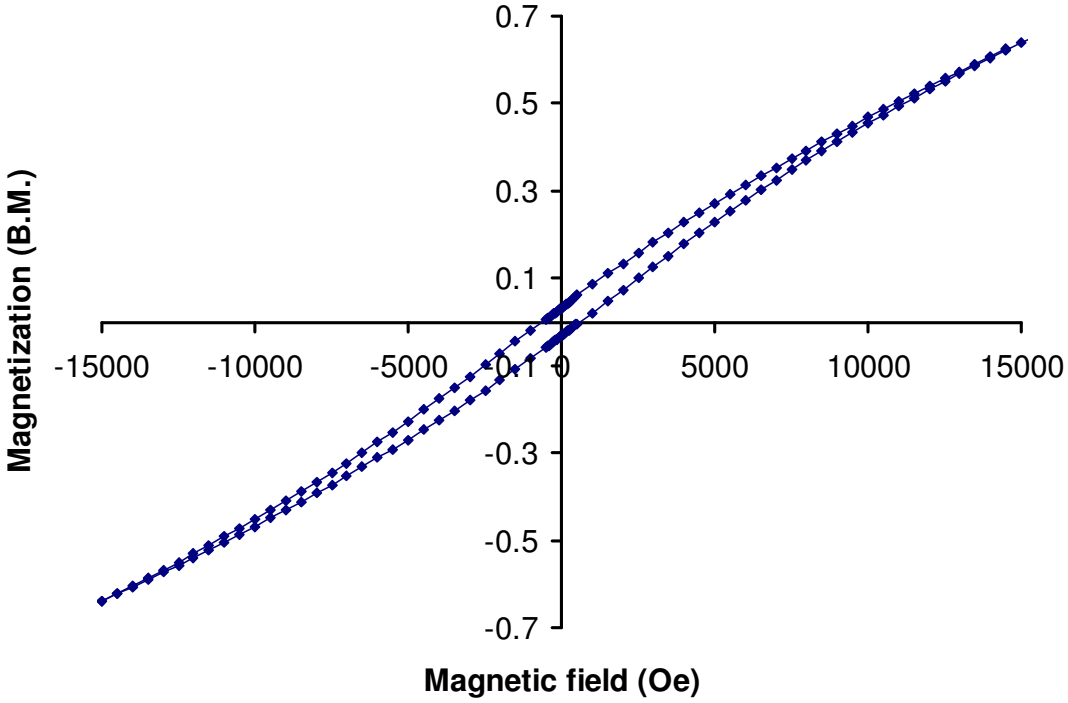

Figure 3.12 Hysteresis loop for $Co(TCNQF_4)^{-\bullet}(TCNQF_4^{-2})_{0.5}(CH_3CN)$ at 1.8 K.

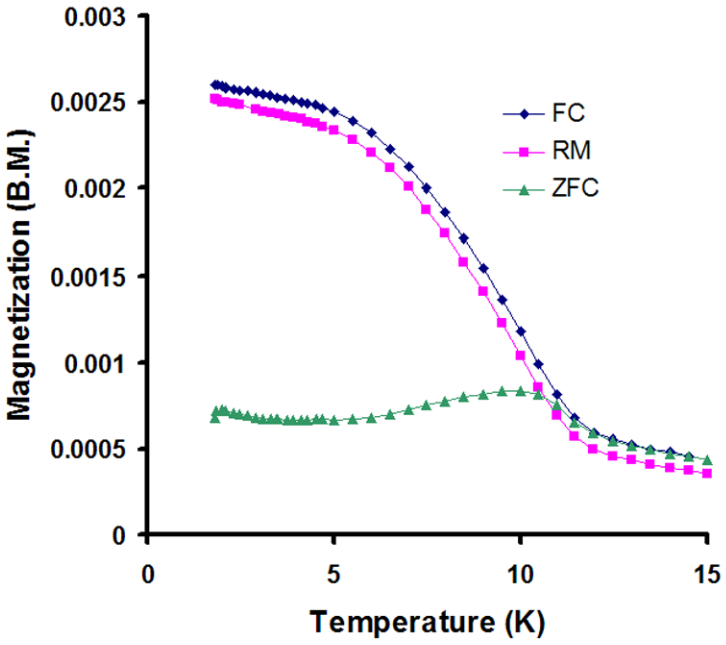

Figure 3.13 Field-cooled (FC), zero-field-cooled (ZFC) and remanent magnetization (RM) of the $Co(TCNQF_4)^{-\bullet}(TCNQF_4^{-2})_{0.5}(CH_3CN)$ complex.

The value of χT for $[Mn(TCNQBr_2)_2(H_2O)_2]_\infty$ at 300 K is 9.67 emu·mol^{-1}·K, which is lower than the expected spin-only value for two non-interacting Mn^{II} ion (S = 5/2, g = 1.99) and four $[TCNQBr_2]^{\bullet}$ radicals (S = 1/2, g = 2.0) χT_{calc} = 10.16 emu·mol^{-1}·K. The low χT value at room temperature is an indication that there are strong antiferromagnetic interactions between π-π interacting $TCNQBr_2$ units. As the temperature is lowered, the χT value decreases smoothly until reaching 45 K, indicating the presence of antiferromagnetic interactions. The χT value increases starting at 45 K and reaches a maximum of 8.10 emu·mol^{-1}·K at 40 K, after which temperature the χT value rapidly decreases reaching 1.78 emu·mol^{-1}·K at 2 K. The data were fitted to the Curie-Weiss law with parameters θ = -16 K and C = 10.15 emu·mol^{-1}·K, results that indicate the presence of antiferromagnetic interactions. (Figure 3.14). The zero-field-cooled (ZFC) versus field-cooled (FC) magnetization data shows a very small bifurcation at 14.6 K (Figure 3.15), but this is not taken to be sufficiently conclusive of a magnetic phase transition at that temperature.

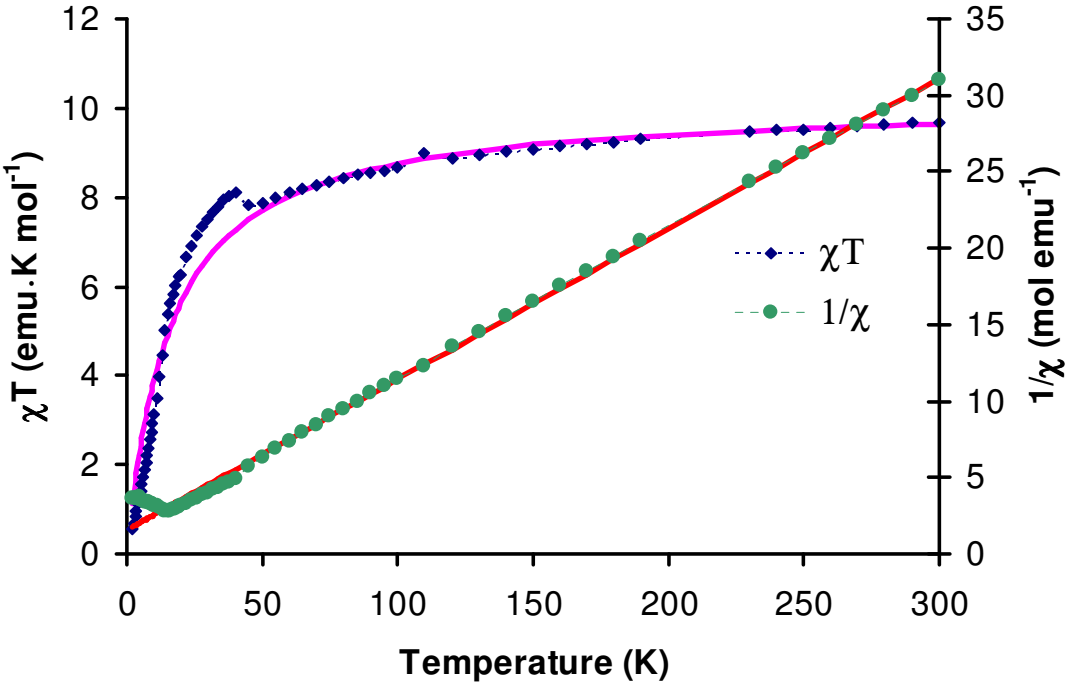

Figure 3.14 Temperature dependence of the χT product for $[Mn(TCNQBr_2)_2(H_2O)_2]_\infty$. The purple line is the best fit to the Curie-Weiss law with parameters θ = -16 K and C = 10.15 emu·mol^{-1}·K.

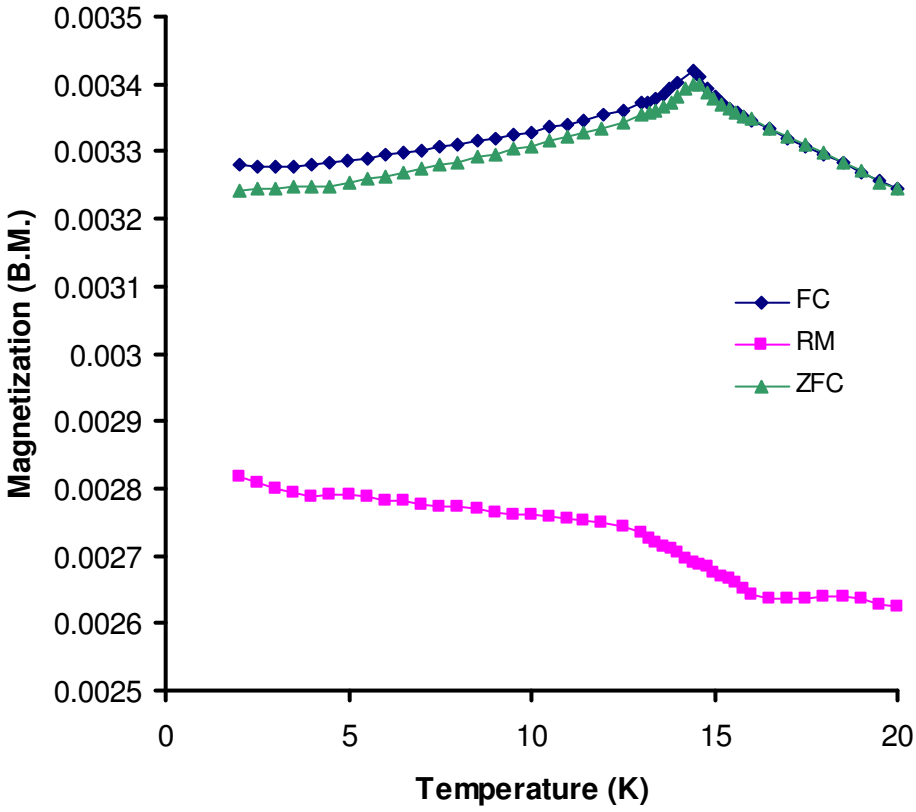

Figure 3.15 Field-cooled (FC), zero-field-cooled (ZFC) and remanent magnetization (RM) of the $[Mn(TCNQBr_2)_2(H_2O)_2]_\infty$ complex.

Alternating-current Magnetic Susceptibility Measurements: The zero-field AC susceptibility measurements were performed in the range of frequencies from 1 to 1000 Hz at H_{AC} = 3 Oe. Compound **1a** show a broad frequency-dependent out-of-phase signal below T_c (Figure 3.16). The Mydosh parameter estimated from this dependence, ϕ = 0.023, is characteristic of a spin-glass phase.[156] The dry sample **1a** was then immersed in methanol for 12 h and the resulting sample (**1b**), covered with methanol in a sealed tube, no longer showed an out-of-phase AC signal (Figure 3.17). Thus, after re-solvation the spin-glass ordering is destroyed. Sample **1b** was filtered and once again dried *in vacuo* for 4 h. The obtained dry sample (**1c**) again showed the presence of a broad frequency-dependent signal in the χ'' vs. T dependence (Figure 3.17), resembling the behavior observed for **1a**. This indicates that upon removal of guest molecules the magnetic glassiness of the host is recovered.

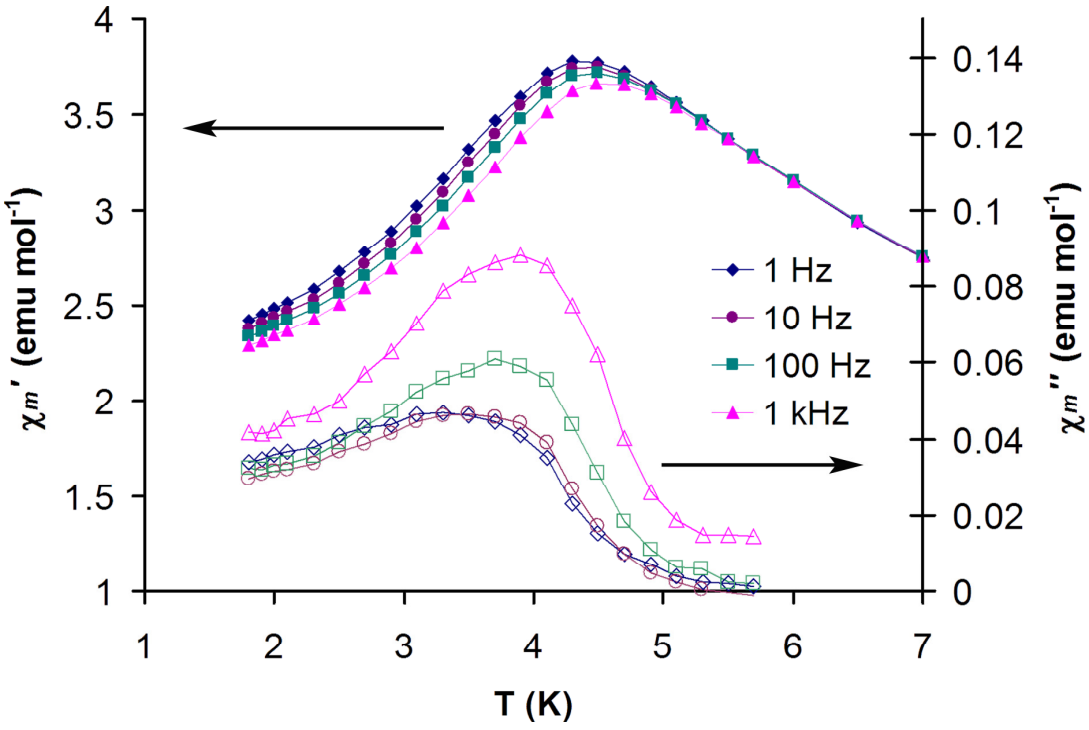

Figure 3.16 Temperature dependences of the real χ' and imaginary χ'' components of the AC magnetic susceptibility of **1a** measured in an oscillating field of 3 Oe at different frequencies.

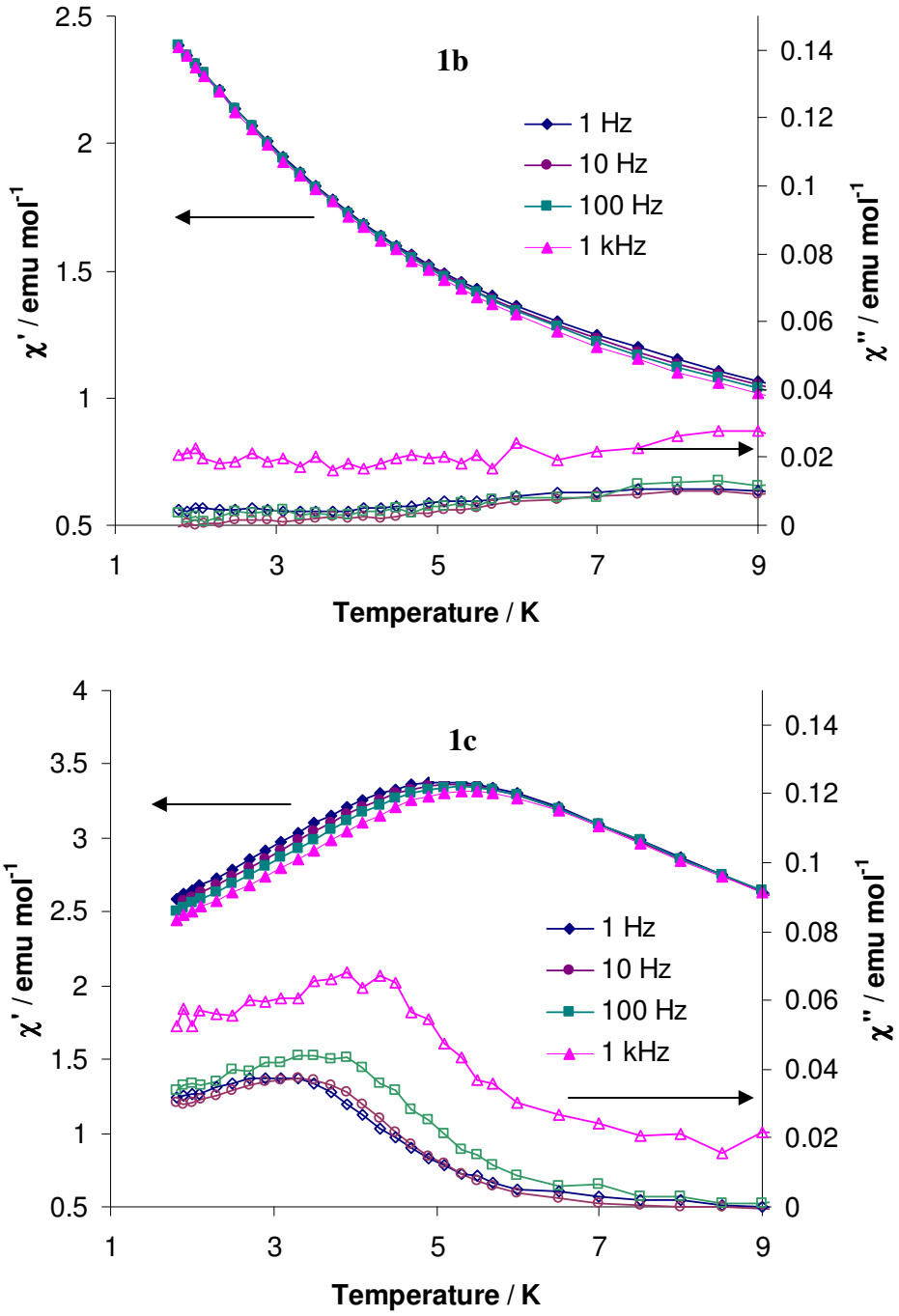

Figure 3.17 Temperature dependence of the real χ' and imaginary χ'' components of the AC magnetic susceptibility of **1b** (top) and **1c** (bottom) measured in an oscillating field of 3 Oe at different frequencies.

The $M(TCNQF_4)^{-\bullet}(TCNQF_4^{-2})_{0.5}(CH_3CN)$, **M/TCNQF$_4$**, (M = Mn, Co) compounds exhibit typical intensities for the AC signals corresponding to bulk magnetic ordering. The maximum of the out-of-phase signal was observed at 6.0 K (M = Mn, Figure 3.18), and 9.7 K (M = Co, Figure 3.19) as shown in the corresponding figures. Conversely, a weaker out-of-phase AC signal was observed for $[Mn(TCNQBr_2)_2(H_2O)_2]_\infty$ (Figure 3.20). Thus, the AC magnetic studies indicate that **Co/TCNQF$_4$** magnetically orders at 9.7 K and that **Mn/TCNQF$_4$** magnetically orders at 6.0 K. Compound **1a** is a glassy magnet with a broad weak out-of-phase AC signal. The very small difference in the ZFC-FC data for $[Mn(TCNQBr_2)_2(H_2O)_2]_\infty$ suggests an absence of long range magnetic ordering.

X-ray Powder Diffraction Studies: The dry sample **1a** is a different phase than **1⊃7.5CH$_3$OH**, as indicated by a comparison of its x-ray powder diffraction pattern to the theoretically simulated pattern of **1**⊃7.5CH_3OH (Figure 3.21). The powder data reveal that, not surprisingly, the material has poor crystallinity in the dried state as well.

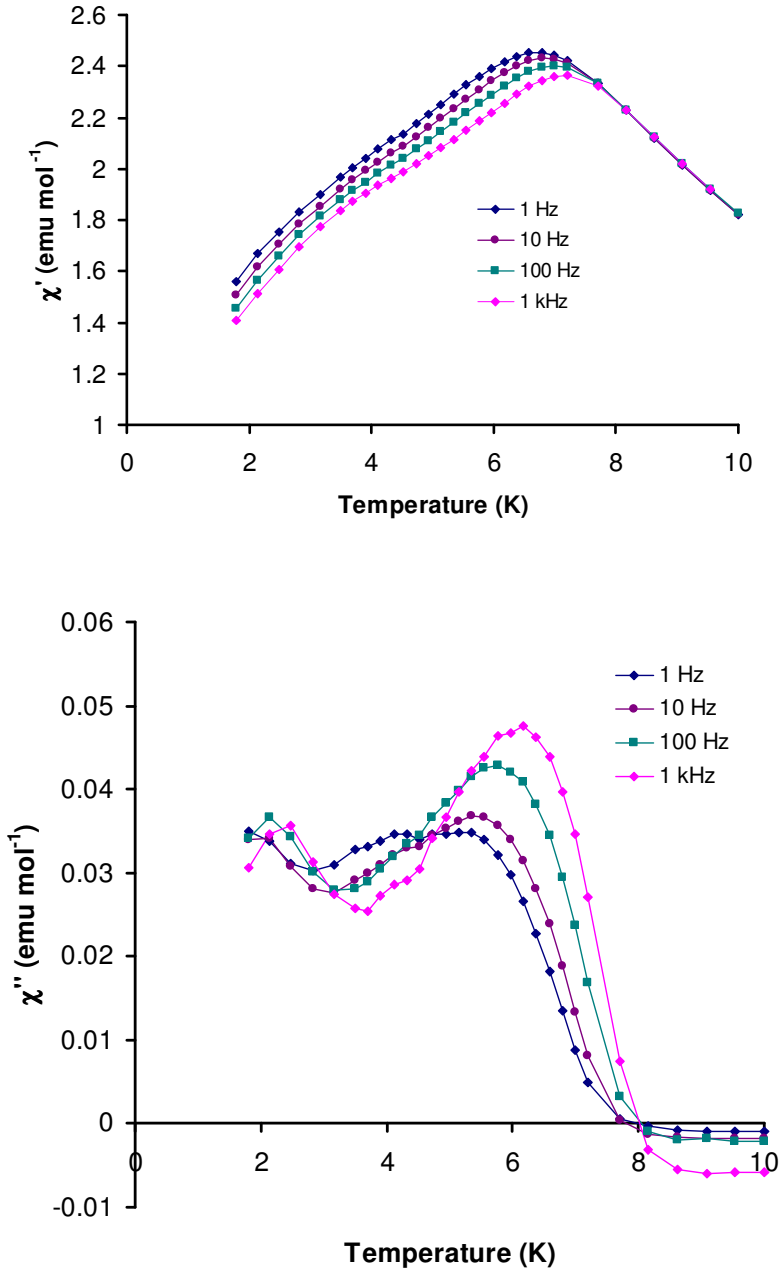

Figure 3.18 Temperature dependence of the real χ' (top) and imaginary χ'' (bottom) components of the AC magnetic susceptibility of $Mn(TCNQF_4)^{\bullet}(TCNQF_4^{-2})_{0.5}(CH_3CN)$ measured in an oscillating field of 3 Oe at different frequencies.

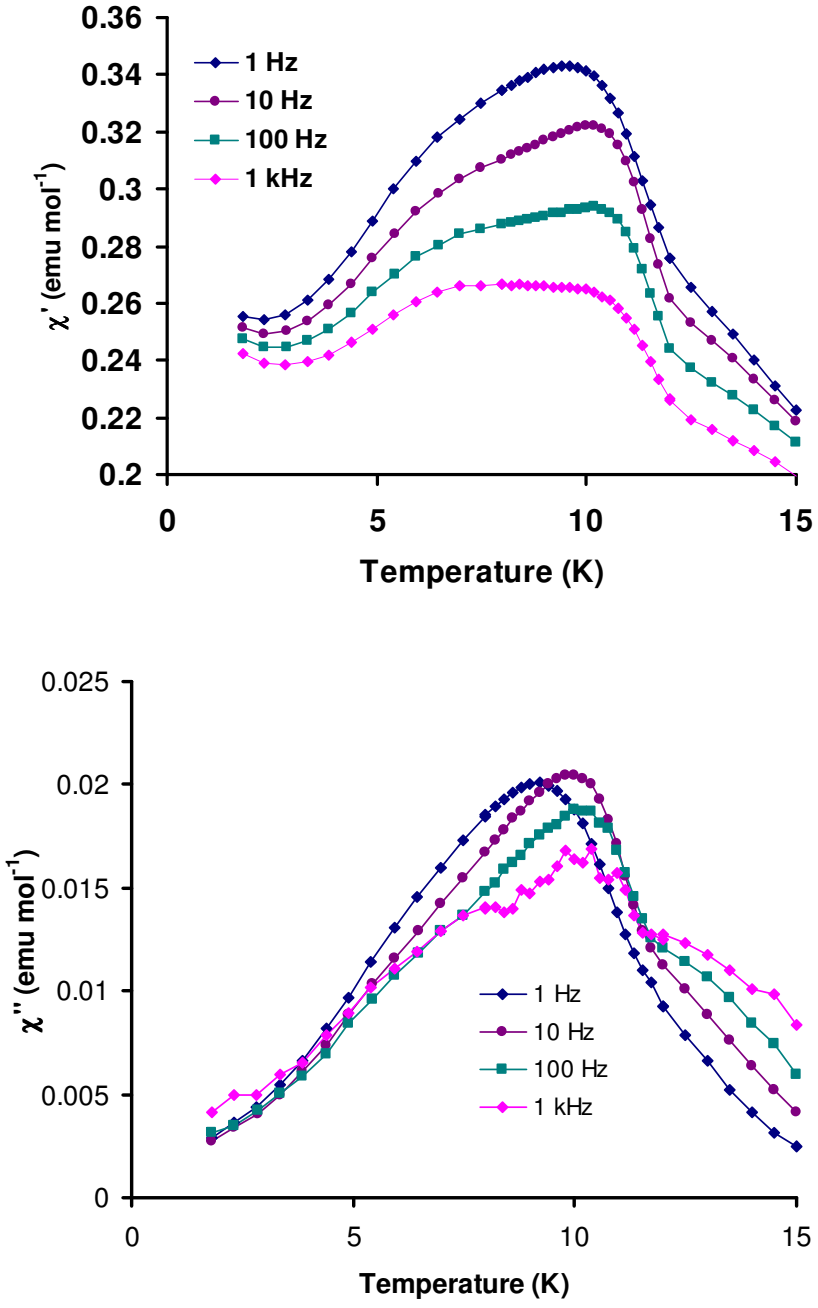

Figure 3.19 Temperature dependence of the real χ' (top) and imaginary χ'' (bottom) components of the AC magnetic susceptibility of $Co(TCNQF_4)^{-\bullet}(TCNQF_4^{-2})_{0.5}(CH_3CN)$ measured in an oscillating field of 3 Oe at different frequencies.

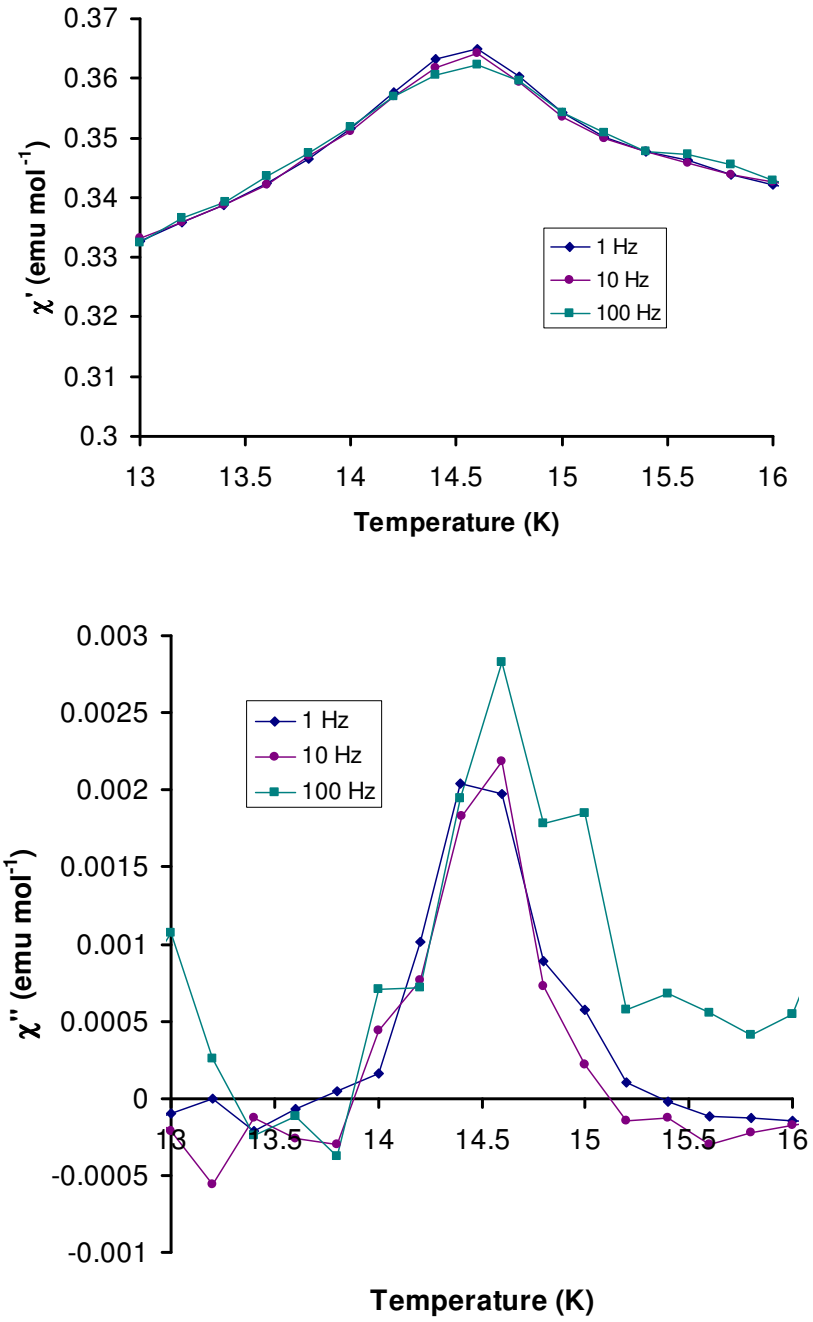

Figure 3.20 Temperature dependence of the real χ' (top) and imaginary χ'' (bottom) components of the AC magnetic susceptibility of $[Mn(TCNQBr_2)_2(H_2O)_2]_\infty$ measured in an oscillating field of 3 Oe at different frequencies.

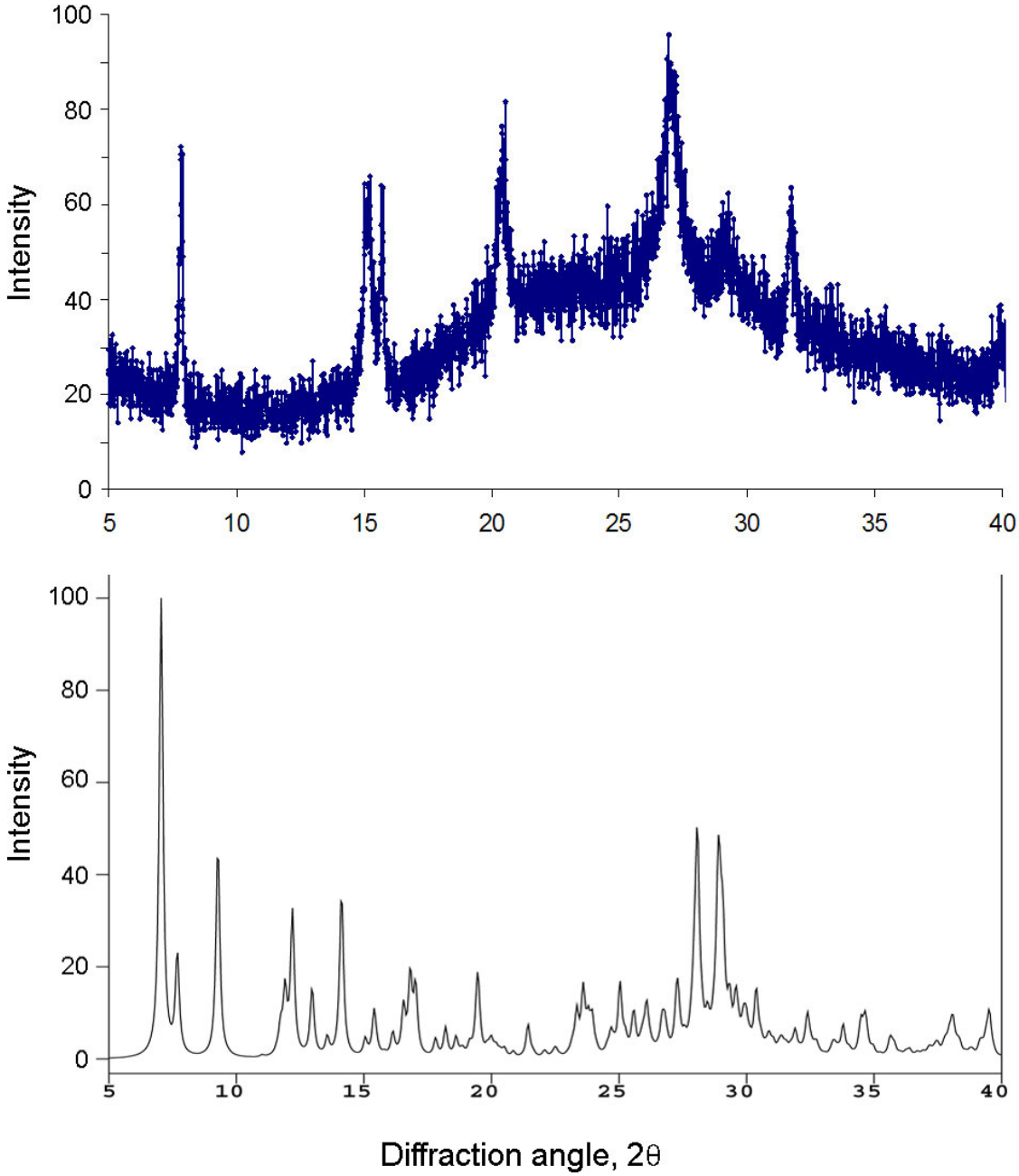

Figure 3.21 X-ray powder diffraction pattern of **1a** (top) and simulated X-ray powder diffraction pattern of **1**⊃7.5CH_3OH (bottom) measured with Cu Kα radiation (λ = 1.54096Å).

Conclusions

As stated earlier, the $[TCNQF_4]^{2-}$ dianion is a poor mediator of magnetic coupling between Mn^{II} ions. On the other hand, it is known that the $[TCNQF_4]^{-\bullet}$ radical provides an efficient pathway for magnetic superexchange between metal ions.[39e] The desolvation of **1**⊃7.5CH_3OH leads to the loss of some coordinated methanol molecules and it is postulated that the accompanying structural rearrangement involves binding of uncoordinated $[TCNQF_4]^{-\bullet}$ radicals to the Mn^{II} ions, the result of which is stronger magnetic communication, as observed for samples **1a** and **1c**. The five-atom bridge Mn–N≡C–C–C≡N–Mn involving the $[TCNQF_4]^{-\bullet}$ radical is expected to provide an efficient pathway for ferromagnetic superexchange between Mn^{II} ions. Furthermore, the similarity of the honeycomb nets present in **1**⊃7.5CH_3OH and $\{[M_2(O_2CCF_3)_4]_2(TCNQ)\cdot 3(C_7H_8)\}_\infty$ (M = Ru, Rh)[56a] suggests that 2-D structures could be formed with both $[TCNQF_x]^{2-}$ dianions and $[TCNQF_x]^{-\bullet}$ radicals.

The family of $M(TCNQ)_2$ molecular magnets has been extended to include the $TCNQF_4$ derivatives $M(TCNQF_4)^{-\bullet}(TCNQF_4^{-2})_{0.5}(CH_3CN)$ (M = Mn, Co) compounds, which order at 6.5 K (Mn) and 11.4 K (Co). The use of the disubstituted derivative $TCNQBr_2$ led to the isolation of two new hydrated $[M(TCNQ)_2(H_2O)_2]_\infty$ compounds $[M(TCNQBr_2)_2(H_2O)_2]_\infty$ (M = Mn, Zn). These materials exhibit a new structural type with no intralayer π-π interactions and extensive interlayer π-π interactions, in contrast to the structure of $[Mn(TCNQ)_2(H_2O)_2]_\infty$ for which there are no interlayer π-π interactions but extensive intralayer π-π interactions. Moreover, the 2-D framework of

$[M(TCNQBr_2)_2(H_2O)_2]_\infty$ presents an interesting possibility for future chemistry given that the separation of the layers could be tuned by the use of long neutral coligands which may lead to strong interactions between Mn ions and $TCNQBr_2$ radicals within the 2-D framework due to the interruption of strong interlayer interactions of $TCNQBr_2$ spin bearing units.

Experimental Section

General Methods: All reactions were performed under nitrogen using standard Schlenk techniques. $[Mn(CH_3CN)_4(BF_4)_2]$, $[Co(CH_3CN)_6(BF_4)_2]$, $TCNQF_4$, and $Li(TCNQF_4)$ were prepared according to the reported procedures.[157] Infrared (IR) spectra were measured as Nujol mulls placed between KBr plates on a Nicolet 740 FTIR spectrometer.

Synthesis: Single crystals of **1**⊃$7.5CH_3OH$ were obtained by layering a solution of $[Mn(CH_3CN)_4(BF_4)_2]$ (150 mg in 4 mL of distilled methanol) with $Li(TCNQF_4)$ (108 mg in 12 mL of distilled methanol) in a Schlenk tube (yield = 3.4 %). IR (Nujol): ν(CN)/cm^{-1} 2211m, 2202s, 2161m (CN).

The compounds $M(TCNQF_4)^{-\bullet}(TCNQF_4^{-2})_{0.5}(CH_3CN)$ (M = Mn, Co) were synthesized using the method previously developed for $M(TCNQ)_2$ materials:[52] In a Schlenk flask 0.1 mmol of the $M^{II}(BF_4)_2(CH_3CN)_6$ in 8ml CH_3CN was stirred and then 0.2mmol of $TBA(TCNQF_4)$ in 8ml CH_3CN was added dropwise to the metal solution. The solution was stirred for 20 minutes and the resulting dark purple precipitate was collected on a Schlenk frit, washed with 4 mL of CH_3CN followed by 8 mL of diethyl ether and then

vacuum dried for 30 minutes. IR (Nujol): ν(CN)/cm^{-1} Mn: 2205, 2170, 2083; Co: 2207, 2134, 2060.

Synthesis of single crystals of $[M(TCNQBr_2)_2(H_2O)_2]_\infty$ (M = Mn, Zn): 30 mg of $TCNQBr_2$ were place in a 20 mL vial with 200 mg of metal chips followed by addition of 10 mL of acetonitrile. A spontaneous redox reaction occurred and dark single crystals were collected after a week. IR (Nujol): ν(CN)/cm^{-1} Mn: 2195, 2168.

X-ray Crystallography, General Procedures: In a typical experiment, a crystal selected for study was suspended in polybutene oil (Aldrich) and mounted on a cryoloop and placed in an N_2 cold stream. Single-crystal X-ray data were collected at 110 K on a Bruker SMART 1000 diffractometer equipped with a CCD detector. The data sets were recorded as three ω-scans of 606 frames each, at 0.3° step width, and integrated with the Bruker SAINT[146] software package. The absorption correction (SADABS)[147] was based on fitting a function to the empirical transmission surface as sampled by multiple equivalent measurements. Solution and refinement of the crystal structures was carried out using the SHELX[148] suite of programs and the graphical interface X-SEED.[149] Preliminary indexing of the data sets established similar monoclinic unit cells for all of the studied compounds. Systematic extinctions indicated the space group $P2_1/c$ (No. 14) for $Mn_2(TCNQF_4)(CH_3OH)_{7.5}(H_2O)_{0.5}](TCNQF_4)_2{\cdot}7.5CH_3OH\}_\infty$ and *C*2/*c* (No. 15) for $[M(TCNQBr_2)_2(H_2O)_2]_\infty$ (M = Mn, Zn). All of the structures were solved by direct methods that resolved the positions of the metal atoms and most of the C, N, F, and Br atoms. The remaining non-hydrogen atoms were located by alternating cycles of least-squares refinements and difference Fourier maps. Hydrogen atoms were placed at

calculated positions. CCDC 619045 contains the supplementary crystallographic data for $\{[Mn_2(TCNQF_4)(CH_3OH)_{7.5}(H_2O)_{0.5}](TCNQF_4)_2 \cdot 7.5CH_3OH\}_\infty$. These data can be obtained free of charge from The Cambridge Crystallographic Data Centre via www.ccdc.cam.ac.uk/data_request/cif.]

Magnetic Susceptibility Measurements: DC magnetic susceptibility measurements were performed with a Quantum Design MPMS-XL SQUID magnetometer operating in the temperature range of 1.8-300 K at 1000 G. AC magnetic susceptibility measurements were performed on the same samples with an oscillating field of 3 Oe without a DC applied field. Magnetization data were measured at 1.8 K with the magnetic field varying from 0 to 70 000 G. The data were corrected for diamagnetic contributions calculated from the Pascal constants.[158]

CHAPTER IV

HETEROSPIN SINGLE-MOLECULE MAGNETS BASED ON TERBIUM IONS AND $TCNQF_4$ RADICALS: INTERPLAY BETWEEN SINGLE-MOLECULE MAGNET AND PHONON BOTTLENECK PHENOMENA INVESTIGATED BY DILUTION STUDIES*

Introduction

One of the most significant contributions of molecular magnetism to the fields of physics and chemistry is the discovery that molecules can mimic magnetic properties typically associated with bulk magnets. Such compounds, commonly known as "Single-Molecule Magnets" (SMMs), exhibit unusual physical behavior such as quantum tunneling of the magnetization and hysteresis at the molecular level.[41] Among other applications, SMMs hold considerable promise as molecular spintronics devices for high density data storage and ultrafast processing speed.[41h,i] In addition to hysteresis of the magnetization, the slow relaxation of the magnetization of SMMs also causes a frequency dependant AC out-of-phase signal, viz., χ'', the imaginary part of the magnetic susceptibility which is one of the characteristic features of SMM behavior. The maximum of χ'' signal corresponds to the blocking temperature (T_b) and varies with frequency.

---

* Reprinted in part with permission from *Chemistry-A European Journal,* N. Lopez, A. V. Prosvirin, H. Zhao, W. Wernsdorfer, K. R. Dunbar, "*Heterospin Single-Molecule Magnets Based on Terbium Ions and $TCNQF_4$ Radicals: Interplay Between Single-Molecule Magnet and Phonon Bottleneck Phenomena Investigated by Dilution Studies*," **2009**, *15*, 11390-11400.

The fact that certain molecules undergo slow paramagnetic relaxation was first noted for the oxide cluster $[Mn_{12}O_{12}(O_2CCH_3)_{16}(OH_2)_4]$ (Mn_{12}-Ac).[41a-c] The slow relaxation of the magnetization of SMMs derives from the existence of an energy barrier (U) that separates the +S and –S ground states whose height is dependent on the magnitude of the axial ZFS parameter $-D_z$. A pressing goal in the field of SMMs is to raise the energy barrier in an effort to increase the blocking temperature, a requisite condition for future applications in data storage and processing. The energy barrier (U) is related to the ground spin state (S) and the negative zero-field splitting term (D) of the molecule by $S^2|D|$ and $(S^2-1/4)|D|$ for integer and half integer S values respectively. The observed effective barrier (U_{eff}), however, is lower than the theoretical energy barrier due to quantum tunneling of the magnetization. A perusal of the literature reveals three main approaches that researchers are pursuing vis-a-vis raising the blocking temperatures of SMMs: (a) the preparation of large clusters with many paramagnetic metal ions to achieve a large ground spin state spin value, (b) the use of highly magnetically anisotropic metal ions to increase the negative zero-field splitting term and, (c) the combination of the two previous approaches which, of course, in tandem will synergistically help to increase the barrier.[41g]

Many new SMMs have been reported since the discovery of Mn_{12}-Ac according to the aforementioned approaches. The majority of examples involve clusters of 3d metal ions, and, in some cases, very large clusters such as Mn_{25} with ground state spin values of S = 51/2 and S = 61/2 have been reported.[61,159-163] The family of SMMs has been extended to include heterospin systems, examples of which include clusters that combine

3d and 5d metal ions,[164,165] metal ions with photoinduced carbenes ligands,[166] 3d-4f mixed clusters,[167] and an organic radical-Tb^{III} ion double decker molecule.[168] Slow relaxation of the magnetization has been also observed for rare earth ion clusters,[169] and molecules with a single lanthanide ion spin center.[170] A few examples of single-chain magnets based on lanthanide(III) ions and organic radicals, as well as combinations of lanthanide(III) ions and cobalt(III) ions have also been reported.[171]

An issue with many of the reported SMM's is that the blocking temperature is below the temperature limit of the magnetometer (which is typically 1.8 K), therefore one typically observes only the beginning of an out-of-phase AC signal without defined maxima. One reason for this situation is fast tunneling effects in the ground state multiplet which hinders the blocking of the spin orientation. Quantum tunneling of the magnetization can be suppressed by the application of a moderate magnetic field, and the values of the relaxation of the magnetization can be used to estimate the corresponding relaxation parameters at zero applied field.[164b] In these cases, it is highly advisable to confirm SMM behaviour by the use of an apparatus such as a micro-SQUID set-up at mK temperatures.[172] The phonon bottleneck (PB) effect is a different relaxation phenomenon that can be detected by microSQUID studies at mK temperatures for small crystals. In the case of the PB effect, the spins are in resonance with only few phonon modes, consequently, the spins cannot relax completely since they are being continually excited by phonons. The result is that slow relaxation of the magnetization is observed.[173] Most importantly, the hysteresis loops at low temperatures caused by the PB effect are distinguishable from those arising from SMM behavior.

As mentioned earlier, the incorporation of lanthanide ions into SMMs is driven by the attempt to increase the blocking temperature by the introduction of anisotropy. This strategy has proven to be quite successful in the case of the single ion double deckers, $[(Pc)_2Ln^{III}]^-$ (Pc = phthalocyaninato; Ln = Tb, Dy, Ho) the Tb analogue of which exhibits the highest blocking temperature of all reported SMMs. In the case of single lanthanide ion SMMs the energy barrier originates from spin-orbit coupled ground states $\pm J_z$ whose origin is ligand field effects operating on the lanthanide ion.[170] Of relevance to the present study, it is noted that one of the phtalocyaninato ligands of the Tb double decker can be oxidized by removal of one electron resulting in an organic radical-lanthanide SMM, the first of its kind.[168] With these results in mind, we embarked on a study of the coordination chemistry of coordinated $TCNQF_4$ organic radicals and Tb^{III} ions in search of new heterospin 2p-4f SMMs.

Results and Discussion

Herein we present the syntheses and characterization, including detailed magnetic studies for a series of heterospin molecules composed of lanthanide organic radical mononuclear complexes $\{M[TCNQF_4]_2[H_2O]_6\}\cdot(TCNQF_4)(3H_2O)$, M = Tb (**Tb**), Y (**Y**), Y:Tb (74:26) ($\mathbf{Y_{0.74}Tb_{0.26}}$), and Y:Tb (97:3) ($\mathbf{Y_{0.97}Tb_{0.03}}$). Compounds **Tb**, $\mathbf{Y_{0.74}Tb_{0.26}}$, and $\mathbf{Y_{0.97}Tb_{0.03}}$ exhibit the beginning of an AC out-of-phase signal above 1.8 K, but their relaxation time remains fast down to 40 mK at zero applied field. The application of a moderate field suppresses the tunneling and magnetic hysteresis is observed for **Tb**. Of particular interest is the observation of the unprecedented co-existence of SMM and PB

behaviors by low temperature micro-SQUID measurements. Recently the PB effect has been induced via microwave irradiation of Fe_8 and Ni_4 SMMs, a topic that is related to the current report, but, in the case of our new compounds, there is no need to irradiate the sample in order to observe the PB effect.[174]

The combination of lanthanide ions with $[TCNQF_4]^{\bullet-}$ organic radicals results in the precipitation of crystalline solids of formula $\{M[TCNQF_4]_2[H_2O]_6\}\cdot(TCNQF_4)(3H_2O)$, M = Tb (**Tb**), Y (**Y**), Y:Tb (74:26) ($\mathbf{Y_{0.74}Tb_{0.26}}$), and Y:Tb (97:3) ($\mathbf{Y_{0.97}Tb_{0.03}}$) respectively. The preparation method is general and was used to obtain an entire series of isostructural M/$TCNQF_4$ complexes reported herein. The facile crystallization of pure samples in this series is attributed to the fact that the complexes are cationic moieties that readily co-crystallize with $[TCNQF_4]^{\bullet-}$ radical anions, the results of which are neutral salts. Compound **Tb** is a combination of Tb spins and organic radical spins. The questions that arise in this study are (1) is the Tb complex a SMM? (2) are the Tb spins coupled to the radical spins and is there direct coupling between Tb spins? and, finally, (3) what is the nature of the coupling between the organic radicals? In order to answer these questions, we synthesized the derivatives **Y**, $\mathbf{Y_{0.74}Tb_{0.26}}$, and $\mathbf{Y_{0.97}Tb_{0.03}}$.

Crystal Structures: Structural descriptions are provided in this section for compound **Tb** only since the other analogs are isostructural (Table 4.1). Compound **Tb** crystallizes in the monoclinic space group $P2_1/c$.

Table 4.1 Crystallographic data for YTb/$TCNQF_4$ coordination compounds.

Compound	**Tb**	**Y**	**$Y_{0.74}Tb_{0.26}$**	**$Y_{0.97}Tb_{0.03}$**
Formula	$C_{36}H_{18}N_{12}O_9F_{12}Tb_1$	$C_{36}H_{18}N_{12}O_9F_{12}Y_1$	$C_{36}H_{18}N_{12}O_9F_{12}Y_{0.74}Tb_{0.26}$	$C_{36}H_{18}N_{12}O_9F_{12}Y_{0.97}Tb_{0.03}$
F_w [g mol^{-1}]	1149.54	1079.49	1097.69	1081.59
Crystal size [mm^3]	0.40 x 0.30 x 0.20	0.63 x 0.16 x 0.16	0.34 x 0.24 x 0.16	0.33 x 0.30 x 0.22
Crystal system	Monoclinic	Monoclinic	Monoclinic	Monoclinic
Space group	$P2_1/c$	$P2_1/c$	$P2_1/c$	$P2_1/c$
a [Å]	13.683(1)	13.660(3)	13.68(6)	13.648(7)
b [Å]	17.608(2)	17.671(5)	17.65(8)	17.67(1)
c [Å]	17.133(2)	17.040(4)	17.13(7)	17.05(1)
β [°]	103.093(2)	103.103(7)	103.1(1)	103.13(2)
V [$Å^3$]	4020.5(7)	4006(2)	4029(31)	4004(4)
Z	4	4	4	4
ρ_{calc} [g cm^{-3}]	1.899	1.790	1.810	1.798
μ ($Mo_{K\alpha}$) [mm^{-1}]	1.887	1.585	1.657	1.605
Reflections collected	29979	11913	11850	25396
Unique reflections	9235	6805	8596	9596
Reflections with $I > 2\sigma(I)$	8553	5311	4851	7840
parameters	686	628	415	704
R(int)	0.0169	0.0830	0.0538	0.0373
$R1$[a]	0.0350	0.0504	0.0583	0.0410
$wR2$[b]	0.0862	0.1269	0.1259	0.1022
GOF	1.145	0.970	1.003	1.091

[a] $R1 = \Sigma||F_o| - |F_c||\Sigma|F_o|$. [b] $wR2 = [\Sigma[w(F_o^2 - F_c^2)^2]/\Sigma[w(F_o^2)^2]]^{1/2}$.

The structure of the cationic complex $[Tb(TCNQF_4)_2(H_2O)_6]^+$ (Figure 4.1) consists of two crystallographically independent σ-bonded $[TCNQF_4]^{-\bullet}$ radicals, and six water molecules in the coordination sphere of the Tb^{III} ion. The coordinated $TCNQF_4$ units are *cis* to each other at a 72.7(1)° angle. An uncoordinated $[TCNQF_4]^{-\bullet}$ radical balances the charge of the cationic complex. In addition, there are three interstitial water molecules per cation unit. The 8-coordinate terbium ion resides in a distorted square antiprismatic environment, in which N1, O1, O3, and O5 form the "A" face and N5, O2, O4, and O6 form the "B" face. The A-B separations range from 2.359 Å to 2.771 Å. A 1-D stack is formed via π-π interactions between one of the coordinated $TCNQF_4$ molecules and the free $[TCNQF_4]^{-\bullet}$ radicals. The inter-planar distances are 3.28 Å (U···U), 3.08 Å (U···C), 3.40 Å (C···C), and 3.12 Å (C···U); U = uncoordinated, C = coordinated (Figure 4.2). The shortest Tb···Tb intermolecular distance is 7.03 Å.

The $TCNQF_4$ molecules are in close proximity due to π-π interactions, a situation that is anticipated to lead to antiferromagnetic interactions as noted for other $[TCNQF_4]^{-\bullet}$ containing materials.[51] One of the coordinated $[TCNQF_4]^{-\bullet}$ radicals, however, is not involved in intermolecular interactions and, given its isolation, is paramagnetic at all temperatures. Therefore, at low temperatures one would expect to observe magnetic contributions in **Tb** from the Tb^{III} ion and the isolated $[TCNQF_4]^{-\bullet}$ radical.

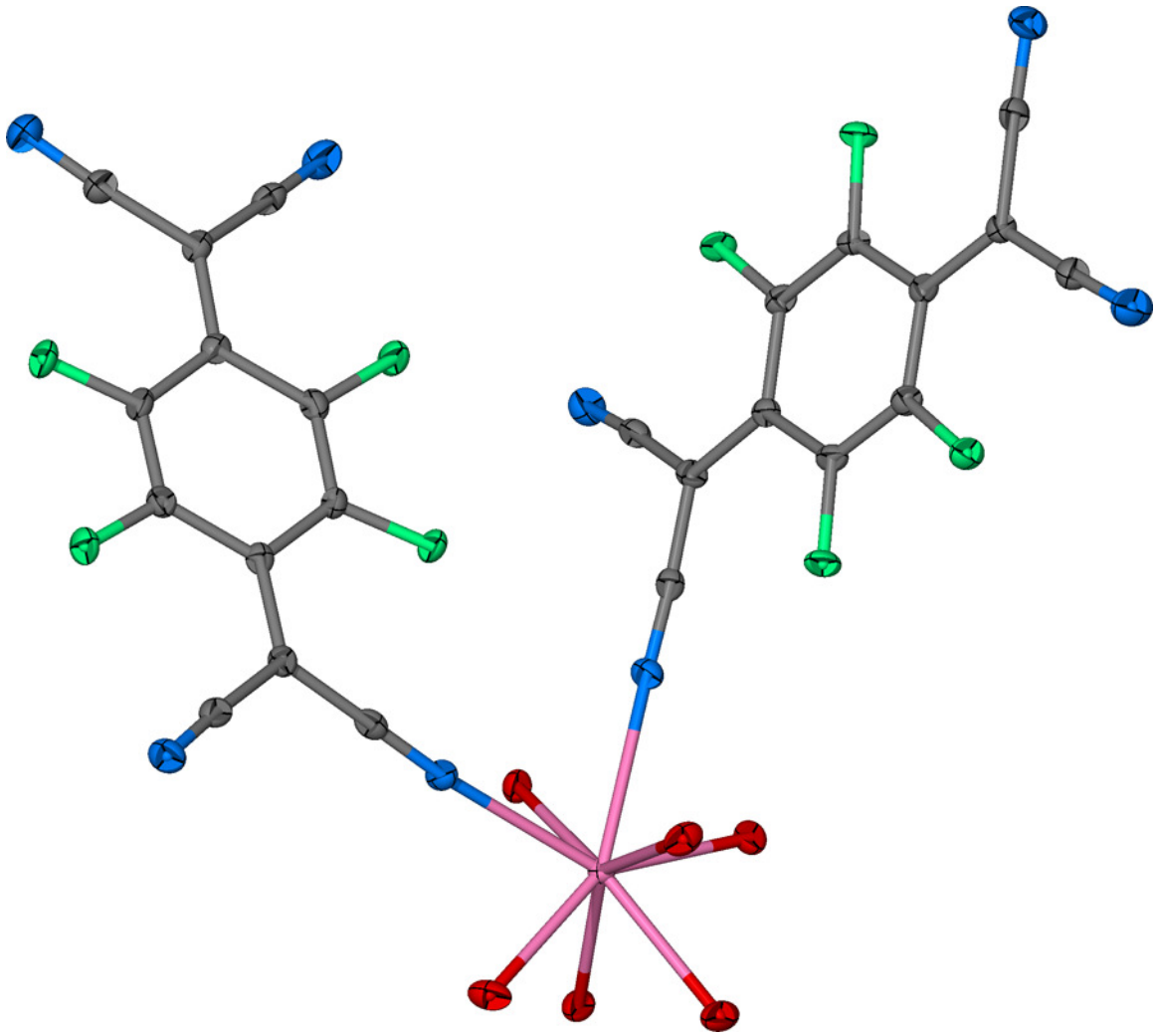

Figure 4.1 Molecular structure of the cationic complex in **Tb**. Interstitial water molecules and hydrogen atoms have been omitted for the sake of clarity. Tb = pink, O = red, N = blue, C = gray F = green.

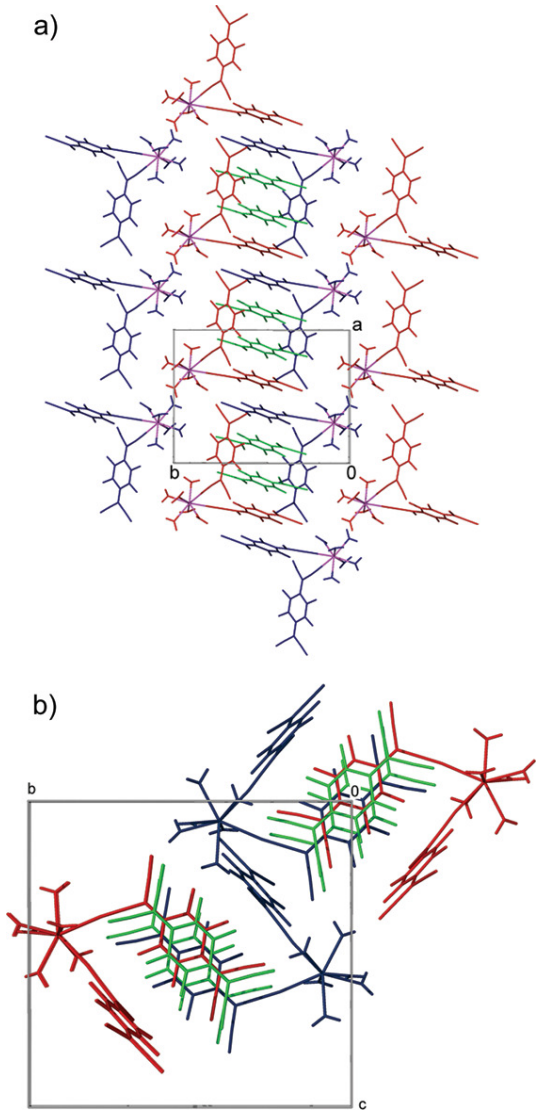

Figure 4.2 Packing diagram parallel to the ab plane depicting π-π stacking interactions in the crystal structure of **Tb** (a). Packing diagram of **Tb** along the a axis (b). The interstitial water molecules are omitted for the sake of clarity. Blue = the cationic complex $[Tb(TCNQF_4)_2(H_2O)_6]^+$, which has the unstacked $TCNQF_4$ moiety pointing down; red = the cationic complex $[Tb(TCNQF_4)_2(H_2O)_6]^+$, for which the unstacked $TCNQF_4$ unit is pointing up; green = uncoordinated $TCNQF_4$ molecules; pink = Tb ions.

IR Spectroscopy: The infrared spectrum of **Tb** exhibits four ν(CN) stretches at 2207, 2196, 2187, and 2180 cm^{-1}, which are shifted to lower energies as compared to neutral $TCNQF_4$ (2227 cm^{-1}), in accord with the presence of the $[TCNQF_4]^{-\bullet}$ radical anion. To support this conclusion, the charge of the $TCNQF_4$ moiety was estimated from the Kistenmacher relationship, $\rho = A[c/(b + d)] + B$ (A = -46.729 and B = 22.308; A and B are determined from neutral $TCNQF_4$ (ρ=0)[152] and the $(n\text{-}Bu_4N)TCNQF_4$ radical anion (ρ = -1).[51] The values of c, b, and d are the $TCNQF_4$ bond distances as defined in Figure 4.3. The bond lengths for $TCNQF_4$ are excellent indicators of the oxidation state of the ligand. The CN bond lengths of $TCNQF_4$ are affected mainly by M-N coordination but the C-C bond lengths are a good reporter parameter of the oxidation state of the ligand. The reference bond distances for $TCNQF_4^0$, $TCNQF_4^-$ and $TCNQF_4^{-2}$ were determined by averaging the crystallographic data for a number of compounds. The corresponding C-C distances in the $TCNQF_4$ units of **Tb** are very similar, thus the estimated charges for the coordinated groups (-1.01 and -1.02), and free groups (-0.92) are nearly the same. These values, taken together with the IR data, support the assignment of singly reduced $[TCNQF_4]^{-\bullet}$ radical anions for all of the units.

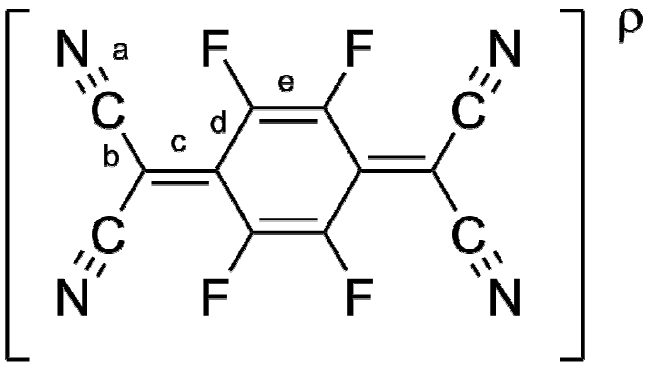

Figure 4.3 Structure of $TCNQF_4$. The bond lengths used in the Kistenmacher relationship are labeled with the corresponding lower case letters. ρ = estimated charge of $TCNQF_4$.

DC Magnetic Susceptibility Measurements: Magnetic susceptibility measurements were performed at 1000 Oe from 1.8 to 300 K with the use of a SQUID magnetometer. The value of χT of **Tb** at 300 K is 12.44 emu·mol^{-1}·K which is close to that expected for one non-interacting Tb^{III} ion ($4f^8$, J = 6, g_J = 3/2, χT = 11.81 emu·mol^{-1}·K) and one and a half $[TCNQF_4]^{-\bullet}$ radicals (S = 1/2, g = 2.0, χT = 0.37 emu·mol^{-1}·K). These data indicate that there are antiferromagnetic interactions between organic radicals even at room temperature. As the temperature is lowered from 300 to 40 K, the χT value decreases smoothly to 11.66 emu·mol^{-1}·K, and from 40 to 2 K the χT value rapidly decreases to 8.23 emu·mol^{-1}·K (Figure 4.4). The magnetic susceptibility of **Tb** cannot be fit to a simple model due to the anisotropy of the Tb^{III} ion. The low symmetry crystal field imposed by the ligands on Ln^{3+} ions (Ln = Tb, Dy, Ho, Er) results in magnetic anisotropy and splitting of the ground state multiplet that, if sufficiently large, can produce an activation barrier, and hence SMM behavior as in the case of single lanthanide ion- bis-phthalocyaninato ligand and single lanthanide ion-bis-polyoxometalate ligand.[170]

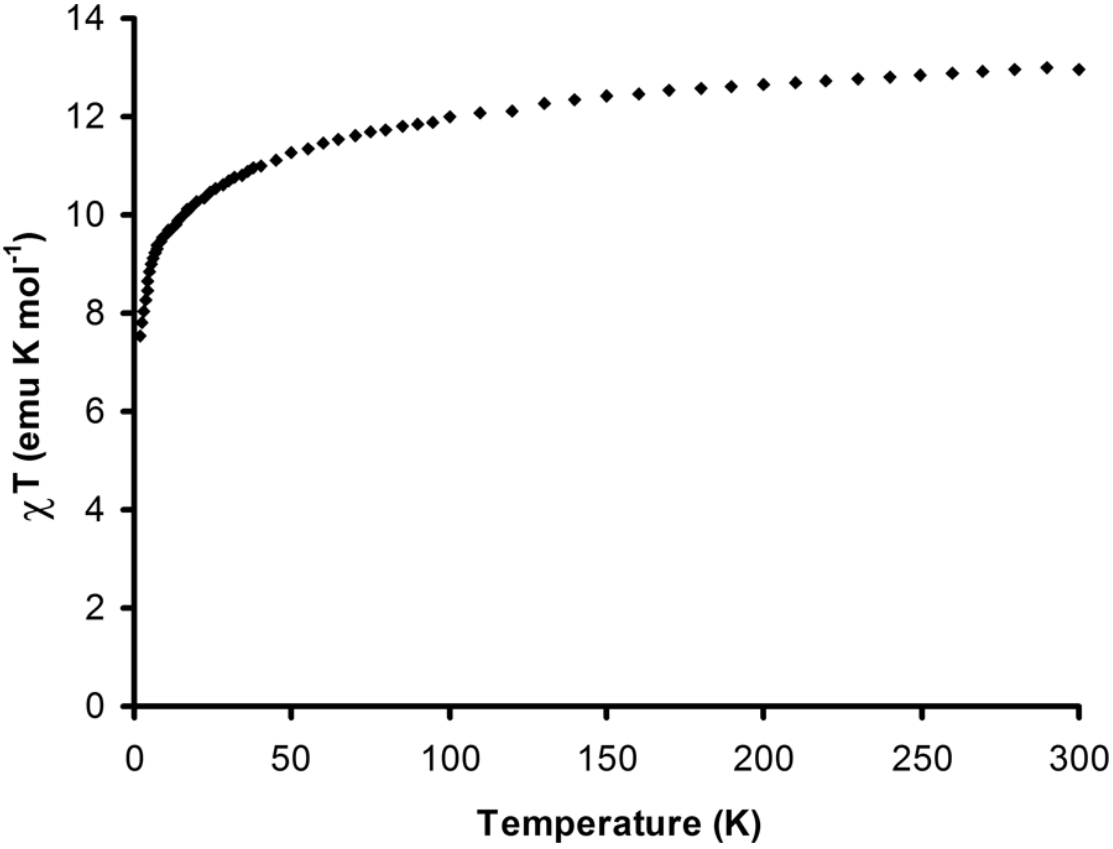

Figure 4.4 Temperature dependence of the χT product for **Tb**.

In **Tb**, the Tb ions are anisotropic due to the low symmetry crystal field imposed by the coordinated molecules. The Tb ions reside at the point symmetry 4e Wyckoff position of the monoclinic space group No. 14 ($P2_1/c$).[175] A model of the magnetic behavior for these compounds that contain anisotropic terbium ions is complicated because a full treatment must take into account all of the following: spin orbit coupling effects, crystal field effects, Tb-organic radical interactions, and organic radical-organic radical interactions. A further complication in the present series of compounds is that the Tb ion is in a significantly distorted square antiprism environment and cannot be considered pseudo D_{4d} for the modeling, thus additional terms would have to be included in the fitting which would lead to unreliable values due to the inclusion of too many parameters. Unfortunately, we cannot model the magnetic behavior of **Tb** using the angle-resolved magnetometry method for anisotropic low symmetry lanthanides reported by Gatteschi *et al.,* because the compound crystallizes in a monoclinic space group with the lanthanide ion residing on a general position.[176] The method is only applicable to molecules that reside on the same point symmetry as the space group. Due to these unavoidable issues, a phenomenological description of the magnetic susceptibility data for **Tb** is presented.

The observed decrease of χT at temperatures lower than 40 K has four possible contributions: the depopulation of excited Stark sub-levels of the Tb^{III} ion with a $^7F_6$ ground state, an antiferromagnetic interaction between the Tb^{III} ion and the coordinated $[TCNQF_4]^{-\bullet}$ radical, antiferromagnetic interactions between π-stacked $[TCNQF_4]^{-\bullet}$ units, and antiferromagnetic interactions between neighboring Tb^{III} ions. The χT value of

Y (0.54 emu·mol^{-1}·K) at 300 K corresponds to approximately 1.5 S = 1/2 spins, which is much lower than the expected value for three uncorrelated organic radicals (1.12 emu·mol^{-1}·K). The low χT value of **Y** is a consequence of strong antiferromagnetic interactions, which, in this case, can be definitively assigned to the interactions between π-stacked $TCNQF_4$ radicals because the Y^{III} ion is diamagnetic. DC susceptibility measurements indicate that the same antiferromagnetic interactions of π-stacked radicals are present in compounds **Tb** and **Y** and they are of the same magnitude. The close proximity of π-stacked $TCNQF_4$ radicals leads to π-dimers of coordinated···uncoordinated units, which considerably lowers the magnetic susceptibility response of this complex. The magnetic susceptibility of **Y** was fitted to a Heisenberg chain model with the Hamiltonian shown in equation 4.1.

$$H = -2J\sum S_i S_{i-1} \tag{4.1}$$

The actual χT values were then fitted with the Bonner and Fisher's numerical approximation shown in equation 4.2.

$$\chi T = \frac{Ng^2\beta^2}{k}\cdot\frac{0.25+0.074975x+0.075235x^2}{1.0+0.09931x+0.172135x^2+0.757825x^3}+\frac{Ng^2\mu_B^2 S(S+1)}{3k} \tag{4.2}$$

with

$$x = |J|/kT \tag{4.3}$$

where the first part of the model refers to the S = ½ Heisenberg chain formed by the π stacked $TCNQF_4$ units and the second part refers to the contribution of magnetically isolated non-π-interacting $TCNQF_4$ units.[177] The fitting results in the following

parameters: J = -230 cm^{-1}, g = 2.00. The strong antiferromagnetic interactions of the π-stacked organic radicals is responsible for the linear shape of the curve in Figure 4.5. At low temperature, χT reaches a value that corresponds to one unpaired electron despite the strong antiferromagnetic interactions, as expected for the presence of one radical that is not involved in π-π stacking interactions. It is important to point out that the model represents the magnetic behavior of **Y** over the range of temperatures measured and that some deviations are possible at lower temperatures than the limit of the cryogenics of the SQUID apparatus (1.8 K).

Magnetization Measurements: The field dependent magnetization of **Tb** at 1.8 K, in the range of 0-7 T, does not saturate and approaches a value of 6 μ_B, which is lower than the expected value of 10 μ_B, (9 μ_B from one Tb^{III} ion with g_J = 3/2 and J = 6 and 1 μ_B from one $[TCNQF_4]^{-\bullet}$ radical with g = 2.00 and S= ½) (Figure 4.6), assuming spin-cancellation of π-π interacting $TCNQF_4$ radicals.[178] These observations are attributed to crystal field effects of the Tb^{III} ion, along with antiferromagnetic interactions between the remaining spin active $[TCNQF_4]^{-\bullet}$ radical and the Tb^{III} ion. The same sequence of data acquisition employed for **Tb** was used to measure the magnetization of compound **Y**. These results indicate that, in compound **Y**, there is also one unpaired electron associated with the coordinated $[TCNQF_4]^{-\bullet}$ anion that remains as a radical without nearest neighbor interactions (Figure 4.7).

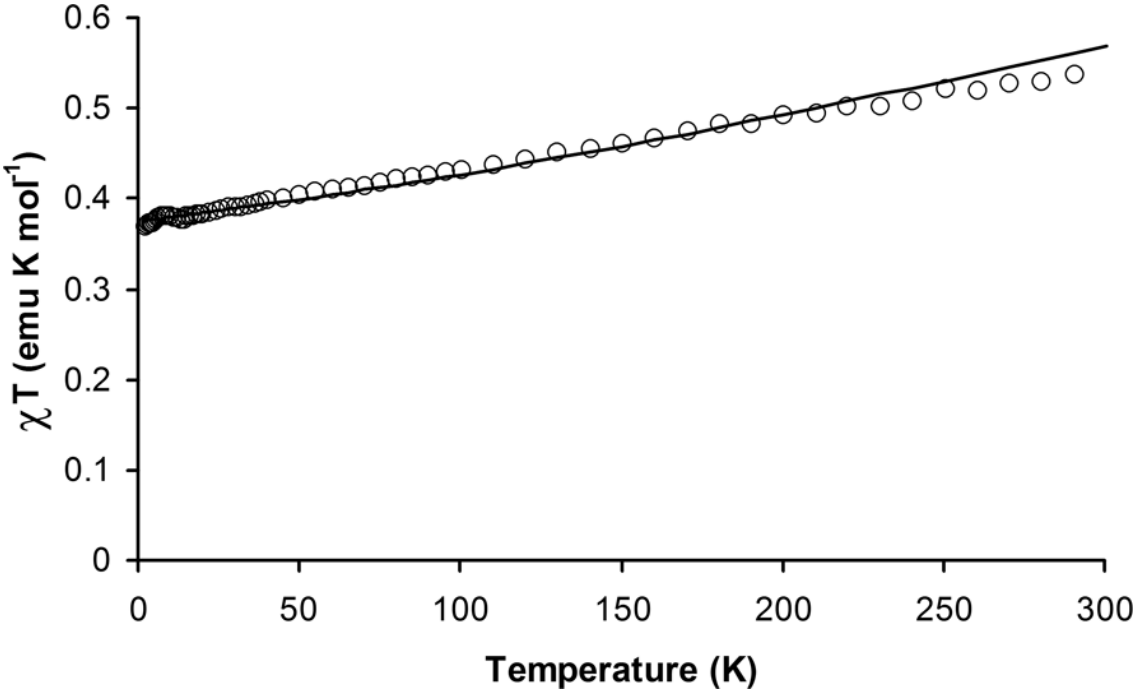

Figure 4.5 Temperature dependence of the χT product for **Y**. The solid line is the best fit to a Heisenberg chain model with the Hamiltonian $H = -2J\Sigma S_i S_{i-1}$, and parameters: J = -230 cm^{-1}, g = 2.00.

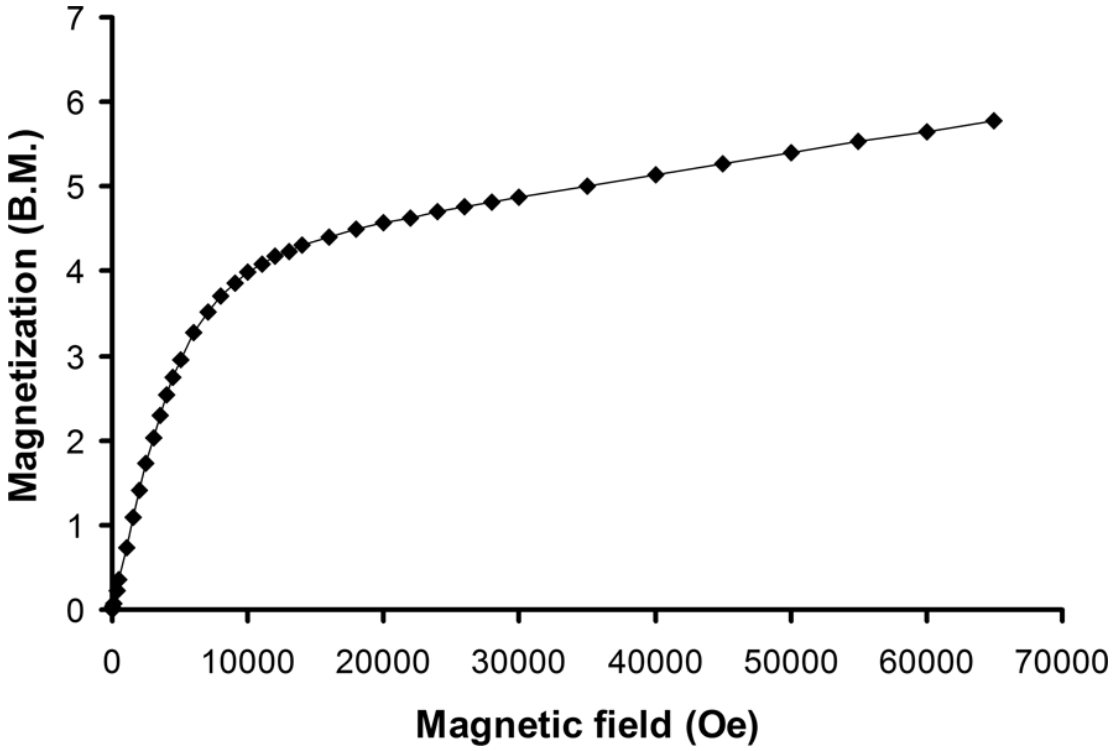

Figure 4.6 Field dependent magnetization curve of **Tb** measured at 1.8 K. The solid line is a guide for the eyes.

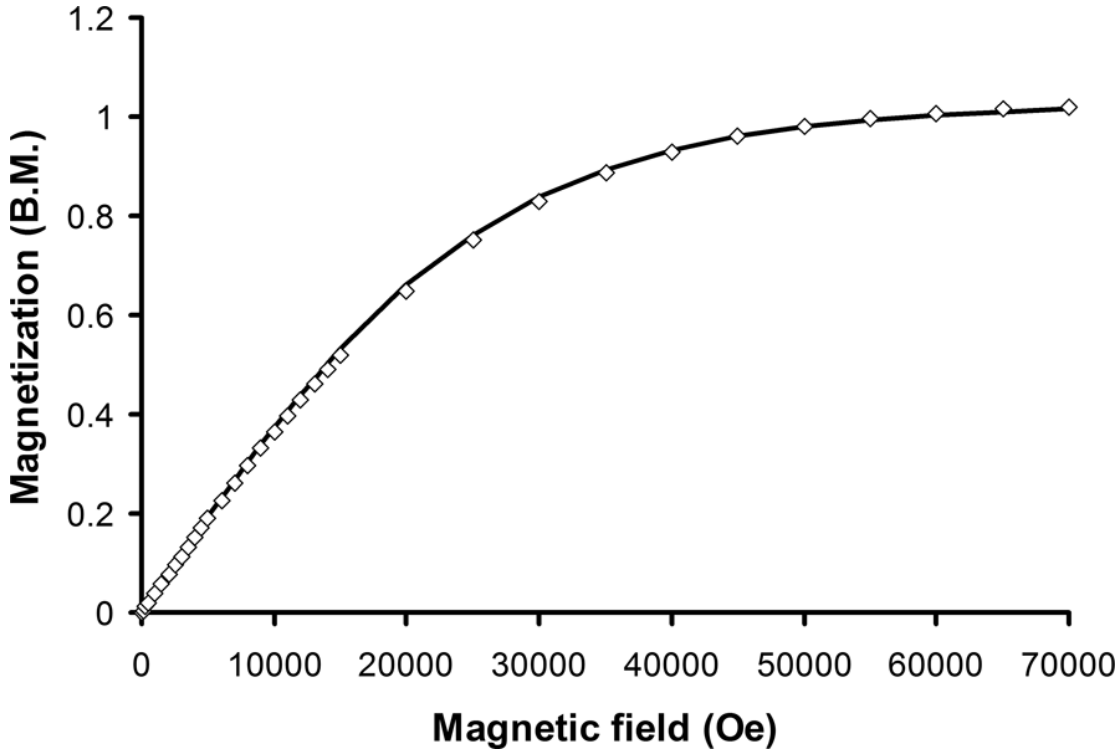

Figure 4.7 Field dependent magnetization curve of **Y** measured at 1.8 K. The solid line is the Brillouin function fit with parameters S = ½ and g = 2.05.

AC Magnetic Susceptibility Measurements: A pure Phonon bottleneck phenomenon can be identified by AC susceptibility studies without resorting to low temperature microSQUID measurements because at zero applied field there will be no out of phase signal and only a very small signal will be observed under moderate applied magnetic fields. In contrast, SMMs that have fast relaxation at zero applied field cannot be identified solely by AC susceptibility studies because fast quantum tunneling leads to low blocking temperatures and often exhibit only the beginning of an out-of-phase signal. In such situations it is impossible to exclude the coexistence of SMM and PB effects and, in these cases, low temperature microSQUID measurements can help to elucidate the behavior based on the shape of the magnetization loops.

The zero-field AC susceptibility measurements for **Tb**, performed in a range of frequencies from 10 to 1500 Hz at H_{AC} = 3 Oe, indicate the onset of a frequency-dependent out-of-phase signal. A maximum was not detected due to the temperature limitations of the low temperature apparatus (Figure 4.8a). Similar magnetic behavior was observed for both diluted samples (**$Y_{0.74}Tb_{0.26}$**, and **$Y_{0.97}Tb_{0.03}$**), with a decrease in the intensity of the signal due to the presence of fewer paramagnetic Tb^{III} ions. No out-of-phase signal was observed for **Y**, an indication that the frequency-dependent out of phase signal observed for **Tb**, **$Y_{0.74}Tb_{0.26}$**, and **$Y_{0.97}Tb_{0.03}$** is due to the relaxation of Tb^{III} ions (Figure 4.8).

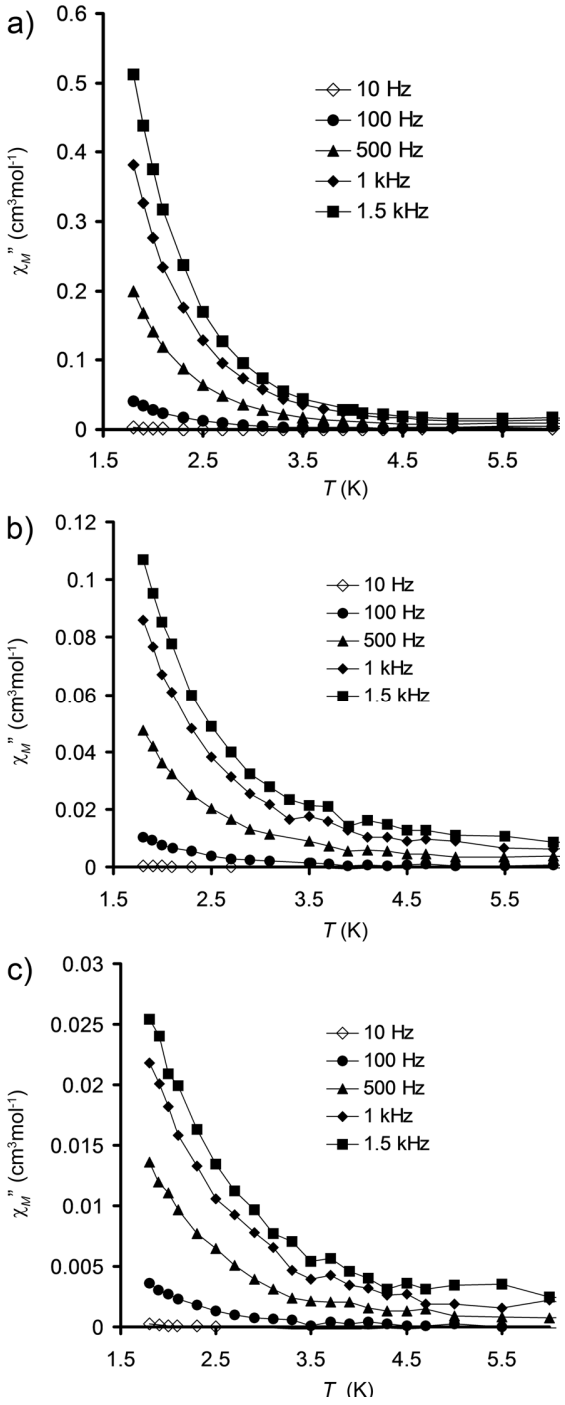

Figure 4.8 Temperature dependence of the imaginary component χ'' of the AC magnetic susceptibility of **Tb** (a), $\mathbf{Y_{0.74}Tb_{0.26}}$ (b), and $\mathbf{Y_{0.97}Tb_{0.03}}$ (c); measured under zero applied field in an oscillating field of 3 Oe at different frequencies.

At this stage, it should be pointed out that long range magnetic ordering can be excluded because the AC signal is observed even after dilutions that involve the replacement of Tb ions with diamagnetic Y ions, which would lead to the blocking of magnetic dipole pathways that are required for ordering. In addition, the existence of an AC signal in the diluted compounds at the same temperature as **Tb** with intensities proportional to the concentration of Tb ions indicates that the AC signal originates from single Tb ions and not larger aggregates.

In the context of this discussion it is worth noting that, unlike the observations for the present system, dilution studies on Ishikawa and co-workers organic radical bis(phthalocyaninato)-terbium complex lead to a shift of the maximum of the AC signal to lower temperature for the highest frequency with no obvious peak being observed for the lower frequencies.[168] Thus, the blocking temperature in the Ishikawa system decreases considerably upon dilution, an indication that the SMM behavior is likely due to dimers of double deckers or larger aggregates.

To further investigate the possibility of SMM behavior in the present series and to understand the influence of the $TCNQF_4$ organic radicals, AC susceptibility measurements were performed under several applied magnetic fields ranging from 500 to 2000 Oe. The fast quantum tunneling of SMMs can be suppressed by applying a small magnetic field and, as exemplified by the $[Ni\{ReCl_4(oxalate)\}_3]^{4-}$ SMM, for which the out-of- phase signal shifts to higher temperatures with increasing applied field.[164b] In our studies, an increase in the applied magnetic field led to a shift in the out-of phase signal of **Tb** to higher temperatures, and, in the case of 1000 and 2000 Oe, the maximum of

one and two frequencies were observed, respectively (Figure 4.9a and 4.9c). Data were collected in the same manner for $\mathbf{Y_{0.74}Tb_{0.26}}$, and, as found for **Tb**, there is a shift in the out-of phase signal to higher temperatures as well as a diminished intensity for the signal due to the lower concentration of Tb ions in comparison to **Tb**. In the case of the 1000 and 2000 Oe applied fields, the maximum of one and two frequencies were observed, respectively as noted for **Tb** (Figure 4.10). The observed shifts in the out of phase signal to higher temperatures correlate well with the slow relaxation observed in **Tb**, which indicates that the SMM behavior is retained in the diluted sample. In contrast, there is no out-of-phase AC signal for compound **Y** at zero applied field and it exhibits a very weak signal with no defined maxima under applied fields of 1000 Oe and 2000 Oe (Figure 4.11); the signal is of comparable intensity to $\mathbf{Y_{0.97}Tb_{0.03}}$ (Figure 4.12) but is noisier. These data lead us to conclude that there is only a PB effect being exhibited by compound **Y**. The data indicate that the origin of the AC-signal is the slow relaxation of individual Tb(III) ions for **Tb**, $\mathbf{Y_{0.74}Tb_{0.26}}$, and $\mathbf{Y_{0.97}Tb_{0.03}}$ and underscore the fact that one can identify a pure PB behavior based on AC susceptibility studies.

A Cole- Cole plot of the in-phase (χ') vs. the out-of-phase (χ'') signal of the magnetic susceptibility of **Tb** exhibits a semicircular shape (Figure 4.9e and 4.9g), which is indicative of a single relaxation process for the magnetization. The linear correlation in the Arrhenius plot also indicates the existence of a single relaxation process (Figure 4.9f and 4.9h).

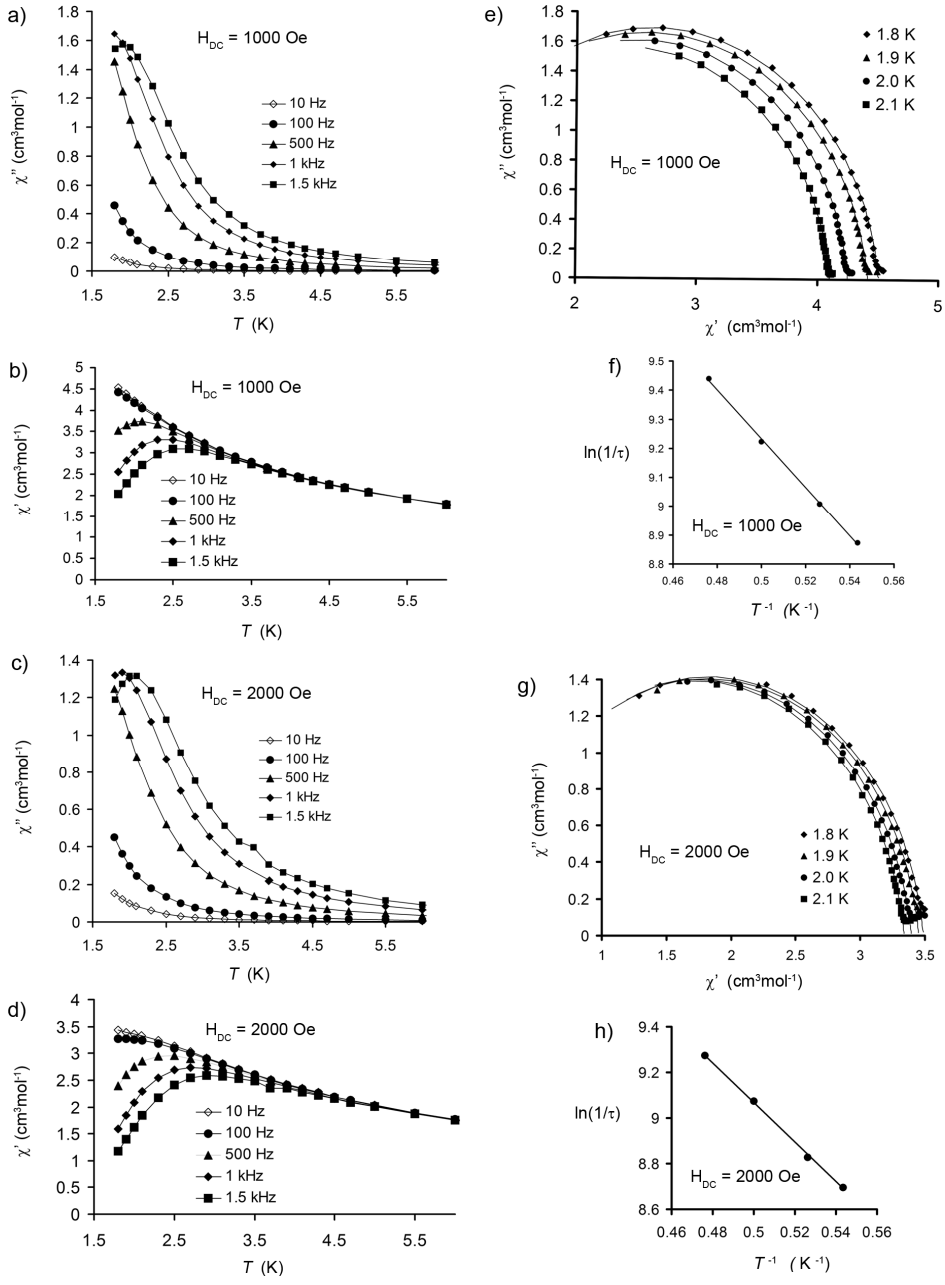

Figure 4.9 Temperature dependence of the real χ' and imaginary χ'' component of the AC magnetic susceptibility for **Tb** measured in an oscillating field of 3 Oe at different frequencies and H_D = 1000 Oe (a and b); H_D = 2000 Oe (c and d). Cole-Cole plot at H_D = 1000 Oe (e); and at H_D = 2000 Oe (g). The solid line is the fitting to the Cole-Cole function shown in equation 4.4. Arrhenius plot at H_D = 1000 Oe (f); and at H_D = 2000 Oe (h).

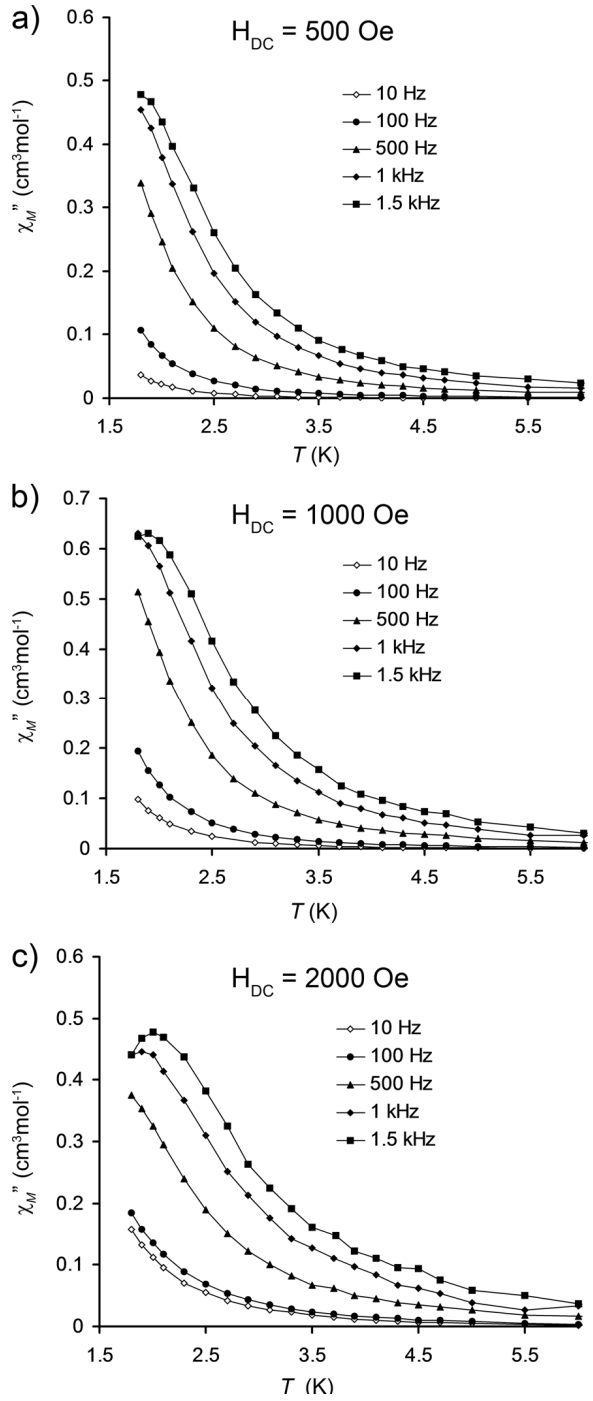

Figure 4.10 Temperature dependence of the imaginary χ'' component of the AC magnetic susceptibility of $\mathbf{Y_{0.74}Tb_{0.26}}$ measured in an oscillating field of 5 Oe at different frequencies under 500 Oe (a), 1000 Oe (b), and 2000 Oe (c) applied magnetic field.

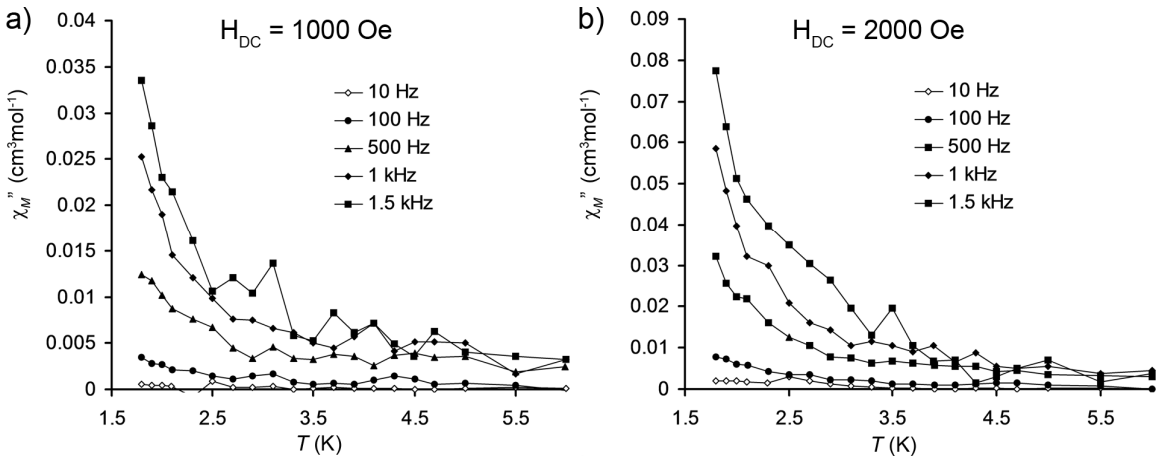

Figure 4.11 Temperature dependence of the imaginary χ'' component of the AC magnetic susceptibility of **Y** measured in an oscillating field of 5 Oe at different frequencies under 1000 Oe (a), and 2000 Oe (b) applied magnetic field.

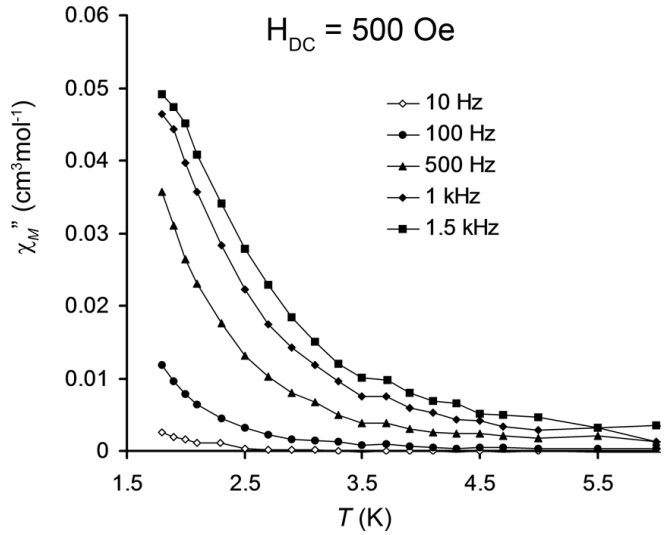

Figure 4.12 Temperature dependence of the imaginary χ'' component of the AC magnetic susceptibility of $\mathbf{Y_{0.97}Tb_{0.03}}$ measured in an oscillating field of 5 Oe at different frequencies under 500 Oe applied magnetic field.

The susceptibility can be phenomenologically expressed by the Cole-Cole correlation shown in equation 4.4.

$$\chi(\omega) = \chi_\infty + \frac{\chi_0 - \chi_\infty}{1 + (i\omega\tau)^{1-\alpha}} \tag{4.4}$$

where $\omega = 2\pi\nu$ is the frequency, χ_0 is the isothermal susceptibility at the limit when $\omega \to 0$ (DC), χ_∞ is the adiabatic susceptibility at the limit when $\omega \to \infty$, τ is the average relaxation time around which a distribution of relaxation times (symmetric on logarithmic scale) is assumed. The α value ($0<\alpha<1$) is representative of the width of the distribution ($\alpha = 1$ for a distribution of infinite width, while $\alpha = 0$ for the Debye form of single relaxation time). This equation can be decomposed into χ' and χ'' to obtain the relations in Eqs. (4.5) and (4.6):

$$x'(\omega) = x_\infty + \frac{(x_0 - x_\infty)\cdot\left[1 + (\omega\tau)^{1-\alpha}\sin(\alpha\pi/2)\right]}{1 + (\omega\tau)^{2(1-\alpha)} + 2\cdot(\omega\tau)^{1-\alpha}\sin(\alpha\pi/2)} \tag{4.5}$$

$$x''(\omega) = \frac{(x_0 - x_\infty)\cdot(\omega\tau)^{1-\alpha}\cos(\alpha\pi/2)}{1 + (\omega\tau)^{2(1-\alpha)} + 2\cdot(\omega\tau)^{1-\alpha}\sin(\alpha\pi/2)} \tag{4.6}$$

Note that $\chi''(\omega)$ will have a maximum at $\omega\tau = 1$, and the relaxation time is determined by the maximum of the imaginary part of the susceptibility versus frequency.

Fits of the curves yield alpha values in the range from 0.04 to 0.1, which corresponds to a narrow distribution of the relaxation times necessary for SMM behavior (see Tables 4.2 to 4.5).[179]

Table 4.2 Parameters of the Cole-Cole correlation (equation 4.4) obtained under 500 Oe applied field.

H_{DC} = 500 Oe	χ'				χ''		
T / K	χ_∞	χ_o	τ	α	χ_o - χ_∞	τ	α
1.8	1.407	3.725	0.0025	0.305	2.491	0.00062	0.04492
1.9	1.452	3.614	0.00188	0.2892	2.4397	0.00055	0.04464
2	1.5	3.4728	0.00151	0.242	2.33512	0.00044	0.04122
2.1	1.55	3.353	0.00112	0.2236	2.23037	0.00037	0.03803

Table 4.3 Parameters of the Cole-Cole correlation (equation 4.4) obtained under 1000 Oe applied field.

H_{DC} = 1000 Oe	χ'				χ''		
T / K	χ_∞	χ_o	τ	α	χ_o - χ_∞	τ	α
1.8	0.86986	4.50663	0.00091	0.06506	3.7794	0.00088	0.06815
1.9	0.747	4.41864	0.00077	0.07348	3.7025	0.00077	0.06702
2	0.78332	4.25195	0.00062	0.06399	3.55658	0.00062	0.06128
2.1	0.77495	4.10169	0.00051	0.05831	3.422	0.0005	0.05631

Table 4.4 Parameters of the Cole-Cole correlation (equation 4.4) obtained under 1500 Oe applied field.

H_{DC} = 1500 Oe	χ'				χ''		
T / K	χ_∞	χ_o	τ	α	χ_o - χ_∞	τ	α
1.8	0.47343	4.01278	0.0011	0.06854	3.7268	0.00104	0.08853
1.9	0.4681	3.9491	0.00095	0.06901	3.6612	0.00091	0.08557
2	0.46905	3.84145	0.00077	0.06513	3.56154	0.00073	0.0808
2.1	0.47274	3.74239	0.00062	0.06281	3.4878	0.00059	0.07734

Table 4.5 Parameters of the Cole-Cole correlation (equation 4.4) obtained under 2000 Oe applied field.

H_{DC} = 2000 Oe	χ'				χ''		
T / K	χ_∞	χ_o	τ	α	χ_o - χ_∞	τ	α
1.8	0.22422	3.48866	0.00107	0.09024	3.34554	0.00105	0.106
1.9	0.17675	3.45356	0.00092	0.09285	3.31246	0.00092	0.10388
2	0.09864	3.39472	0.00072	0.09151	3.29894	0.00072	0.10338
2.1	0.18697	3.33904	0.00061	0.08375	3.2498	0.00059	0.09636

In Glauber's theory,[180] thermal variation of τ is described by the Arrhenius expression (Eq. (4.7)):

$$\tau(T) = \tau_0 \cdot \exp\left(\frac{U_{eff}}{k_B T}\right) \tag{4.7}$$

where τ_0 is a pre-exponential factor and U_{eff} is the effective energy barrier for reversing the magnetization direction. The parameters of the Arrhenius equation for **Tb** obtained under several applied fields. were found to have a linear dependence on the applied field and were used to extrapolate the values corresponding to zero applied field, namely a pre-exponential factor (τ_0) of 1.4×10^{-6}s and an effective energy barrier (U_{eff}) of 5.2 cm^{-1}, both of which are in the range of reported SMMs (Figure 4.13 and Table 4.6).[164c,167i,181] Linear field dependence of the Arrhenius parameters was observed for $[Ni\{ReCl_4(oxalate)\}_3]^{4-}$ under small applied fields.[164b]

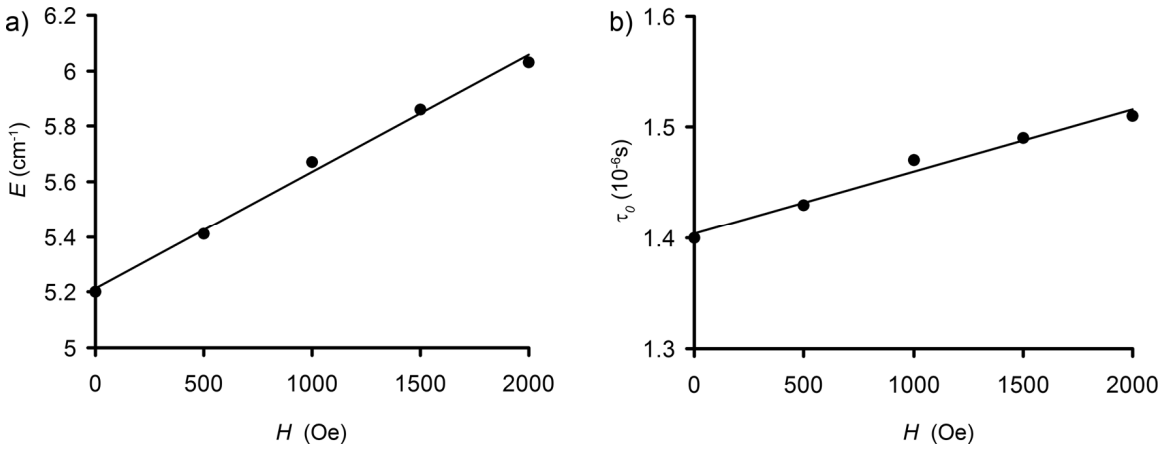

Figure 4.13 Field dependence of the energy barrier of **Tb** (a). Field dependence of the pre-exponential factor of the Arrhenius equation for **Tb** (b).

Table 4.6 Values of the energy barrier and pre-exponential factor of the Arrhenius equation for **Tb**.

Applied Field / Oe	**U_{eff} / cm^{-1} [a]**	**τ_0 / 10^{-6} s [b]**
2000	6.03	1.51
1500	5.86	1.49
1000	5.67	1.47
500	5.41	1.44
0 (extrapolation)	5.20	1.40

[a] U_{eff} = Effective energy barrier. [b] τ_0 = pre-exponential factor.

Low Temperature Magnetization Measurements: To further explore the magnetic behavior at very low temperatures a micro-SQUID apparatus was used to find the easy-axis of magnetization by the reported transverse field method.[182] It was found with this technique that all the easy axes of the Tb ions are approximately aligned. From the packing diagram of Figure 4.2 one can see that all the Tb ions are arranged in columns that run parallel to the columns of the $TCNQF_4$ molecules. There are four different orientations of Tb ions (Figure 4.2a), with two having the coordinated $TCNQF_4$ radical pointing up (red complexes) and two with it pointing down (blue complexes). They can all be approximated to having one easy axis that corresponds to the *a* axis, which is parallel to the columns of the stacked $TCNQF_4$ units. Hysteresis loops were collected on easy-axis oriented single-crystals (Figure 4.14). In general, due to its molecular origin, the slow relaxation of SMMs is characterized by an *increase* of coercivity for increasing field sweep rates; which is in strikingly contrast to the phonon bottleneck (PB) effect which leads to a *decrease* in coercivity with increasing field sweep rates.[183] This is easily explained by the fact that, for phonon bottlenecks, very fast field scans overcome the rate of exchange of phonons with the cryostat and the hysteresis loop collapses. Compound **Tb** exhibits a butterfly-shaped hysteresis loop, and a monotonical increase of the coercivity is observed when the rate of applied field increases, an indication of SMM behavior arising from ligand field effects of the Tb ion. In fact, the monotonical increase of the butterfly-shape hysteresis is observed for 3d, 3d-5d, and 3d-4f SMMs with no coercivity observed at H = 0. Such SMMs, including compound **Tb**, exhibit fast relaxation at zero applied field due to fast quantum tunneling. [164b,167b,181b,184] Magnetic

ordering was not observed at temperatures higher than 40mK as illustrated by the results of the microsquid measurements performed at several temperatures from 40 mK to 1 K and from 40 mK to 6 K (Figure 4.15).

The exchange fields (H_{ef}) were estimated from the inflection point of the M vs H curves and are indicated with a dotted line in figure 4.14. Moreover, the maximum of the dH/dM vs H plots indicate the inflection point clearly (Figures 4.16 to 4.18). The exchange interaction (J_e) is proportional to the exchange field (H_{ef}) as shown in equation 4.8.[185]

$$J_e = g\beta H_{ef} / (2zS) \tag{4.8}$$

In the case of lanthanide ions, the spin value (S) is no longer a good quantum number, instead one must use the total angular momentum (J) with g being replaced by g_J. Compound **Y** offers valuable information about the interactions between radicals. The radical spins are decoupled at higher temperatures and, of course, no SMM behavior is expected for S = ½ radicals, but below T = 0.3 K, antiferromagnetic coupling was observed, with an exchange field of about 950 G, which was estimated from the inflection point of the M vs H curve (Figure 4.14c). The exchange interaction in **Y** is attributed to antiferromagnetic superexchange between unstacked $TCNQF_4$ radicals through the columns of π-stacked $TCNQF_4$ units.

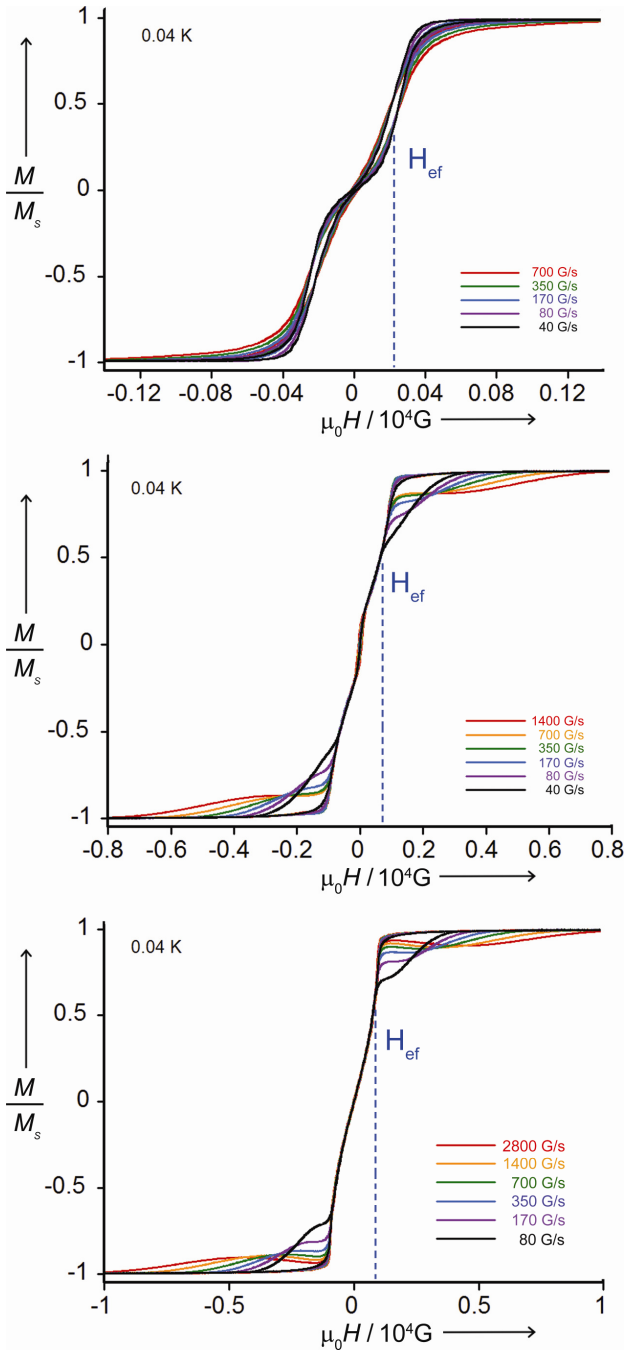

Figure 4.14 Field-dependent micro-SQUID magnetization scans collected for **Tb** (a), $\mathbf{Y_{0.97}Tb_{0.03}}$ (b) and **Y** (c) at 0.04 K showing double-s shape hysteresis for **Tb** and phonon bottleneck effect for **Y** and $\mathbf{Y_{0.97}Tb_{0.03}}$. Magnetization values are normalized to the magnetization value at 10000 G. H_{ef} (exchange field) indicates the position of the inflection point which corresponds to the exchange field.

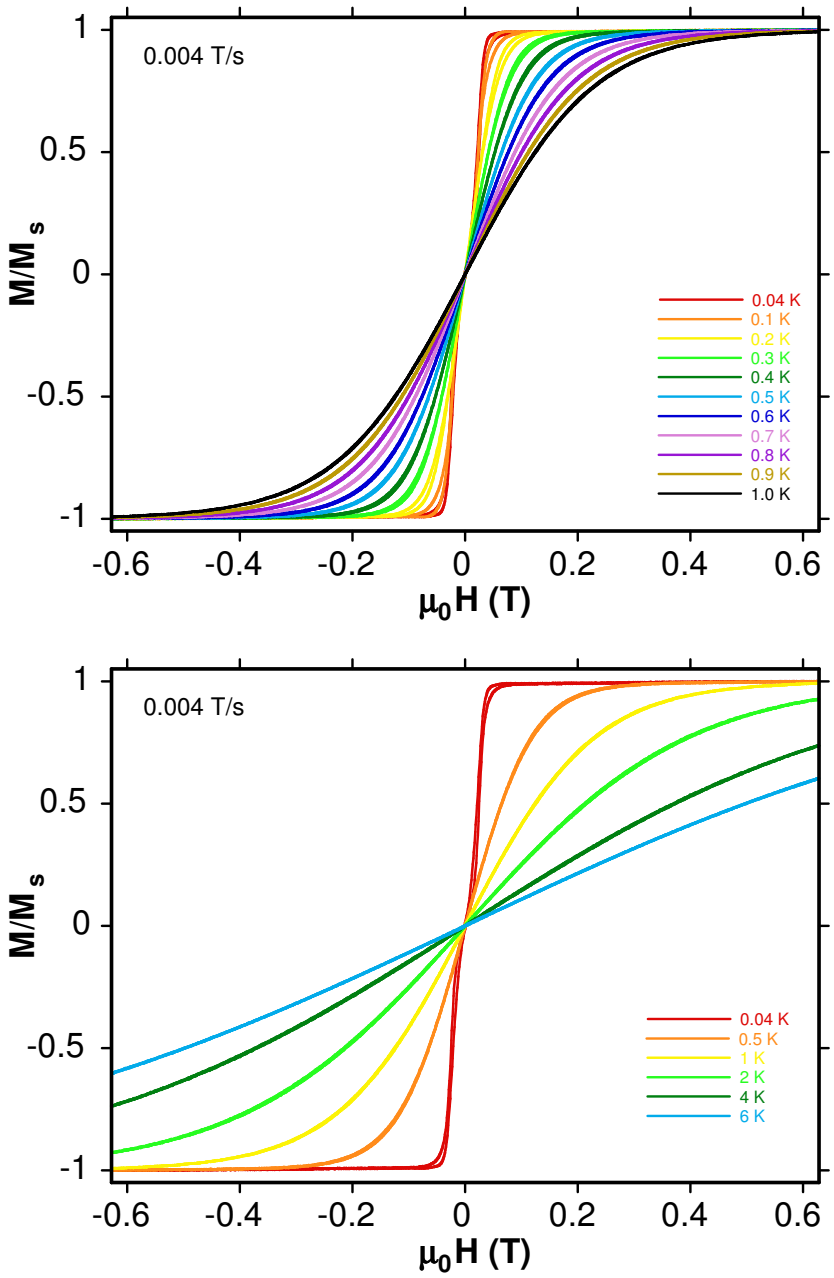

Figure 4.15 Micro-SQUID magnetization scans collected for **Tb** at temperatures from 0.04 K to 1.0 K (top), and from 0.04 K to 6.0 K (bottom) at 0.004 T/s. Magnetization values are normalized to the magnetization value at 1.0 T.

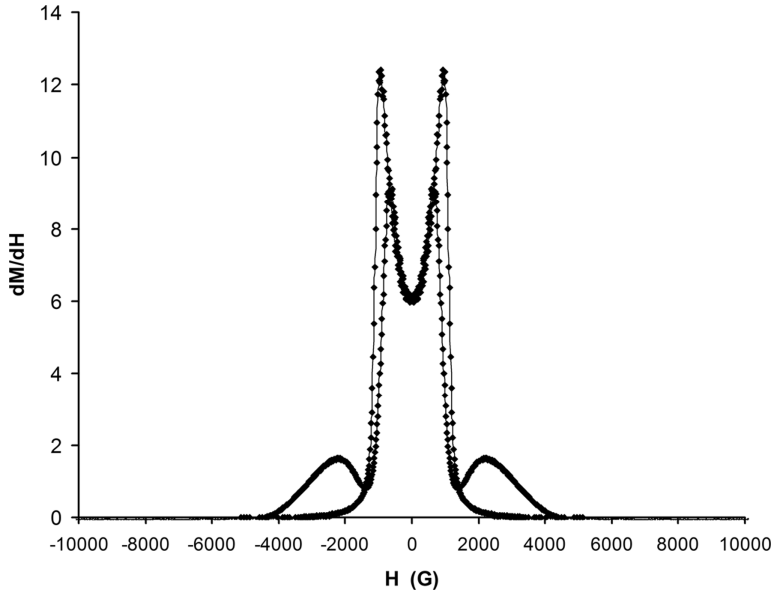

Figure 4.16 Plot of the first derivative (d*M*/d*H*) of the magnetization versus magnetic field for a single crystal of **Y** at 0.04 K and 80 G/s sweep rate, where the magnetic field is oriented parallel to the axis of the crystal.

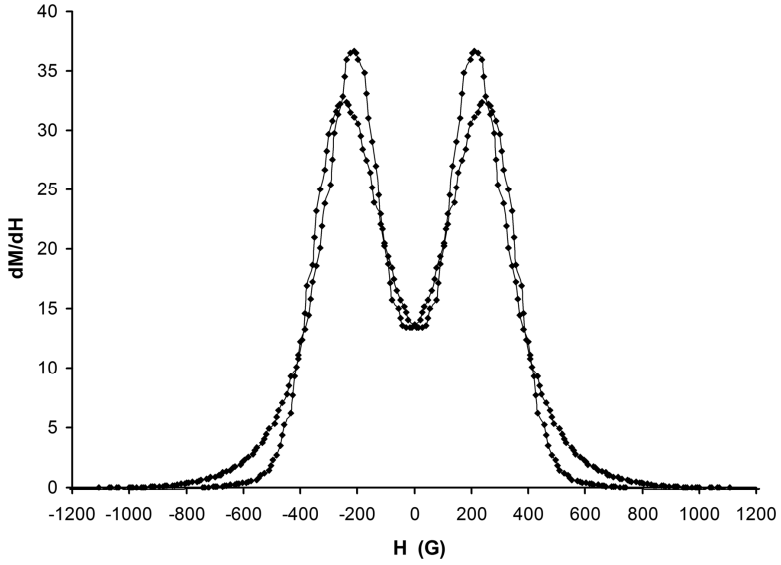

Figure 4.17 Plot of the first derivative (d*M*/d*H*) of the magnetization versus magnetic field for a single crystal of **Tb** at 0.04 K and 40 G/s sweep rate, where the magnetic field is oriented parallel to the axis of the crystal.

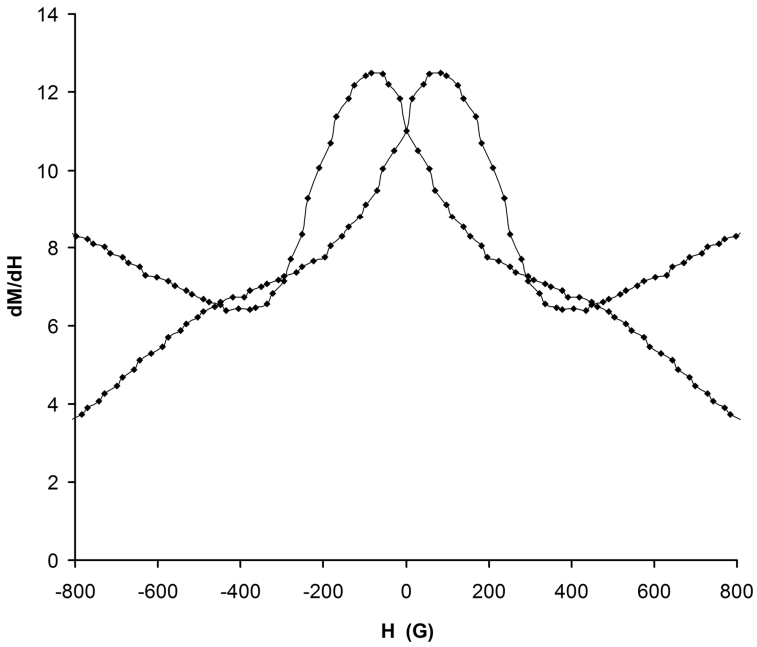

Figure 4.18 Plot of the first derivative (d*M*/d*H*) of the magnetization versus magnetic field for a single crystal of $\mathbf{Y_{0.97}Tb_{0.03}}$ at 0.04 K and 40 G/s sweep rate, where the magnetic field is oriented parallel to the axis of the crystal.

We also observed strong PB behavior, as expected for small spins without anisotropy (Figure 4.14c).[183] The PB effect was detected for fields higher than the exchange fields and temperatures above the ordering temperature of ~ 0.25 K for all fields except H = 0. Turning again to **Tb**, we observed an additional antiferromagnetic interaction between Tb spins, but at a lower temperature (T < 0.2 K) and with a smaller exchange field of 240 G, which was estimated from the inflection point of the M vs H curve (Figure 4.14a). Because the interaction (exchange field) is very different from **Y**, we conclude that the interaction between Tb spins is most likely not directly mediated by the radical spins. This interpretation is confirmed by the properties of $\mathbf{Y_{0.97}Tb_{0.03}}$ which contains a small concentration of Tb (3%). In this case, the Tb spins lead to a small step at H = 0, which is not influenced (shifted) by the antiferromagnetically coupled radical spins (Figure 4.14b). Thus, the organic radicals couple rather strongly to the Tb spins, localizing them, and therefore the interactions between radicals is rendered weaker. Simply put, the exchange interactions for **Tb** can be assigned as antiferromagnetic interactions of Tb ions with unstacked $TCNQF_4$ radicals, along with weak antiparallel magnetic dipolar interactions between adjacent Tb ions. The combination of such competing interactions reduces the observed exchange interaction in comparison to **Y** which has only one exchange pathway. In any case, the magnetic dipolar interaction between Tb spins is very small and at higher temperatures (1.8 K and above), it can be neglected. Hence, the AC signal is reminiscent of SMM behavior for **Tb**, $\mathbf{Y_{0.74}Tb_{0.26}}$, and $\mathbf{Y_{0.97}Tb_{0.03}}$. The microSQUID studies and AC susceptibility studies indicate that the PB effect does not cancel the SMM behavior of the Tb complex as both events coexist,

but the magnitude of SMM behavior in compounds $\mathbf{Y_{0.74}Tb_{0.26}}$, and $\mathbf{Y_{0.97}Tb_{0.03}}$ is much less pronounced than that of **Tb** because of the high dilution for these derivatives.

As a final discussion point, we point out that, at low temperatures, all spins are slightly coupled, resulting in complex dynamics that serves to obscure any subtle details. For example, the hyperfine coupling of Tb should lead to a nice fine structure at low T as observed in the bis(phthalocyaninato)terbium anion reported by Ishikawa.[170c] In the present case, however, this effect is obscured by the interactions of Tb ions with the radicals. In general, such interactions between spins accelerate the relaxation, i.e., the SMM behavior is diminished. The deviation from the square antiprismatic coordination environment of the Tb ion is also expected to contribute to a reduction in the SMM behavior exhibited by **Tb**. The coordination environment is significantly more distorted than the slightly distorted square antiprismatic environment of the single lanthanide complexes reported by Ishikawa.[170c] In general, interactions lead to ordering at low temperatures unless the tunneling is so strong that the dynamics are not quenched by the ordering. In the present case, however, the sweep rate dependence of **Tb** at 0.04 K is rather small, an indication that the small hysteresis below 0.2 K is influenced by the ordering.

Conclusions

The findings of this study highlight an important issue, namely that the beginning of an out-of-phase signal in this particular system is not reliable evidence for SMM behavior and that low temperature measurements such as the micro-SQUID technique were necessary to fully elucidate the behavior. In the present series of materials, interplay between single molecule magnetic behavior and a phonon bottleneck effect is evidenced by studies of diluted samples. A combination of SMM and PB behavior is found for **Tb** with an increase in the PB effect being observed with increasing dilution until eventually a pure PB effect is observed for **Y**. The dilution studies indicate that the "sea of organic S = 1/2 radicals" is responsible for the PB effect observed in the present compounds.

Experimental Section

General Methods: Solvents and chemicals were obtained from commercial sources and used without further purification. Infrared (IR) spectra were measured as Nujol mulls placed between KBr plates on a Nicolet 740 FTIR spectrometer. Elemental analyses were performed by Atlantic Microlab Inc., P.O. Box 2288, Norcross, GA 30091

Experimental Details: The synthesis of $TCNQF_4$ was performed according to the reported procedure.[157a] $LiTCNQF_4$ was prepared by the same method as the one for LiTCNQ.[42b] All reactions were performed under nitrogen using standard Schlenk-line techniques.

Synthesis of Tb: Block-shaped single crystals of **Tb** were obtained after three days by layering a dark blue solution of $Li[TCNQF_4]$ (0.2 mmol) in H_2O (15 mL) on top of a colorless solution of $TbCl_3 \cdot 6H_2O$ (0.2 mmol) in H_2O (5mL) in a Schlenk tube. The crystals were harvested by filtration, washed with copious quantities of water, and dried *in vacuo*; yield: 60 %. FW = 1149.54. C, H, N, O, F analysis (%) calcd for $C_{36}H_{18}N_{12}O_9F_{12}Tb_1$ (**Tb**): C 37.61, H 1.58, N 14.62, O 12.53, F 19.83; found C 37.56, H 1.53, N 14.47, O 12.43, F 19.67. IR (Nujol, cm^{-1}): ν(CN) = 2207 (s), 2196 (s), 2187 (m), 2180 (w) cm^{-1}.

Compounds **Y**, $\mathbf{Y_{0.74}Tb_{0.26}}$, and $\mathbf{Y_{0.97}Tb_{0.03}}$ were obtained by the same method as **Tb**, namely by starting with mixtures of the rare earth chloride salts in the proportions indicated in the composition of the products.

Synthesis of Y: $C_{36}H_{18}N_{12}O_9F_{12}Y_1$, FW = 1079.49, Yield: 30%. C, H, N, O, F analysis (%) calcd: C 40.05, H 1.68, N 15.57, O 13.34, F 21.11; found C 39.96, H 1.68, N 15.51, O 13.14, F 20.93. IR (Nujol, cm^{-1}): ν(CN) = 2201 (s), 2193 (w) cm^{-1}.

Synthesis of $\mathbf{Y_{0.74}Tb_{0.26}}$: $C_{36}H_{18}N_{12}O_9F_{12}Y_{0.74}Tb_{0.26}$, FW = 1097.69, Yield: 22.2%. C, H, N, O, F analysis (%) calcd: C 39.39, H 1.65, N 15.31, O 13.12, F 20.77; found C 39.40, H 1.66, N 15.34, O 13.27, F 20.90. IR (Nujol, cm^{-1}): ν(CN) = 2208 (s), 2197 (s), 2187 (s) 2179 (m) cm^{-1}.

Synthesis of $\mathbf{Y_{0.97}Tb_{0.03}}$: $C_{36}H_{18}N_{12}O_9F_{12}Y_{0.97}Tb_{0.03}$, FW = 1081.59, Yield: 33%. C, H, N, O, F analysis (%) calcd: C 39.98, H 1.68, N 15.54, O 13.31, F 21.08; C 40.12, H 1.67,

N 15.63, O 13.41, F 21.19. IR (Nujol, cm^{-1}): ν(CN) = 2205 (m), 2196 (s), 2186 (s), 2178 (m) cm^{-1}.

X-ray Crystallography, General Procedures: In a typical experiment, a crystal selected for study was suspended in polybutene oil (Aldrich) and mounted on a cryoloop, which was placed in an N_2 cold stream. Single-crystal X-ray data were collected at 110 K on a Bruker SMART 1000 diffractometer equipped with a CCD detector. The data sets were recorded as three ω-scans of 606 frames each, at 0.3° step width, and integrated with the Bruker SAINT[146] software package. The absorption correction (SADABS)[147] was based on fitting a function to the empirical transmission surface as sampled by multiple equivalent measurements. Solution and refinement of the crystal structures was carried out using the SHELX[148] suite of programs and the graphical interface X-SEED.[149] Preliminary indexing of the data sets established similar monoclinic unit cells for all of the studied compounds. Systematic extinctions indicated the space group $P2_1/c$ (No. 14). All of the structures were solved by direct methods that resolved the positions of the metal atoms and most of the C, N and F atoms. The remaining non-hydrogen atoms were located by alternating cycles of least-squares refinements and difference Fourier maps. Hydrogen atoms were placed at calculated positions. CCDC 669346 (**Tb**), CCDC 699042 (**Y**), CCDC 699043 ($\mathbf{Y_{0.74}Tb_{0.26}}$), and CCDC 699044 ($\mathbf{Y_{0.97}Tb_{0.03}}$) contain the supplementary crystallographic data for this chapter. These data can be obtained free of charge from the Cambridge Crystallographic Data Centre via www.ccdc.cam.ac.uk/data_request/cif.

Field-dependent Micro-SQUID Magnetization Scans: Field-dependent micro-SQUID magnetization scans were performed at 0.04 K with sweep rates varying from 40 $G \cdot s^{-1}$ to 2800 $G \cdot s^{-1}$ on an individual single crystal at a time, which was oriented on its easy axis of magnetization found by the transverse field method.[182] All measurements were performed with a micro-SQUID array that has been described elsewhere.[186]

DC Magnetic Susceptibility Measurements: DC magnetic susceptibility measurements were performed on crushed single crystals with a Quantum Design MPMS-XL SQUID magnetometer operating in the temperature range of 1.8-300 K at 1000 G. AC magnetic susceptibility measurements were performed on the same samples with an oscillating field of 3 Oe under zero dc applied field, 500 Oe, 1000 Oe, and 2000 Oe applied dc field. Magnetization data were measured at 1.8 K with the magnetic field varying from 0 to 70 000 G. The data were corrected for diamagnetic contributions calculated from the Pascal constants.[178b]

CHAPTER V

A HOMOLOGOUS HETEROSPIN SERIES OF MONONUCLEAR LANTHANIDE/$TCNQF_4$ ORGANIC RADICAL COMPLEXES*

Introduction

The field of molecular magnetism has experienced remarkable growth over the last decade due, in part, to the discovery of high-temperature molecule-based magnets,[39] multiproperty magnetic materials[40] and single molecule magnets (SMMs).[41] Although heterometallic molecular magnets based on transition metals are quite common, analogous materials including 4f elements are still relatively scarce. The reason for the relative lack of rare earth molecular magnets as compared to d block elements is the fact that 4f electrons do not participate in strong superexchange interactions through bridging ligands due to shielding from the outer shell electrons. In spite of this fact, the incorporation of lanthanide ions into magnetic materials is still a promising venue, given the strong magnetic anisotropy and large magnetic moments associated with these ions. Gadolinium is the most studied lanthanide ion in molecular complexes because the magnetic properties are easier to model. The Gd^{III} ion has no orbital contribution and no spin orbit coupling and therefore it follows Curie Law behavior.

---

*Reprinted in part with permission from *Dalton Transactions*, N. Lopez, H. Zhao, A. V. Prosvirin, W. Wernsdorfer, K. R. Dunbar, "*A Homologous Heterospin Series of Mononuclear Lanthanide/$TCNQF_4$ Organic Radical Complexes*," **2010**, *39*, 4341-4352.

Lanthanide ions have been exploited for the design of 3d-4f mixed clusters that behave as SMMs with some fascinating results being reported.[167] SMM behavior has been observed in rare earth ion clusters[169] and even in single ion double deckers, $[(Pc)_2Ln^{III}]^-$ (Pc = phthalocyaninato; Ln = Tb, Dy, Ho), the Tb analogue of which exhibits the highest blocking temperature of all reported SMMs.[170] Another promising avenue is the combination of 4f ions with organic radicals with s and p based magnetic orbitals. The use of organic radicals which can act both as spin carriers and as bridging ligands connecting paramagnetic metal centers has proven to be an attractive route to obtain magnetically coupled mixed 4f-organic radical heterospin systems.[187] For example, Gatteschi *et al.* discovered magnetic ordering for 1-D chains composed of rare earth metal ions and the organic radical 2-ethyl-4,4,5,5-tetramethyl-4,5dihydro-1H-imidazolyl-1-oxyl 3-oxide (NITEt) $[Ln(hfac)_3(NITEt)_2]$ (Ln = Dy, Tb, Ho, Er),[188] Miller and coworkers reported $Ln(TCNE)_3$ (TCNE = tetracyanoethylene) materials that order ferrimagnetically at 8.5 K (Dy) and 3.5 K (Gd),[189] and our group reported a 2-D material $[\{[Gd_2(TCNQ)_5(H_2O)_9][Gd(TCNQ)_4(H_2O)_3]\}\cdot 4H_2O]_\infty$ (TCNQ = 7,7,8,8-tetracyanoquinodimethane) that shows ferrimagnetic ordering at 3.5 K.[122]

The Ln^{III}/nitronyl-nitroxide radical system is the most extensively studied family as evidenced by numerous reports on discrete complexes[190] and 1D chains.[191] Recently heterospin 2p-4f SMMs[192] and single chain magnets (SCMs)[171] based on lanthanide ions and nitronyl-nitroxide radicals have also been reported. Additional heterospin 2p-4f SMMs composed of an organic radical bis(phthalocyaninato)-terbium complex,[168] and a $\{Tb[TCNQF_4]_2[H_2O]_6\}^+$ complex,[54c] provide supporting evidence for the contention that

SMM behavior, and possibly SCM behavior, can be achieved for a wide variety of Ln-organic radical combinations. In this vein, there is much interest in the combination of Ln ions with other types of organic radicals, such as derivatives of tetrathiafulvalene (TTF) cations,[193] semiquinones,[194] carboxylic-substituted polychlorotriphenylmethyl,[195] imino nitroxide,[196] tetracyanoethylene,[197] tetracyanobenzene,[198]and verdazyl radicals.[199] Excellent examples of members of a growing family of fascinating compounds based on 2p-3d-4f and 3p-3d-4f heterospin combinations are$[\{CuL\}_2(Gd(TCNQ)_2]\cdot TCNQ^{-\bullet}CH_3OH\cdot CH_3CN$ (L = *N,N′*-propylenebis(3methoxy-salicylideneiminato))[200] and $[\{(CH_3OH)CuL^2\}\{CuL^2\}Gd\text{-}(O_2NO)\{Ni(mnt)_2\}][Ni(mnt)_2]\cdot CH_2Cl_2$ (L^2 = *N,N′*-ethylene-di(3-methoxysalicylidene-iminato), mnt = maleonitriledithiolate).[201]

In spite of all the recent progress, the use of TCNQ organic radicals to generate 2p-4f heterospin systems remains relatively unexplored as evidenced by the small number of reports, namely $Ln(N\text{-}N)_x(TCNQ)_3$ (Ln = Pr, Nd; N-N = 1,10-phenanthroline, dipyridylamine; x = 2, 4) and $Ln(N\text{-}N)_4(TCNQ)_4$,[202] a series of lanthanide/TCNQ compounds,[203] and the aforementioned Gd/TCNQ 2D framework obtained in our laboratories.[122] A natural extension of the 4f TCNQ chemistry is the use of the stronger electron acceptor derivative $TCNQF_4$. Herein we report the synthesis and characterization of a family of $M^{III}/[TCNF_4]^{-\bullet}$ molecular complexes; M = La (**La**), Pr (**Pr**), Nd (**Nd**), Sm (**Sm**), La:Sm (80:20) ($\mathbf{La_{0.8}Sm_{0.2}}$), Eu (**Eu**), Gd (**Gd**), Y:Gd (74:26) ($\mathbf{Y_{0.74}Gd_{0.26}}$), Dy (**Dy**), Y:Dy (68:32) ($\mathbf{Y_{0.68}Dy_{0.32}}$), Ho (**Ho**), Er (**Er**), Yb (**Yb**), and Y (**Y**). This homologous series of compounds offers a rare opportunity for studying the magnetic interactions of related rare earth mononuclear complexes with an organic

radical ligand. Recently, we reported detailed low temperature micro-SQUID studies for the Tb complex in this series whose complex magnetic properties involve an interplay between SMM and phonon bottleneck (PB) behavior. It was found that these properties depend on the degree of dilution with diamagnetic Yttrium ions.[54c] The results described in this chapter offer additional insight into the role of the rare earth ion in dictating the magnetism of these $TCNQF_4$ radical complexes.

Results

Syntheses: The reaction of lanthanide ions with $[TCNQF_4]^{\bullet-}$ organic radicals results in the precipitation of crystalline solids of general formula $\{M[TCNQF_4]_2[H_2O]_x\}\cdot(TCNQF_4)(3H_2O)$ (M = La, Pr, Nd, Sm, $La_{0.8}Sm_{0.2}$, and Eu: $x = 7$; M = Gd, $Y_{0.74}Gd_{0.26}$, Dy, $Y_{0.68}Dy_{0.32}$, Ho, Er, Yb, and Y: $x = 6$). The same preparation method was used to obtain the entire series of $Ln/TCNQF_4$ complexes. Table 5.1 lists the formulas of the compounds as well as yields for the respective reactions. To render it easier for the reader to follow the discussion, the compounds will be referred to by short abbreviations whose assignments are found in Table 5.1.

The facile crystallization of pure samples of this series of compounds is attributed to the fact that the species are cationic and that they cocrystallize with $[TCNQF_4]^{\bullet-}$ organic radicals, resulting in the formation of salts. All of the products are readily soluble in most common solvents. The solids are air-stable and can be stored without specific precautions for prolonged periods of time.

Table 5.1 Experimental data for the Ln/$TCNQF_4$ homologous series.

Compound	Molecular Formula	ν(C≡N), cm^{-1} [a]	Yield (%)	χT_{obs}	χT_{calc} [b]	χT_{calc} [c]
La	$\{La[TCNQF_4]_2[H_2O]_7\}\cdot(TCNQF_4)(3H_2O)$	2209, 2190	16	0.77	0.75	NA
Pr	$\{Pr[TCNQF_4]_2[H_2O]_7\}\cdot(TCNQF_4)(3H_2O)$	2204, 2189	10	2.52	2.35	NA
Nd	$\{Nd[TCNQF_4]_2[H_2O]_7\}\cdot(TCNQF_4)(3H_2O)$	2214, 2199, 2190	50	2.22	2.39	NA
Sm	$\{Sm[TCNQF_4]_2[H_2O]_7\}\cdot(TCNQF_4)(3H_2O)$	2209, 2202, 2189	31	0.70	0.84	NA
Eu	$\{Eu[TCNQF_4]_2[H_2O]_7\}\cdot(TCNQF_4)(3H_2O)$	2201, 2189	19	2.41	0.75	NA
Gd	$\{Gd[TCNQF_4]_2[H_2O]_6\}\cdot(TCNQF_4)(3H_2O)$	2207	16	9.01	NA	8.44
Dy	$\{Dy[TCNQF_4]_2[H_2O]_6\}\cdot(TCNQF_4)(3H_2O)$	2208, 2196, 2186, 2179	23	14.31	NA	14.73
Ho	$\{Ho[TCNQF_4]_2[H_2O]_6\}\cdot(TCNQF_4)(3H_2O)$	2207, 2196, 2186, 2179	17	14.51	NA	14.62
Er	$\{Er[TCNQF_4]_2[H_2O]_6\}\cdot(TCNQF_4)(3H_2O)$	2207, 2196, 2186, 2179	49	11.82	NA	12.04
Yb	$\{Yb[TCNQF_4]_2[H_2O]_6\}\cdot(TCNQF_4)(3H_2O)$	2208, 2195, 2187, 2179	59	2.78	NA	3.12
Y	$\{Y[TCNQF_4]_2[H_2O]_6\}\cdot(TCNQF_4)(3H_2O)$	2201 , 2193	30	0.55	NA	0.56

[a] : ν(C≡N) values of neutral $TCNQF_4$ = 2227 cm^{-1}, monoreduced $Li[TCNQF_4]$ = 2198 cm^{-1}, and doubly reduced $[Fe(C_5H_5)_2]_2[TCNQF_4]$ = 2167, 2133 cm^{-1}.[46b]

[b] : The calculated room temperature χT value includes the contribution of two $[TCNQF_4]^{\bullet-}$ radicals.

[c] : The calculated room temperature χT value includes the contribution of 1.5 $[TCNQF_4]^{\bullet-}$ radicals.

Single-Crystal X-ray Structures: Single-crystal X-ray studies revealed that isostructural **La**, **Pr**, **Nd**, **Sm**, and $\mathbf{La_{0.8}Sm_{0.2}}$ crystallize in the monoclinic space group $P2_1/n$, hence the structural description will be given for compound **Sm** for illustrative purposes. Compounds **Gd**, $\mathbf{Y_{0.74}Gd_{0.26}}$, **Dy**, $\mathbf{Y_{0.68}Dy_{0.32}}$, **Ho**, **Er**, **Yb**, and **Y** comprise a second isostructural series and crystallize in the monoclinic space group $P2_1/c$. Compound **Eu** also crystallizes in the monoclinic space group $P2_1/c$ with different unit cell parameters in comparison to compounds **Gd**-**Y**.

In the same manner as above, we will describe the structure of only the **Ho** compound as a guide for understanding all the others. A summary of pertinent information relating to unit cell parameters is provided in Table 5.2. Compounds **La**, **Pr**, **Nd**, **Sm**, $\mathbf{La_{0.8}Sm_{0.2}}$, and **Eu** consist of the nonacoordinate cationic complex $[M(TCNQF_4)_2(H_2O)_7]^+$ where the metal ion is in a distorted tricapped trigonal prism coordination environment. The Ln-O distances in **Sm** range from 2.405 Å to 2.567 Å and the Sm-N distances are longer than the aforementioned distances (Sm-N5 = 2.566 and Sm-N1 = 2.591 Å). The $TCNQF_4$ molecules are cis to each other with an angle of 76.78° for **La**; 76.82° **Pr**; 77.22° **Nd**; 76.38° **Sm**; and 75.66° for **Eu**. The asymmetric unit consists of the whole molecule along with three interstitial water molecules and one uncoordinated $[TCNQF_4]^{-\bullet}$ radical (Figure 5.1).

Compounds **Gd**, $\mathbf{Y_{0.74}Gd_{0.26}}$, **Dy**, $\mathbf{Y_{0.68}Dy_{0.32}}$, **Ho**, **Er**, **Yb**, and **Y** are octacoordinate with the lower coordination number being due to the lanthanide contraction effect (Figure 5.2).

Table 5.2 Crystallographic data for the Ln/$TCNQF_4$ series.

Compound	**La**	**Pr**	**Nd**	**Sm**
Formula	$C_{36}H_{20}N_{12}O_{10}F_{12}La_1$	$C_{36}H_{20}N_{12}O_{10}F_{12}Pr_1$	$C_{36}H_{20}N_{12}O_{10}F_{12}Nd_1$	$C_{36}H_{20}N_{12}O_{10}F_{12}Sm_1$
F_w [g mol^{-1}]	1147.50	1149.51	1152.84	1158.96
Crystal size [mm^3]	0.35 x 0.25 x 016	0.30 x 0.30 x 0.15	0.35 x 0.25 x 0.15	0.40 x 0.35 x 0.07
Crystal system	Monoclinic	Monoclinic	Monoclinic	Monoclinic
Space group	$P2_1/n$	$P2_1/n$	$P2_1/n$	$P2_1/n$
a [Å]	13.626(5)	13.82(1)	13.552(7)	13.562(2)
b [Å]	17.548(5)	17.65(2)	17.43(1)	17.394(3)
c [Å]	18.367(7)	18.57(2)	18.30(1)	18.316(3)
β [°]	96.71(1)	97.10(2)	96.83(2)	97.016(4)
V [$Å^3$]	4362(3)	4496(9)	4292(4)	4288(1)
Z	4	4	4	4
ρ_{calc} [g cm^{-3}]	1.748	1.698	1.784	1.899
μ ($Mo_{K\alpha}$) [mm^{-1}]	1.101	1.202	1.333	1.493
Reflections collected	44243	24159	40335	43788
Unique reflections	10298	10149	10301	10346
Reflections with I >2σ(I)	8336	5675	8402	8412
parameters	652	640	687	641
R(int)	0.0311	0.1465	0.0633	0.0610
$R1$[a]	0.0589	0.0998	0.0662	0.0590
$wR2$[b]	0.1480	0.2263	0.1427	0.1333
GOF	1.067	0.961	1.092	1.071

[a] $R1 = \Sigma||F_o| - |F_c||\Sigma|F_o|$. [b] $wR2 = [\Sigma[w(F_o^2 - F_c^2)^2]/\Sigma[w(F_o^2)^2]]^{1/2}$.

Table 5.2 Continued.

Compound	**$La_{0.8}Sm_{0.2}$**	**Eu**	**Gd**	**$Y_{0.74}Gd_{0.26}$**
Formula	$C_{36}H_{20}N_{12}O_{10}F_{12}$ $La_{0.8}Sm_{0.2}$	$C_{36}H_{20}N_{12}O_{10}F_{12}$ Eu_1	$C_{36}H_{18}N_{12}O_9F_{12}$ Gd_1	$C_{36}H_{18}N_{12}O_9F_{12}$ $Y_{0.74}Gd_{0.26}$
F_w [g mol^{-1}]	1149.80	1160.56	1147.83	1097.26
Crystal size [mm^3]	0.39 x 0.19 x 0.15	0.11 x 0.07 x 0.05	0.32 x 0.28 x 0.20	0.25 x 0.16 x 0.13
Crystal system	Monoclinic	Monoclinic	Monoclinic	Monoclinic
Space group	$P2_1/n$	$P2_1/c$	$P2_1/c$	$P2_1/c$
a [Å]	13.648(2)	13.551(1)	13.701(3)	13.668(3)
b [Å]	17.556(2)	17.399(1)	17.671(4)	17.670(3)
c [Å]	18.392(2)	21.519(1)	17.104(3)	17.065(5)
β [°]	96.919(8)	122.257(4)	103.18(3)	103.13(1)
V [$Å^3$]	4374.7(8)	4290.6(6)	4032(1)	4014(2)
Z	4	4	4	4
ρ_{calc} [g cm^{-3}]	1.746	1.797	1.891	1.818
μ ($Mo_{K\alpha}$) [mm^{-1}]	1.171	1.1592	1.773	1.638
Reflections collected	38452	25708	25969	34184
Unique reflections	10612	6109	9739	9602
Reflections with I >2σ(I)	9251	3553	8443	8137
parameters	679	625	703	671
R(int)	0.0368	0.1013	0.0295	0.0380
$R1$[a]	0.0441	0.0716	0.0236	0.0298
$wR2$[b]	0.1136	0.1793	0.0518	0.0746
GOF	1.034	0.987	1.050	1.086

[a] $R1 = \Sigma||F_o| - |F_c||\Sigma|F_o|$. [b] $wR2 = [\Sigma[w(F_o^2 - F_c^2)^2]/\Sigma[w(F_o^2)^2]]^{1/2}$.

Table 5.2 Continued.

Compound	**Dy**	**$Y_{0.68}Dy_{0.32}$**	**Ho**	**Er**
Formula	$C_{36}H_{18}N_{12}O_9F_{12}Dy_1$	$C_{36}H_{18}N_{12}O_9F_{12}Y_{0.68}Dy_{0.32}$	$C_{36}H_{18}N_{12}O_9F_{12}Ho_1$	$C_{36}H_{18}N_{12}O_9F_{12}Er_1$
F_w [g mol^{-1}]	1153.08	1103.04	1155.55	1157.84
Crystal size [mm^3]	0.42 x 0.28 x 0.20	0.34 x 0.19 x 0.12	0.45 x 0.37 x 0.22	0.46 x 0.39 x 0.26
Crystal system	Monoclinic	Monoclinic	Monoclinic	Monoclinic
Space group	*P2$_1$/c*	*P2$_1$/c*	*P2$_1$/c*	*P2$_1$/c*
a [Å]	13.694(3)	13.643(2)	13.666(2)	13.651(3)
b [Å]	17.664(4)	17.639(2)	17.643(2)	17.646(5)
c [Å]	17.068(3)	17.018(3)	17.045(3)	17.024(5)
β [°]	103.12(3)	103.198(7)	103.119(7)	103.122(8)
V [Å^3]	4021(1)	3987(1)	4002(1)	3994(2)
Z	4	4	4	4
ρ_{calc} [g cm^{-3}]	1.905	1.831	1.918	1.926
μ ($Mo_{K\alpha}$) [mm^{-1}]	1.987	1.701	2.106	2.231
Reflections collected	24979	35568	40702	40642
Unique reflections	9244	9675	9584	9597
Reflections with I >2σ(I)	8156	8859	8975	9136
parameters	698	687	703	672
R(int)	0.0284	0.0277	0.0290	0.0262
*R*1[a]	0.0229	0.0213	0.0172	0.0202
*wR*2[b]	0.0552	0.0546	0.0425	0.0514
GOF	1.031	1.029	1.015	1.060

[a] $R1 = \Sigma||F_o| - |F_c||\Sigma|F_o|$. [b] $wR2 = [\Sigma[w(F_o^2 - F_c^2)^2]/\Sigma[w(F_o^2)^2]]^{1/2}$.

Table 5.2 Continued.

Compound	**Yb**	**Y**
Formula	$C_{36}H_{18}N_{12}O_9F_{12}Yb_1$	$C_{36}H_{18}N_{12}O_9F_{12}Y_1$
F_w [g mol^{-1}]	1163.62	1079.49
Crystal size [mm^3]	0.50 x 0.40 x 0.30	0.63 x 0.16 x 0.16
Crystal system	Monoclinic	Monoclinic
Space group	$P2_1/c$	$P2_1/c$
a [Å]	13.649(8)	13.660(3)
b [Å]	17.65(1)	17.671(5)
c [Å]	16.98(1)	17.040(4)
β [°]	103.09(3)	103.103(7)
V [Å^3]	3985(5)	4006(2)
Z	4	4
ρ_{calc} [g cm^{-3}]	1.940	1.790
μ ($Mo_{K\alpha}$) [mm^{-1}]	2.477	1.585
Reflections collected	16036	11913
Unique reflections	8617	6805
Reflections with I >2σ(I)	7479	5311
parameters	655	628
R(int)	0.0392	0.0830
$R1$[a]	0.0487	0.0504
$wR2$[b]	0.1284	0.1269
GOF	1.025	0.970

[a] $R1 = \Sigma||F_o| - |F_c||\Sigma|F_o|$. [b] $wR2 = [\Sigma[w(F_o^2 - F_c^2)^2]/\Sigma[w(F_o^2)^2]]^{1/2}$.

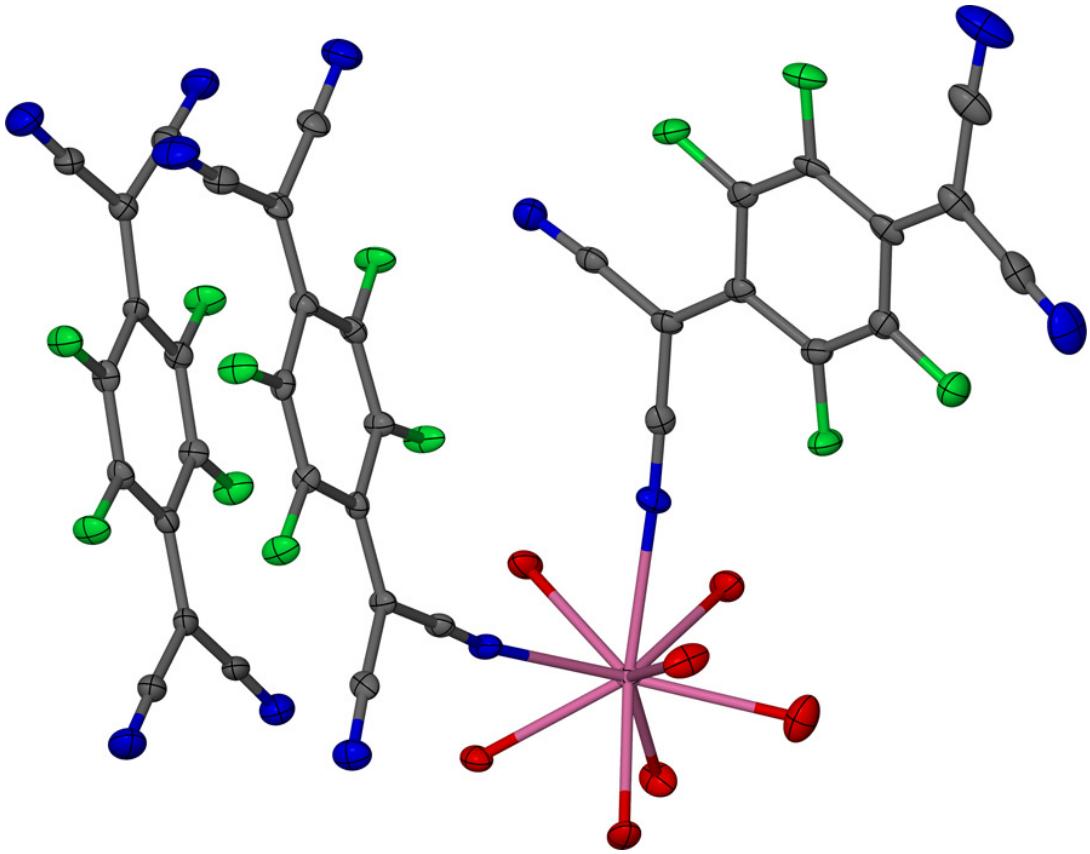

Figure 5.1 Molecular structure of the cationic complex along with the uncoordinated $TCNQF_4$ molecule in **Sm**. Interstitial water molecules and hydrogen atoms have been omitted for the sake of clarity. Sm = pink, O = red, N = blue, C = gray F = green.

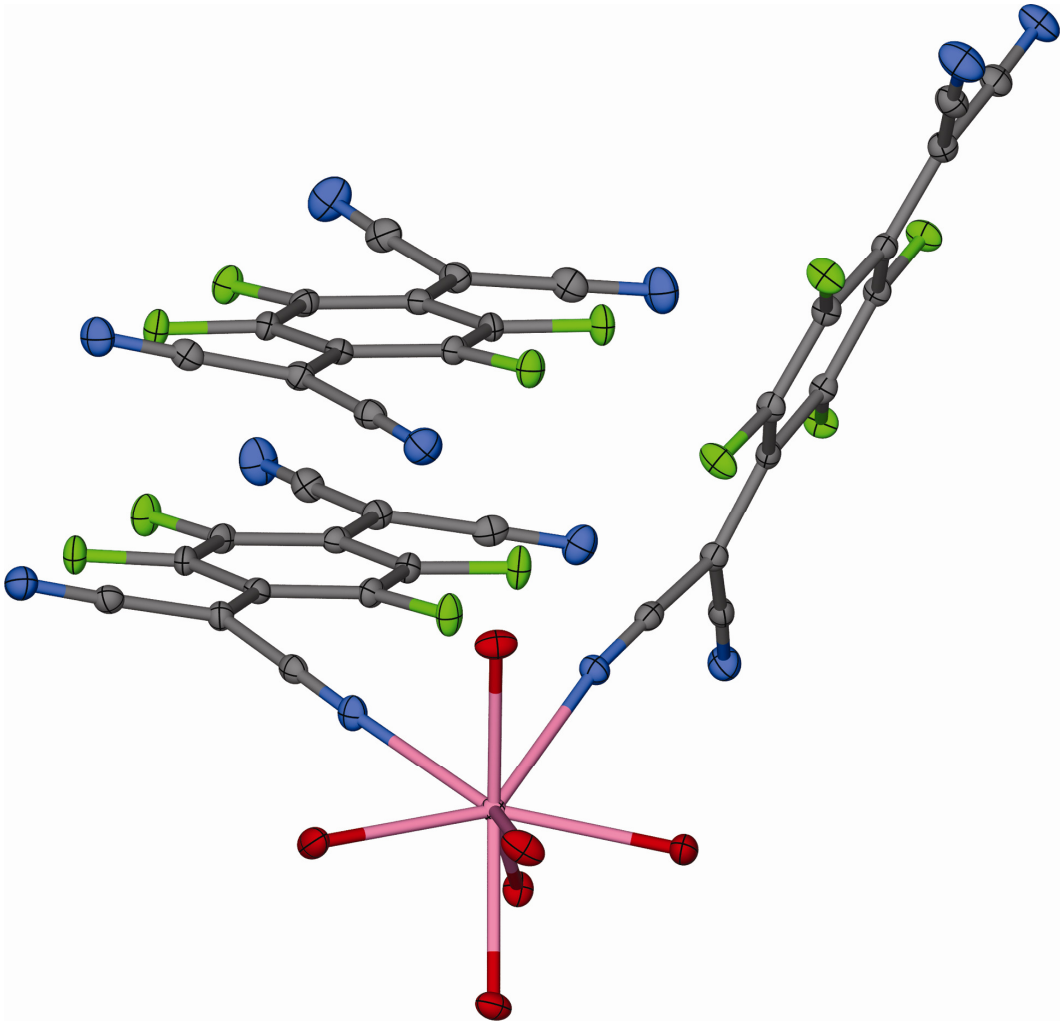

Figure 5.2 Molecular structure of the cationic complex along with the uncoordinated $TCNQF_4$ molecule in **Ho**. Interstitial water molecules and hydrogen atoms have been omitted for the sake of clarity. Ho = pink, O = red, N = blue, C = gray, F = green.

The mononuclear cationic complex in compounds **Gd**, $\mathbf{Y_{0.74}Gd_{0.26}}$, **Dy**, $\mathbf{Y_{0.68}Dy_{0.32}}$, **Ho**, **Er**, **Yb**, and **Y** are analogous to the one observed for **La**, **Pr**, **Nd**, **Sm**, $\mathbf{La_{80}Sm_{20}}$, and **Eu** except that they have one less water molecule bound to the metal center. The metal ion is in a distorted square antiprismatic environment, in which N1, N5, O3, O4 are the A vertices and O1, O2, O5, O6 are the B vertices.

In the **Ho** analogue the A-B separations range from 2.34 Å to 2.76 Å. The lanthanide contraction leads to a quasi-periodic shrinking of the unit cell volume along the series (Table 5.2) and results in a smaller angle between the coordinated $TCNQF_4$ molecules than the ~76° angle observed in compounds **La**-**Eu**, namely: 72.45° for **Gd**, 72.48° **Dy**, 72.01° **Ho**, 72.22° **Er**, 72.22° **Yb**, and 72.39° for **Y**. One of the $TCNQF_4$ ligands is involved in intermolecular π-π interactions with uncoordinated $TCNQF_4$ molecules. The inter-planar π distances for **Sm** are 3.30 Å (U···U), 3.12 Å (U···C), 3.40 Å (C···C), and 3.16 Å (C···U) where U = uncoordinated, C = coordinated. The interplanar distances for **Ho** are 3.28 Å (U···U), 3.09 Å (U···C), 3.40 Å (C···C), and 3.12 Å (C···U); which are shorter than those of **Sm** (Figure 5.3). The $TCNQF_4$ molecules are in close proximity due to π-π interactions, a situation that is anticipated to result in antiferromagnetic interactions as noted for other $[TCNQF_4]^{-\bullet}$ containing materials.[51] Moreover one would expect the antiferromagnetic interactions to be stronger for compounds **Gd**-**Y** due to the closer approach of the $TCNQF_4$ units than found for **La**-**Eu**.

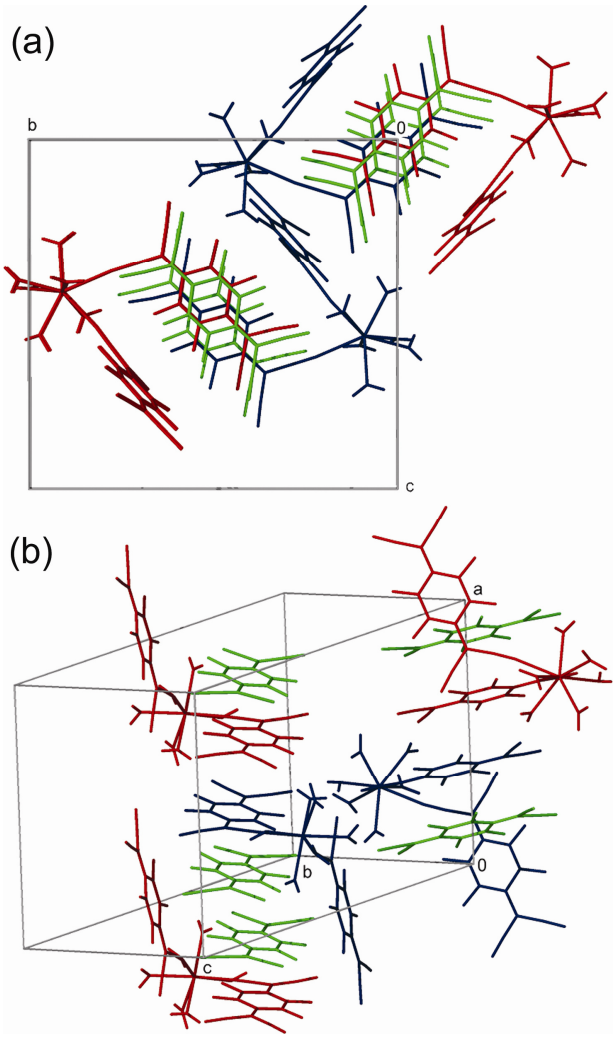

Figure 5.3 Packing diagrams of the **Ho** compound (a) viewed along the *a* axis and (b) depicting π–π stacking interactions. The interstitial water molecules are omitted for the sake of clarity. Blue = the cationic complex $[Ho(TCNQF_4)_2(H_2O)_6]^+$, which has the unstacked $TCNQF_4$ moiety pointing down; red = the cationic complex $[Ho(TCNQF_4)_2(H_2O)_6]^+$, for which the unstacked $TCNQF_4$ unit is pointing up; green = uncoordinated $TCNQF_4$ molecules.

In both series of compounds, the molecules are connected by hydrogen bonds to generate networks. In the first network there are four distinct hydrogen bonds involving an uncoordinated water molecule that resides between adjacent lanthanide complexes with O-O distances in the C···U···C repeat sequence of 3.06 Å (C···U), 2.72 Å (U···C), 2.97 Å (C···U), and 2.79 Å (U···C) for the **Sm** compound; for **Ho** the distances are slightly longer: 3.15 Å (C···U), 2.72 Å (U···C), 3.22 Å (C···U), and 3.58 Å (U···C); U = uncoordinated, C = coordinated. There are two distinct Ln---Ln distances of 6.9 Å and 8.2 Å for **Sm**, which are slightly longer, 7.1 Å and 8.6 Å, for **Ho**. The 1-D hydrogen bonded network is generated by an alternating array of the long and short H-bond interactions for the C···U···C repeat sequences (Figure 5.4). The second set of hydrogen bond interactions forms a 2-D network for compounds **La**-**Eu** whereas a 3-D network is observed for compounds **Gd**-**Y**.

The zigzag 2-D H-bonded network found in compounds **La**-**Eu** is formed by coordinated water molecules and coordinated non-π interacting $TCNQF_4$ units where the three dangling CN groups of $TCNQF_4$ are used to form hydrogen bonds to coordinated water molecules of three neighboring Sm complexes; the N-O distances are 2.73 Å, 2.82 Å, and 2.93 Å. The 3-D H-bonded network observed in compounds **Gd**-**Y** is formed by coordinated water molecules and coordinated non-π interacting $TCNQF_4$ units where two of the dangling CN groups of $TCNQF_4$ are used for hydrogen bonding to coordinated water molecules of three neighboring Ho complexes, with N-O distances of 2.78 Å, 2.90 Å, and 2.94 Å.

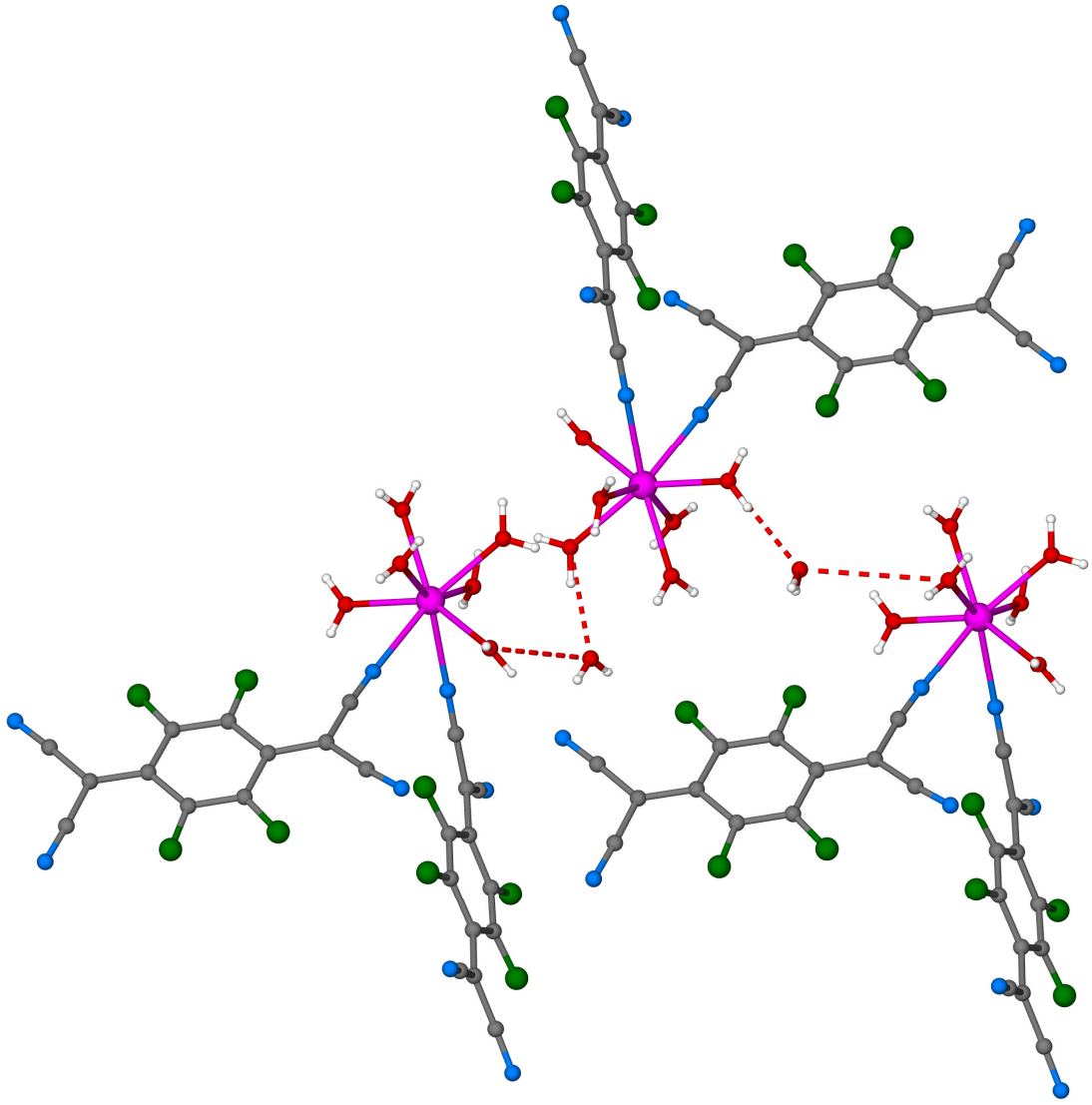

Figure 5.4 View of the 1-D hydrogen bonded network in the **Ho** complex. Ho = pink, O = red, N = blue, C = gray, F = green, H = light gray.

Discussion

The bond distances in TCNQ molecules and its derivatives are indicative of the oxidation state of the molecule due to the fact that the C-C distances in the TCNQ ring reflect changes as the molecule changes from a quinonoid to a benzenoid form with increasing charge. The bond lengths for $TCNQF_4^0$, $TCNQF_4^-$ and $TCNQF_4^{2-}$ were determined by averaging the crystallographic data for a number of compounds. The charges on the $TCNQF_4$ units were estimated from the Kistenmacher relationship, $\rho = A[c/(b + d)] + B$ (A = - 46.729 and B = 22.308; A and B are determined from neutral $TCNQF_4$ ($\rho = 0$)[152] and monoreduced (n-Bu_4N)$TCNQF_4$ ($\rho = -1$).[51] The values of c, b, and d in the $TCNQF_4$ ring are defined in the scheme of Table 5.3. The Kistenmacher formula was used to estimate the charges for coordinated groups (-0.89 and -0.95), and free groups (-0.89) for the **Sm** compound, which are nearly the same and correspond to monoreduced $[TCNQF_4]^{\bullet-}$. The same analysis was performed for the **Ho** derivative with similar results: the estimated charges correspond to monoreduced units for the coordinated groups (-0.99 and -1.06) and free groups (-0.99). An analysis of the entire series of compounds leads to the same conclusion; a summary of the estimated charges and bond distances of $TCNQF_4$ molecules is presented in Table 5.3.

Table 5.3 Calculated charge of $TCNQF_4$ ligands in the $Ln/TCNQF_4$ series.

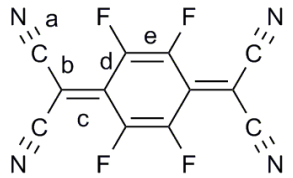

Compound	a	b	c	d	e	b + d	c/(b + d)	ρ
La C-π	1.148	1.425	1.418	1.416	1.365	2.841	0.4991	-1.01
La C-non-π	1.151	1.417	1.423	1.414	1.357	2.831	0.5026	-1.18
La U-π	1.153	1.421	1.412	1.421	1.363	2.842	0.4968	-0.91
Pr C-π	1.157	1.436	1.424	1.432	1.368	2.868	0.4965	-0.89
Pr C-non-π	1.166	1.438	1.460	1.426	1.384	2.864	0.5098	-1.51
Pr U-π	1.169	1.437	1.429	1.430	1.363	2.867	0.4984	-0.98
Nd C-π	1.138	1.429	1.408	1.418	1.351	2.847	0.4945	-0.80
Nd C-non-π	1.147	1.418	1.416	1.411	1.346	2.829	0.5005	-1.08
Nd U-π	1.144	1.426	1.409	1.417	1.358	2.843	0.4956	-0.85
Sm C-π	1.142	1.425	1.414	1.416	1.361	2.841	0.4977	-0.95
Sm C-non-π	1.149	1.421	1.409	1.417	1.352	2.838	0.4964	-0.89
Sm U-π	1.150	1.425	1.413	1.421	1.355	2.846	0.4965	-0.89
$La_{0.8}Sm_{0.2}$ C-π	1.149	1.426	1.416	1.421	1.365	2.847	0.4974	-0.93
$La_{0.8}Sm_{0.2}$ C-non-π	1.149	1.424	1.420	1.418	1.361	2.842	0.4996	-1.04
$La_{0.8}Sm_{0.2}$ U-π	1.151	1.429	1.414	1.422	1.365	2.851	0.4960	-0.87

Table 5.3 Continued.

Compound	**a**	**b**	**c**	**d**	**e**	**b + d**	**c/(b+d)**	**ρ**
Eu C-π	1.136	1.433	1.426	1.413	1.348	2.846	0.5010	-1.11
Eu C-non-π	1.285	1.423	1.420	1.416	1.328	2.839	0.5002	-1.06
Eu U-π	1.148	1.433	1.406	1.416	1.372	2.849	0.4935	-0.75
Gd C-π	1.147	1.422	1.419	1.417	1.358	2.839	0.4998	-1.05
Gd C-non-π	1.148	1.418	1.420	1.415	1.356	2.833	0.5012	-1.11
Gd U-π	1.147	1.423	1.417	1.416	1.358	2.839	0.4991	-1.02
$\mathbf{Y_{0.74}Gd_{0.26}}$ C-π	1.151	1.428	1.419	1.422	1.361	2.850	0.4979	-0.96
$\mathbf{Y_{0.74}Gd_{0.26}}$ C-non-π	1.152	1.421	1.421	1.418	1.362	2.839	0.5005	-1.08
$\mathbf{Y_{0.74}Gd_{0.26}}$ U-π	1.150	1.425	1.416	1.422	1.360	2.847	0.4974	-0.93
Dy C-π	1.148	1.425	1.418	1.419	1.358	2.844	0.4986	-0.99
Dy C-non-π	1.148	1.420	1.420	1.417	1.353	2.837	0.5005	-1.08
Dy U-π	1.147	1.423	1.415	1.418	1.358	2.841	0.4981	-0.97
$\mathbf{Y_{0.68}Dy_{0.32}}$ C-π	1.147	1.425	1.418	1.419	1.363	2.844	0.4986	-0.99
$\mathbf{Y_{0.68}Dy_{0.32}}$ C-non-π	1.149	1.419	1.415	1.416	1.358	2.835	0.4991	-1.02
$\mathbf{Y_{0.68}Dy_{0.32}}$ U-π	1.148	1.422	1.417	1.417	1.359	2.839	0.4991	-1.02
Ho C-π	1.149	1.427	1.419	1.419	1.363	2.846	0.4986	-0.99
Ho C-non-π	1.151	1.421	1.419	1.417	1.363	2.838	0.5000	-1.06
Ho U-π	1.149	1.425	1.418	1.419	1.362	2.844	0.4986	-0.99
Er C-π	1.149	1.426	1.421	1.421	1.360	2.847	0.4991	-1.02
Er C-non-π	1.152	1.420	1.419	1.417	1.359	2.837	0.5002	-1.06
Er U-π	1.149	1.426	1.416	1.419	1.362	2.845	0.4977	-0.95
Yb C-π	1.154	1.424	1.421	1.426	1.349	2.850	0.4986	-0.99
Yb C-non-π	1.148	1.419	1.425	1.416	1.362	2.835	0.5026	-1.18
Yb U-π	1.151	1.426	1.414	1.424	1.352	2.850	0.4961	-0.88
Y C-π	1.145	1.431	1.415	1.423	1.357	2.54	0.4958	-0.86
Y C-non-π	1.151	1.423	1.412	1.413	1.357	2.836	0.4979	-0.96
Y U-π	1.152	1.425	1.417	1.420	1.355	2.845	0.4981	-0.97

Infrared Spectroscopy: Infrared spectroscopy is very useful for ascertaining the binding and redox state of TCNQ molecules including those involved in coordination to metal ions.[54b,204] Given that compounds **La**-**Eu** all exhibit similar absorption bands in the ν(C≡N) region, only the IR data of the **Sm** compound will be discussed. The same reasoning is applied to the isostructural **Gd**-**Y** series and only the infrared data for **Ho** will be discussed. The IR spectrum of **Sm** exhibits ν(C≡N) stretches at 2209, 2202, 2189 cm^{-1}, values that are typical of monoreduced $TCNQF_4$ (2198 cm^{-1}). Similar ν(C≡N) stretches were observed for compound **Ho** at 2207, 2196, 2186 and 2179 cm^{-1}. Thus, one can conclude that the complexes are cationic and that the uncoordinated $[TCNQF_4]^{\bullet}$ radical balances the charge. An analysis of the entire series of compounds leads to the same conclusion. A compilation of the IR data is presented in Table 5.1.

Static Magnetic Properties: The dc magnetic properties of the entire series of compounds were measured in the 2-300 K temperature range at an applied magnetic field of 1000 G. Combined plots of the χT versus T data are presented in Figure 5.5 and the experimental and calculated room temperature χT values are listed in Table 5.1. It is convenient to begin the discussion with the **Sm**, **Gd** and **Dy** compounds because of their interesting magnetic properties. Two model compounds, namely **La** and **Y** that contain diamagnetic La^{III} and Y^{III} ions serve as references for assessing the magnetic behavior of the paramagnetic $[TCNQF_4]^{\bullet}$ radical portion of the compounds. Compounds $\mathbf{La_{0.8}Sm_{0.2}}$, $\mathbf{Y_{0.74}Gd_{0.26}}$, and $\mathbf{Y_{0.68}Dy_{0.32}}$, with diamagnetic ions are convenient models for determining the magnetic behavior of the cationic complexes based on Sm^{III}, Gd^{III} and Dy^{III} ions respectively.

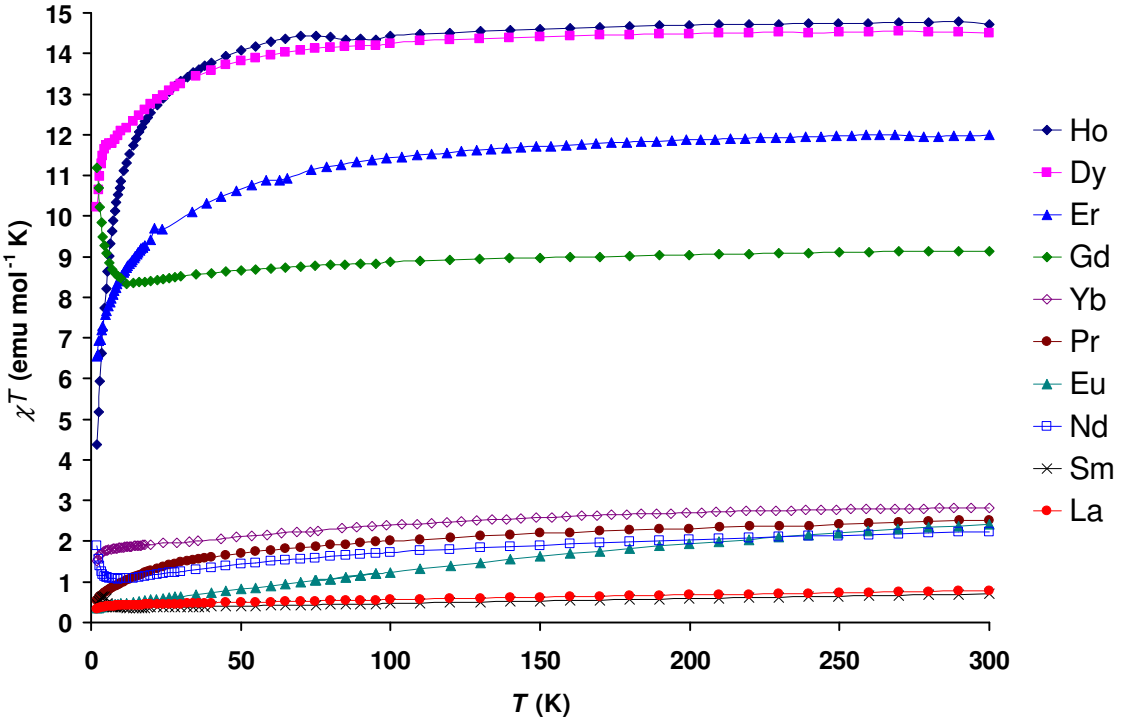

Figure 5.5 Temperature dependence of the χT versus T plots for the Ln/$TCNQF_4$ series.

Fitting magnetic data for anisotropic lanthanide ions is complicated because a full treatment must take into account spin orbit coupling effects, crystal field effects, Ln-organic radical interactions, and organic radical-organic radical interactions. Including all the necessary terms would have to be in the fitting, however, would lead to unreliable values due to overparameterization. Unfortunately, we cannot model the magnetic behavior of these series of compounds using the angle-resolved magnetometry method for anisotropic low symmetry lanthanides reported by Gatteschi *et al.,* because the compounds crystallize in a monoclinic space group with the lanthanide ion residing on a general position.[176] The method is only applicable to molecules or arrays that pack in such a way that there is an orientation of molecular axes with respect to the crystal axes that can be analyzed. Due to these issues, only a phenomenological description of the magnetic susceptibility data is possible for most of the compounds in this series with the exception of the **La**, **Y**, and **Gd** derivatives. In these three cases, the magnetic properties were fit using standard models given that the first two cases contain diamagnetic lanthanide ions and that Gd^{III} ions are magnetically isotropic.

The room-temperature χT value of **La** is 0.77 emu·mol^{-1}·K, which is less than the expected value for a spin-only case of an uncoupled diamagnetic La^{III} ion (χT = 0.00 emu·mol^{-1}·K) and three $[TCNQF_4]^{\bullet}$ (S = ½, χT = 0.375 emu·mol^{-1}·K) radicals (χT_{calc} = 1.12 emu·mol^{-1}·K). It corresponds to approximately two unpaired electrons from two $[TCNQF_4]^{\bullet}$ radicals (χT = 0.75 emu·mol^{-1}·K), which indicates that there are strong antiferromagnetic interactions between radicals in the columns. DC susceptibility data for the other members of the **La**-**Eu** series indicate that the same antiferromagnetic

interactions of π-stacked radicals are operative and are of a similar magnitude. The close proximity of π-stacked $TCNQF_4$ radicals leads to π-dimers of coordinated and uncoordinated units whose interactions considerably reduce the magnetic susceptibility response of this complex. The χT value continuously decreases from the value at room temperature and reaches a minimum of 0.34 $emu \cdot mol^{-1} \cdot K$ at 2 K, which is slightly lower than the contribution of one unpaired electron (Figure 5.6), as expected for the presence of one radical that is not involved in π-π stacking interactions. The magnetic susceptibility of **La** was fitted to a Heisenberg chain model with the Hamiltonian shown in equation 5.1.

$$H = -2J\sum S_i S_{i-1} \tag{5.1}$$

The actual χT values were then fitted with the Bonner and Fisher's numerical approximation shown in equation 5.2.

$$\chi T = \frac{Ng^2\beta^2}{k} \cdot \frac{0.25 + 0.074975x + 0.075235x^2}{1.0 + 0.09931x + 0.172135x^2 + 0.757825x^3} + \frac{Ng^2\mu_B^2 S(S+1)}{3k} \tag{5.2}$$

with

$$x = |J| / kT \tag{5.3}$$

where the first part of the model refers to the S = ½ Heisenberg chain formed by the π stacked $TCNQF_4$ units and the second part refers to the contribution of magnetically isolated non-π-interacting $TCNQF_4$ units.[205] The fitting results in the following parameters: J = -140 cm^{-1}, g = 2.00 (Figure 5.6).

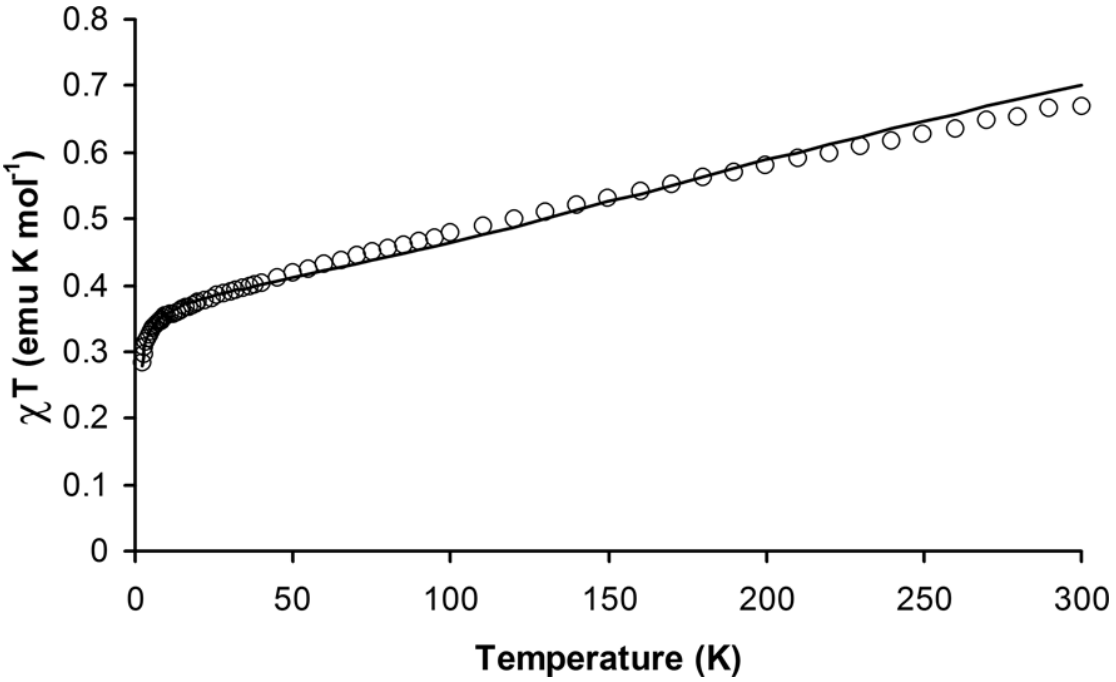

Figure 5.6 Temperature dependence of the χT product for **La**. The solid line is the best fit to a Heisenberg chain model with the Hamiltonian $H = -2J\Sigma S_i S_{i-1}$, and parameters: $J = -140$ cm^{-1}, g = 2.00.

The Brillouin function calculated for 1.12 of S_{total} = 1/2 and g = 2.02 fits well with the experimental data obtained by the measurement of the field-dependent magnetization at 1.8 K (Figure 5.7). These data indicate that, at low temperature, there is approximately one unpaired electron instead of three from the three $[TCNQF_4]^{\bullet-}$ radicals. Therefore, there are antiferromagnetic interactions between the uncoordinated $TCNQF_4$ units and the coordinated $TCNQF_4$ molecules involved in the π-π stacking. This interaction generates diamagnetic $[(TCNQF_4)_2]^{2-}$ dimers, whereas the other coordinated $TCNQF_4$ that is not involved in π-π interactions remains as a radical and is responsible for the observed behavior of an unpaired electron from the magnetic studies.

The room-temperature χT value of **Y** is 0.55 emu·mol^{-1}·K, which is lower than the expected value for a spin-only case of an uncoupled diamagnetic Y^{III} ion (χT = 0.00 emu·mol^{-1}·K) and three $[TCNQF_4]^{\bullet}$ (S = ½, χT = 0.375 emu·mol^{-1}·K) radicals (χT_{calc} = 1.12 emu·mol^{-1}·K). The room temperature χT value corresponds to ~1.5 $[TCNQF_4]^{\bullet}$ S = 1/2 radicals (χT = 0.56 emu·mol^{-1}·K).

These data indicate that, as in the case of **La**, there are considerable interactions between radicals even at room temperature. The χT value continuously decreases from the value observed at room temperature and reaches a minimum of 0.38 emu·mol^{-1}·K at 2 K which corresponds to the value of one unpaired electron (Figure 5.8). Equation 1 was used to calculate the interactions between radicals, as in the case of **La**, the results of which are estimated values of J = -230 cm^{-1}, g = 2.00.

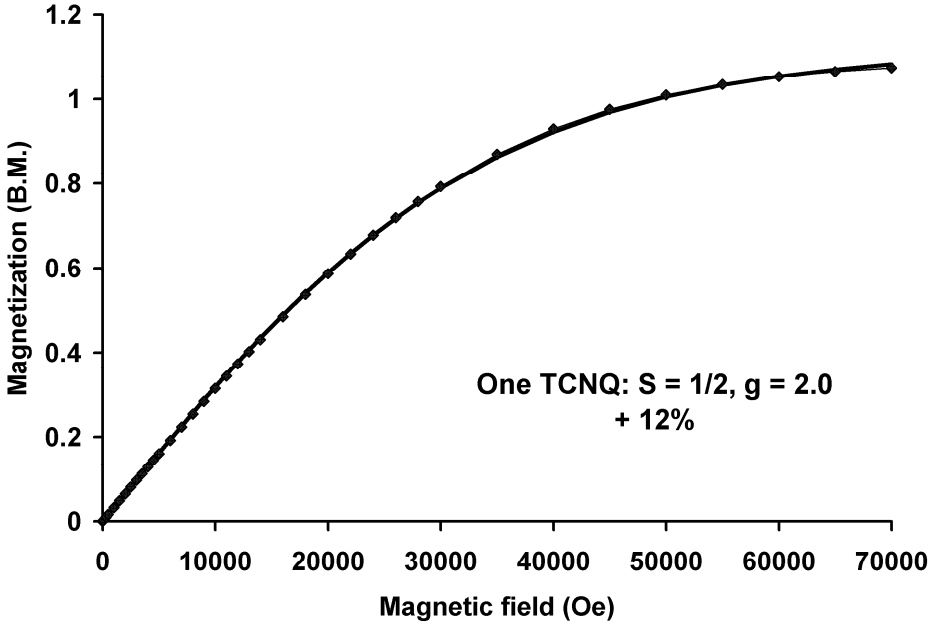

Figure 5.7 The field dependent magnetization of the **La** complex at 1.8 K, in the range of 0-7 T. The solid line is the Brillouin function fit with parameters of 1.12 S = ½ and g = 2.0.

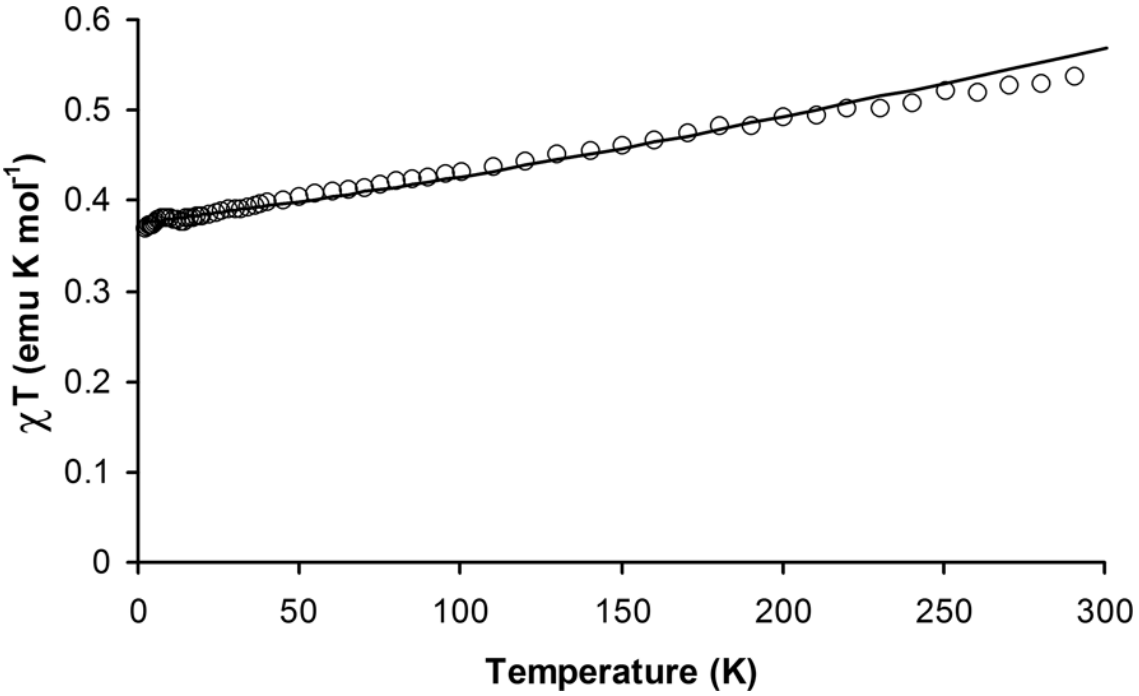

Figure 5.8 Temperature dependence of the χT product for **Y**. The solid line is the best fit to a Heisenberg chain model with the Hamiltonian $H = -2J\Sigma S_i S_{i-1}$, and parameters: J = -230 cm^{-1}, g = 2.00.

The Brillouin function calculated for S_{total} = 1/2 and g = 2.02 is in accord with the experimental data obtained by the field-dependent magnetization measurements at 1.8 K (Figure 5.9). The behavior of **La** is expected to apply to **Y**, as it is also composed of a diamagnetic ion, a Y^{III} ion, and three $TCNQF_4$ molecules. Thus, in the uncorrelated spin regime at room temperature, we expect to observe χT values close to the contributions of the lanthanide ion and either 2 or 1.5 unpaired electrons from $TCNQF_4$ units for the compounds isostructural to **La** and **Y** respectively.

The antiferromagnetic interactions are stronger for compound **Y**, as indicated by the estimated coupling values, due to the closer approach of the $TCNQF_4$ units in the stacks than found for compound **La**. It is noted that only 0.5 out of two unpaired electrons from the stacked $TCNQF_4$ units are accounted for at room temperature in compound **Y**, whereas there is approximately one unpaired electron out of two for compound **La**. Thus, the antiferromagnetic interactions are about twice as strong for compound **Y**; indeed the J values calculated from Equation 5.1 are -230 cm^{-1} for **Y** and -140 cm^{-1} for **La**. The similar stacking distance of $TCNQF_4$ units in the **La**-**Eu** series indicates similar antiferromagnetic interactions between the $TCNQF_4$ units and therefore 1.5 unpaired spins were accounted for the contribution to the room temperature χT value of $TCNQF_4$ units. An analogous observation was done for the **Gd**-**Y** series and two unpaired spins were accounted for the contribution to the room temperature χT value of $TCNQF_4$ units.

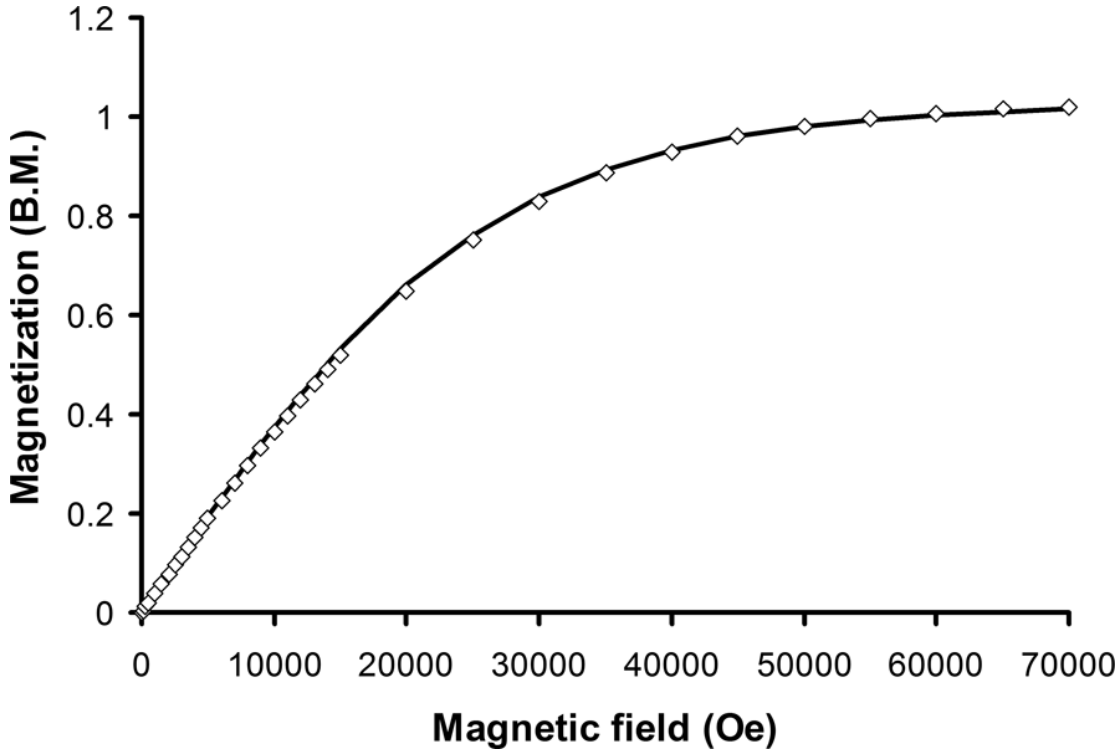

Figure 5.9 The field dependent magnetization of the **Y** complex at 1.8 K, in the range of 0-7 T. The solid line is the Brillouin function fit with parameters S = ½ and g = 2.02.

The room-temperature χT value for **Eu** is 2.41 emu·mol^{-1}·K, which is higher than the expected value for an uncoupled Eu^{III} ion ($^7F_0$, χT = 0.00 emu·mol^{-1}·K) and two $[TCNQF_4]^{\bullet}$ (S = ½, χT = 0.375 emu·mol^{-1}·K) radicals (χT_{calc} = 0.75 emu·mol^{-1}·K). The value continuously decreases as the temperature is lowered and reaches a minimum of 0.35 emu·mol^{-1}·K at 2 K, corresponding to approximately one unpaired electron attributed to the coordinated non-π-interacting $TCNQF_4$ ligand (The $^7F_0$ ground state of Eu^{III} ion is nonmagnetic) (Figure 5.5). The higher χT value at room temperature is likely due to the thermal population of excited states which is well documented for Eu complexes.[206]

The room-temperature χT value for **Sm** is 0.70 emu·mol^{-1}·K, which is slightly lower than the expected value for an uncoupled Sm^{III} ion ($^6H_{5/2}$, g_J = 2/7, χT = 0.09 emu·mol^{-1}·K) and two $[TCNQF_4]^{\bullet}$ (S = ½, χT = 0.375 emu·mol^{-1}·K) radicals (χT_{calc} = 0.84 emu·mol^{-1}·K). The value decreases as the temperature is lowered and reaches a minimum of 0.36 emu·mol^{-1}·K at 12 K, (Figure 5.5). Below 12 K, the χT value increases to reach a maximum of 0.64 emu·mol^{-1}·K at 4.5 K and decreases again, reaching a minimum of 0.45 emu·mol^{-1}·K at 2 K. A hysteresis loop was observed for the magnetization versus field measurement with a coercive field of 450 Oe and a remnant magnetization of 0.0240 μ_B (Figure 5.10).

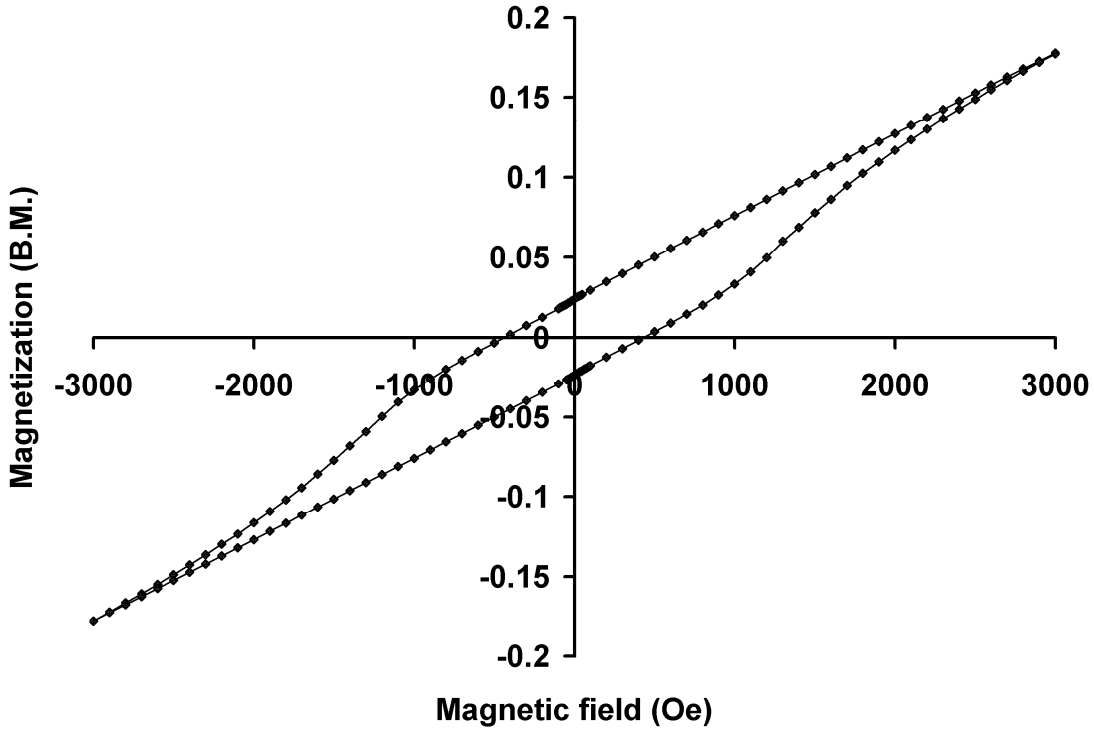

Figure 5.10 Hysteresis loop for the **Sm** complex.

The zero-field-cooled (ZFC) versus field-cooled (FC) magnetization data show a bifurcation at 4.5 K (Figure 5.11), which is indicative of a magnetic phase transition at that temperature.

The room-temperature χT value for **Gd** is 9.01 emu·mol^{-1}·K, which is higher than the expected value for an uncoupled Gd^{III} ion ($^8S_{7/2}$, $g_J = 2$, $\chi T = 7.88$ emu·mol^{-1}·K) and 1.5 $[TCNQF_4]^{\bullet}$ (S = ½, $\chi T = 0.375$ emu·mol^{-1}·K) radicals ($\chi T_{calc} = 8.44$ emu·mol^{-1}·K). The value decreases as the temperature is lowered and reaches a minimum of 8.22 emu·mol^{-1}·K at 12 K, (Figure 5.12). Below 12 K, the χT value increases to a maximum of 11.03 emu·mol^{-1}·K at 2 K. The data were fit by a combination of two models due to two magnetic pathways (Figure 5.12): The first one is the Heisenberg chain model for the π-stacked columns of $TCNQF_4$ units shown in the first part of equation 2.

The second pathway involves a chain of Gd ions and coordinated non-π interacting $TCNQF_4$ units where the $TCNQF_4$ is hydrogen bonded to the coordinated water molecule of the neighboring Gd complex at a N-O distance of 2.78 Å. The equation for this pathway is the ferrimagnetic isotropic chain model shown in equation 3:

$$\chi_0 = N_A\beta\frac{\mu_B^2}{6}\left[M^2\frac{1+P}{1-P} + \delta M^2\frac{1-P}{1+P}\right] \qquad (3)$$

where $P = \coth(\beta J) - (\beta J)^{-1}$; $M = M_a + M_b$; $\delta M = M_a - M_b$; $J \rightarrow J[S_a(S_a + 1)S_b(S_b + 1)]^{1/2}$; $M_i = g_i(S_i(S_i + 1))^{1/2}$ (i = a, b).[207]

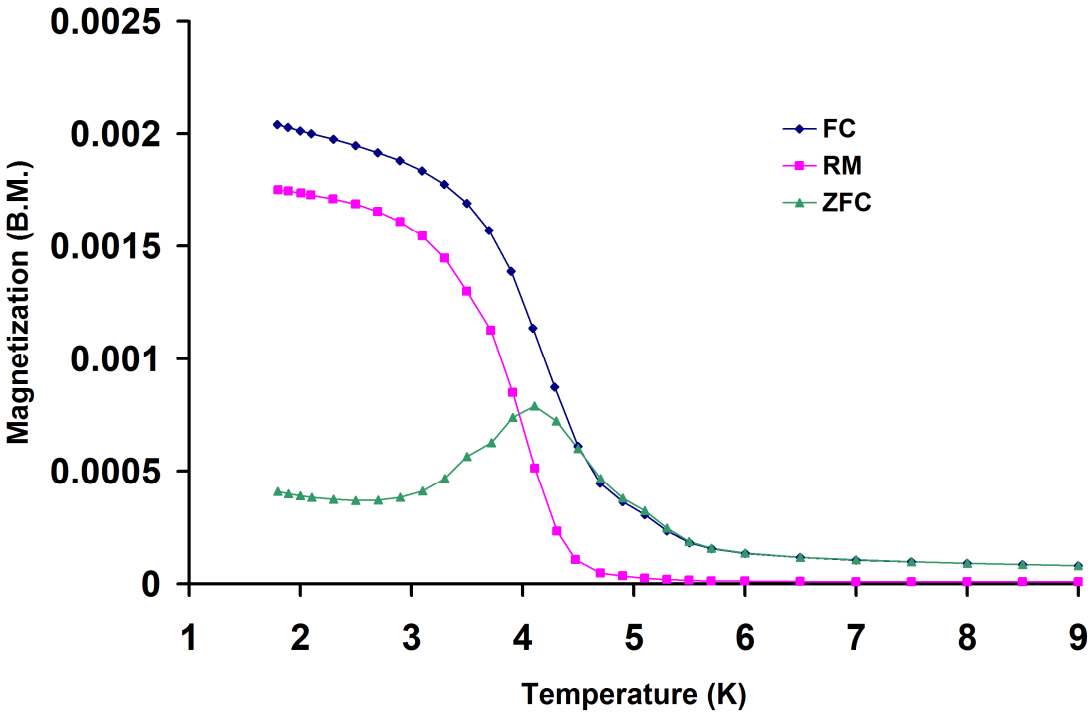

Figure 5.11 Field-cooled (FC), zero-field-cooled (ZFC) and remanent magnetization (RM) of the **Sm** complex.

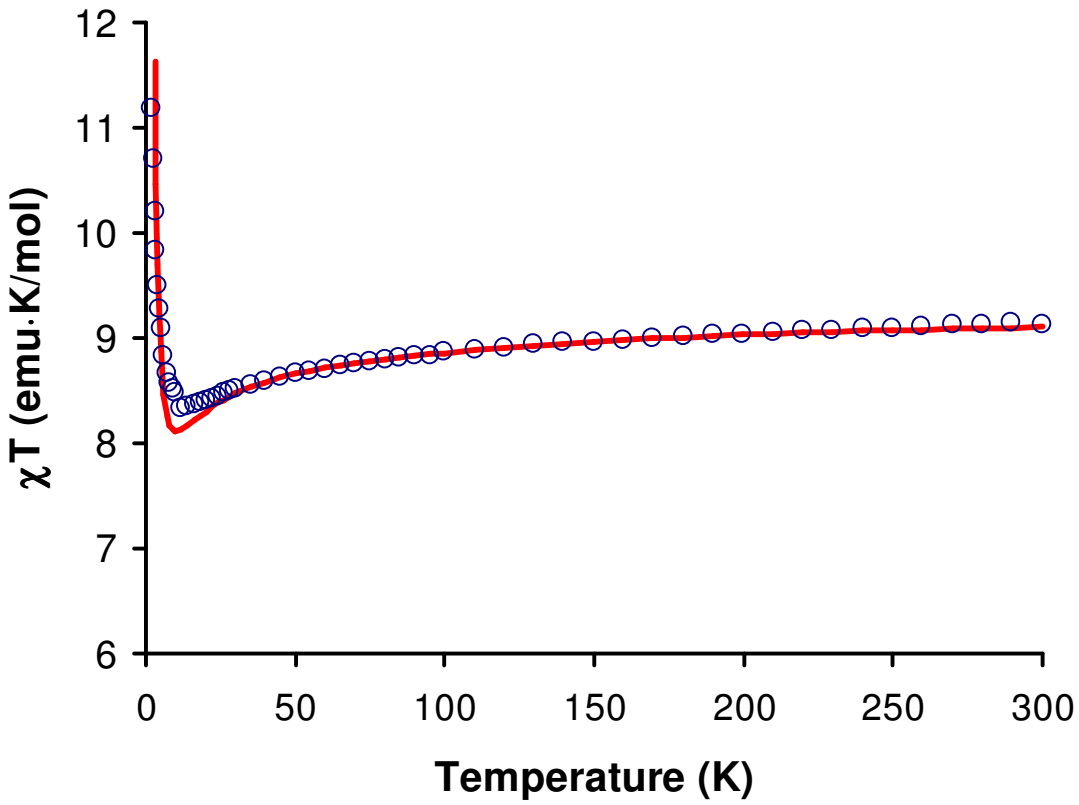

Figure 5.12 Temperature dependence of the χT product for **Gd**. The solid line is the best fit to a combination of a Heisenberg chain model (J_1 = -200 cm^{-1}, g = 2.00) and a ferromagnetic chain model (J_2 = -1.4 cm^{-1}, g = 2.00).

The interaction between the two magnetic pathways was considered to be negligible, which resulted in the use of a linear combination of the two models. In the case of lanthanide ions, the spin value (S) is no longer a good quantum number, instead one must use the total angular momentum (J) with g being replaced by g_J. The fitting results in the following parameters: isotropic g = 2.00 values for all the spin centers, J_1 = -200 cm^{-1} and J_2 = -1.4 cm^{-1} for the Heisenberg chain and the ferrimagnetic chain respectively. The Brillouin function calculated for the ground state of one Gd^{III} ion ($^8S_{7/2}$ and g_J = 2.00) and one unpaired electron from a $TCNQF_4$ anion is higher than the experimental data obtained by the measurement of the field-dependent magnetization at 1.8 K. The curve corresponds to the contribution of approximately one Gd^{III} ion only (Figure 5.13). Thus, these data indicate that there are antiferromagnetic interactions occurring between the non-π interacting coordinated $TCNQF_4$ units and the Gd^{III} ions. No hysteresis was observed for the **Gd** compound.

The room-temperature χT value for **Dy** is 14.31 emu·mol^{-1}·K, which is slightly lower than expected for an uncoupled Dy^{III} ion ($^6H_{15/2}$, g_J = 4/3, χT = 14.17 emu·mol^{-1}·K) and 1.5 $[TCNQF_4]^{-\bullet}$ (S = ½, χT = 0.375 emu·mol^{-1}·K) radicals (χT_{calc} = 14.73 emu·mol^{-1}·K). As the temperature is lowered from 300 to 30 K, the χT value decreases smoothly to 13.07 emu·mol^{-1}·K, and from 30 to 2 K the χT value rapidly decreases to 10.08 emu·mol^{-1}·K (Figure 5.5). A hysteresis loop was observed for the magnetization versus field measurement with a coercive field of 30 Oe and a remnant magnetization of 0.0204 μ_B (Figure 5.14).

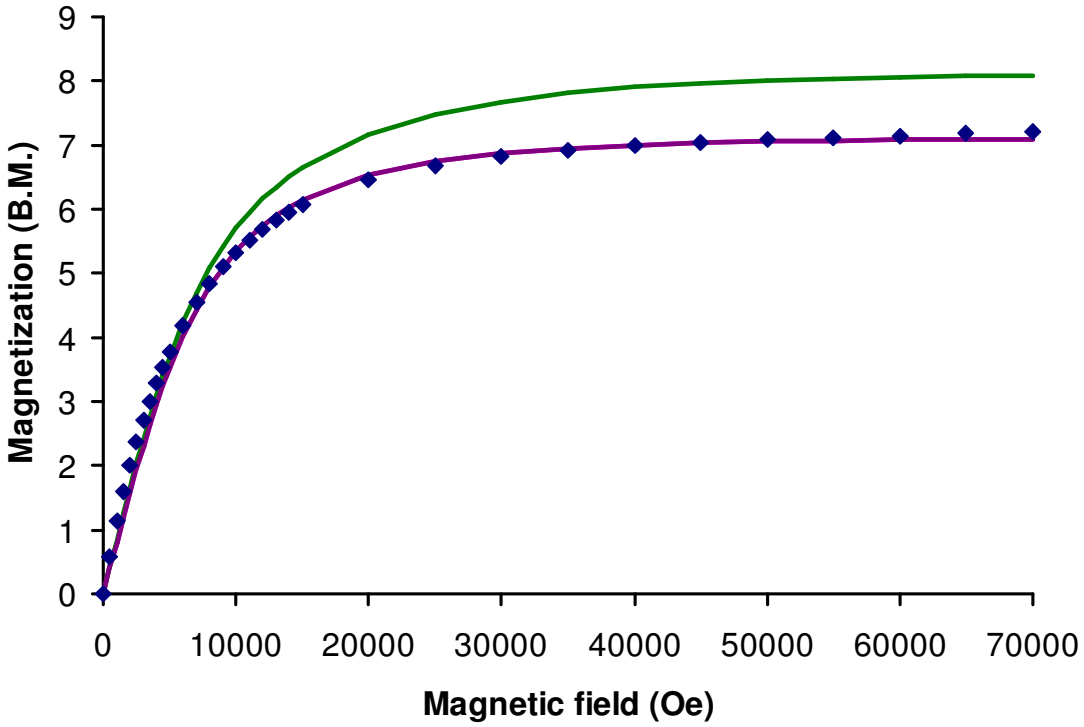

Figure 5.13 The field dependent magnetization of the **Gd** complex at 1.8 K, in the range of 0-7 T. The solid purple line is the Brillouin function fit with parameters for Gd^{III} ion $^8S_{7/2}$ and g_J = 2.00. The solid green line is the combined Brillouin function fit for one unpaired electron from the non-π interacting coordinated $TCNQF_4$ radical (S = ½, g = 2.00) and one Gd^{III} ion ($^8S_{7/2}$, g_J = 2.00).

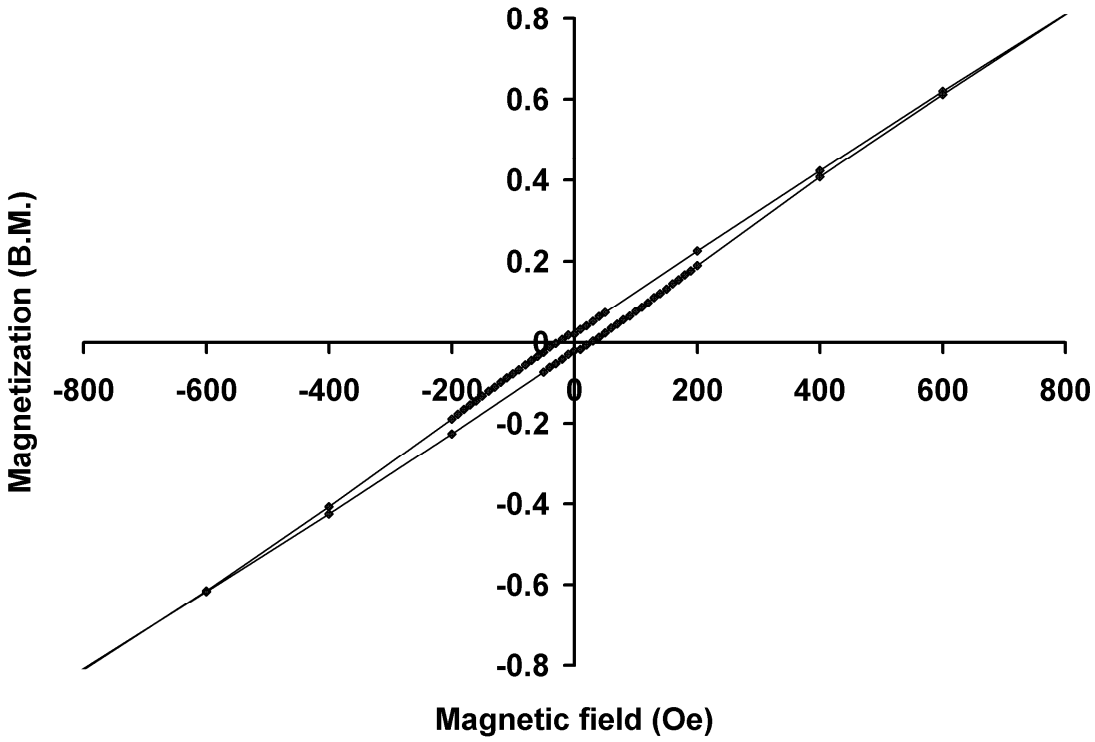

Figure 5.14 Hysteresis loop for the **Dy** complex.

The zero-field-cooled (ZFC) field-cooled (FC) magnetization data show a bifurcation at 4.7 K (Figure 5.15), which is indicative of magnetic ordering at that temperature.

The fact that the hysteresis loops are very narrow and the signals for the ZFC-FC studies are very weak indicate that only a small fraction of the sample is responsible for such behavior; we attribute this situation to partial loss of interstitial water molecules during the measurements which leads to small islands of an "impurity" material that has different magnetic pathways due to loss of solvent.

The observed and calculated room temperature χT values of the remaining compounds are summarized in Table 5.1.

Dynamic Magnetic Properties: Zero-field AC susceptibility measurements were performed in the range of frequencies from 10 to 1500 Hz at H_{AC} = 3 Oe. The **Sm** compound exhibits typical intensities for the AC signal corresponding to bulk magnetic ordering. Conversely, a very weak out-of-phase AC signal was observed for compounds **Gd** and **Dy** and no out-of-phase signal was observed for the remaining compounds. The maximum of the out-of-phase signal was observed at 4.4 K (**Sm**, Figure 5.16), 3.7 K (**Gd**, Figure 5.17), and 4.3 K (**Dy**, Figure 5.18) as shown in the corresponding figures. Thus, the AC magnetic studies indicate that **Sm** magnetically orders at 4.4 K but that only a small fraction of the **Gd** and **Dy** samples magnetically order at 3.7 K and 4.3 K, respectively due to partial removal of interstitial water molecules.

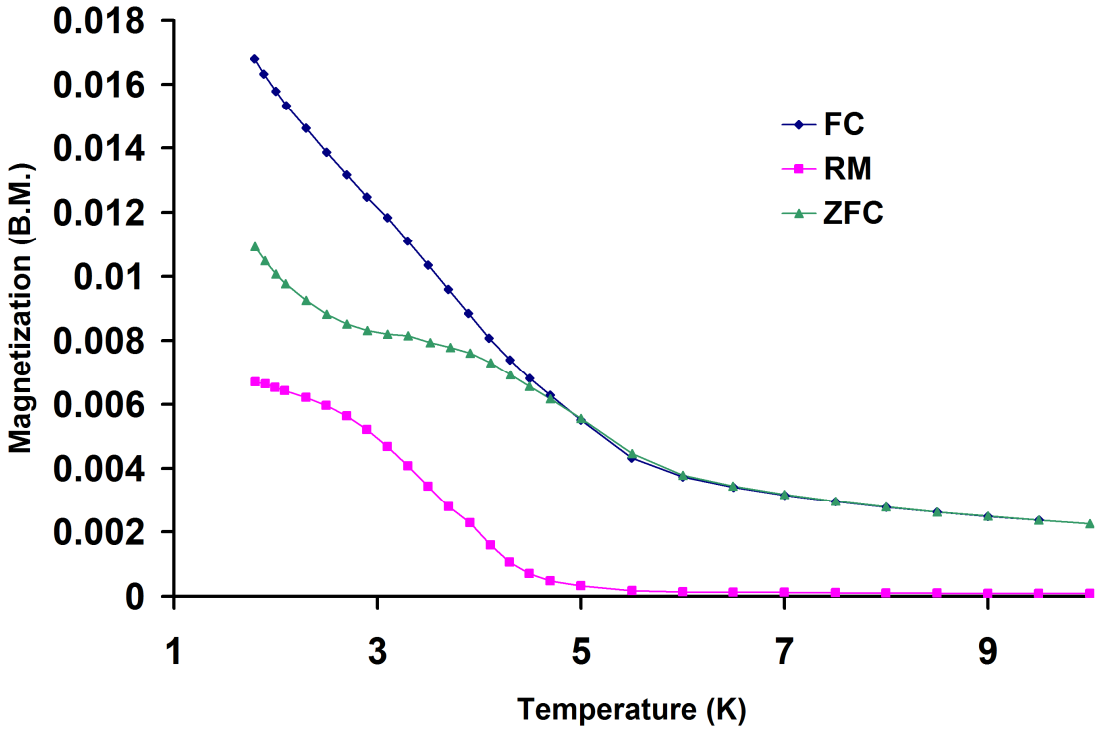

Figure 5.15 Field-cooled (FC), zero-field-cooled (ZFC) and remanent magnetization (RM) of the **Dy** complex.

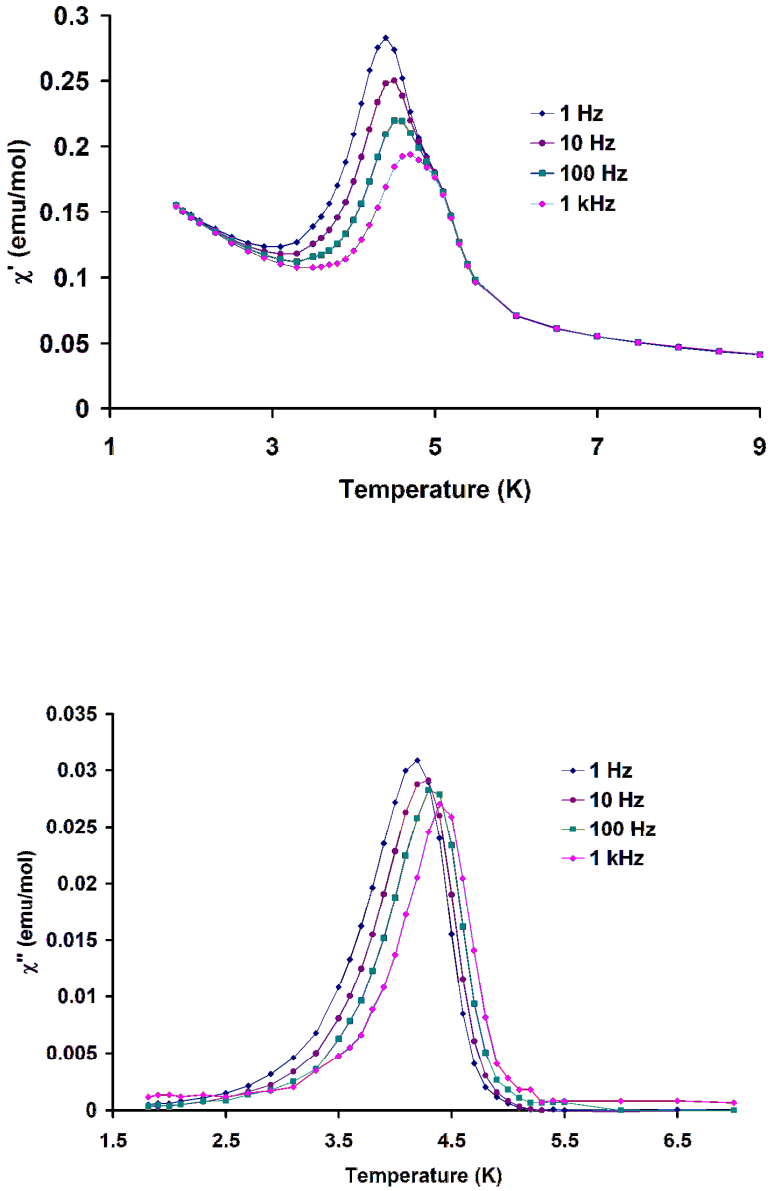

Figure 5.16 Temperature dependence of the real χ' and imaginary χ'' components of the AC magnetic susceptibility of the **Sm** complex measured in an oscillating field of 3 Oe at different frequencies.

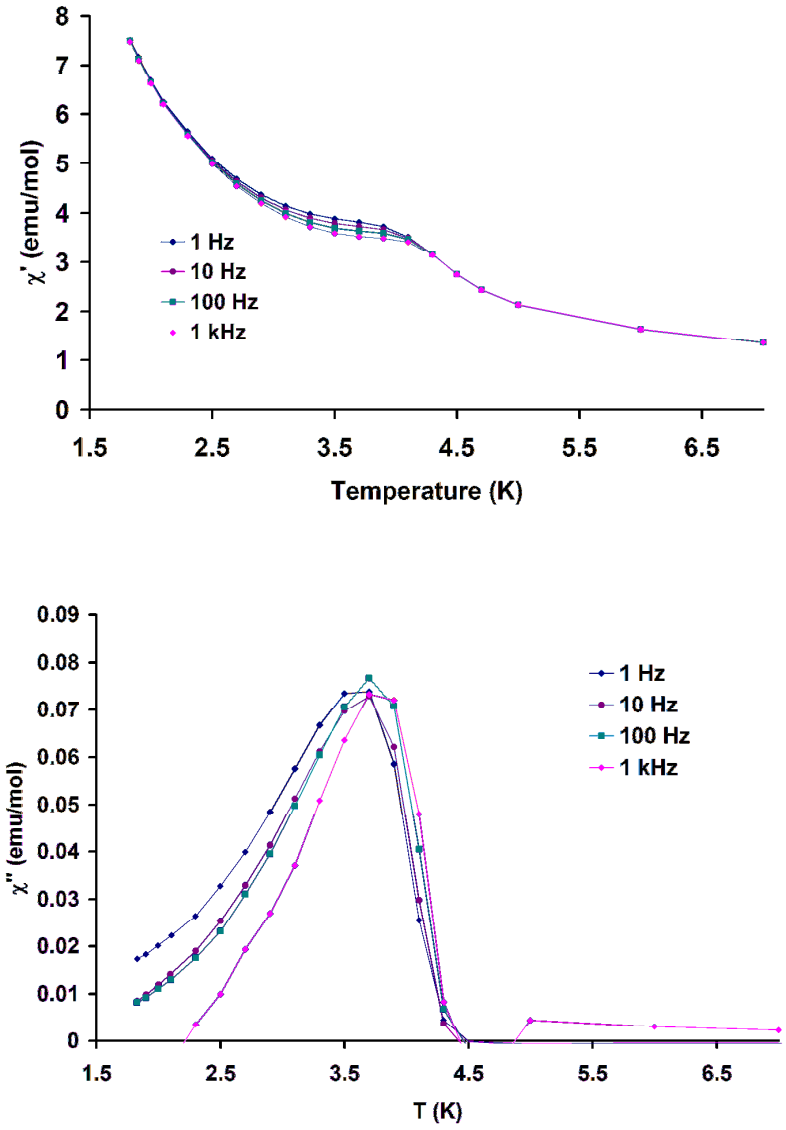

Figure 5.17 Temperature dependence of the real χ' and imaginary χ'' components of the AC magnetic susceptibility of the **Gd** complex measured in an oscillating field of 3 Oe at different frequencies.

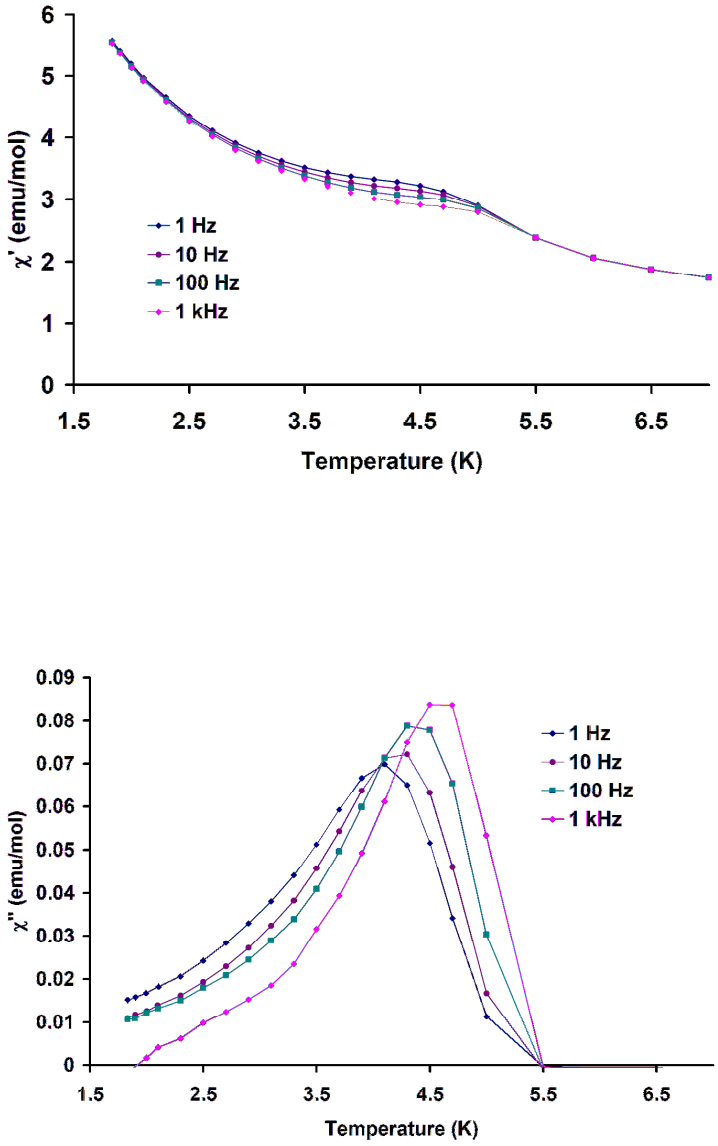

Figure 5.18 Temperature dependence of the real χ' and imaginary χ'' components of the AC magnetic susceptibility of the **Dy** complex measured in an oscillating field of 3 Oe at different frequencies.

Dilution Studies: AC susceptibility studies were performed on samples diluted with diamagnetic metal ions, namely $\mathbf{La_{0.8}Sm_{0.2}}$, $\mathbf{Y_{0.74}Gd_{0.26}}$, and $\mathbf{Y_{0.68}Dy_{0.32}}$. The compounds that had shown bulk (**Sm**) or partial (**Gd**, and **Dy**) magnetic ordering were selected for this study. The lanthanide ions were diluted with the metal ion of similar ionic radii, which resulted in formation of single crystals isostructural to the undiluted compounds. The percentage content of paramagnetic ions was 20%, 26%, and 32% for Sm, Gd, and Dy respectively. The zero-field AC susceptibility measurements were performed in the range of frequencies from 10 to 1500 Hz at H_{AC} = 3 Oe. No out-of-phase signal was observed for these compounds, which indicates an absence of magnetic ordering (Figure 5.19). It can be concluded, then, that the replacement of paramagnetic Ln ions with diamagnetic ions leads to a situation in which the already small portion of the original samples with paramagnetic nearest neighbors is reduced even further with dilution and these "impurities" of a desolvated ordered phase become undetectable.

MicroSQUID Studies: To further explore the magnetic behavior of **Dy** at very low temperatures a microSQUID apparatus was used to find the easy-axis of magnetization by the reported transverse field method.[182] It was found with this technique that all the easy-axes of the Dy ions are approximately aligned. From the packing diagram of Figure 5.3 one can see that all the Dy ions are arranged in columns that run parallel to the columns of the $TCNQF_4$ molecules. There are four different orientations of Dy ions (Figure 5.3), with two having the coordinated $TCNQF_4$ radical pointing up (red complexes) and two with it pointing down (blue complexes).

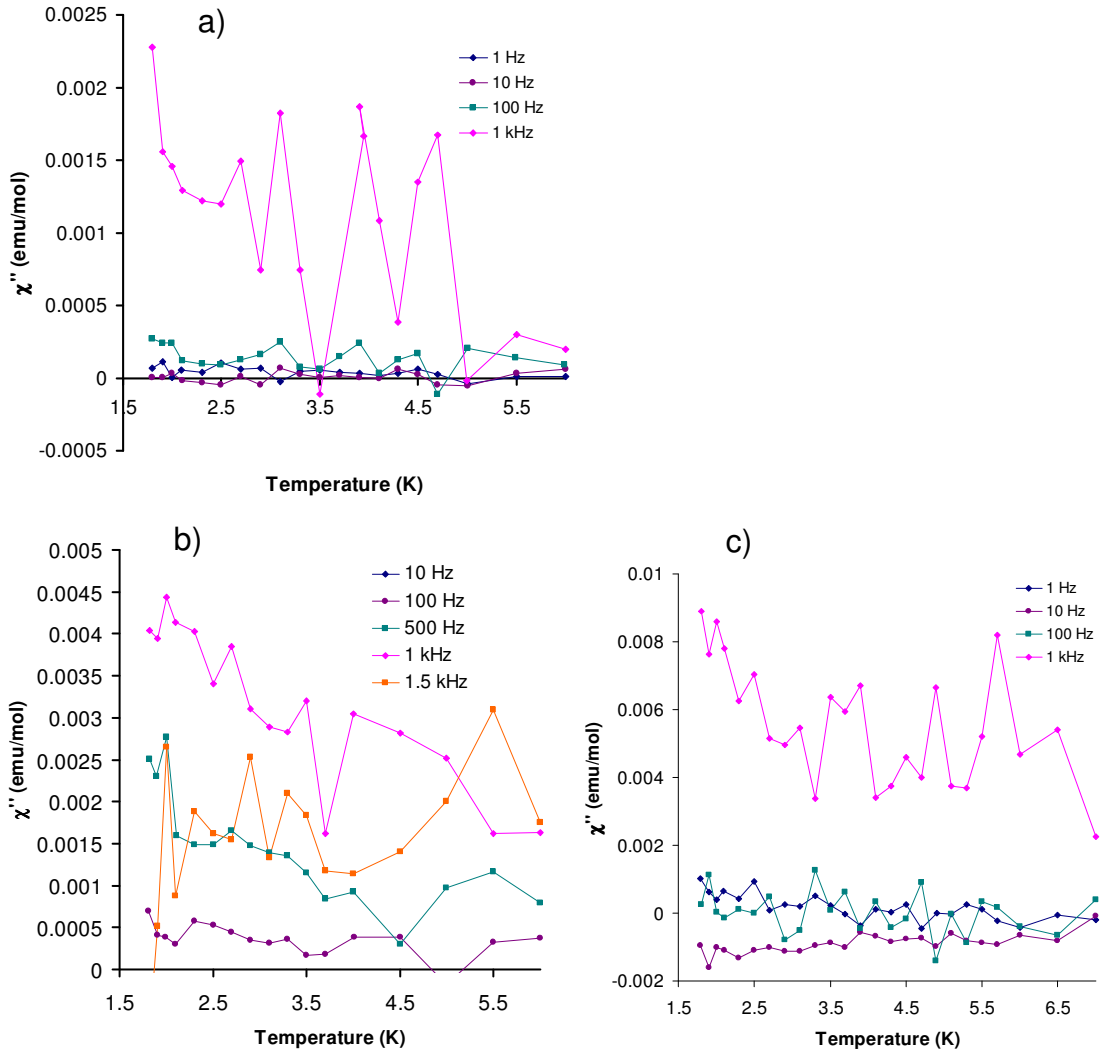

Figure 5.19 Temperature dependence of the imaginary χ'' component of the AC magnetic susceptibility for compounds $\mathbf{La_{0.8}Sm_{0.2}}$ (a), $\mathbf{Y_{0.74}Gd_{0.26}}$ (b), and $\mathbf{Y_{0.68}Dy_{0.32}}$ (c) measured in an oscillating field of 5 Oe at zero applied magnetic field.

They can all be approximated to having one easy axis that corresponds to the *a* axis, which is parallel to the columns of the stacked $TCNQF_4$ units. Hysteresis loops were collected on easy-axis oriented single-crystals. Magnetic ordering was not observed at temperatures higher than 40 mK as illustrated by the results of the microSQUID measurements performed at several temperatures from 40 mK to 1.1 K (Figure 5.20). We note that the microSQUID studies are performed at ambient atmosphere, thus the vacuum applied in the regular SQUID apparatus leads to partial removal of interstitial water molecules and consequently a small fraction of the sample exhibits magnetic ordering.

Conclusions

A homologous family of new lanthanide-$TCNQF_4$ molecular complexes was prepared and fully characterized by X-ray crystallography, infrared spectroscopy, and SQUID magnetometry. The family of compounds presented in this chapter adds valuable new information to the database of magnetism research on lanthanide/organic radical compounds. We have found that antiferromagnetic interactions occur between Gd^{III} ions and $TCNQF_4$ organic radicals, bulk magnetic ordering was observed for **Sm** and partial magnetic ordering was observed for the **Gd** and **Dy** compounds. The dilution with diamagnetic ions of the samples that exhibited ordering results in isolated paramagnets. The stability of the compounds and their solubility in most common organic solvents taken together with the large magnetic anisotropy make them promising candidates for use as heterospin paramagnetic building blocks. These studies are in progress and will be reported in due course.

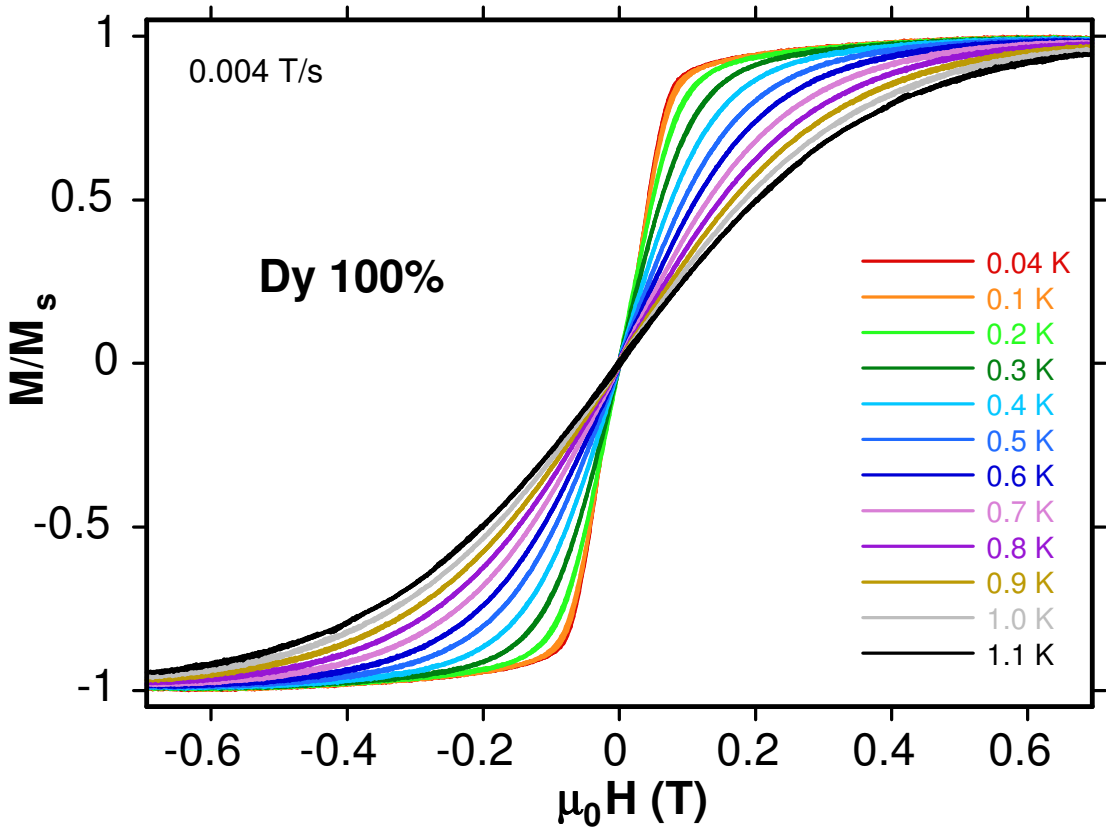

Figure 5.20 Micro-SQUID magnetization scans collected for **Dy** at temperatures from 0.04 K to 1.1 K at 0.004 T/s. Magnetization values are normalized to the magnetization value at 1.0 T.

Experimental Section

Materials: Starting materials were of reagent grade and used without further purification. Solvents were of HPLC grade. The $LnCl_3 \cdot 6H_2O$ starting materials were obtained from Aldrich (99.9%). The $TCNQF_4$ ligand and its reduced form, $Li[TCNQF_4]$ were prepared by literature procedures.[157a] All reactions were performed under an atmosphere of dry N_2 by Schlenk-line procedures. All solvents were dried by standard methods, distilled under nitrogen, and deoxygenated prior to use.

Physical Measurements: Infrared (IR) spectra were measured as Nujol mulls placed between KBr plates on a Nicolet 740 FTIR spectrometer. Magnetic measurements were performed on crushed polycrystalline samples with a Quantum Design SQUID magnetometer MPMS-XL. DC magnetic susceptibility measurements were carried out in an applied field of 1000 G over the temperature range of 2-300 K. AC magnetic susceptibility measurements were performed in a 3 G AC field in the frequency range of 1 - 1000 Hz. Magnetization data were measured at 1.8 K with the magnetic field varying from 0 to 7 Tesla. The data were corrected for diamagnetic contributions calculated from the Pascal constants. Elemental analyses were performed using a Perkin-Elmer 2400 CHN elemental analyzer by Atlantic Microlab Inc., P.O. Box 2288, Norcross, GA 30091.

X-ray Crystallography, **General Procedures:** In a typical experiment, a crystal selected for study was suspended in polybutene oil (Aldrich), mounted on a cryoloop and placed in an N_2 cold stream. Single-crystal X-ray data were collected at 110(1) K on a Bruker APEX or Bruker SMART 1000 diffractometer equipped with a CCD detector.

The data sets were recorded as three ω-scans of 606 frames each, at 0.3° step width, and integrated with the Bruker SAINT[146] software package. The absorption correction (SADABS)[147] was based on fitting a function to the empirical transmission surface as sampled by multiple equivalent measurements. Solution and refinement of the crystal structures was carried out using the SHELX[148] suite of programs and the graphical interface X-SEED.[149] Preliminary indexing of the data sets established two groups with similar monoclinic unit cells for all of the studied compounds. Systematic extinctions indicated the space group $P2_1/n$ for **La**, **Pr**, **Nd**, **Sm**, and $\mathbf{La_{0.8}Sm_{0.2}}$ and $P2_1/c$ for **Eu**, **Gd**, $\mathbf{Y_{0.74}Gd_{0.26}}$, **Dy**, $\mathbf{Y_{0.68}Dy_{0.32}}$, **Ho**, **Er**, **Yb**, and **Y**. All the structures were solved by direct methods which resolved the positions of the metal atoms and most of the C and N atoms. The remaining non-hydrogen atoms were located by alternating cycles of least-squares refinements and difference Fourier maps. Hydrogen atoms were placed at calculated positions. The final refinements were carried out with anisotropic thermal parameters for all non-hydrogen atoms with exception of the solvent molecules which were refined using isotropic thermal parameters. A summary of pertinent information relating to unit cell parameters is provided in Table 5.2. CCDC 749360-749371, 669348, and 699042 contain the supplementary crystallographic data for this chapter. These data can be obtained free of charge from the Cambridge Crystallographic Data Centre via www.ccdc.cam.ac.uk/data_request/cif.

Syntheses: $\mathbf{\{M[TCNQF_4]_2[H_2O]_{\mathit{x}}\}\cdot(TCNQF_4)(3H_2O)}$ In a typical preparation, an aqueous solution of 1 equivalent of $Li[TCNQF_4]$ (0.2 mmol, 15 ml) was layered on top of an aqueous solution of 1 equivalent of the metal salt (0.2 mmol, 5ml) in degassed

water and the mixture was left to stand undisturbed for 2 to 3 days. After this period of time, X-ray-quality block-shaped crystals were harvested by filtration, washed with copious quantities of water, and dried under a stream of nitrogen. M: La, Pr, Nd, Sm, $La_{0.8}Sm_{0.2}$, Eu, Gd, $Y_{0.74}Gd_{0.26}$, Dy, $Y_{0.68}Dy_{0.32}$, Ho, Er, Yb, and Y. C, H, N, O, analysis (%) calcd for $C_{36}H_8N_{12}O_4F_{12}La_1$ (**La**): C 41.60, H 0.78, N 16.17, O 6.16; found C 41.74, H 0.61, N 16.19, O 6.07. Calcd (%) $C_{36}H_{20}O_{10}N_{12}F_{12}Pr_1$ (**Pr**): C 37.60, H 1.75, N 14.62, O 13.92, F 19.84; found C 38.41, H 1.50, N 15.23, O 10.42, F 18.27. Calcd (%) $C_{36}H_{20}O_{10}N_{12}F_{12}Nd_1$ (**Nd**): C 37.56, H 1.75, N 14.61, O 13.91, F 19.82; found C 38.24, H 1.50, N 15.14, O 11.75, F 18.53. Calcd (%) $C_{36}H_{14}O_7N_{12}F_{12}Sm_1$ (**Sm**): C 39.13, H 1.27, N 15.21, O 10.14, F 20.63; found C 38.72, H 1.18, N 15.08, O 10.60, F 19.96. Calcd (%) $C_{36}H_{20}O_{10}N_{12}F_{12}Eu_1$ (**Eu**): C 37.21, H 1.74, N 14.47, O 13.78, F 19.64; found C 37.71, H 1.60, N 14.81, O 12.78, F 17.94. Calcd (%) $C_{36}H_{18}O_9N_{12}F_{12}Gd_1$ (**Gd**): C 37.67, H 1.58, N 14.64, O 12.54, F 19.86; found C 37.73, H 1.42, N 14.57, O 12.44, F 19.89. Calcd (%) $C_{36}H_{18}O_9N_{12}F_{12}Dy_1$ (**Dy**): C 37.50, H 1.57, N 14.58, O 12.49, F 19.77; found C 37.34, H 1.39, N 14.44, O 12.19, F 19.49. Calcd (%) $C_{36}H_{18}O_9N_{12}F_{12}Y_{0.74}Dy_{0.26}$ (**$Y_{0.68}Dy_{0.32}$**): C 39.20, H 1.64, N 15.24, O 13.05, F 20.67; found C 39.15, H 1.53, N 15.25, O 13.20, F 20.47. Calcd (%) $C_{36}H_{18}O_9N_{12}F_{12}Ho_1$ (**Ho**): C 37.42, H 1.57, O 12.46; found C 37.76, H 1.56, O 12.25. Calcd (%) $C_{36}H_{18}N_{12}O_9F_{12}Er_1$ (**Er**): C 37.34, H 1.57, N 14.52, O 12.44, F 19.69; found: C 37.34, H 1.46, N 14.55, O 12.16, F 19.43. Calcd (%) $C_{36}H_{18}O_9N_{12}F_{12}Yb_1$ (**Yb**): C 37.16, H 1.56, N 14.44, O 12.37 F 19.59; found: C 37.05, H 1.42, N 14.53, O 12.43, F 19.46. Calcd (%) $C_{36}H_{18}N_{12}O_9F_{12}Y_1$ (**Y**): C 40.05, H 1.68, N

15.57, O 13.34, F 21.11; found C 39.96, H 1.68, N 15.51, O 13.14, F 20.93. The infrared data are listed in Table 5.1.

CHAPTER VI

LANTHANIDE-3D CYANOMETALLATE CHAINS WITH THE TRIDENTATE LIGAND 2,4,6-TRI(2-PYRIDYL)-1,3,5-TRIAZINE (TPTZ): EVIDENCE FOR FERROMAGNETIC INTERACTIONS FOR THE SM(III)-M(III) COMPOUNDS (M = FE, CR) AND THE ISOLATION OF A POROUS NANOTUBE*

Introduction

Research aimed at designing multi-dimensional cyanide-bridged bimetallic assemblies of transition metals with interesting architectures and magnetic properties has been increasing in recent years.[58a,208,209] Conversely, analogous efforts with rare-earth ions have been comparatively fewer,[210] despite the rather large anisotropic magnetic moments inherent to most lanthanide(III) ions. This lack of attention is attributed to the relatively weak interactions between lanthanide ions, due to the effective shielding by the outer-shell electrons, which may be enhanced, however, when the f electrons interact with the more expanded d electrons of transition metal ions.[187] The most well investigated compounds with magnetically coupled 4f-3d block ions are Gd(III)-Cu(II) or Gd(III)-organic radical systems.[187] Recently, various cyanide bridged networks comprising 4f ions and polycyanometallates[211] have been studied, including 3-D arrays of Fe(III),

---

Reprinted in part with permission from *Dalton Transactions,* H. Zhao, N. Lopez, A. V. Prosvirin, H. T. Chifotides, K. R. Dunbar, "*Lanthanide–3d cyanometalate chains Ln(III)–M(III) (Ln = Pr, Nd, Sm, Eu, Gd, Tb; M = Fe) with the tridentate ligand 2,4,6-tri(2-pyridyl)-1,3,5-triazine (tptz): evidence of ferromagnetic interactions for the Sm(III)–M(III) compounds (M = Fe, Cr)*," **2007**, 878-888.

Co(III), Cr(III),[212,213] 2-D structures of Cr(III) and Fe(III),[214-216] and 1-D structures of Fe(III), Co(III), Cr(III) and Mn(III)[217-229] as well as those of the diamagnetic ions $[M(CN)_4]^{2-}$ (M = Ni, Pd, Pt).[230-234] Compounds with three spin carriers including a rare earth ion[235,236] and discrete 3d-4f molecular complexes[222,237-240] have also shown promising magnetic or photo-induced magnetic behavior.[241,242] The quest for molecules or molecular chains that exhibit slow paramagnetic relaxation, referred to 'single molecule magnets' or 'single chain magnets' respectively, has fueled increasing interest in lanthanide ions as components of molecular materials. Although the field is still in its nascence, a number of lanthanide containing 'single molecule magnets'[167a,243-254] and 'single chain magnets',[171,255,256] have been reported which indicate promising possibilities for this research. Herein, we report the preparation of a series of cyanide-bridged mixed chain compounds Ln(III)/Fe(III) (Ln = Pr, Nd, Sm, Eu, Gd, Tb) with the tridentate ligand 2,4,6-tri (2-pyridyl)-1,3,5-triazine (tptz; Chart 6.1a)[257-259] as a capping group for compounds of composition $\{[Pr(tptz)(H_2O)_4Fe(CN)_6]\cdot 8H_2O\}_\infty$ (**PrFe**), $\{[Nd(tptz)(H_2O)_4Fe(CN)_6]\cdot 8H_2O\}_\infty$ (**NdFe**), $\{[Sm(tptz)(H_2O)_4Fe(CN)_6]\cdot 8H_2O\}_\infty$ (**SmFe**), $\{[Eu(tptz)(H_2O)_4Fe(CN)_6]\cdot 6H_2O\}_\infty$ (**EuFe**), $\{[Gd(tptz)(H_2O)_4Fe(CN)_6]\cdot 6H_2O\}_\infty$ (**GdFe**), and $\{[Tb(tptz)(H_2O)_4Fe(CN)_6]\cdot 8H_2O\}_\infty$ (**TbFe**). The present homologous series of 3d-4f transition metal chain compounds provides an opportunity to correlate 1-D magnetic behavior with the corresponding structural frameworks. To compare the magnetic behavior of the tptz Sm(III)/Fe(III) complex **SmFe**, the cyanide-bridged Sm(III)/Fe(III) and Sm(III)/Cr(III) chain compounds with the bidentate ligand 3,4,7,8-tetramethyl-1,10-phenanthroline (tmphen; Chart 6.1b) were also prepared.

Chart 6.1 Structures of the ligands tptz and tmphen.

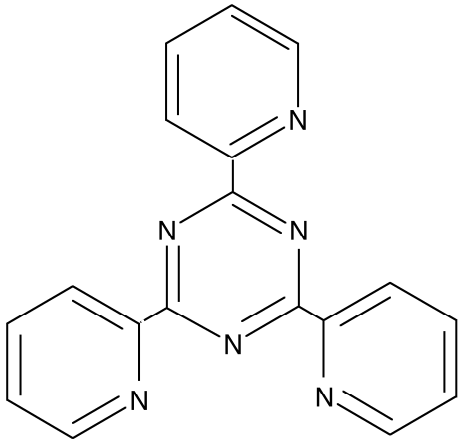

(a) tptz

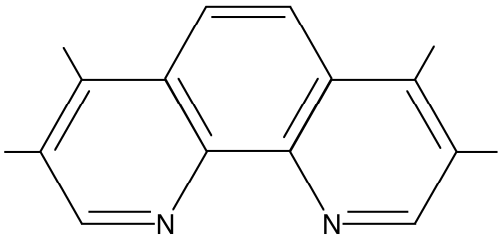

(b) tmphen

It also reported that during the course of these studies a supramolecular nanotube was identified by single crystal diffraction studies. The nanotube of formula $\{[Pr(tptz)(HCOO)_3]\cdot 2.5H_2O\}_\infty$ was first serendipitously isolated in low yields from $Pr(tptz)(Cl)_3$ in the solvent DMF which generate small amounts of formate ions. Subsequently a second example of the nanotube material was synthesized in high yield by combining $Sm(tptz)(H_2O)_3(triflate)_3$ with formate ions in methanol. The crystal structure revealed that, in the solid state, there are tubes with 1D internal channels for the tubes themselves as well as an additional 1D channels generated by the infinite network of π interactions between tptz units from adjacent nanotubes. The packing of the tubes affords two types of channels of different sizes (3.3 Å and 6.9 Å after subtraction of van der Waals radii) in a hexagonal honeycomb arrangement.

Results and Discussion

Syntheses and Properties: In the case of most reported examples of chain compounds containing cyano-bridged 3d-4f paramagnetic transition metal ions, the coordination sphere of the lanthanide ion consists of two molecules of a bidentate blocking ligand (e.g, bpy[224,225,228,260]) or solvent molecules such as DMF or water.[213] For the compounds reported in this chapter, the lanthanide ions are coordinated to three nitrogen atoms of the tridentate ligand, 2,4,6-tri (2-pyridyl)-1,3,5-triazine (tptz) which act as capping groups. Initially, the lanthanide nitrate salts $Ln(NO_3)_3\cdot 6H_2O$ (Ln = Pr, Nd, Sm, Eu, Gd, Tb) are reacted with tptz to produce the complexes $Ln(tptz)(solvent)_n$. Similar compounds with acetate ligands have been reported and characterized by single crystal

X-ray diffraction.[257] The compounds Ln(tptz)(solvent)$_n$ (Ln = Pr, Nd, Sm, Eu, Gd, Tb) are then reacted with $K_3Fe(CN)_6$ to produce the mixed Fe(III)/Ln(III) cyanide-bridged chain compounds. If the $SmCl_3$ solution is layered with the tmphen ligand dissolved in a mixed MeOH/DMF solvent system, the 1:1 Sm:tmphen based chain $Sm(tmphen)(DMF)_3(H_2O)Fe(CN)_6]\cdot 2H_2O\}_\infty$ (**DMF-L$_2$SmFe**), is formed, whereas in the presence of MeOH only, the 1:2 Sm:tmphen containing products $\{[Sm(tmphen)_2(H_2O)_2Fe(CN)_6]\cdot MeOH\cdot 13H_2O\}_\infty$ (**L$_2$SmFe**) and $\{[Sm(tmphen)_2(H_2O)_2$-$Cr(CN)_6]\cdot MeOH\cdot 9H_2O\}_\infty$ (**L$_2$SmCr**) are formed (L_2 = tmphen). These compounds are air-stable, but interstitial solvent molecules are easily lost when the crystals are dried under vacuum (the elemental analysis results reflect the solvent loss issue). The IR spectra of the complexes exhibit two or three sharp features in the range 2100-2200 cm^{-1}, which are attributed to the ν(C≡N) stretching modes. The presence of several ν(C≡N) stretches supports the presence of both bridging and dangling CN ligands.

X-ray Crystallography: The thermal ellipsoid plots of $\{[Sm(tptz)(H_2O)_4Fe(CN)_6]\cdot 8H_2O\}_\infty$ (**SmFe**), $\{[Sm(tmphen)(DMF)_3(H_2O)Fe(CN)_6]$-$\cdot 2H_2O\}_\infty$ (**DMF-L$_2$SmFe**), $\{[Sm(tmphen)_2(H_2O)_2Fe(CN)_6]\cdot MeOH\cdot 13H_2O\}_\infty$ (**L$_2$SmFe**) and $\{[Sm(tmphen)_2(H_2O)_2Cr(CN)_6]\cdot MeOH\cdot 9H_2O\}_\infty$ (**L$_2$SmCr**) are shown in Figures 6.1, 6.2, 6.3, and 6.4, respectively. Isostructural crystals of $\{[Ln(tptz)(H_2O)_4M(CN)_6]\cdot 8H_2O\}_\infty$ (Ln = Pr, Nd, Sm, Eu, Gd, Tb; M = Fe), **SmCo**, and **LaFe** are monoclinic and belong to the space group *C2/c*. Crystals of **DMF-L$_2$SmFe** and **L$_2$SmCr** are triclinic and belong to the space group *P-1*. Crystals of **L$_2$SmFe** are monoclinic and crystallize in the space group $P2_1/c$. The extended structures of **SmFe**, **SmCo**, **DMF-L$_2$SmFe**, **L$_2$SmFe**, and

L_2SmCr are shown in Figures 6.5, 6.6, 6.7, 6.8, and 6.9, respectively. The crystal parameters and information pertaining to the data collection and refinement for the crystals are summarized in Tables 6.1-6.4. Selected bond distances and angles are provided in Tables 6.5-6.9.

Compounds **LnFe** (Ln = Pr, Nd, Sm, Eu, Gd, and Tb) and **SmCo** comprise chains of cyanide trans-bridged alternating arrays of $M(CN)_6$ and $Ln(tptz)(H_2O)_4$ fragments. The Ln (Ln = Pr, Nd, Sm, Eu, Gd, and Tb) ion is nine-coordinate; each 2,4,6-tri (2-pyridyl)-1,3,5-triazine (tptz) ligand chelates through three nitrogen atoms, with the Ln(III) coordination sphere being completed by two bridging cyanide ligands and four water molecules. The Ln-N distances to the nitrogen atoms of tptz in **LnFe** (Ln = Pr, Nd, Sm, Eu, Gd, and Tb) are in the range 2.486-2.683 Å. The average Ln-N bond length slightly decreases on going from the Pr to the Tb compound. Two bridging cyanides are coordinated to the Ln(III) ions in these structures. One cyanide bridge is nearly linear with bond angles of C(1)-N(1)-Ln(1) in the range 169.9-171.4° with N(1)-Ln(1) distances spanning 2.566-2.473 Å, whereas the other cyanide forms a bent interaction with bond angles of C(2)-N(2)-Ln(1) in the range 147.1-149.7° and distances N(2)-Ln(1) between 2.536 and 2.487 Å.

Table 6.1 Crystallographic data and structural refinement parameters for $\{[Pr(tptz)(H_2O)_4Fe(CN)_6]\cdot 8H_2O\}_\infty$ (**PrFe**), $\{[Nd(tptz)(H_2O)_4Fe(CN)_6]\cdot 8H_2O\}_\infty$ (**NdFe**) and $\{[Sm(tptz)(H_2O)_4Fe(CN)_6]\cdot 8H_2O\}_\infty$ (**SmFe**).

	PrFe	**NdFe**	**SmFe**
Formula	$C_{24}H_{36}N_{12}O_{12}FePr$	$C_{24}H_{36}N_{12}O_{12}FeNd$	$C_{24}H_{36}N_{12}O_{12}FeSm$
Formula weight	881.41	884.74	890.85
Space group	*C2/c*	*C2/c*	*C2/c*
T (K)	110	110	110
a (Å)	16.036(3)	15.927(3)	15.897(3)
b (Å)	14.195(3)	14.139(3)	14.130(3)
c (Å)	31.546(6)	31.462(6)	31.522(6)
α (°)	90.00	90.00	90.00
β (°)	103.22(3)	103.18(3)	103.19(3)
γ (°)	90.00	90.00	90.00
V (Å^3)	6991(2)	6898(2)	6894(2)
Z	8	8	8
Description, color	yellow block	yellow prism	yellow plate
Crystal size (mm^3)	0.16 x 0.13 x 0.10	0.14 x 0.13 x 0.08	0.18 x 0.06 x 0.02
λ (Å)	0.71073	0.71073	0.71073
D_{calc} (g cm^{-3})	1.675	1.704	1.717
μ (cm^{-1})	1.867	1.985	2.183
F(000)	3560	3568	3584
θ range (°)	1.94 to 28.28	1.95 to 28.27	2.52 to 28.28
Reflections collected	20562	19961	20560
Diffraction limits (h, k, l)	$-20 < h < 19$, $-16 < k < 17$, $-41 < l < 27$	$-16 < h < 20$, $-17 < k < 18$, $-38 < l < 40$	$-21 < h < 21$, $-17 < k < 17$, $-40 < l < 23$
Independent reflections	7923 [R(int) = 0.0395]	7907 [R(int) = 0.0599]	7815 [R(int) = 0.0374]
Observed data [$I > 2\sigma(I)$]	6579	6564	6122
Completeness to θ_{max} (%)	91.1	92.3	91.3
Data/parameters/restraints	7923/446/0	7907/451/0	7815/451/0
R^a, wR^b *(I>2σ(I))*	0.0587, 0.1305	0.0752.0.1708	0.0639/0.1571
R^a, wR^b *(all data)*	0.0729, 0.1375	0.0904/0.1787	0.0822/0.1711
Goodness of fit parameter (F^2)^c	1.088	1.111	1.055
Largest diff. peak and hole (e Å^{-3})	1.298 and -2.125	2.780 and -2.921	2.244 and -1.535

[a] $R = \Sigma \left| \left| F_o \right| - \left| F_c \right| \right| / \Sigma \left| F_o \right|$.

[b] $wR = \{\Sigma [w(F_o^2 - F_c^2)^2] / \Sigma w(F_o^2)^2]\}^{1/2}$.

[c] Goodness-of-fit = $\{\Sigma [w(F_o^2 - F_c^2)^2] / (n-p)\}^{1/2}$, where n is the number of reflections and p is the total number of parameters refined.

Table 6.2 Crystallographic data and structural refinement parameters for $\{[Eu(tptz)(H_2O)_4Fe(CN)_6]\cdot 6H_2O\}_\infty$ (**EuFe**), $\{[Gd(tptz)(H_2O)_4Fe(CN)_6]\cdot 6H_2O\}_\infty$ (**GdFe**) and $\{[Tb(tptz)(H_2O)_4Fe(CN)_6]\cdot 8H_2O\}_\infty$ (**TbFe**).

	EuFe	**GdFe**	**TbFe**
Formula	$C_{24}H_{32}N_{12}O_{10}FeEu$	$C_{24}H_{32}N_{12}O_{10}FeGd$	$C_{24}H_{36}N_{12}O_{12}FeTb$
Formula weight	856.43	861.72	899.42
Space group	*C2/c*	*C2/c*	*C2/c*
T (K)	110	110	110
a (Å)	16.067(3)	16.074(4)	15.951(4)
b (Å)	14.056(3)	14.072(4)	14.086(4)
c (Å)	31.350(6)	31.417(8)	31.266(8)
α (°)	90.00	90.00	90.00
β (°)	103.34(3)	103.383(4)	103.017(4)
γ (°)	90.00	90.00	90.00
V (Å^3)	6889(2)	6913(3)	6844(3)
Z	8	8	8
Description, color	yellow prism	yellow block	yellow plate
Crystal size (mm^3)	0.15 x 0.14 x 0.11	0.11 x 0.10 x 0.07	0.10 x 0.10 x 0.03
λ (Å)	0.71073	0.71073	0.71073
D_{calc} (g cm^{-3})	1.651	1.655	1.745
μ (cm^{-1})	2.293	2.389	2.550
F(000)	3432	3440	3608
θ range (°)	1.95 to 28.40	2.15 to 27.50	2.53 to 27.61
Diffraction limits (h, k, l)	$-20 < h < 19$, $-16 < k < 17$ $-41 < l < 27$	$-20 < h < 20$, $-18 < k < 18$ $-18 < l < 40$	$-20 < h < 11$, $-18 < k < 18$ $-32 < l < 39$
Reflections collected	27567	20278	20122
Independent reflections	7986 [R(int) = 0.0501]	7671 [R(int) = 0.0947]	7611 [R(int) = 0.0500]
Observed data [$I > 2\sigma(I)$]	6863	4676	6024
Completeness to θ_{max} (%)	92.2	96.9	95.7
Data/parameters/restraints	7986/424/0	7671/433/0	7611/451/0
R^a, wR^b *(I>2σ(I))*	0.0617, 0.1502	0.0716, 0.1727	0.0619, 0.1339
R^a, wR^b *(all data)*	0.0728, 0.1559	0.1288, 0.1947	0.829, 0.1425
Doodness-of-fit[c] on F^2	1.186	1.046	1.088
Largest diff. peak and hole (e Å^{-3})	2.528 and -2.303	2.119 and -1.319	1.830 and -2.146

[a] $R = \Sigma \left| \left| F_o \right| - \left| F_c \right| \right| / \Sigma \left| F_o \right|$.

[b] $wR = \{\Sigma [w(F_o^2 - F_c^2)^2] / \Sigma w(F_o^2)^2]\}^{1/2}$.

[c] Goodness-of-fit = $\{\Sigma [w(F_o^2 - F_c^2)^2] / (n-p)\}^{1/2}$, where n is the number of reflections and p is the total number of parameters refined.

Table 6.3 Crystallographic data and structural refinement parameters for $\{[Sm(tptz)(H_2O)_4Co(CN)_6]\cdot 8H_2O\}_\infty$ (**SmCo)** and $\{[La(tptz)(DMF)(H_2O)_3Fe(CN)_6]\cdot 5H_2O\}_\infty$ (**LaFe**).

	SmCo	**LaFe**
Formula	$C_{24}H_{36}N_{12}O_{12}CoSm$	$C_{27}H_{35}N_{13}O_9FeLa$
Formula weight	893.93	880.44
Space group	*C2/c*	*C2/c*
T (K)	150	110
a (Å)	15.813(3)	16.069(3)
b (Å)	14.070(3)	14.390(3)
c (Å)	31.523(6)	32.076(6)
α (°)	90.00	90.00
β (°)	103.31(3)	102.45(3)
γ (°)	90.00	90.00
V (Å^3)	6825(2)	7243(3)
Z	8	8
Crystal description, color	Colorless plate	Yellow block
Crystal size (mm^3)	0.13 x 0.06 x 0.02	0.21 x 0.16 x 0.11
λ (Å)	0.71073	0.71073
D_{calc} (g cm^{-3})	1.740	1.617
μ (cm^{-1})	2.266	1.631
F(000)	2694	3544
θ range (°)	1.33 to 28.37	1.92 to 28.35
Reflections collected	20483	40258
Diffraction limits	$-20 < h < 20$, $-12 < k < 18$	$-21 < h < 21$, $-19 < k < 18$
(h, k, l)	$-38 < l < 41$	$-42 < l < 41$
Independent reflections	7758 [R(int) = 0.0561]	8648 [R(int) = 0.0751]
Observed data [$I > 2\sigma(I)$]	5905	7157
Completeness to θ_{max} (%)	90.9	95.4
Data/parameters/restraints	7758/446/0	8648/420/0
R^a, wR^b ($I>2\sigma(I)$)	0.0564, 0.1272	0.0606.0.1510
R^a, wR^b (all data)	0.0806, 0.1374	0.0756/0.1604
Goodness-of-fit[c] on F^2	1.036	1.069
Largest diff. peak and hole (e Å^{-3})	1.716 and -1.620	2.461 and -1.369

[a] $R = \Sigma \left| \left| F_o \right| - \left| F_c \right| \right| / \Sigma \left| F_o \right|$.

[b] $wR = \{\Sigma [w(F_o^2 - F_c^2)^2] / \Sigma w(F_o^2)^2]\}^{1/2}$.

[c] Goodness-of-fit = $\{\Sigma [w(F_o^2 - F_c^2)^2] / (n-p)\}^{1/2}$, where n is the number of reflections and p is the total number of parameters refined.

Table 6.4 Crystallographic data and structural refinement parameters for $\{[Sm(tmphen)(DMF)_3(H_2O)Fe(CN)_6]\cdot 2H_2O\}_\infty$ (**DMF-L_2SmFe**), $\{[Sm(tmphen)_2(H_2O)_2$-$Fe(CN)_6]\cdot MeOH\cdot 13H_2O\}_\infty$ (**L_2SmFe**) and $\{[Sm(tmphen)_2(H_2O)_2Cr(CN)_6]\cdot MeOH$- $\cdot 9H_2O\}_\infty$ (**L_2SmCr**).

	DMF-L_2SmFe	**L_2SmFe**	**L_2SmCr**
Formula	$C_{31}H_{43}N_{11}O_6FeSm$	$C_{39}H_{66}N_{10}O_{16}FeSm$	$C_{40}H_{58}N_{10}O_{12}CrSm$
Formula weight	871.96	1137.22	1061.30
Space group	*P*-1	$P2_1/c$	*P*-1
T (K)	110	110	110
a (Å)	9.7240(19)	20.322(4)	13.214(3)
b (Å)	13.477(3)	19.728(4)	13.998(3)
c (Å)	16.552(3)	13.473(3)	14.075(3)
α (°)	74.62(3)	90.00	105.38(3)
β (°)	88.44(3)	106.48(3)	92.56(3)
γ (°)	81.45(3)	90.00	92.76(3)
V (Å^3)	2068.1(7)	5179.6(18)	2502.8(9)
Z	2	4	2
Crystal description, color	yellow block	light yellow prism	colorless prism
Crystal size (mm^3)	0.32 x 0.24 x 0.21	0.12 x 0.08 x 0.08	0.20 x 0.10 x 0.10
λ (Å)	0.71073	0.71073	0.71073
D_{calc} (g cm^{-3})	1.400	1.4581	1.408
μ (cm^{-1})	1.807	1.475	1.442
F(000)	884	2344	1088
θ range (°)	1.28 to 27.61	1.88 to 23.32	1.50 to 23.34
Reflections collected	12589	22489	10850
Independent reflections	9062 [*R*(int) = 0.0339]	7431 [*R*(int) = 0.0520]	7067 [*R*(int) = 0.0509]
Observed data [$I > 2\sigma(I)$]	7392	5854	5299
Completeness to θ_{max} (%)	94.2	99.1	97.5
Data/parameters/restraints	9062/453/0	7431/636/7	7067/577/0
R^a, wR^b ($I>2\sigma(I)$)	0.0636, 0.1661	0.0476.0.1028	0.0813/0.2042
R^a, wR^b (all data)	0.0826, 0.1753	0.0677/0.1100	0.1107/0.2224
Goodness-of-fit[c] on F^2	1.107	1.070	1.049
Largest diff. peak and hole (e Å^{-3})	2.611 and -2.032	1.284 and -0.761	2.375 and -1.215

[a] $R = \Sigma \| |F_o| - |F_c| | / \Sigma |F_o|$.

[b] $wR = \{\Sigma [w(F_o^2 - F_c^2)^2] / \Sigma w(F_o^2)^2]\}^{1/2}$.

[c] Goodness-of-fit = $\{\Sigma [w(F_o^2 - F_c^2)^2] / (n-p)\}^{1/2}$, where *n* is the number of reflections and *p* is the total number of parameters refined.

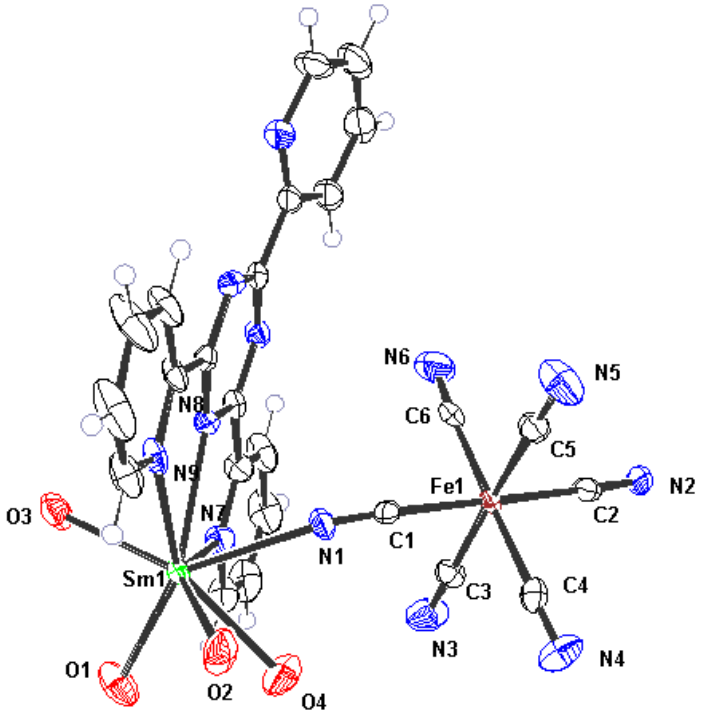

Figure 6.1 Thermal ellipsoid plot for $\{[Sm(tptz)(H_2O)_4Fe(CN)_6]\cdot 8H_2O\}_\infty$ (**SmFe**) drawn at the 50% probability level; crystallization molecules of water in the lattice have been omitted for the sake of clarity.

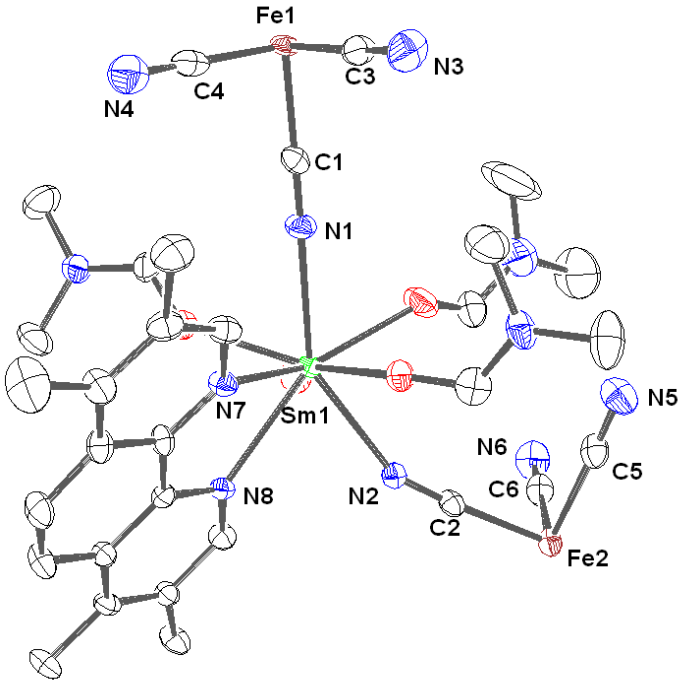

Figure 6.2 Thermal ellipsoid plot for $\{[Sm(tmphen)(DMF)_3(H_2O)Fe(CN)_6]\cdot 2H_2O\}_\infty$ (**DMF-L_2SmFe**) drawn at the 50% probability level; solvent crystallization molecules in the lattice and hydrogen atoms have been omitted for the sake of clarity.

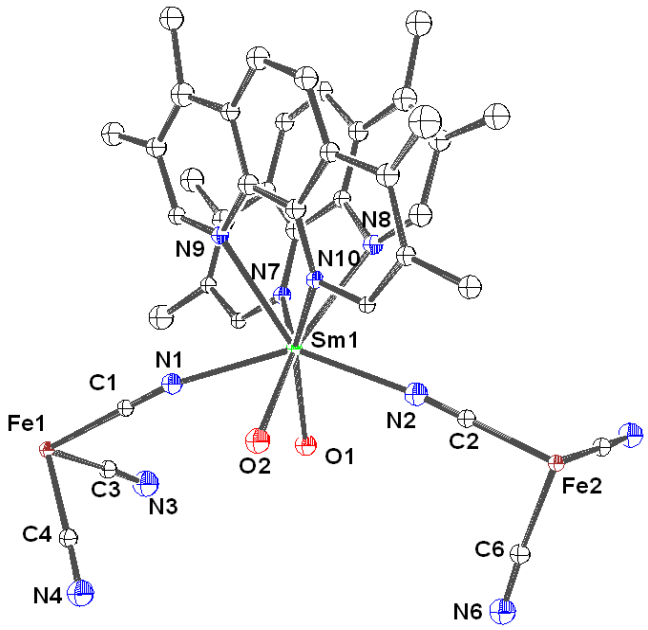

Figure 6.3 Thermal ellipsoid plot for $\{[Sm(tmphen)_2(H_2O)_2Fe(CN)_6]\cdot MeOH\cdot 13H_2O\}_\infty$ (**L_2SmFe**) drawn at the 50% probability level; solvent crystallization molecules in the lattice and hydrogen atoms have been omitted for the sake of clarity.

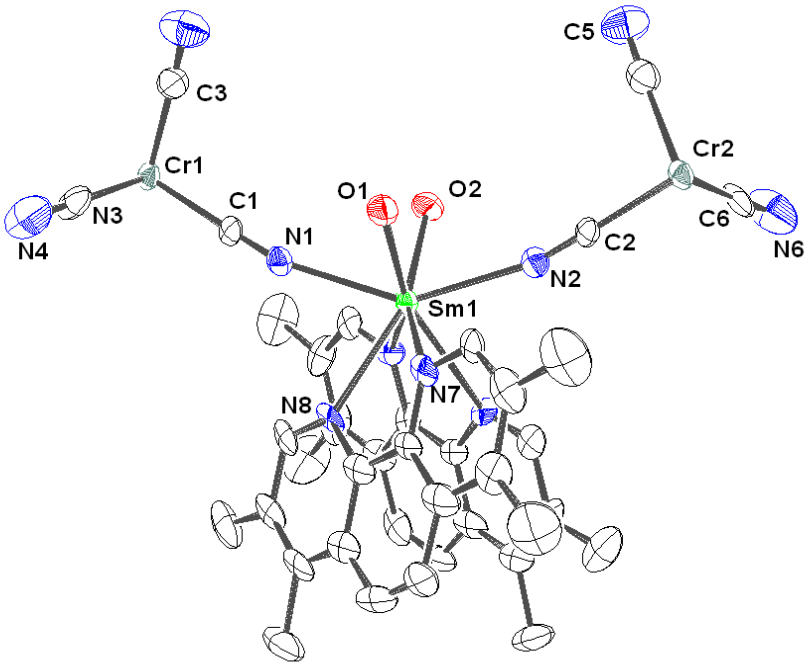

Figure 6.4 Thermal ellipsoid plot for $\{[Sm(tmphen)_2(H_2O)_2Cr(CN)_6]\cdot MeOH\cdot 9H_2O\}_\infty$ (**L_2SmCr**) drawn at the 50% probability level; solvent crystallization molecules in the lattice and hydrogen atoms have been omitted for the sake of clarity.

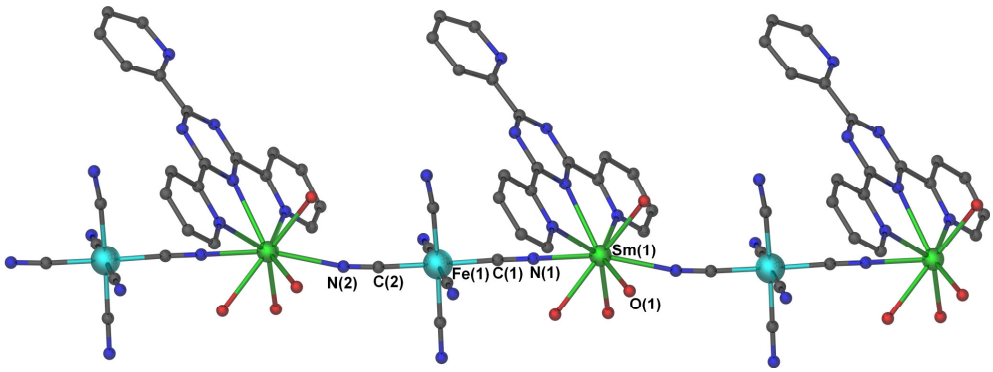

Figure 6.5 View of the linear chain 1-D structure of **SmFe**; interstitial water molecules have been omitted for the sake of clarity.

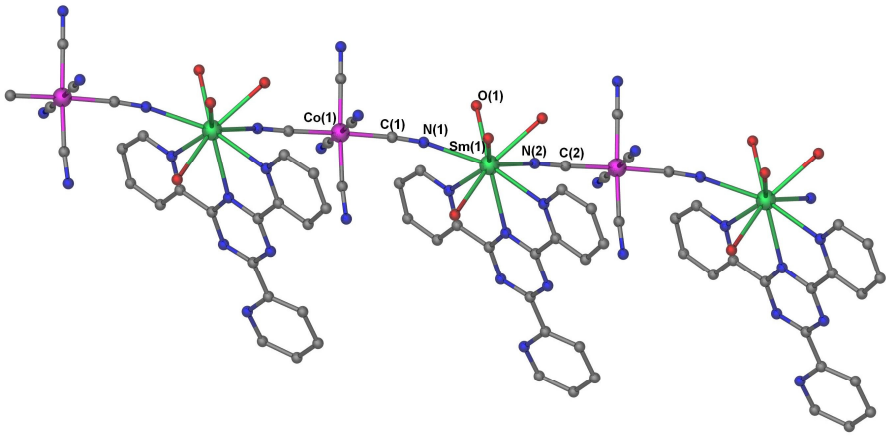

Figure 6.6 View of the linear chain 1-D structure of **SmCo** emphasizing its similarity to that of **SmFe**; interstitial water molecules have been omitted for the sake of clarity.

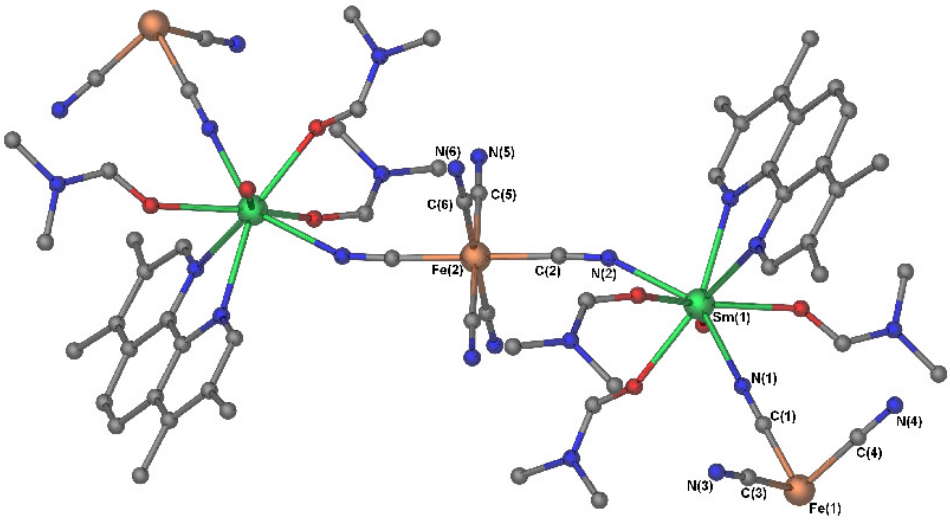

Figure 6.7 View of the 1-D chain structure of **DMF-L$_2$SmFe**; interstitial water molecules and hydrogen atoms have been omitted for the sake of clarity.

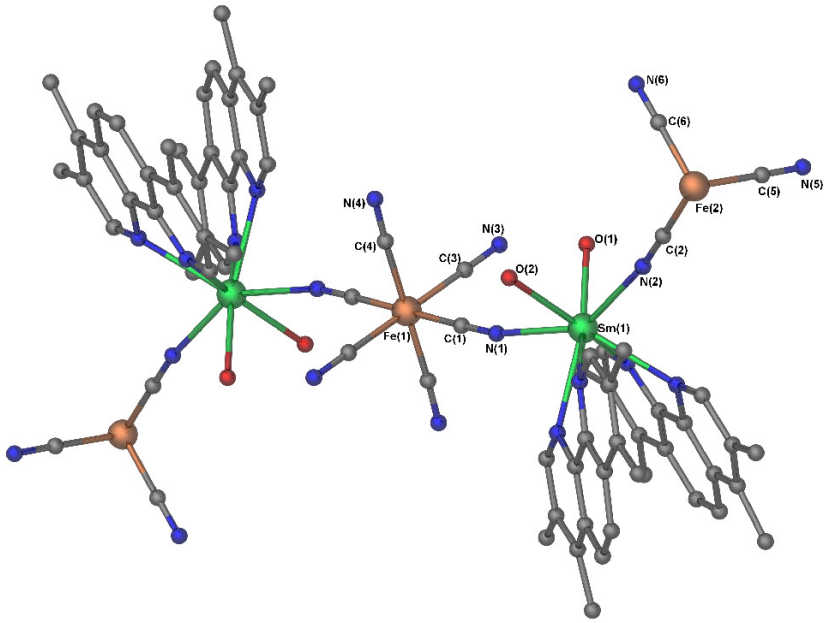

Figure 6.8 View of the 1-D chain structure of **L_2SmFe**; interstitial solvent molecules and hydrogen atoms have been omitted for the sake of clarity.

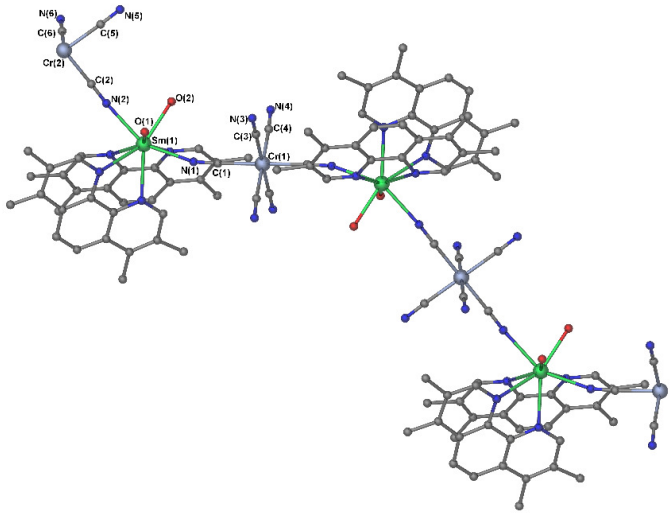

Figure 6.9 View of the 1-D chain structure of **L_2SmCr**, which is similar to that of **L_2SmFe**; interstitial solvent molecules and hydrogen atoms have been omitted for the sake of clarity.

The Fe-C bond lengths for the bridging coordinated cyanides to the Ln(III) ions are shorter than those of the non-bridging cyanide ligands. In the case of **PrFe**, the Fe(1)-C(1) and Fe(2)-C(2) distances are 1.923 and 1.917 Å, respectively. The Fe-C bond lengths of the dangling cyanides are in the range 1.935-1.941 Å.

In the packing diagram of **SmFe**, depicted in Figure 6.10, it can be seen that the two sets of chains run in perpendicular directions. The Fe-Fe, Fe-Sm and Sm-Sm distances between neighboring aligned parallel chains are 10.635, 10.274 and 10.635 Å, respectively. The chains do not exhibit a zig-zag motif, which is the typical architecture adopted by chains containing DMF;[222,263] instead, in **LnFe** (Ln = Pr, Nd, Sm, Eu, Gd, and Tb) linear chains are present with interstitial molecules of water located between the chains. Linear chains have been observed for the recently prepared 1D chain complexes comprising cyanide bridged alternating $Ln(bpy)(H_2O)_4$-$M(CN)_6$ fragments with bpy as a capping ligand on the Ln(III) ion.[225,228]

The distances between the Sm(III) ion and the nitrogen atoms of tptz in $\{[Sm(tptz)(H_2O)_4Co(CN)_6]\cdot 8H_2O\}_\infty$ (**SmCo**) are in the range 2.580-2.627 Å (Table 6.5). The bond lengths to the two bridging cyanides in **SmCo** are very close to the values found for $\{[Sm(tptz)(H_2O)_4Fe(CN)_6]\cdot 8H_2O\}_\infty$ (**SmFe**) (2.589-2.638 Å; Table 6.6).

The structure of **DMF-L_2SmFe** consists of a cyanide *trans*-bridged alternating array of $Fe(CN)_6$ and $Sm(tmphen)(DMF)_3(H_2O)$ fragments. Each Sm(III) ion is eight-coordinate with four oxygen atoms from one water and three DMF molecules, two nitrogen atoms from the tmphen ligands, and two nitrogen atoms from the bridging CN ligands with Sm-O distances ranging from 2.353(4) to 2.402(4) Å.

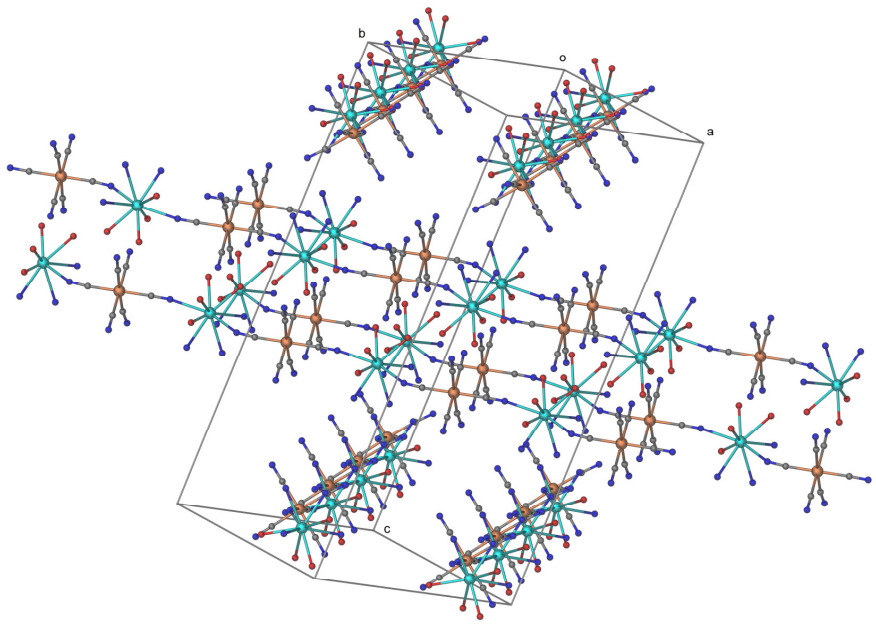

Figure 6.10 Unit cell packing diagram of **SmFe** illustrating the 1D structure extending in two directions; interstitial water molecules and partial atoms of tptz have been omitted for the sake of clarity.

Table 6.5 Selected bond lengths (Å) and angles (º) for compound **SmCo**.

Sm1-O(3)	2.461(5)	Co(1)-C(5)	1.889(7)
Sm1-O(4)	2.498(6)	Co(1)-C(6)	1.896(7)
Sm(1)-N(1)	2.517(5)	C(1)-N(1)	1.157(8)
Sm(1)-N(2)	2.496(6)	C(2)-N(2)	1.150(8)
Sm(1)-N(7)	2.627(6)	C(3)-N(3)	1.143(8)
Sm(1)-N(8)	2.580(5)	C(4)-N(4)	1.146(9)
Co(1)-C(1)	1.882(6)	C(5)-N(5)	1.149(9)
Co(1)-C(2)	1.881(6)	C(6)-N(6)	1.148(9)
N1-Sm1-N2	136.37(19)	C1-Co1-C2	176.8(3)
N1-Sm1-N7	84.04(17)	C1-Co1-C3	88.1(3)
N1-Sm1-N8	66.48(16)	C1-Co1-C4	91.1(3)
N1-Sm1-N9	76.33(16)	N1-C1-Co1	174.6(5)
N2-Sm1-N7	139.56(18)	N2-C2-Co1	175.4(6)
C1-N1-Sm1	148.3(5)	C2-N2-Sm1	170.3(5)

Table 6.6 Selected bond lengths (Å) and angles (º) for compound **SmFe**.

Sm1-O(1)	2.453(5)	Fe(1)-C(3)	1.942(7)
Sm1-O(2)	2.428(5)	Fe(1)-C(4)	1.945(7)
Sm1-O(3)	2.454(5)	Fe(1)-C(5)	1.942(7)
Sm1-O(4)	2.503(6)	Fe(1)-C(6)	1.940(8)
Sm(1)-N(1)	2.519(5)	C(1)-N(1)	1.148(8)
Sm(1)-N(2)	2.501(5)	C(2)-N(2)	1.142(8)
Sm(1)-N(7)	2.637(6)	C(3)-N(3)	1.144(9)
Sm(1)-N(8)	2.587(5)	C(4)-N(4)	1.147(9)
Fe(1)-C(1)	1.929(6)	C(5)-N(5)	1.141(9)
Fe(1)-C(2)	1.921(7)	C(6)-N(6)	1.157(10)
N1-Sm1-N2	135.61(19)	C1-Fe1-C2	177.1(3)
N1-Sm1-N7	84.60(18)	C1-Fe1-C3	87.9(2)
N1-Sm1-N8	66.17(18)	C1-Fe1-C4	90.1(3)
N1-Sm1-N9	75.79(17)	N1-C1-Fe1	173.9(5)
N2-Sm1-N7	139.74(19)	N2-C2-Fe1	175.9(6)
C1-N1-Sm1	148.1(5)	C2-N2-Sm1	169.6(5)

Table 6.7 Selected bond lengths (Å) and angles (º) for compound **PrFe**.

Pr1-O(1)	2.492(5)	Fe(1)-C(3)	1.935(6)
Pr1-O(2)	2.484(5)	Fe(1)-C(4)	1.938(7)
Pr1-O(3)	2.512(4)	Fe(1)-C(5)	1.941(6)
Pr1-O(4)	2.533(5)	Fe(1)-C(6)	1.939(7)
Pr(1)-N(1)	2.566(5)	C(1)-N(1)	1.151(7)
Pr(1)-N(2)	2.535(5)	C(2)-N(2)	1.151(7)
Pr(1)-N(7)	2.683(5)	C(3)-N(3)	1.143(8)
Pr(1)-N(8)	2.640(4)	C(4)-N(4)	1.144(9)
Fe(1)-C(1)	1.923(6)	C(5)-N(5)	1.142(8)
Fe(1)-C(2)	1.917(6)	C(6)-N(6)	1.154(9)
N1-Pr1-N2	135.37(18)	C1-Fe1-C2	177.1(3)
N1-Pr1-N7	84.68(16)	C1-Fe1-C3	87.6(2)
N1-Pr1-N8	65.99(15)	C1-Fe1-C4	90.3(3)
N1-Pr1-N9	75.09(15)	N1-C1-Fe1	174.8(5)
N2-Pr1-N7	139.80(17)	N2-C2-Fe1	176.0(5)
C1-N1-Pr1	147.1(4)	C2-N2-Pr1	169.9(5)

Table 6.8 Selected bond lengths (Å) and angles (º) for compound **L_2SmFe**.

Sm(1)-N(1)	2.457(5)	Fe(1)-C(4)	1.938(6)
Sm(1)-N(2)	2.456(5)	Fe(2)-C(2)	1.907(6)
Sm(1)-N(7)	2.573(4)	C(1)-N(1)	1.158(7)
Sm(1)-N(8)	2.579(4)	C(2)-N(2)	1.154(7)
Fe(1)-C(1)	1.906(6)	C(3)-N(3)	1.159(7)
Fe(1)-C(3)	1.948(6)	C(4)-N(4)	1.162(7)
N1-Sm1-N2	145.04(15)	N2-C2-Fe2	177,6(5)
N1-Sm1-O1	76.14(15)	C1-Fe1-C3	88.3(2)
N1-Sm1-O2	72.44(15)	C1-Fe1-C4	89.7(2)
C1-N1-Sm1	164.5(4)	C3-Fe1-C4	88.9(2)
C2-N2-Sm1	168.8(4)	O1-Sm1-O2	83.77(13)
N1-C1-Fe1	176.8(5)		

Table 6.9 Selected bond lengths (Å) and angles (º) for compound **L_2SmCr**.

Sm(1)-N(1)	2.525(10	Cr(1)-C(4)	2.069(13)
Sm(1)-N(2)	2.509(10)	Cr(2)-C(2)	2.071(12)
Sm(1)-N(7)	2.555(10)	C(1)-N(1)	1.153(15)
Sm(1)-N(8)	2.580(9)	C(2)-N(2)	1.154(14)
Cr(1)-C(1)	2.082(13)	C(3)-N(3)	1.166(18)
Cr(1)-C(3)	2.051(15)	C(4)-N(4)	1.138(17)
N1-Sm1-N2	146.3(3)	N2-C2-Cr2	177.0(10)
N1-Sm1-O1	75.6(3)	C1-Cr1-C3	91.2(5)
N1-Sm1-O2	79.2(3)	C1-Cr1-C4	88.6(5)
C1-N1-Sm1	164.9(9)	C3-Cr1-C4	90.1(5)
C2-N2-Sm1	163.9(8)	O1-Sm1-O2	84.0(3)
N1-C1-Cr1	175.6(10)		

As noted earlier for the other compounds, the Sm(III) ion is linked by two bridging cyanide ligands, one with a nearly linear bond angle C(1)-N(1)-Sm(1) = 177.41° and another with a markedly non-linear interaction C(2)-N(2)-Sm(1) = 154.39°.

In compounds **L_2SmFe** and **L_2SmCr**, the $[M(CN)_6]^{3-}$ (M = Fe, Cr) units are linked through cyanide bridges in a *trans* geometry. The eight-coordinate Sm(III) ion is bound to four nitrogen atoms from two tmphen ligands, which are oriented in a *cis* disposition, and two water molecules. The M-C distances in the $[M(CN)_6]^{3-}$ units are in the ranges 1.906-1.948 and 2.048-2.095 Å for **L_2SmFe** and **L_2SmCr**, respectively. The intramolecular distances Sm-Fe1 and Sm-Fe2 are 5.483 Å and 5.459 Å for **L_2SmFe** and **L_2SmCr**, respectively. The Fe1-Sm-Fe2 angle is 136.46°, which is an indication of the zig-zag chain structure. In **L_2SmCr**, the intramolecular distances Sm-Cr1 and Sm-Cr2 are 5.665 Å and 5.692 Å, respectively, which are longer than those observed in **L_2SmFe**. The Cr1-Sm-Cr2 angle in **L_2SmCr** is 131.76°, which is smaller than the angles in **L_2SmFe**.

Crystal Structure of $\{[Ln(tptz)(HCOO)_3]\cdot 2.5H_2O\}_\infty$ (Ln = Pr, Sm): Single-crystal X-ray studies revealed that the isostructural compounds $\{[Ln(tptz)(HCOO)_3]\cdot 2.5H_2O\}_\infty$ (Ln = Pr, Sm) crystallize in the trigonal system with space group *P*-3*c*1, hence the structural description will be provided only for the Sm analogue for illustrative purposes (Table 6.10). Compounds $\{[Ln(tptz)(HCOO)_3]\cdot 2.5H_2O\}_\infty$ (Ln = Pr, Sm) consist of a nonacoordinate neutral building block $[Ln(tptz)(HCOO)_3]$ where the metal ion is in a distorted tricapped trigonal prism coordination environment.

Table 6.10 Crystallographic data and structural refinement parameters for $\{[Pr(tptz)(HCOO)_3]\cdot 2.5H_2O\}_\infty$ (**Pr-tube**) and $\{[Sm(tptz)(HCOO)_3]\cdot 2.5H_2O\}_\infty$ (**Sm-tube**).

	Pr-tube	**Sm-tube**
Formula	$C_{21}H_{20.2}N_6O_{8.6}Pr$	$C_{21}H_{20.2}N_6O_{8.6}Sm$
Formula weight	635.13	644.58
Space group	*P*-3*c*1	*P*-3*c*1
T (K)	110	110
a (Å)	25.213(4)	25.158(4)
b (Å)	25.213(4)	25.158(4)
c (Å)	6.752(1)	6.704(1)
α (°)	90	90
β (°)	90	90
γ (°)	120	120
V (Å^3)	3717(1)	3675(1)
Z	6	6
Crystal description, color	colorless	colorless
Crystal size (mm^3)	$0.19 \times 0.11 \times 0.11$	$0.40 \times 0.37 \times 0.15$
λ (Å)	0.71073	0.71073
D_{calc} (g cm^{-3})	1.394	1.798
μ (cm^{-1})	2.008	2.465
F(000)	1518	1948
Reflections collected	42024	23457
Independent reflections	3098 [*R*(int) = 0.0271]	3023 [*R*(int) = 0.0885]
Observed data [$I > 2\sigma(I)$]	3045	2366
Data/parameters/restraints	3098/177/6	3023/166/0
R^a, wR^b ($I>2\sigma(I)$)	0.0577, 0.1447	0.0673, 0.1396
R^a, wR^b (all data)	0.0585, 0.1450	0.0879, 0.1490
Goodness-of-fit[c] on F^2	1.178	1.133
Largest diff. peak and hole (e Å^{-3})	1.441, -1.961	2.955, -2.397

[a] $R = \Sigma \left| \left| F_o \right| - \left| F_c \right| \right| / \Sigma \left| F_o \right|$.

[b] $wR = \{\Sigma [w(F_o^2 - F_c^2)^2] / \Sigma w(F_o^2)^2]\}^{1/2}$.

[c] Goodness-of-fit = $\{\Sigma [w(F_o^2 - F_c^2)^2] / (n-p)\}^{1/2}$, where *n* is the number of reflections and *p* is the total number of parameters refined.

The tptz ligand chelates through three nitrogen atoms, with the Sm(III) coordination sphere being completed by six formate ions (Figure 6.11). The Ln-O distances in the Sm analogue range from 2.359 Å to 2.461 Å and the Sm-N distances are longer than the aforementioned distances (Sm-N2 = 2.638 and Sm-N1 = 2.658 Å).

The asymmetric unit consists of one half of the $[Ln(tptz)(HCOO)_3]$ building block along with three interstitial water molecules. The formate ions are bound to two different lanthanide ions in the common *anti-anti* mode. The C-O bond lengths (1.22 Å) and O-C-O angles (126º) of the formate ligand that is perpendicular to the plane of tptz differs from the corresponding values at approximately 45º with respect to the plane of tptz with C-O bond lengths of 1.17 Å and O-C-O angles of 124º. The formate ion that is perpendicular to the plane of tptz is bound to the Sm(tptz) unit that resides directly on top of the former Sm(tptz) unit, thus the interplanar separation of the tptz units (6.70 Å) is dictated by the length of the formate ions and; such an interaction leads to the formation of a linear chain composed of formate ions and Sm(tptz) units. The formate ligands that are at approximately 45º degrees with respect to the plane of tptz are bound to other Sm(tptz) units. Thus, the compound can be described as linear $Sm(tptz)(HCOO)^{2+}$ chains connected sideways to other chains by formate ligands resulting in a tubular coordination polymer (Figure 6.12).

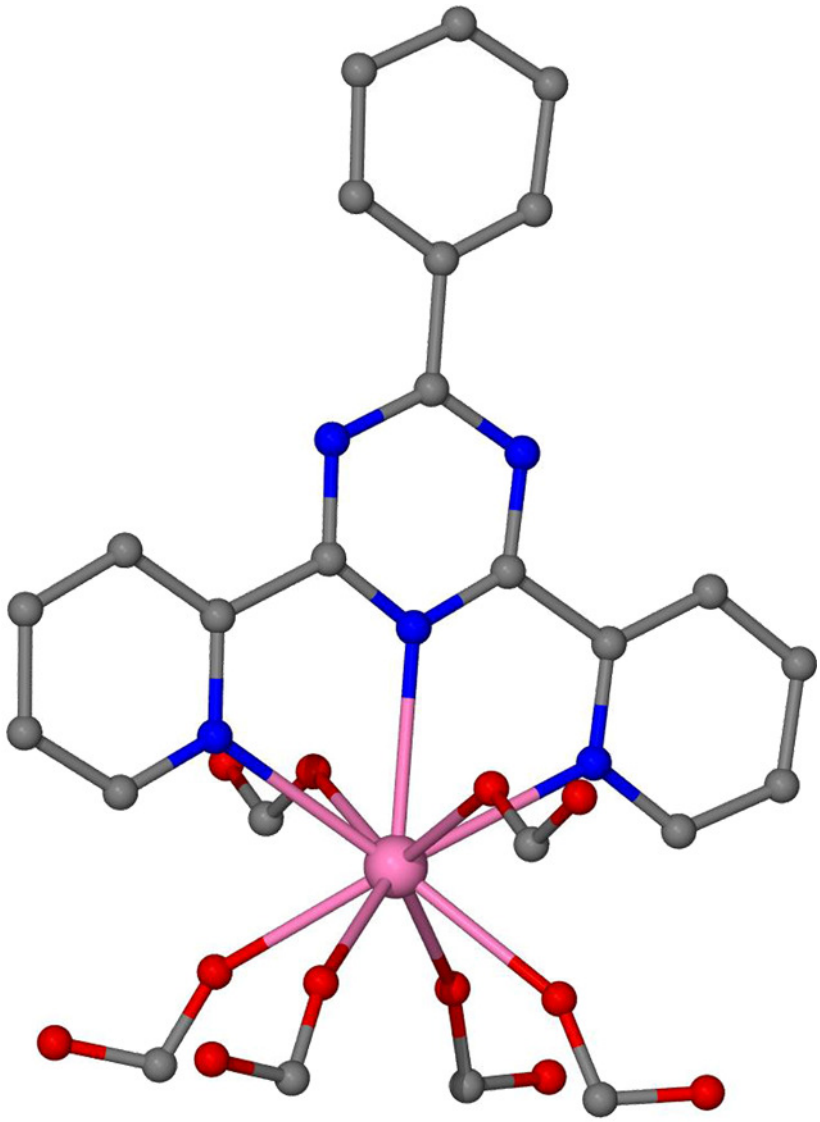

Figure 6.11 A view of the [Sm(tptz)(HCOO)$_3$] building block from the crystal structure of {[Sm(tptz)(HCOO)$_3$]·2.5H$_2$O}$_\infty$, depicting the coordination environment of the Sm^{III} ion. The hydrogen atoms and interstitial water molecules are omitted for the sake of clarity. Tb = pink, O = red, N = blue, C = gray.

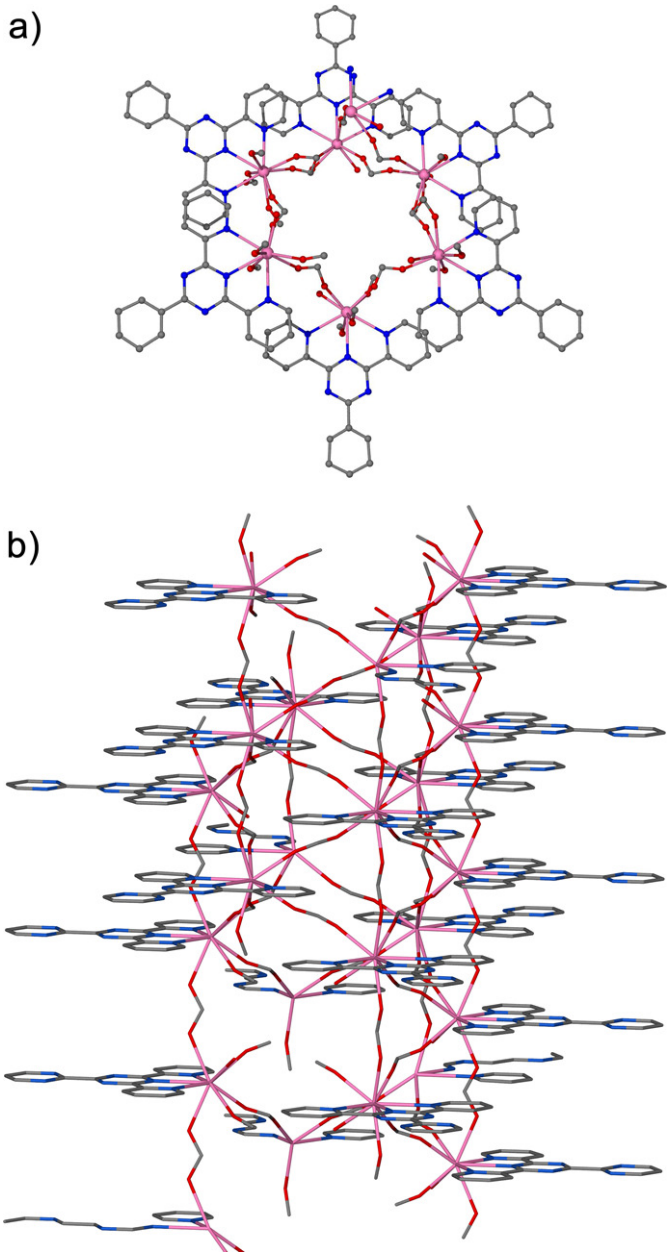

Figure 6.12 a) A top view of the [Sm(tptz)(HCOO)$_3$] nanotube depicting π-π interactions of adjacent tptz ligands. b) A side view of the nanotube depicting the available space to intercalate with neighboring tubes via π-π interactions of tptz ligands. The hydrogen atoms and interstitial water molecules are omitted for the sake of clarity. Tb = pink, O = red, N = blue, C = gray.

The formate ion that is perpendicular to the plane of tptz is bound to the Sm(tptz) unit that resides directly on top of the former Sm(tptz) unit, thus the interplanar separation of the tptz units (6.70 Å) is dictated by the length of the formate ions and; such an interaction leads to the formation of a linear chain composed of formate ions and Sm(tptz) units. The formate ligands that are at approximately 45º degrees with respect to the plane of tptz are bound to other Sm(tptz) units. Thus, the compound can be described as linear $Sm(tptz)(HCOO)^{2+}$ chains connected sideways to other chains by formate ligands resulting in a tubular coordination polymer (Figure 6.12). The pyridyl rings on the tptz ligand also contribute to the formation of the nanotube; there are π-π intra-tube interactions between the pyridyl groups of adjacent tptz ligands from the Sm(tptz) units that are connected sideways by formate ligands with an interplanar distance of 3.34 Å with a slipped ring-over-ring conformation. The nanotubes have an internal 1D channel with a diameter of 3.3 Å after subtraction of van der Waals radii. The tptz ligands are located on the periphery of the nanotubes and the interplanar distance of the tptz units (6.70 Å) within the linear $Sm(tptz)(HCOO)^{2+}$ chain is sufficient for π-π interactions to occur with aromatic molecules (Figure 6.12).

In these materials, the nanotubes engage in intermolecular π-π interactions with neighboring nanotubes. The intercalation of nanotubes leads to an additional 1D channel with a diameter of 6.9 Å after subtraction of van der Waals radii (Figure 6.13).

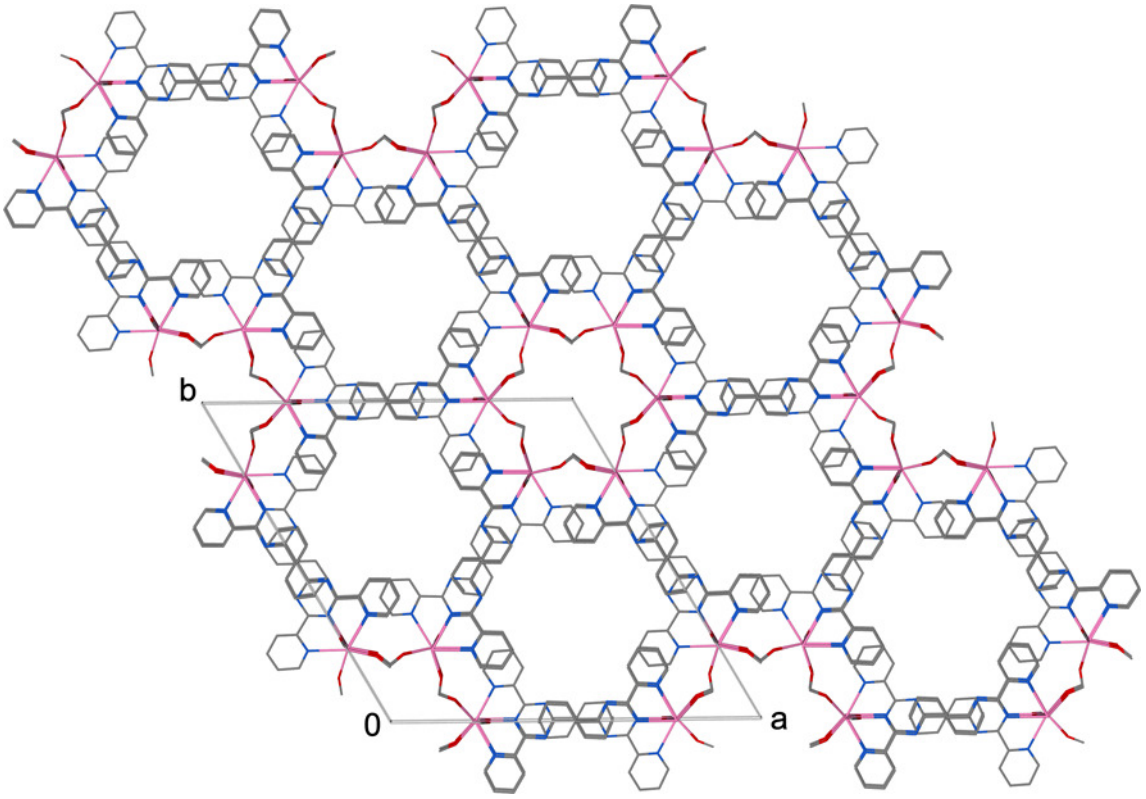

Figure 6.13 Packing diagram of $\{[Sm(tptz)(HCOO)_3]\cdot 2.5H_2O\}_\infty$ along the *c* axis emphasizing the internal cavity of the coordination tubes and the intercalation of nanotubes which forms an additional 1D channel. The hydrogen atoms and interstitial water molecules are omitted for the sake of clarity. Tb = pink, O = red, N = blue, C = gray.

The water molecules that reside in the smaller tube are involved in hydrogen bonding interactions (O···O = 3.38 Å) and are arranged in a regular chain; in a similar manner, there are three chains of hydrogen bonded water molecules inside the larger cavity with O···O distances of 3.38 Å.

At this stage it is important to point out that there are a limited number of coordination nanotubes in the literature and that most of them contain transition metals.[261] In fact there is only one report of a coordination nanotube based on lanthanum(III) ions.[262] Thus, the present isostructural family of coordination tubes is of interest because it represents an extension of such low dimensional materials by the use of lanthanide ions. The use of lanthanide ions also represents an opportunity to obtain coordination tubes with luminescent properties and also it could be possible to obtain single molecule magnets based on the single ion anisotropy of the lanthanide due to crystal field effects. All of the lanthanide ions might could their easy axis of magnetization preferentially oriented in the same direction due to the formation of regular arrays of tubes in the solid state of $\{[Ln(tptz)(HCOO)_3]\cdot 2.5H_2O\}_\infty$, a condition that could lead to the observation of hysteresis due to slow paramagnetic relaxation.

Powder X-ray Diffraction Studies: The powder X-ray diffraction (XRD) of products from bulk and slow diffusion syntheses matched the simulated pattern of the $\{[Sm(tptz)(HCOO)_3]\cdot 2.5H_2O\}_\infty$ single crystal. The $\{[Sm(tptz)(HCOO)_3]\cdot 2.5H_2O\}_\infty$ compound was subjected to thermal studies, and the stability of the framework was probe by XRD studies. Powder XRD patterns of $[Sm(tptz)(HCOO)_3]\cdot 2.5H_2O\}_\infty$ prepared by slow diffusion reactions between $Sm(tptz)(Otf)_3$ and $[NH_4][HCOO]$ in a 1:3 ratio in

methanol were collected first on a fresh sample. After taking the first diffraction pattern the sample was heated at 150°C under vacuum for 24 hours and the diffraction pattern matched the simulation (Figure 6.14). Thus, the framework is stable and retains its crystallinity presumably due to the extensive π-π interactions between the nanotubes. The stability of the framework was tested under more rigorous conditions by preparing $[Sm(tptz)(HCOO)_3]\cdot 2.5H_2O\}_\infty$ in bulk by a reaction between $Sm(tptz)(Otf)_3$ and $[NH_4][HCOO]$ in a 1:3 ratio in methanol under reflux from the beginning of the reaction. The course of the reaction was monitored periodically by collecting data on the white powder that formed nearly instantaneously. The diffraction pattern of a sample taken after refluxing for 15 minutes matched the simulated patterns of the $[Sm(tptz)(HCOO)_3]\cdot 2.5H_2O\}_\infty$ crystal structure. The diffraction pattern of a sample measured after refluxing for 90 minutes exhibited very weak intensities that did not match the simulated patterns of the $[Sm(tptz)(HCOO)_3]\cdot 2.5H_2O\}_\infty$ crystal structure. The diffraction pattern of a sample measured after refluxing for 2 days was very weak and only exhibited two peaks, one of which was very broad which is a clear indication of the loss of original crystallinity (Figure 6.15). Thus, the $[Sm(tptz)(HCOO)_3]\cdot 2.5H_2O\}_\infty$ material retains its crystallinity when heated under vacuum in the solid state, but the crystallinity is rapidly lost under refluxing conditions as expected for a material that is held together in the solid state by intermolecular π-π interactions.

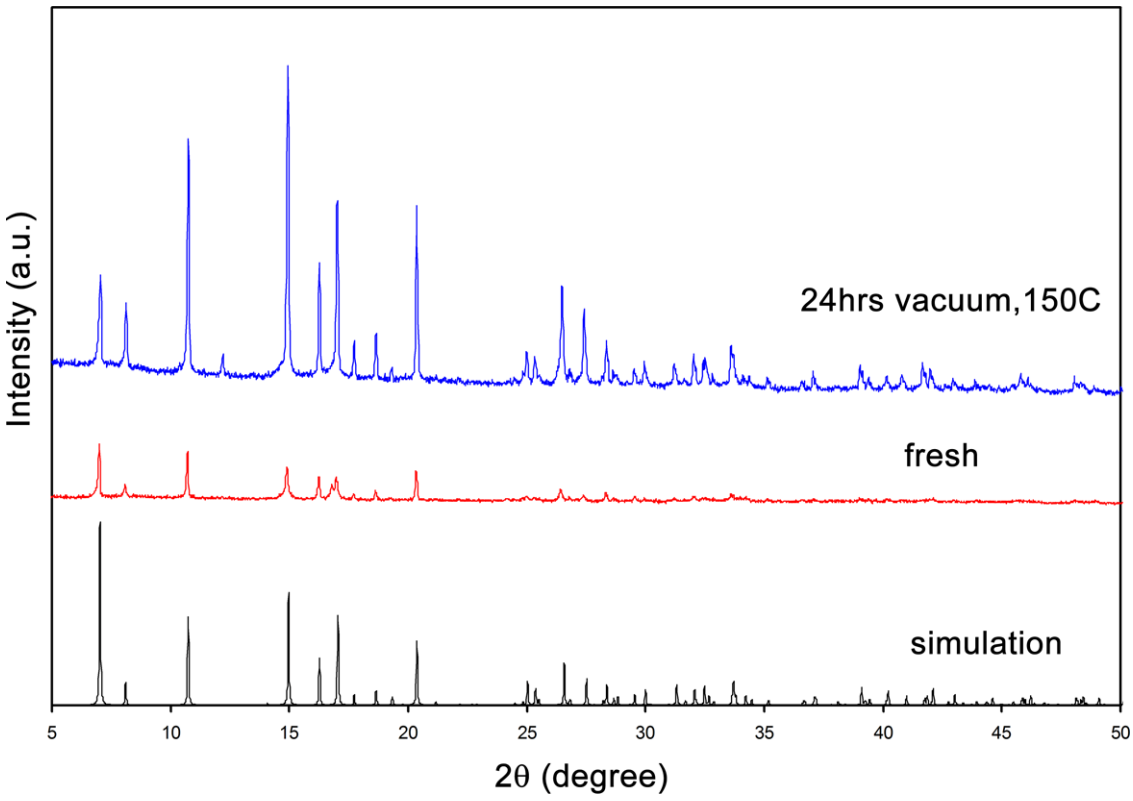

Figure 6.14 XRD powder patterns obtained from ground crystals after one week of slow diffusion of $Sm(tptz)(Otf)_3$ and $[NH_4][HCOO]$ in a 1:3 ratio in methanol. Fresh sample (red), evacuated for 24 hours at 150°C (blue); XRD powder pattern of $[Sm(tptz)(HCOO)_3]\cdot 2.5H_2O\}_\infty$ simulated (black).

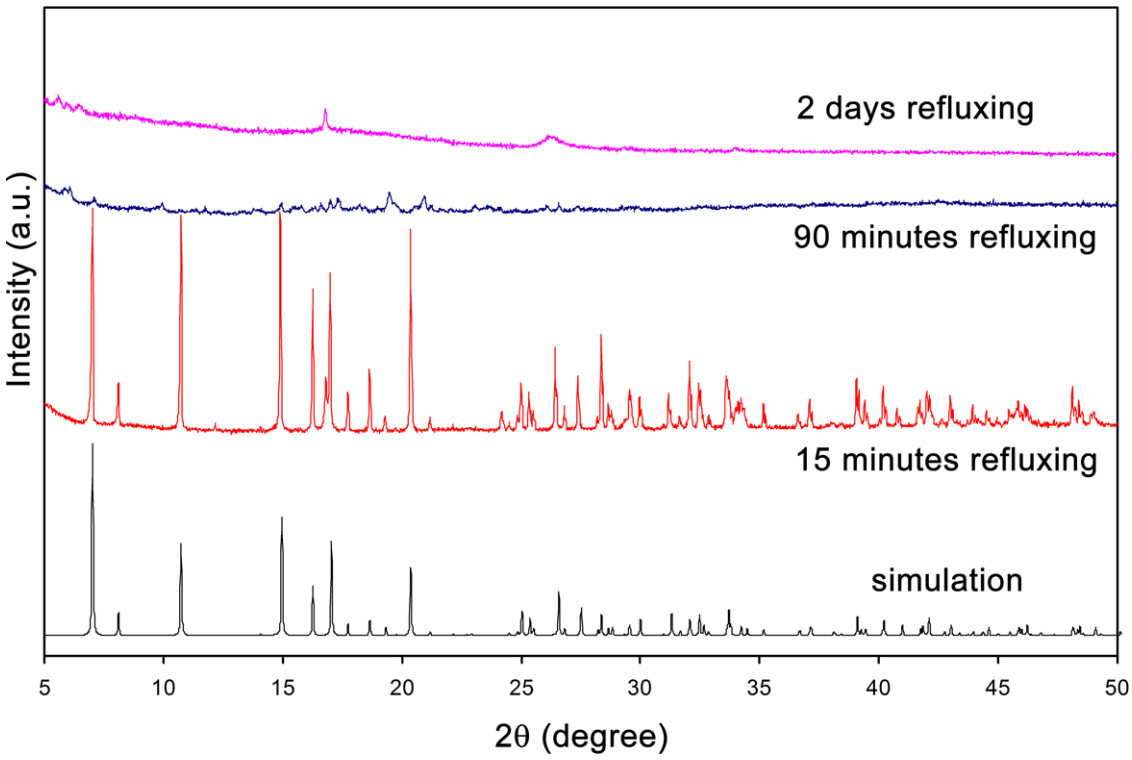

Figure 6.15 Experimental XRD powder pattern obtained from the bulk reaction between Sm(tptz)$(Otf)_3$ and $[NH_4][HCOO]$ in methanol under refluxing conditions after 15 minutes (red), 90 minutes (blue) and two days (pink); XRD powder pattern of $[Sm(tptz)(HCOO)_3]\cdot 2.5H_2O\}_\infty$ simulated (black).

Magnetic Studies: Magnetic susceptibility measurements for Ln-$M(CN)_6$ compounds were performed on polycrystalline samples at 1000 Oe over the temperature range 1.8-300 K by using a SQUID magnetometer. The room temperature χT values for **PrFe**, **NdFe**, **EuFe**, **GdFe**, and **TbFe** are close to the theoretical ones for the superposition of isolated Ln(III) and low-spin Fe(III) ions, namely 2.21, 2.16, 1.85, 8.16 and 12.05 emu·mol^{-1}·K, respectively (Figure 6.16). The χT values decrease smoothly with decreasing temperature, due to the depopulation of excited Stark sublevels, reaching values of 0.53, 1.1, 0.44, 7.08 and 8.86 emu·mol^{-1}·K at 2 K for compounds **PrFe**, **NdFe**, **EuFe**, **GdFe**, **TbFe**, respectively. No significant magnetic interactions were observed for these compounds.

Significantly different magnetic behavior was observed for the Sm(III) compounds **SmFe**, **DMF-L_2SmFe**, and **L_2SmFe**. The room temperature χT values (1.08, 1.06 and 1.09 emu·mol^{-1}·K, respectively) are close to the theoretical values for the superposition of isolated Sm(III) and low-spin Fe(III) ions as expected. The values decrease smoothly with decreasing temperature, reaching minimum values of 0.54, 0.56 and 0.6 emu·mol^{-1}·K at 12 K for compounds **SmFe**, **DMF-L_2SmFe**, and **L_2SmFe**, respectively. A continued decrease in the temperature leads to a sharp increase in χT at 2 K (Figures 6.17, 6.18, 6.19). Such behavior was previously attributed to that expected for ferrimagnets. The magnetic interaction between Sm(III) and low-spin Fe(III) has been postulated to be antiferromagnetic[212,218,222,225,263,264] or negligible.[226]

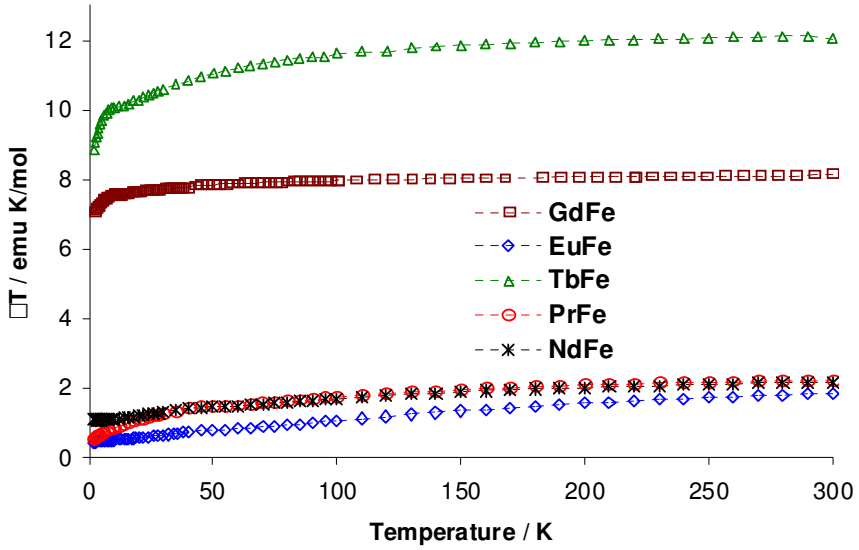

Figure 6.16 Temperature dependence of χT for compounds **PrFe** (o), **NdFe** (*), **EuFe** (◊), **GdFe** (□), **TbFe** (Δ).

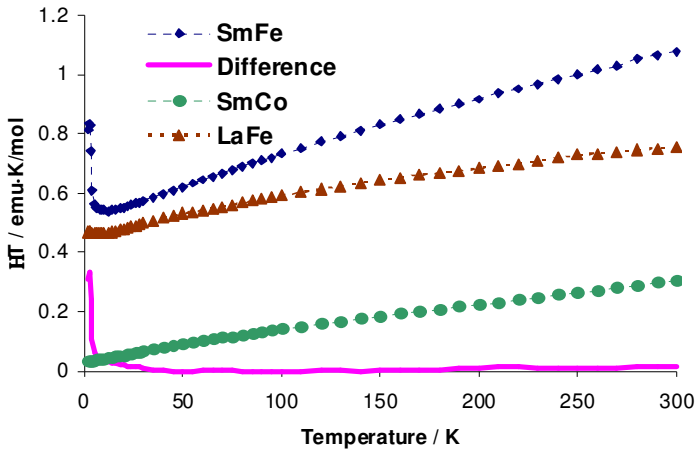

Figure 6.17 Temperature dependence of χT for compounds **Sm** (◊), **SmCo** (o), **LaFe** (Δ). The solid line represents the difference $\Delta\chi T = \chi T$ (**SmFe**) − χT (**SmCo**) − χT (**LaFe**).

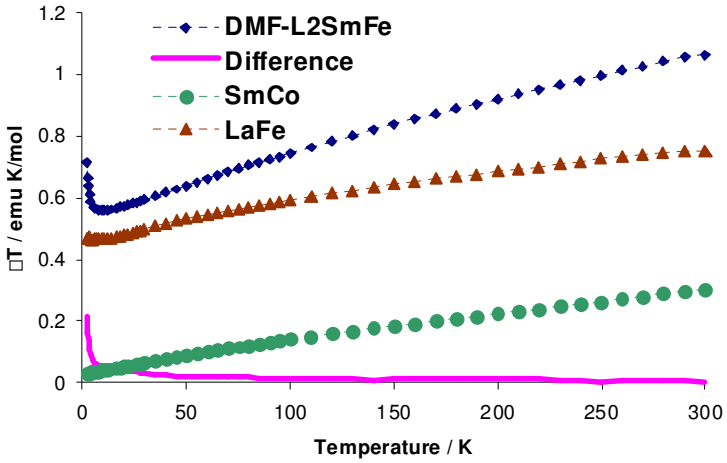

Figure 6.18 Temperature dependence of χT for compounds **DMF-L$_2$SmFe** (◊), **SmCo** (o), **LaFe** (Δ). The solid line represents the difference $\Delta\chi T = \chi T$ (**DMF-L$_2$SmFe**) - χT (**SmCo**) - χT (**LaFe**).

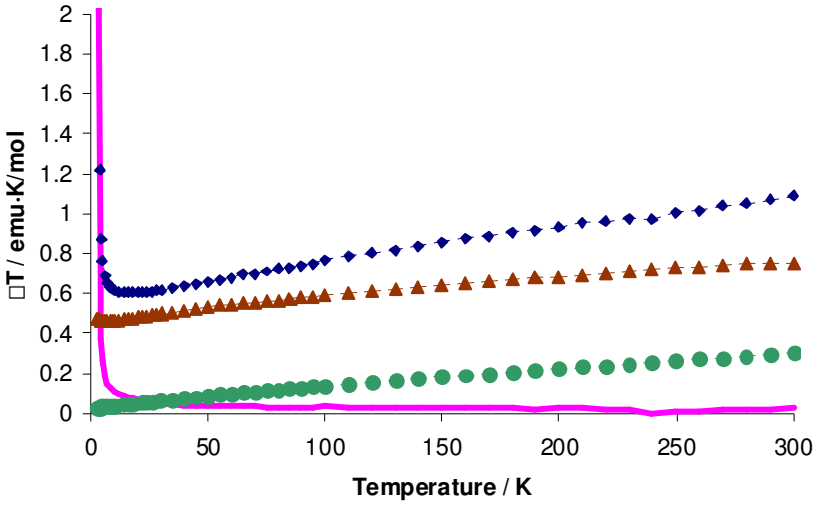

Figure 6.19 Temperature dependence of χT for compounds **L_2SmFe** (◊),**SmCo** (o), **LaFe** (Δ). The solid line represents the difference $\Delta\chi T = \chi T$ (**L_2SmFe**) - χT (**SmCo**) - χT (**LaFe**).

It should be noted, however, that the sign of the Sm(III)–Fe(III) interaction is best determined by a comparison of the χT-curves of the rare earth ferricyanide complex with the isostructural Sm(III)-Co(III) and La(III)-Fe(III) compounds.

For complexes **3**, **9**, **10** the following function has been calculated:

$$\Delta\chi T = \chi T\ (\mathbf{Ln\text{-}M}) - \chi T\ (\mathbf{La\text{-}M}) - \chi T(\mathbf{Ln\text{-}Co}) \qquad (6.1)$$

where χ(**Ln-M**), χ(**La-M**) and χ(**Ln-Co**) refer to the magnetic susceptibility of the [**Ln-M**], [**La-M**] and [**Ln-Co**] compounds, respectively. A continuously increasing $\Delta\chi$T curve with decreasing temperature, indicates a ferromagnetic interaction between the Ln(III) and M(III) ions (M = Fe, Cr), whereas a decrease followed by an increase at low temperatures indicates the presence of an antiferromagnetic interaction.[214,225,226] Figures 6.17, 6.18, 6.19 clearly indicate that the magnetic interaction between the Sm(III) and Fe(III) ions is ferromagnetic for **SmFe**, **DMF-L$_2$SmFe**, and **L$_2$SmFe**, respectively. To further support this conclusion, we undertook the synthesis of a series of 3D rare-earth cyanometalates[212] and reinvestigated their magnetic properties. According to our data (Figure 6.20), the Gd(III)-Fe(III) complex is antiferromagnetic,[212] but unexpectedly the Sm(III)-Fe(III) complex is ferromagnetic, which contradicts the previously reported data for other Sm(III)-Fe(III) compounds.[212,218,222,225,226,263,264] Most likely, in the previous reports, the authors interpreted the strong depopulation of the excited Stark sublevels as a result of antiferromagnetic interactions (*i.e.*, a ferrimagnetic behavior overall).

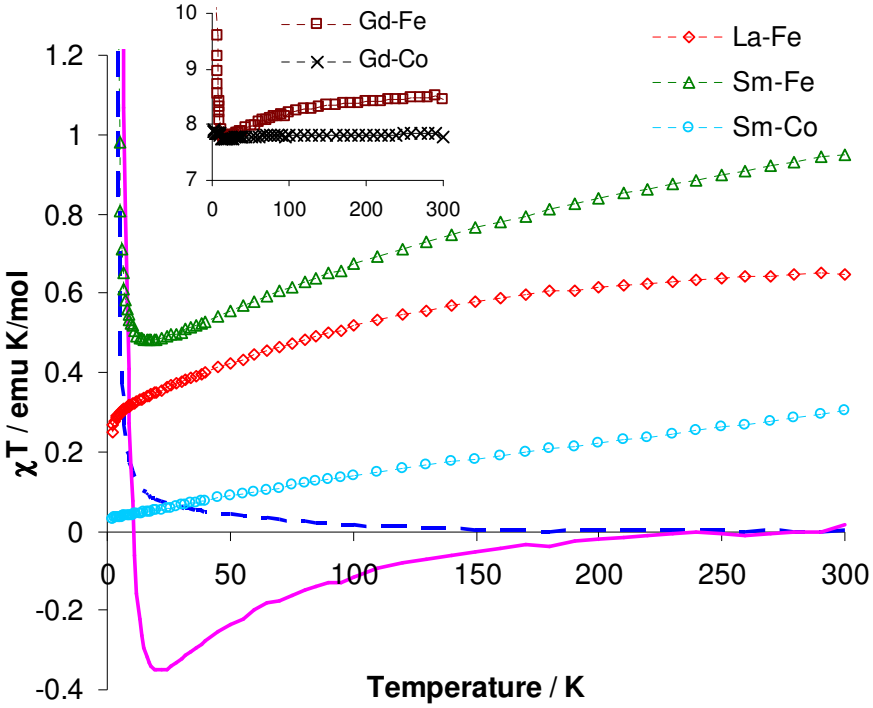

Figure 6.20 Temperature dependence of χT for rare-earth ferricyanides.[212] The solid line represents the difference $\Delta\chi$T(**Gd-Fe**) = χT (**Gd-Fe**) – χT (**Gd–Co**) – χT (**La-Fe**). The dashed line represents the difference $\Delta\chi$T(**Sm-Fe**) = χT (**Sm-Fe**) - χT (**Sm-Co**) – χT (**La-Fe**).

The same ferromagnetic behavior observed for **SmFe**, **DMF-L_2SmFe**, and **L_2SmFe** was found for **L_2SmCr** (Figure 6.21), which correlates very well with similar Sm(III)-Cr(III) compounds that have been recently reported.[214]

To further investigate the low-temperature properties of the compounds that contain samarium, we undertook ZFC-FC measurements at 10 Oe (Figures 6.22, 6.23, 6.24); the latter indicate the initiation of 3-D magnetic ordering at 3.7 K, possibly due to interchain interactions mediated by hydrogen bonds and/or π-π stacking. The divergence of DC χ_{ZFC} and χ_{FC} reveals the history dependence of the magnetization process. To confirm the onset of the ordering, hysteresis was measured at 1.8 K with coercivity of ~100 Oe. The region of ±1500 Oe is shown for the sake of clarity in Figure 6.25. To verify the nature of long-range ordering, the temperature dependences of the AC magnetic susceptibility were studied for the compounds that contain samarium (Figures 6.26 to 6.30).

Below the phase transition, the small frequency dependence of AC magnetic susceptibilities suggests the presence of a degree of spin-glass like behavior (Figure 6.30). The relaxation time (τ) was obtained from the Arrhenius law (Figure 15, inset, bottom):

$$\tau(T) = \tau_0 \cdot \exp\left(\frac{U}{k_B T}\right) \tag{6.2}$$

The best-fit parameters are U=313 cm^{-1}; $\tau_0 = 10^{-62}$ s^{-1} for **SmFe**. It is obvious that the obtained U and τ_0 values are in the range of the previously reported spin glasses (U>100 cm^{-1}; $\tau_0 < 10^{-10}$ s^{-1}).[52,214,265-268]

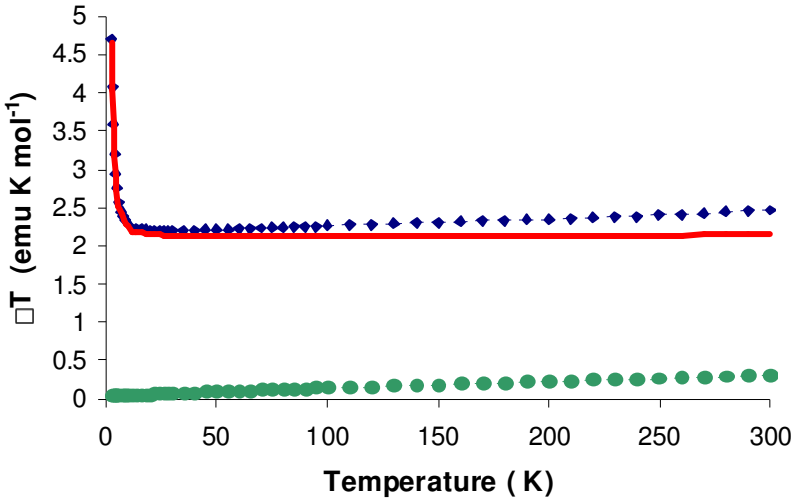

Figure 6.21 Temperature dependence of χT for compounds **L_2SmCr** (◊), **SmCo** (o). The solid line represents the difference $\Delta\chi T = \chi T$ (**L_2SmCr**) - χT (**SmCo**).

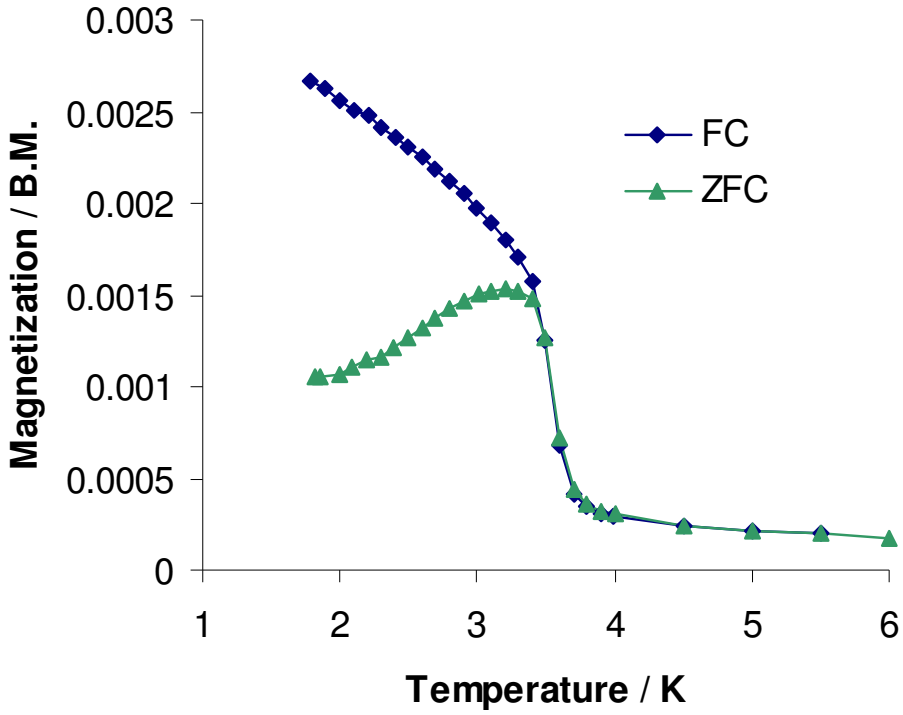

Figure 6.22 Temperature dependence of the magnetization in the zero-field-cooling (ZFC) and field-cooling (FC) modes for **SmFe** in a magnetic field of 10 Oe.

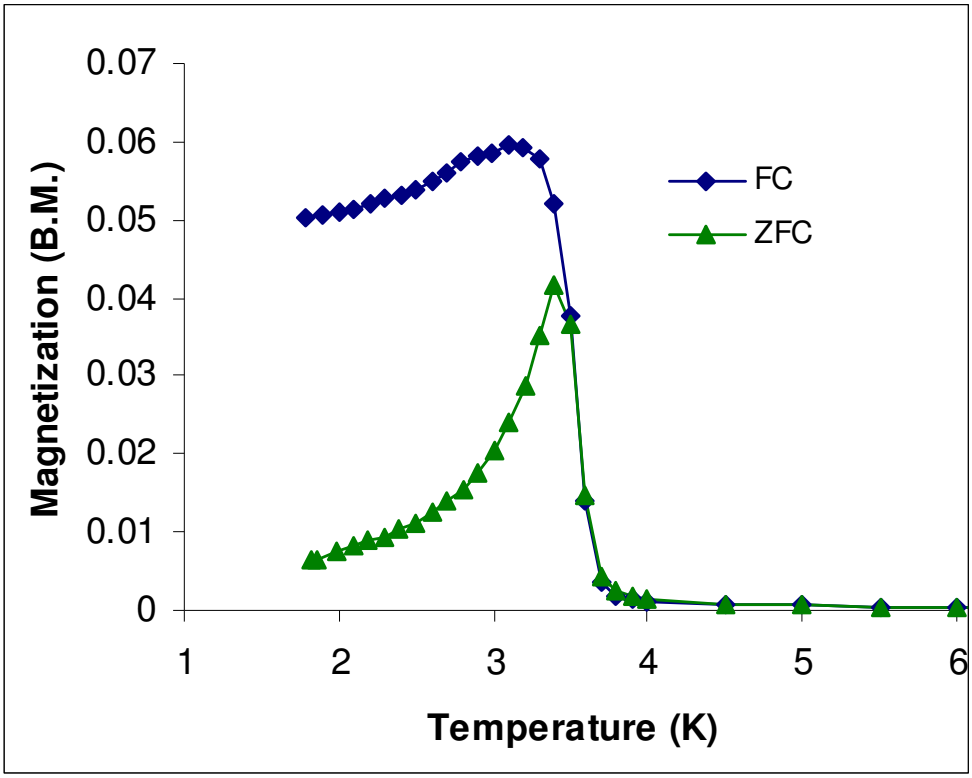

Figure 6.23 Temperature dependence of magnetization in the zero-field-cooling (ZFC) and field-cooling (FC) modes for **L_2SmFe** at magnetic field of 10 Oe.

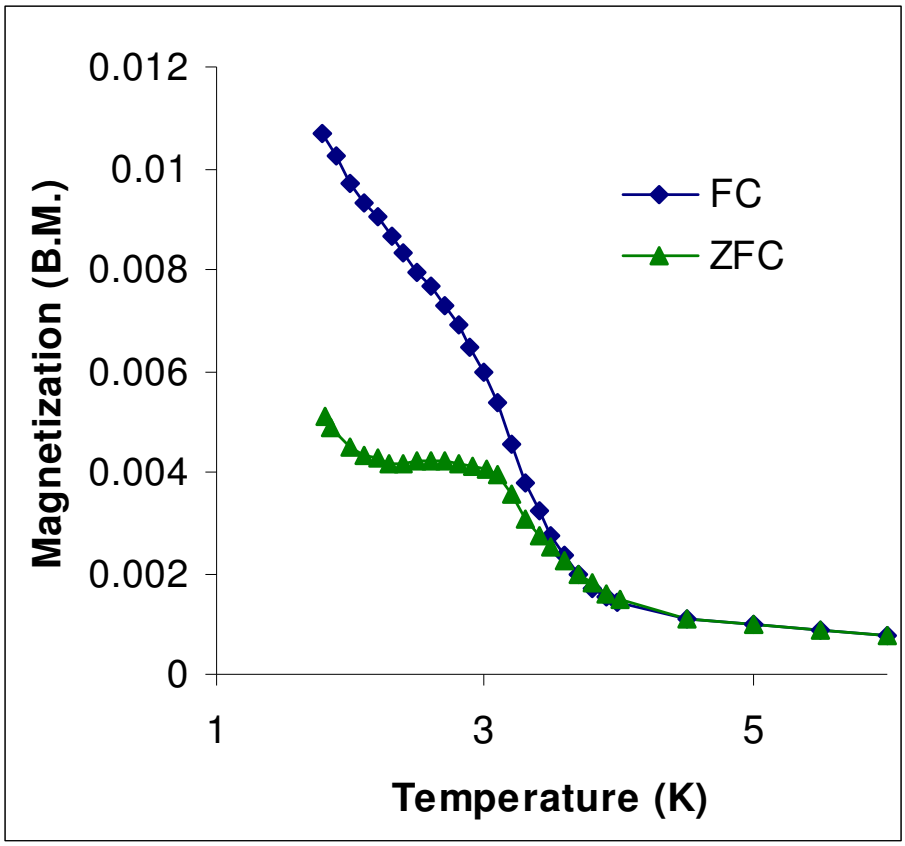

Figure 6.24 Temperature dependence of magnetization in the zero-field-cooling (ZFC) and field-cooling (FC) modes for **L_2SmCr** at magnetic field of 10 Oe.

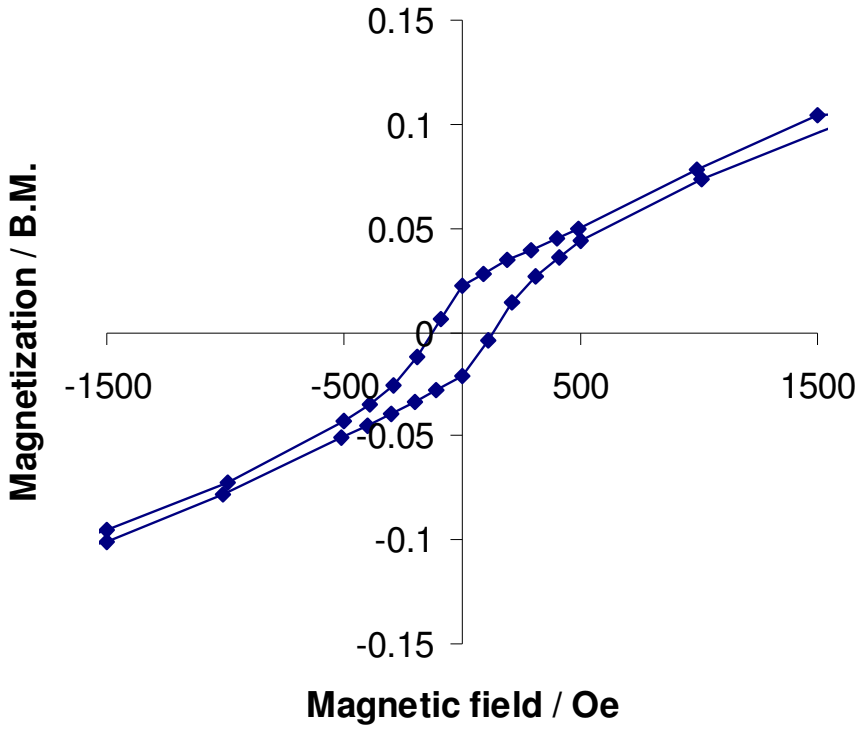

Figure 6.25 Hysteresis loop for **SmFe** at 1.8 K.

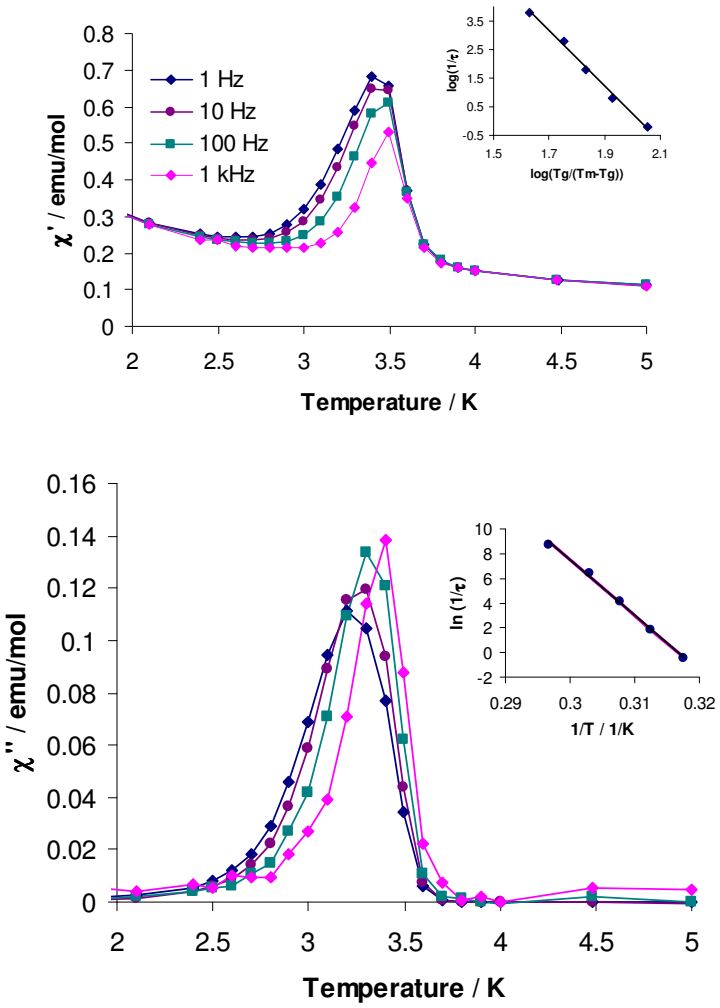

Figure 6.26 Temperature dependence of the real χ´ (top) and imaginary χ´´ (bottom) components of the ac susceptibility in an oscillating field of 3 Oe at different frequencies for **SmFe**. Insets: Critical scaling law (top) and Arrhenius plot (bottom).

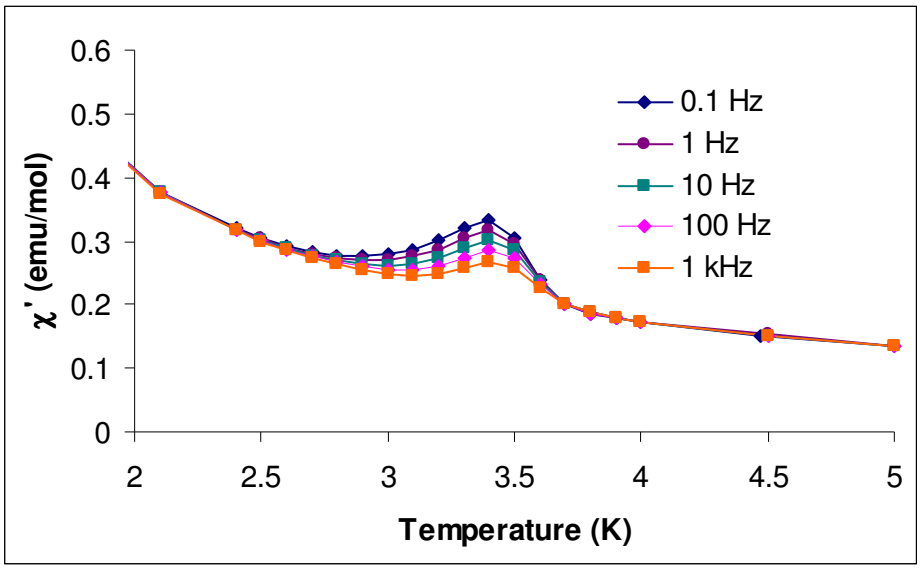

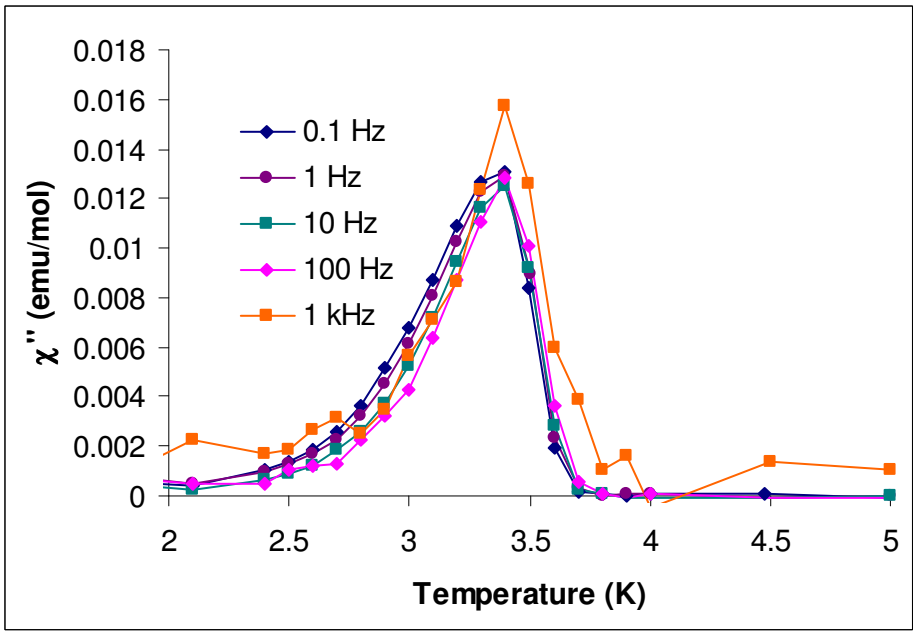

Figure 6.27 Temperature dependence of the real χ´ (top) and imaginary χ´´ (bottom) components of the ac susceptibility in an oscillating field of 3 Oe at different frequencies for **DMF-L_2SmFe**.

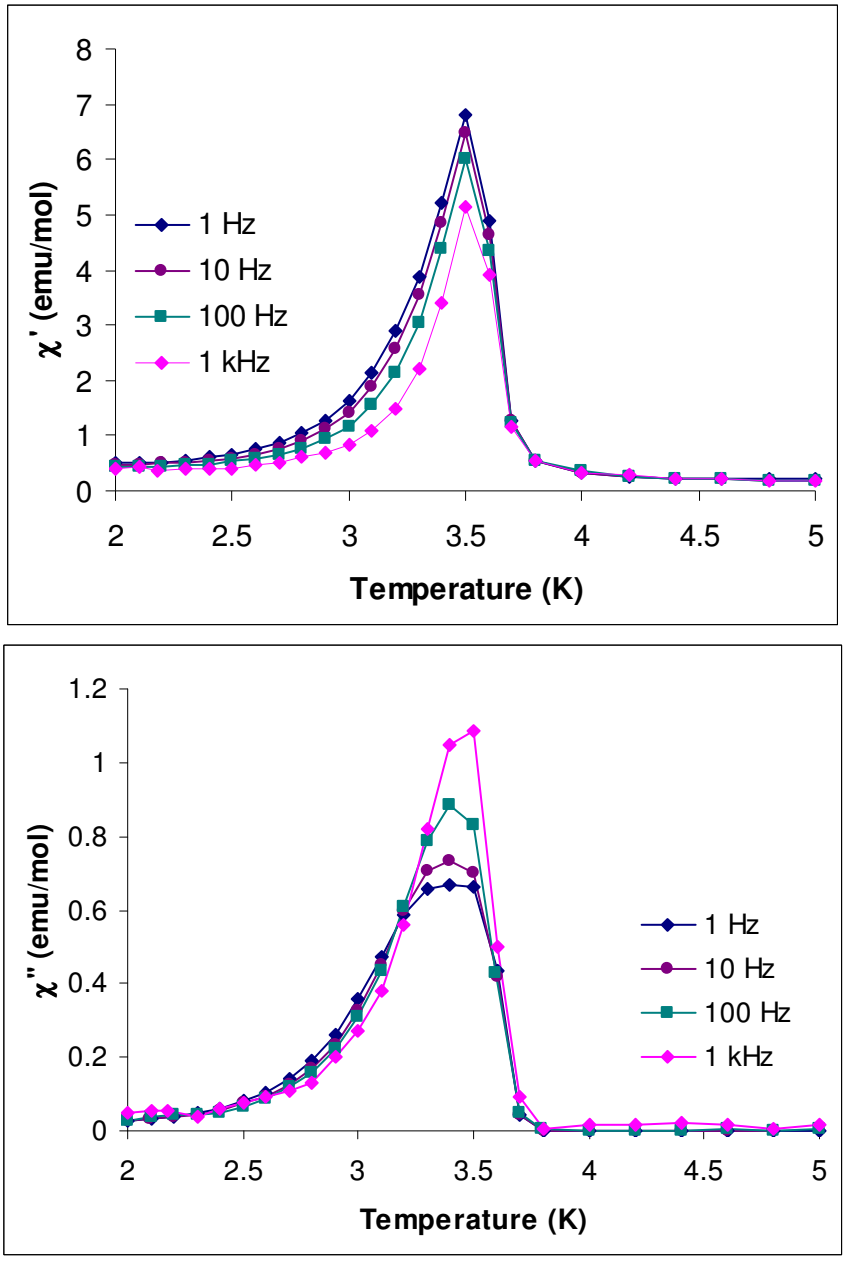

Figure 6.28 Temperature dependence of the real χ´ (top) and imaginary χ´´ (bottom) components of the ac susceptibility in an oscillating field of 3 Oe at different frequencies for **L_2SmFe**.

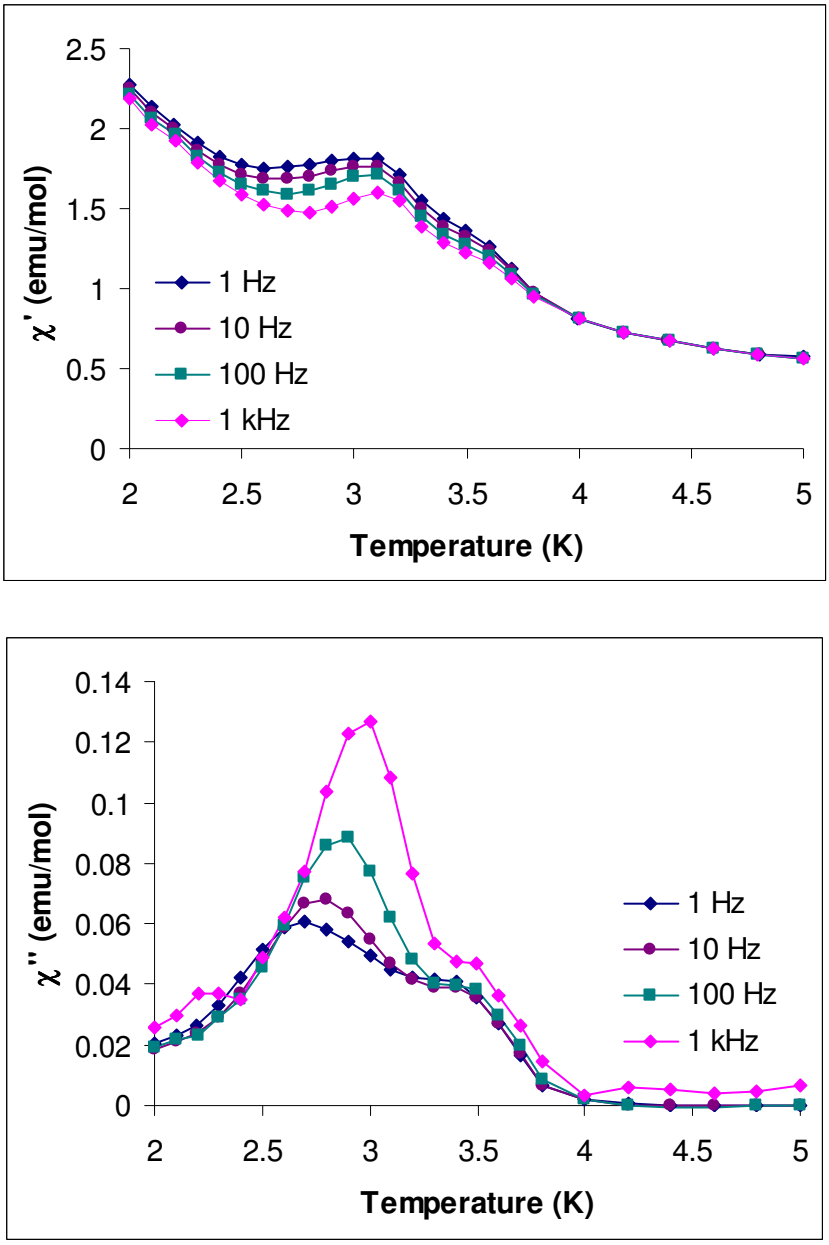

Figure 6.29 Temperature dependence of the real χ´ (top) and imaginary χ´´ (bottom) components of the ac susceptibility in an oscillating field of 3 Oe at different frequencies for **L_2SmCr**.

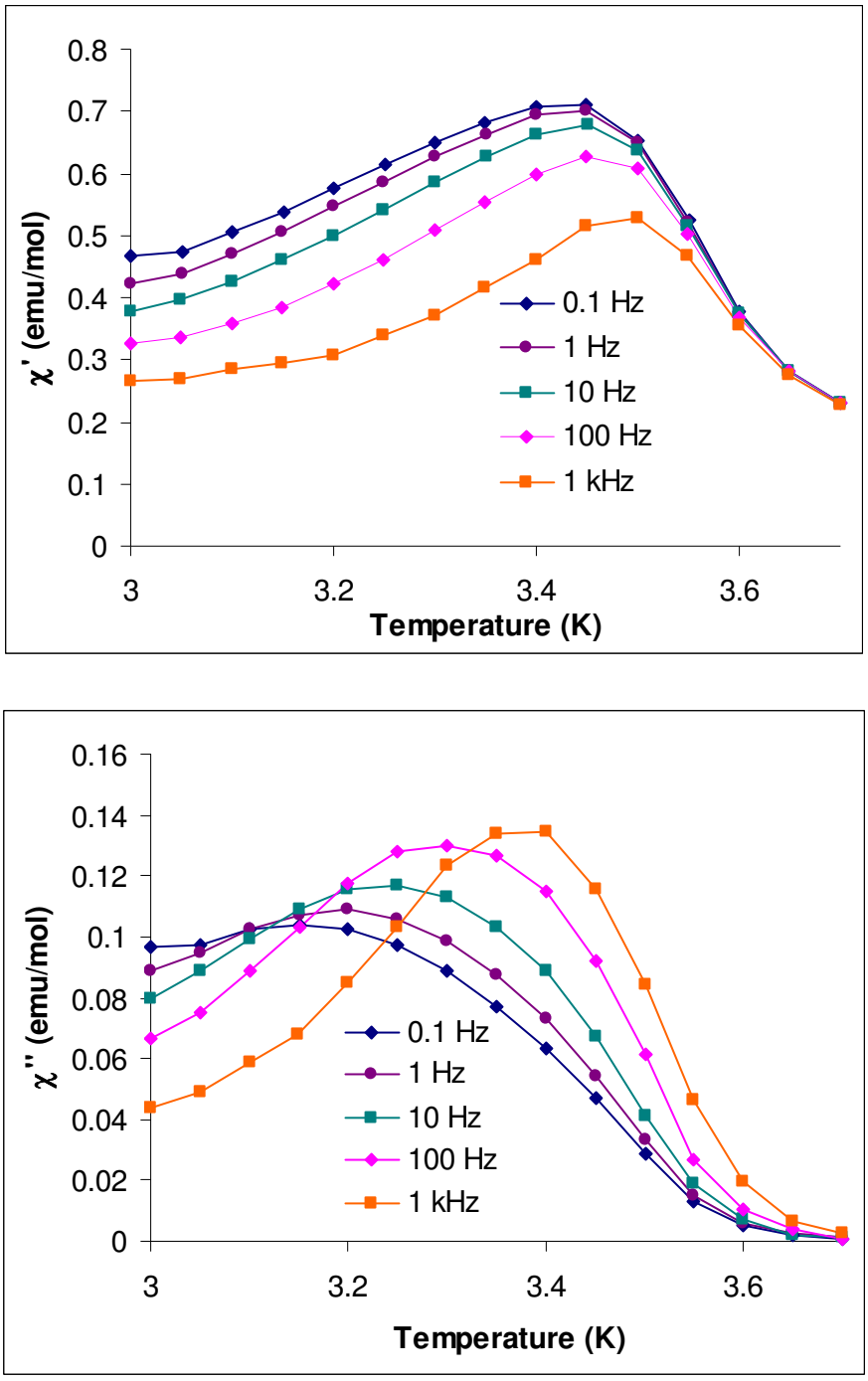

Figure 6.30 Temperature dependence of the real χ´ (top) and imaginary χ´´ (bottom) components of the ac susceptibility in an oscillating field of 3 Oe at different frequencies for **SmFe** in the vicinity of the phase transition.

For spin glasses and other disordered magnetic compounds, two well-known criteria have often been used for characterization of its behavior. The disorder parameter

$$\phi = \Delta T_m / T_g / \Delta log\ \omega \tag{6.3}$$

where ΔT_m is the shift of the peak in χ', $log\ \omega$ is the logarithm of the applied frequency, and T_g, the position of the peak at zero frequency, the so-called freezing temperature can be used as a criterion to distinguish between different categories of materials exhibiting spin glass-like behavior. The value $\phi = 0.004$ for **SmFe** places this compound in the range of canonical spin-glasses which have the typical value $\phi < 0.1$.

Alternatively, the data are well described by assuming critical dynamics of a spin-glass with a finite static glass temperature T_g [265-268] as described by:

$$\tau = \tau_0((T_m - T_g)/T_g)^{-zv} \tag{6.4}$$

where $\tau = 1/2\pi\omega$ and zv is the dynamical critical exponent which varies between 4 and 12 for different spin-glasses. Figure 6.26 (inset, top) displays the best fits of the data for **SmFe** in the range ω = 0.1-1000Hz, indicating that the spin-glass state can be well described by the conventional critical scaling law of the spin dynamics model. The best fit yields T_g = 3.4 K, $\tau_0 = 10^{-19}$ s and zv = 9.7, parameters that are within the realm of the conventional spin glass phase.[265-268] The spin glass-like behavior of the compounds that contain Sm is attributed to competing interchain and intrachain interactions.[265-268]

Conclusions

In this study, a series of cyanide-bridged mixed chain compounds Fe(III)/Ln(III) (Ln = Pr, Nd, Sm, Eu, Gd, Tb) with the tridentate 2,4,6-tri (2-pyridyl)-1,3,5-triazine (tptz) ligand as a capping group were prepared, and their structures and magnetic properties determined. The complexes represent rare examples in which a planar tridentate ligand, in this case tptz, behaves as a capping group for the lanthanide ions via three of its six nitrogen atoms. These Ln(III) building blocks are bridged by cyanide groups of Fe(III) and Cr(III) cyanometallates, which leads to the formation of one-dimensional chains. Magnetic susceptibility measurements of the compounds that contain Sm indicate that the Sm(III) ion is ferromagnetically coupled to the Fe(III) and Cr(III) ions through the cyanide bridge. At low temperature the compounds exhibit spin-glass-like magnetic ordering.

In addition, a family of supramolecular nanotubes of general formula $\{[Ln(tptz)(HCOO)_3]\cdot 2.5H_2O\}_\infty$ (Ln = Pr, Sm) has been prepared. The crystal structures reveal that, in the solid state, there are tubes with 1D internal channels as well as additional 1D channels generated by the infinite network of π interactions between tptz units from adjacent nanotubes. The present compounds are rare cases of mixed types of channels; one of them is based on coordination bonds and the other is based on supramolecular π-π interactions in the solid state. The material retains its crystallinity when heated in the solid state under vacuum at 150°C, but rapidly loses crystallinity when heated to refluxing conditions in methanol presumably due to disruption of the intermolecular π-π interactions that hold the tubes together. These findings are

interesting additions to the relatively unexplored field of MOFs based on lanthanide ions given that most of the MOFs studies have been devoted to transition metals complexes.

Experimental

Starting Materials: All chemicals and solvents were used as received. The reagents 3,4,7,8-tetramethyl-1,10-phenanthroline (tmphen), 2,4,6-tri(2-pyridyl)-1,3,5-triazine (tptz), and 18-crown-6 were purchased from Aldrich and used without further purification. The salt $[(18\text{-crown-6})K]_3Cr(CN)_6$ was prepared *in situ* by stirring an excess of $K_3Fe(CN)_6$ in a solution of 18-crown-6 in methanol. The salt $[NH_4][HCOO]$ was prepared by adding formic acid (73 gr, 1.59 moles) to a 1 liter round bottomed flask in an ice bath followed by slow addition of ethanol (150 ml) while stirring. Then, NH_4OH was added slowly with fuming and after 10 minutes of stirring the ice bath was removed and the contents were stirred for another 30 minutes. The solvent was removed under reduced pressure in a rotatory evaporator followed by overnight storage in the freezer. The colorless crystalline product was collected. Yield 95.35 g (95%).

Physical Measurements: IR spectra were measured as Nujol mulls between KBr plates on a Nicolet 740 FT-IR spectrometer. Magnetic susceptibility and magnetization measurements were carried out with a Quantum Design SQUID magnetometer MPMS-XL. DC magnetic measurements were performed in an applied field of 1000 G in the 2 - 300 K temperature range. AC magnetic susceptibility measurements were performed in a 3 G AC field in the frequency range of 1 - 1000 Hz. Magnetization data were collected in the 0 - 7 T range beginning at zero field at 2 K. The data were corrected for diamagnetic contributions as calculated from Pascal constants.[269]

Syntheses: $\{[Pr(tptz)(H_2O)_4Fe(CN)_6]\cdot 8H_2O\}_\infty$ **(PrFe),** $\{[Nd(tptz)(H_2O)_4Fe(CN)_6]\cdot 8H_2O\}_\infty$ **(NdFe),** $\{[Sm(tptz)(H_2O)_4Fe(CN)_6]\cdot 8H_2O\}_\infty$ **(SmFe),** $\{[Eu(tptz)(H_2O)_4Fe(CN)_6]\cdot 6H_2O\}_\infty$ **(EuFe),** $\{[Gd(tptz)(H_2O)_4Fe(CN)_6]\cdot 6H_2O\}_\infty$ **(GdFe),** and $\{[Tb(tptz)(H_2O)_4Fe(CN)_6]\cdot 8H_2O\}_\infty$ **(TbFe).** To a solution of $LnCl_3\cdot 6H_2O$ or $Ln(NO_3)_3\cdot 6H_2O$ (0.1 mmol in water (2.5 mL) was added dropwise, with stirring, a solution of 2,4,6-tri(2-pyridyl)-1,3,5-triazine (tptz) in methanol (2 mL). The resulting light yellow solution was layered with a solution of $K_3Fe(CN)_6$ (33 mg, 0.10 mmol) in MeOH/H_2O (2 mL/2.5mL). Yellow crystals were obtained after one week. Compound **PrFe**: Yield 52 mg (48%). Calculated for $C_{24}H_{20}N_{12}O_4FePr$: C, 39.10%; H, 2.73%; N, 22.80%. Found: C, 38.65%; H, 3.29%; N, 21.75%. IR data (Nujol, cm^{-1}): ν(C≡N), 2117, 2131, 2143. Compound **NdFe**: Yield 51 mg (51%). Calculated for $C_{24}H_{20}N_{12}O_4FeNd$: C, 38.92%; H, 2.72%; N, 22.70%. Found: C, 38.01%; H, 3.35%; N, 21.37 %. IR data (Nujol, cm^{-1}): ν(C≡N), 2120, 2130, 2154. Compound **SmFe**: Yield 41 mg (45%). Calculated for $C_{24}H_{36}N_{12}O_{12}FeSm$: C, 32.36%; H, 4.07%; N, 18.87%. Found: C, 33.87%; H, 3.57%; N, 19.48%. IR data (Nujol, cm^{-1}): ν(C≡N), 2114, 2144. Compound **EuFe**: Yield 55 mg (54 %). Calculated for $C_{24}H_{20}N_{12}O_4FeEu$: C, 38.52%; H, 2.69%, N, 22.46%. Found: C, 36.57%; H, 3.10 %; N, 21.09%. IR data (Nujol, cm^{-1}): ν(C≡N) 2120, 2132, 2158. Compound **GdFe**: Yield 58 mg (44 %). Calculated for $C_{24}H_{22}N_{12}O_5FeGd$: C, 37.35%; H, 2.87%; N, 21.79%. Found: C, 37.17%; H, 2.97%; N, 21.23%. IR data (Nujol, cm^{-1}): ν(C≡N), 2112, 2130, 2142 cm^{-1}. Compound **TbFe**: Yield 39 mg (42%).

Calculated for $C_{24}H_{36}N_{12}O_{12}FeTb$: C, 32.00%; H, 4.00%; N, 18.70%. Found: C, 33.27%; H, 2.93%; N, 18.96%. IR data (Nujol, cm^{-1}): ν(C≡N) 2110, 2143.

$\{[Sm(tptz)(H_2O)_4Co(CN)_6]\cdot 8H_2O\}_\infty$ (**SmCo**). $SmCl_3\cdot 6H_2O$ (0.1 mmol in 2.5 mL of water) was added dropwise to a solution of 2,4,6-tri(2-pyridyl)-1,3,5-triazine (tptz) in methanol (2 mL) with stirring. The resulting colorless solution was layered with a solution of $K_3Co(CN)_6$ (35 mg, 0.10 mmol) in MeOH/H_2O (2 mL/2.5mL). IR data (Nujol, cm^{-1}): ν(C≡N), 2116, 2133, 2146.

$\{[La(tptz)(DMF)(H_2O)_3Fe(CN)_6]\cdot 5H_2O\}_\infty$ **(LaFe).** To a solution of $LaCl_3\cdot 6H_2O$ or $Ln(NO_3)_3\cdot 6H_2O$ (0.1 mmol in water (2 mL) was added dropwise with stirring a solution of 2,4,6-tri(2-pyridyl)-1,3,5-triazine (tptz) in methanol (3 mL). The resulting light yellow solution was layered over a solution of $K_3Fe(CN)_6$ (33 mg, 0.10 mmol) in MeOH/H_2O/DMF (2 mL/2 mL/1 mL) and the reaction was left to stand undisturbed. Yellow crystals were obtained after approximately one week. Yield 57 mg (67%). IR data (Nujol, cm^{-1}): ν(C≡N), 2121, 2151.

$\{[Sm(tmphen)(DMF)_3(H_2O)Fe(CN)_6]\cdot 2H_2O\}_\infty$ **(DMF-L_2SmFe).** A sample of $SmCl_3\cdot 6H_2O$ (36 mg, 0.10 mmol) was dissolved in 3 mL of methanol and combined with 1 equivalent of tmphen (24 mg, 0.10 mmol) dissolved in 3 mL of methanol. This solution was layered over a solution of $K_3Fe(CN)_6$ (33 mg, 0.10 mmol) in MeOH/DMF (3 mL/1mL) and the layered solutions were left undisturbed for one week after which time colorless crystals were harvested. Yield 59 mg (68%). IR data (Nujol, cm^{-1}): ν(C≡N), 2123, 2207, ν(C=O), 1643.

$\{[Sm(tmphen)_2(H_2O)_2Fe(CN)_6]\cdot MeOH\cdot 13H_2O\}_\infty$ **(L_2SmFe).** A quantity of $SmCl_3\cdot 6H_2O$ (36 mg, 0.10 mmol) in 3 mL of methanol was combined with 2 equivalents of tmphen (48 mg, 0.20 mmol) dissolved in 3 mL of methanol. The solution was layered with $K_3Fe(CN)_6$ (33 mg, 0.10 mmol) in methanol (3 mL). After approximately one week. Colorless crystals were obtained. In 70% yield (80 mg). IR data (Nujol, cm^{-1}): ν(C≡N), 2114, 2141 cm^{-1}.

$\{[Sm(tmphen)_2(H_2O)_2Cr(CN)_6]\cdot MeOH\cdot 9H_2O\}_\infty$ **(L_2SmCr).** A sample of $SmCl_3\cdot 6H_2O$ (36 mg, 0.10 mmol) in 3 mL of methanol was mixed with tmphen (48 mg, 0.20 mmol) in 3 mL of methanol and layered with a solution of $[(18\text{-crown-}6)K]_3Cr(CN)_6$ (112 mg, 0.10 mmol) in MeOH/DMF (3 ml/1ml). Colorless crystals were obtained after one week. Yield 40 mg (37%). IR data (Nujol, cm^{-1}): ν(C≡N), 2111, 2141, 2151.

Synthesis of Single Crystals of $[Sm(tptz)(HCOO)_3]\cdot 2.5H_2O\}_\infty$: To a solution of $Sm(Otf)_3\cdot 6H_2O$ (0.5 mmol) in methanol (5 mL) was added dropwise, with stirring, a solution of 2,4,6-tri(2-pyridyl)-1,3,5-triazine (tptz) (0.5 mmol) in methanol (5 mL) and the mixture was stirred for 20 minutes. Methanol (4 mL) was added to the top of the resulting light purple solution to slow down the diffusion and then a solution of $[NH_4][HCOO]$ (95 mg, 1.5 mmol) in methanol (6 mL) was layered on top. Colorless single crystals were collected after 1 week and washed three times with aliquots of methanol (10 mL). Yield 213 mg (66%).

Bulk Synthesis of $[Sm(tptz)(HCOO)_3]\cdot 2.5H_2O\}_\infty$: To a solution of $Sm(Otf)_3\cdot 6H_2O$ (352 mg, 0.5 mmol) in methanol (5 mL) was added dropwise, with stirring, a solution of 2,4,6-tri(2-pyridyl)-1,3,5-triazine (tptz) (156 mg, 0.5 mmol) in methanol (4 mL) and

stirring was kept for 20 minutes. The resulting light purple solution was stirred with a solution of $[NH_4][HCOO]$ (95 mg, 1.5 mmol) in methanol (3 mL). White microcrystalline material was collected after 30 minutes and washed three times with aliquots of methanol (10 mL). Yield 222 mg (69%).

X-ray Crystallography: Single crystal X-ray data sets were collected on a Bruker APEX CCD X-ray diffractometer for **PrFe**, **NdFe**, **GdFe**, **TbFe**, and **LaFe**. For compounds **SmFe**, **EuFe**, **SmCo**, **LaFe**, **DMF-L$_2$SmFe**, **L$_2$SmFe**, **L$_2$SmCr**, and $\{[Ln(tptz)(HCOO)_3]\cdot 2.5H_2O\}_\infty$ (Ln = Pr, Sm) the data sets were collected on a Bruker SMART 1000 CCD X-ray diffractometer. In both cases the diffractometers were equipped with graphite monochromated Mo-K_α radiation (λ = 0.71073 Å). Crystal data and details of the data collection and refinement parameters are summarized in Tables 6.1-6.4. Important bond distances and angles for **PrFe**, **SmFe**, **SmCo**, **L$_2$SmFe**, and **L$_2$SmCr** are listed in Tables 6.5-6.9.

A total of 1271 frames were collected for each crystal. The first 50 frames were recollected at the end of the data collections to monitor for decay. In each case, the crystals used for the diffraction studies showed no decomposition during data collection. The integration process led to a total of 20,562 reflections for **PrFe**, 19,961 for **NdFe**, 20,560 for **SmFe**, 27,567 for **EuFe**, 20,278 for **GdFe,** 20,122 for **TbFe**, 20,483 for **SmCo**, 40,258 for **LaFe**, 12,589 reflections for **DMF-L$_2$SmFe**, 22,489 for **L$_2$SmFe**, 10,850 for **L$_2$SmCr**, 42,024 for $\{[Pr(tptz)(HCOO)_3]\cdot 2.5H_2O\}_\infty$, and 23,457 for $\{[Sm(tptz)(HCOO)_3]\cdot 2.5H_2O\}_\infty$, of which 7923 [R(int) = 0.0395], 7907 [R(int) = 0.0599], 7815 [R(int) 0.0374], 7986 [R(int) 0.0501], 7671 [R(int) 0.0947], 7611 [R(int)

0.0500], 7758 [R(int) 0.0561], 8648 [R(int) 0.0751], 9062 [R(int) 0.0339], 7431 [R(int) 0.0520], 7067 [R(int) 0.0509], 3098 [R(int) 0.0271], 3023 [R(int) 0.0885] were unique, respectively. The frames were integrated with the use of the Bruker SAINT software package,[270] and the data were corrected for absorption using the program SADABS.[147] The structures were solved and refined using X-SEED,[271] a graphical interface to the SHELX[272] suite of programs. All non-solvent atoms were refined anisotropically. Hydrogen atoms were included in calculated positions and refined in the riding mode, except for the water molecules, which were located by residual density maps and refined in fixed positions in the riding mode.

For **PrFe**, the final refinement cycle was based on 7923 reflections with $F_\sigma > 4\sigma(F_o)$ and 446 parameters ($R1 = 0.0595$, $wR2 = 0.1375$). The maximum and minimum peaks in the final difference Fourier map corresponded to 1.298 and –2.125 e/Å^3, respectively, with a goodness-of-fit value of 1.088. The final refinement cycle for **NdFe** was based on 7907 reflections with $F_\sigma > 4\sigma(F_o)$ and 451 parameters ($R1 = 0.0752$, $wR2 = 0.1787$). The maximum and minimum peaks in the final difference Fourier map corresponded to 2.780 and –2.921 e/Å^3, respectively, with a goodness-of-fit value of 1.111. For **SmFe**, the final refinement cycle was based on 7815 reflections with $F_\sigma > 4\sigma(F_o)$ and 451 parameters ($R1 = 0.0639$, $wR2 = 0.1711$). The maximum and minimum peaks in the final difference Fourier map corresponded to 2.244 and –1.535 e/Å^3, respectively, with a goodness-of-fit value of 1.055. The final refinement cycle for **EuFe** was based on 7986 reflections with $F_\sigma > 4\sigma(F_o)$ and 424 parameters ($R1 = 0.0617$, $wR2 = 0.1559$). The maximum and minimum peaks in the final difference Fourier map corresponded to 2.528 and –2.303

e/Å^3, respectively, with a goodness-of-fit value of 1.186. For **GdFe**, the final refinement cycle was based on 7671 reflections with $F_\sigma > 4\sigma(F_o)$ and 433 parameters ($R1$ = 0.0716, $wR2$ = 0.1947). The maximum and minimum peaks in the final difference Fourier map corresponded to 2.119 and –1.319 e/Å^3, respectively, with a goodness-of-fit value of 1.046. In the case of compound **TbFe**, the final refinement cycle was based on 7611 reflections with $F_\sigma > 4\sigma(F_o)$ and 451 parameters ($R1$ = 0.0619, $wR2$ = 0.1425). The maximum and minimum peaks in the final difference Fourier map corresponded to 1.830 and –2.146 e/Å^3, respectively, with a goodness-of-fit value of 1.088. The final refinement cycle for **SmCo** was based on 7758 reflections with $F_\sigma > 4\sigma(F_o)$ and 446 parameters ($R1$ = 0.0564, $wR2$ = 0.1374). The maximum and minimum peaks in the final difference Fourier map corresponded to 1.716 and –1.620 e/Å^3, respectively, with a goodness-of-fit value of 1.036. For compound **LaFe**, the final refinement cycle was based on 8648 reflections with $F_\sigma > 4\sigma(F_o)$ and 420 parameters ($R1$ = 0.0606, $wR2$ = 0.1604). The maximum and minimum peaks in the final difference Fourier map corresponded to 2.461 and –1.369 e/Å^3, respectively, with a goodness-of-fit value of 1.069. For **DMF-L$_2$SmFe**, the final refinement cycle was based on 9062 reflections with $F_\sigma > 4\sigma(F_o)$ and 453 parameters ($R1$ = 0.0636, $wR2$ = 0.1753). The maximum and minimum peaks in the final difference Fourier map corresponded to 2.611 and –2.032 e/Å^3, respectively, with a goodness-of-fit value of 1.107. The final refinement cycle for **L$_2$SmFe** was based on 7431 reflections with $F_\sigma > 4\sigma(F_o)$ and 636 parameters ($R1$ = 0.0476, $wR2$ = 0.1100). The maximum and minimum peaks in the final difference Fourier map corresponded to 1.284 and –0.761 e/Å^3, respectively, with a goodness-of-fit

value of 1.070. The final refinement cycle for **L_2SmCr** was based on 7067 reflections with $F_\sigma > 4\sigma(F_o)$ and 577 parameters ($R1$ = 0.0813, $wR2$ = 0.2224). The maximum and minimum peaks in the final difference Fourier map corresponded to 2.375 and –1.215 e/Å^3, respectively, with a goodness-of-fit value of 1.049.

For {[Pr (tptz)$(HCOO)_3$]·2.5H_2O}$_\infty$, the final refinement cycle was based on 3098 reflections with $F_\sigma > 4\sigma(F_o)$ and 177 parameters ($R1$ = 0.0577, $wR2$ = 0.1450). The maximum and minimum peaks in the final difference Fourier map corresponded to 1.441 and –1.961 e/Å^3, respectively, with a goodness-of-fit value of 1.178. For {[Sm(tptz)$(HCOO)_3$]·2.5H_2O}$_\infty$, the final refinement cycle was based on 3023 reflections with $F_\sigma > 4\sigma(F_o)$ and 166 parameters ($R1$ = 0.0673, $wR2$ = 0.1490). The maximum and minimum peaks in the final difference Fourier map corresponded to 2.955 and –2.397 e/Å^3, respectively, with a goodness-of-fit value of 1.133.

Crystallographic data for the structural analyses have been deposited at the Cambridge Crystallographic Data Center: **PrFe** (CCDC 296493), **NdFe** (CCDC 296494), **SmFe** (CCDC 296495), **EuFe** (CCDC 296496), **GdFe** (CCDC 296497), **TbFe** (CCDC 296498), **SmCo** (CCDC 296499), **LaFe** (CCDC 296500), **DMF-L_2SmFe** (CCDC 296501), **L_2SmFe** (CCDC 296502), and **L_2SmCr** (CCDC 296503). Copies of this information may be obtained free from the Director, CCDC, 12 Union Road, Cambridge CB2 1EW, UK (Fax: +44 1223 336 033; E-mail: deposit@ccdc.cam.ac.uk or www: http://www.ccdc.com.ac.uk).

CHAPTER VII

SUMMARY OF CHAPTERS

In order for the eventual realization of the aforementioned goals in the fields of molecular conductors and magnets, chemists need to design and synthesize new molecular materials with well understood properties. Our interest in TCNQ derivatives originated from the observation that, although a vast amount of research has been directed at understanding binary $M(TCNQ^{\bullet-})_x$ (x = 1,2) systems, analogous materials based on substituted derivatives of TCNQ are surprisingly scarce. Given this situation, we initiated a broad survey of binary metal-containing TCNQ derivatives in order to probe the steric and electronic influences of the substituent on the structure and properties of these materials.

Chapter II describes the syntheses and characterization of molecular conductors based on Cu^{I} ions and TCNQ derivatives. Although much effort has been expended to understand the Cu(TCNQ) system, there is still a debate about the nature of the properties and new compounds based on TCNQ derivatives that may help to lend insight have not been pursued. Results in this chapter include the isolation of large single crystals of a new structure type for the $M^{+}(TCNQ)^{\bullet-}$ family that were isolated from reactions of two dihalogenated TCNQ derivatives with Cu^{+} ions. The materials were fully characterized by X-ray diffraction, conductivity measurements, SEM studies and infrared and XPS spectroscopies. The new compound $Cu(TCNQCl_2)$ exhibits the highest room temperature conductivity (1.15 Scm^{-1}) of the $M^{+}(TCNQ)^{\bullet-}$ series, in spite of the

fact that the $TCNQCl_2$ units exhibit a large separation in the stacks. The surprisingly high conductivities of $Cu(TCNQCl_2)$ and $Cu(TCNQBr_2)$ are attributed to charge-carrier transport through copper ions, which is unprecedented for $M^+(TCNQ)^{\bullet-}$ materials. Structural characterization for the second product of the dibromo derivative, namely $Cu(TCNQBr_2)(CH_3CN)$, indicates that acetonitrile has a similar affinity to Cu^I ions as the reduced $TCNQBr_2$ ligand. The product is a 2D framework with $[\mu_3\text{-}TCNQBr_2]^-$ ligands, Studies performed with $TCNQI_2$ indicate that the larger size of the iodo group leads to single crystals of a 1D zigzag chain with trans-μ_2-$TCNQI_2$ and two acetonitrile molecules bound to the copper ions, which is further evidence of the similar affinity of TCNQ derivatives and acetonitrile for copper(I) ions.

The focus of Chapter III is the syntheses and characterization of 2D molecular magnets based on first row transition metals and TCNQ derivatives. The use of first row metal ions and substituted TCNQ derivatives is a relatively unexplored topic with the only report being the $V(TCNQX_2)\cdot zCH_2Cl_2$ (z ~ 1.38-0.02; X = H, Br, Me, Et, i-Pr, OMe, OEt, and OPh) study from the group of Miller and coworkers.[151] Thus, it is of considerable interest to obtain more molecular magnets with other first row transition metals. We successfully synthesized a Mn^{II}-$TCNQF_4$ material of formula $\{[Mn_2(TCNQF_4)(CH_3OH)_{7.5}(H_2O)_{0.5}](TCNQF_4)_2\cdot 7.5CH_3OH\}_\infty$ whose structure consists of a 2D hexagonal net based on a $[\mu_4\text{-}TCNQF_4]^{2-}$ dianion with free $[TCNQF_4]^{\bullet-}$ radical anions residing between the layers. Removal of methanol molecules from the interstices of the 2D hexagonal metal-organic framework results in stronger magnetic interactions

and leads to a glassy magnetically ordered state; the magnetic behavior can be reversibly cycled upon solvation-desolvation of the material.

In another effort, the method previously developed in our laboratories[52] for preparing $M^{II}(TCNQ)_2$ magnets was extended to the preparation of M/$TCNQF_4$ binary phases. The reaction of the fully solvated precursors $[M^{II}(CH_3CN)_6](BF_4)_2$ and $TBA(TCNQF_4)$ in acetonitrile leads to materials that magnetically order at 10 K and 6 K for Co^{II} and Mn^{II} respectively. In related studies, spontaneous electron transfer occurs between zero-valent metals and neutral $TCNQBr_2$ in acetonitrile produced isostructural compounds of formula $[M(TCNQBr_2)_2(H_2O)_2]_\infty$ (M^{II} = Mn and Zn; $TCNQBr_2$ = 2,5-dibromo-7,7,8,8-tetracyanoquinodimethane). These materials, which have scavenged water from ambient sources, crystallize as a 2D double layer. The equatorial positions of the metal ions are occupied by nitrogen atoms from different $TCNQBr_2$ units, with the axial positions being occupied by water molecules. The $TCNQBr_2$ ligand is present as a radical and is coordinated to two metal ions in a trans-μ_2 fashion.

Chapter IV is concerned with the use of TCNQ derivatives for the generation of 2p-4f heterospin molecular magnets, an area that is quite unexplored. The synthesis and characterization of a discrete terbium/$TCNQF_4$ mononuclear complex was undertaken and the magnetic properties were probed by performing dilution studies on the Tb compound with diamagnetic Y ions. A series of isostructural compounds of general formula $\{M[TCNQF_4]_2[H_2O]_6\}\cdot(TCNQF_4)(3H_2O)$, M = Tb (**Tb**), Y (**Y**), Y:Tb (74:26) ($\mathbf{Y_{0.74}Tb_{0.26}}$), and Y:Tb (97:3) ($\mathbf{Y_{0.97}Tb_{0.03}}$) was prepared and the magnetic properties of the members were investigated. Compounds **Tb**, $\mathbf{Y_{0.74}Tb_{0.26}}$, and $\mathbf{Y_{0.97}Tb_{0.03}}$ show the

beginning of a frequency-dependent out-of-phase ac signal with a decrease in the intensity of the signal being observed with decreased concentration of Tb^{III} ions in the diluted samples. No out-of-phase signal was observed for **Y**, an indication that the behavior of **Tb**, $\mathbf{Y_{0.74}Tb_{0.26}}$, and $\mathbf{Y_{0.97}Tb_{0.03}}$ is due to slow paramagnetic relaxation of Tb^{III} ions in the samples. A more detailed micro-SQUID study at low temperature, carried out in collaboration with Dr. Wolfgang Wernsdorfer from the Institut Néel at Grenoble, revealed an interplay between single molecule magnetic (SMM) behavior and a phonon bottleneck (PB) effect, and that these properties depend on the concentration of diamagnetic Yttrium ions. A combination of SMM and PB phenomena was found for **Tb** with an increase in the PB effect being observed with increasing dilution until eventually a pure PB effect is observed for **Y**. The PB behavior is interpreted as being due to the presence of the "sea of organic S = 1/2 radicals" from the $TCNQF_4$ radicals in these compounds. These data underscore the fact that the presence of an out-of-phase ac signal may not, in fact, be caused by SMM behavior, particularly when magnetic metal ions are combined with organic radical ligands such as those found in the organocyanide family.

Chapter V describes the syntheses and characterization of a homologous family of lanthanide/$TCNQF_4$ heterospin system. This is the first family of 2p-4f molecular magnets based on TCNQ derivatives, moreover there are no prior reports on the coordination chemistry of lanthanide ions and any TCNQ derivatives. Reactions between trivalent rare earth ions (M^{III} = La, Pr, Nd, Sm, Eu, Gd, Dy, Ho, Er and Yb) and the radical anion of 2,3,5,6-tetrafluoro-7,7,8,8-tetracyanoquinodimethane ($TCNQF_4$) produce a family of mononuclear complexes $\{M[(TCNQF_4)]_2[H_2O]_x\}\cdot(TCNQF_4)(3H_2O)$,

x = 6, 7. The cationic complex $\{M^{III}([TCNQF_4]^{-\bullet})_2[H_2O]_x\}^+$ cocrystallizes with one $[TCNQF_4]^{-\bullet}$ radical anion and three water molecules. One of the coordinated $[TCNQF_4]^{-\bullet}$ radicals is involved in π-π stacking interactions with the uncoordinated $[TCNQF_4]^{-\bullet}$ radicals which leads to the antiferromagnetic coupling for these $((TCNQF_4)_2)^{2-}$ π-dimers. The second coordinated $[TCNQF_4]^{-\bullet}$ remains as a radical ligand and is not involved in π-π interactions. Magnetic studies indicate that the **Sm** compound magnetically orders at 4.4 K and that a fraction of the **Gd** and **Dy** samples undergo magnetic ordering at 3.7 K and 4.3 K respectively due to partial dehydration (loss of interstitial water molecules). Diamagnetic metal ions were used to generate magnetically dilute **Sm**, **Gd**, and **Dy** compounds that do not exhibit any signs of magnetic ordering.

Chapter VI focuses on the syntheses and characterization of 3d-4f heterospin 1D arrays generated by the use of blocking ligands bound to lanthanide ions as a molecular building block, which, upon coordination to cyanometallates or formate anions, forms 1D chains or 1D coordination nanotubes respectively. We discovered that the Sm^{III}-$[Fe^{III}(CN)_6]^{3-}$compound is ferromagnetically coupled with 3-D ordering occurring below 3.5 K. The Sm-Fe interaction in similar 1-D chains was previously assigned as antiferromagnetic, but we were able to refute this claim by carefully subtracting the contributions of Sm^{III} and Fe^{III} ions from model compounds that are isostructural to the original chain. A series of cyanide-bridged chain mixed Fe(III)/Ln(III) (Ln = Pr, Nd, Sm, Eu, Gd, Tb) complexes with the tridentate ligand 2,4,6-tri(2-pyridyl)-1,3,5-triazine (tptz) used as a capping group has been prepared. Reactions of tptz and $LnCl_3$ with $K_3Fe(CN)_6$ yield a family of air-stable 1-D compounds $\{[Pr(tptz)(H_2O)_4Fe(CN)_6]\cdot 8H_2O\}_\infty$ (**PrFe**),

$\{[Nd(tptz)(H_2O)_4Fe(CN)_6]\cdot 8H_2O\}_\infty$ (**NdFe**), $\{[Sm(tptz)(H_2O)_4Fe(CN)_6]\cdot 8H_2O\}_\infty$ (**SmFe**), $\{[Eu(tptz)(H_2O)_4Fe(CN)_6]\cdot 6H_2O\}_\infty$ (**EuFe**), $\{[Gd(tptz)(H_2O)_4Fe(CN)_6]\cdot 6H_2O\}_\infty$ (**GdFe**), and $\{[Tb(tptz)(H_2O)_4Fe(CN)_6]\cdot 8H_2O\}_\infty$ (**TbFe**). Temperature dependent magnetic susceptibility studies reveal that, in the case of **SmFe**, the Sm(III) and Fe(III) ions are ferromagnetically coupled with 3-D ordering occurring below 3.5 K. The appearance of the frequency dependent out-of-phase signal is explained in terms of an ordering with a spin-glass like behavior. To compare the magnetic behavior of **SmFe** with related compounds, $\{[Sm(tptz)(H_2O)_4Co(CN)_6]\cdot 8H_2O\}_\infty$ (**SmCo**) and $\{[La(tptz)(DMF)(H_2O)_3Fe(CN)_6]\cdot 5H_2O\}_\infty$ (**LaFe**), $\{[Sm(tmphen)(DMF)_3(H_2O)$-$Fe(CN)_6]\cdot 2H_2O\}_\infty$ (**DMF-L$_2$SmFe**), $\{[Sm(tmphen)_2(H_2O)_2Fe(CN)_6]\cdot MeOH\cdot 13H_2O\}_\infty$ (**L$_2$SmFe**) and $\{[Sm(tmphen)_2(H_2O)_2Cr(CN)_6]\cdot MeOH\cdot 9H_2O\}_\infty$ (**L$_2$SmCr**) with 3,4,7,8-tetramethyl-1,10-phenanthroline (L_2 = tmphen) were also prepared.

The isolation of a family of supramolecular nanotubes of general formula $\{[Ln(tptz)(HCOO)_3]\cdot 2.5H_2O\}_\infty$ (Ln = Pr, Sm) is also described in this chapter. It was first serendipitously isolated in low yields from $Pr(tptz)(Cl)_3$ in the solvent DMF which generate small amounts of formate ions. Later the nanotubes were synthesized in high yields by combining $Sm(tptz)(H_2O)_3(triflate)_3$ with formate ions in methanol. The crystal structures reveal that, in the solid state, there are tubes with 1D internal channels as well as additional 1D channels generated by the infinite network of π interactions between tptz units from adjacent nanotubes. The resulting material has a combination of two types of tubular channels of different sizes (3.3 Å and 6.9 Å after subtraction of van der Waals radii) in a hexagonal honeycomb arrangement. It is important to point out that

there are a limited number of coordination nanotubes in the literature and that most of them contain transition metals. In fact there is only one report of a coordination nanotube based on La^{III} ions. Thus, the present isostructural family of coordination tubes is of interest because it represents an extension of such low dimensional materials by the use of lanthanide ions.

REFERENCES

[1] J. Yamada, H. Akutsu, H. Nishikawa, K. Kikuchi, *Chem. Rev*. **2004**, *104*, 5057-5083.

[2] H. Yamochi, G. Saito in *Multifunctional Conducting Molecular Materials*, (Eds.: G. Saito, F. Wudl, R. C. Haddon, K. Tanigaki, T. Enoki, H. E. Katz, M. Maesato), The Royal Society of Chemistry: Cambridge, UK, **2007**; pp. 107-114.

[3] H. Kobayashi, Y. Okano, H. Fujiwara, H. Tanaka, M. Tokumoto, W. Suzuki, E. Fujiwara, A. Kobayashi, in *Organic Conductors, Superconductors and Magnets: From Synthesis to Molecular Electronics, Nato Science Series II*, *Vol 139* (Eds.: L. Ouahab, E. Yagubskii), Kluwer Academic Publishers, Dordrecht, The Netherlands, **2004**, pp. 81-98.

[4] K. Xiao, J. Tao, Z. Pan, A. A. Puretzky, I. N. Ivanov, S. J. Pennycook, D. B. Geohegan, *Angew. Chem. Int. Ed*. **2007**, *46*, 2650-2654.

[5] a) U. Geiser, H. H. Wang, C. Y. Han, G. A. Willing, in *Organic Conductors, Superconductors and Magnets: From Synthesis to Molecular Electronics, Nato Science Series II*, *Vol 139* (Eds.: L. Ouahab, E. Yagubskii), Kluwer Academic Publishers, Dordrecht, The Netherlands, **2004**, pp. 213-240; b) L. Valade, D. De Caro, I Malfant, in *Organic Conductors, Superconductors and Magnets: From Synthesis to Molecular Electronics, Nato Science Series II*, *Vol 139* (Eds.: L. Ouahab, E. Yagubskii), Kluwer Academic Publishers, Dordrecht, The Netherlands, **2004**, pp. 241-268.

[6] *Single-Molecule Magnets and Related Phenomena, Structure and Bonding, Vol 122* (Ed.: R. Winpenny), Springer, Heidelberg, **2006**.

[7] a) C. Coulon, H. Miyasaka, R. Clérac in *Single-Molecule Magnets and Related Phenomena, Structure and Bonding, Vol 122* (Ed.: R. Winpenny), Springer, Heidelberg, **2006**, pp. 163-206; b) H. Miyasaka, M. Julve, M. Yamashita, R. Clérac, *Inorg. Chem*. **2009**, *48*, 3420-3437.

[8] O. Sato, J. Tao, Y.-Z. Zhang, *Angew. Chem. Int. Ed*. **2007**, *46*, 2152-2187.

[9] a) E. Coronado, P. Day, *Chem. Rev.* **2004**, *104*, 5419-5448; b) L. Oauahab, in *Organic Conductors, Superconductors and Magnets: From Synthesis to Molecular Electronics, Nato Science Series II*, *Vol 139* (Eds.: L. Ouahab, E. Yagubskii), Kluwer Academic Publishers, Dordrecht, The Netherlands, **2004**, pp. 99-114.

[10] a) A. Cornia, A. F. Costantino, L. Zobbi, A. Caneschi, D. Gatteschi, M. Mannini, R. Sessoli in *Single-Molecule Magnets and Related Phenomena, Structure and Bonding, Vol 122* (Ed.: R. Winpenny), Springer, Heidelberg, **2006**, pp. 133-161; b) D. Gatteschi, A. Cornia, M. Mannini, R. Sessoli, *Inorg. Chem*. **2009**, *48*, 3408-3419.

[11] a) K. Katoh, Y. Yoshida, M. Yamashita, H. Miyasaka, B. K. Breedlove, T. Kajiwara, S. Takaishi, N. Ishikawa, H. Isshiki, Y. F. Zhang, T. Komeda, M. Yamagishi, J. Takeya, *J. Am. Chem. Soc*. **2009**, 131, 9967-9976; b) M. Mannini, F. Pineider, P. Sainctavit, L. Joly, A. Fraile-Rodríguez, M.-A. Arrio, C. C. dit Moulin, W. Wernsdorfer, A. Cornia, D. Gatteschi, R. Sessoli, *Adv. Mater*. **2009**, 21, 167–171; c) L. Bogani, C. Danieli, E. Biavardi, N. Bendiab, A.-L. Barra, E. Dalcanale, W. Wernsdorfer, A. Cornia, *Angew. Chem. Int. Ed*. **2009**, 48, 746 –750; d) L. Bogani, L.

Cavigli, M. Gurioli, R. L. Novak, M. Mannini, A. Caneschi, F. Pineider, R. Sessoli, M. Clemente-León, E. Coronado, A. Cornia, D. Gatteschi, *Adv. Mater.* **2007**, *19*, 3906–3911; e) D. Ruiz-Molina, J. Gomez, M. Mas-Torrent, A. I. Balana, N. Domingo, J. Tejada, M. T. Martinez, C. Rovira, J. Veciana, *Proc. SPIE Int. Soc. Opt. Eng.* **2003**, *5118*, 594-601.

[12] H. N. McCoy, W. C. Moore, *J. Am. Chem. Soc.*, **1911**, *33*, 273–292.

[13] M. Konno, Y. Saito, *Acta Cryst. B.* **1975**, *31*, 2007.

[14] M. Konno, T. Ishii, Y. Saito, *Acta Cryst. B.* **1977**, *33*, 763.

[15] H. Kobayashi, *Bull. Chem. Soc. Jpn.* **1981**, *54*, 3669.

[16] R. A. Heintz, H. Zhao, X. Ouyang, G. Grandinetti, J. Cowen, K. R. Dunbar, *Inorg. Chem*. **1999**, *38*, 144-156.

[17] L. Shields, *J. Chem. Soc., Faraday Trans. 2* **1985**, *81*, 1.

[18] a) D. L. Coffen, P. E. Garret, *Tetrahedron Lett*., **1969**, *10*, 2043; b) D. L. Coffen, *Tetrahedron Lett*., **1970**, *30*, 2633; c) D. L. Coffen, J. Q. Chambers, D. R. Williams, P. E. Garret, N. D. Canfield, *J. Am. Chem. Soc.*, **1971**, *93*, 2258.

[19] a) F. Wudl, G. M. Smith, E. J. Hufnagel, *J. Chem. Soc., Chem. Commun.,* **1970**, 1453; b) F. Wudl, D. Wobschal, E. J. Hufnagel, *J. Am. Chem. Soc.*, **1972**, *94*, 670.

[20] R. Zahradnik, P. Carsky, S. Hünig, G. Kiesslich, D. Scheutzow, *Int. J. Sulfur Chem. C.*, **1971**, *6*, 109.

[21] a) R. P. Shibaeva, E. B. Yagubskii, *Chem. Rev*., **2004**, *104*, 5347–5378; b) N. Toyota, M. Lang, J. Müller, in *Low Dimensional Molecular Metals*, *Solid State*

Sciences, Vol 154, (Eds.: M. Cardona, P. Fulde, K. von Klitzing, H. J. Queisser, R. Merlin, H. Störmer), Springer, Heidelberg, **2007**, pp. 1-6.

[22] D. Jérome, A. Mazaud, M. Ribault, K. Bechgaard, *J. Physique Lett.* **1980**, *41*, 95.

[23] G. Saito, H. Yamochi, M. Maesato, Y. Yoshida, A. Ota, Y. Shimizu, in *Organic Conductors, Superconductors and Magnets: From Synthesis to Molecular Electronics, Nato Science Series II*, *Vol 139* (Eds.: L. Ouahab, E. Yagubskii), Kluwer Academic Publishers, Dordrecht, The Netherlands, **2004**, pp. 19-44.

[24] E. B. Yagubskii, in *Organic Conductors, Superconductors and Magnets: From Synthesis to Molecular Electronics, Nato Science Series II*, *Vol 139* (Eds.: L. Ouahab, E. Yagubskii), Kluwer Academic Publishers, Dordrecht, The Netherlands, **2004**, pp. 45-64.

[25] a) R. Kondo, T. Hasegawa, T. Mochida, S. Kagoshima, Y. Iwasa, *Chem. Lett*., **1999**, 333-334; b) R. Kondo, T. Hasegawa, T. Mochida, S. Kagoshima, Y. Iwasa, K.-I. Hiraki, T. Takahashi, *J. Phys. Soc. Jpn*., **2001**, *70*, 3023-3030.

[26] A. Aumüller, S. Hünig, *Angew Chem. Int. Ed.,* **1984**, *23*, 447-448.

[27] A. Aumüller, E. Hädicke, S. Hünig, A. Schätzle, J. U. von Schütz, *Angew Chem. Int. Ed.,* **1984**, *23*, 449-450.

[28] a) A. Aumüller, P. Erk, G. Klebe, S. Hünig, J. U. von Schütz, H.-P. Werner, *Angew Chem. Int. Ed.* **1986**, *25*, 740-741; b) R. Kato, H. Kobayashi, A. Kobayashi, *J. Am. Chem. Soc.***1989**, *111*, 5224-5232; c) K. Sinzger, S. Hünig, M. Jopp, D. Bauer, W. Bietsch, J. U. von Schütz, H. C. Wolf, R. K. Kremer, T. Metzenthin, R. Bau, S. I.

Khan, A. Lindbaum, C. L. Lengauer, E. Tillmanns, *J. Am. Chem. Soc.* **1993**, *115,* 7696; d) S. Hünig, E. Herberth, *Chem. Rev*., **2004**, *104*, 5535-5563.

[29] M. Nakano, M. Kato, K. Yamada, *Physica* **1993**, *186-188,* 1077-9.

[30] J. U. von Schuetz, D.; Bauer, H. Wachtel, H. C. Wolf, *Synth. Met.* **1995**, *71*, 2089-90.

[31] D. Bauer, B. Maier, D. Schweitzer, J. U. von Schuetz, *Synth. Met.* **1995**, *71*, 1887-8.

[32] J. U. von Schuetz, D. Gomez, H. Wachtel, H. C. Wolf, *J. Chem. Phys*. **1996**, *105*, 6538-6545.

[33] J. U. von schutz, D. Gomez, H. Schmitt, H. Wachtel, *Synth. Met.* **1997**, *86,* 2095-2096.

[34] H. Schmitt, J. U. von Schutz, H. Wachtel, H. C. Wolf, *Synth. Met.* **1997**, *86*, 2257-2258.

[35] F. O. Karutz, J. U. von Schutz, H. Wachtel, H. C. Wolf, *Phys. Rev. Lett.* **1998**, *81*, 140-143.

[36] a) H. Tanaka, Y. Okano, H. Kobayashi, W. Suzuki, A. Kobayashi, *Science*, **2001**, *291*, 285-287; b) A. Kobayashi, E. Fujiwara, H. Kobayashi, *Chem. Rev*., **2004**, *104*, 5243–5264.

[37] A. N. Holden, B. T. Matthias, P. W. Anderson, H. W. Lewis, *Phys. Rev*., **1956**, *102*, 1463.

[38] H. H. Wickman, A. M. Trozzolo, H. J. Williams, G. W. Hull, F. R. Merritt, *Phys. Rev.,* **1967**, *155*, 563-566

[39] a) J. M. Manriquez, G. T. Yee, R. S. McLean, A. J. Epstein, J. S. Miller, *Science,* **1991,** *252,*1415-1417; b) T. Mallah, S. Thiébaut, M. Verdaguer, P. Veillet, *Science,***1993,** *262,* 1554-1557; c) W. R. Entley, G. S. Girolami, *Science,***1995,** *268,* 397-400; d) J. S. Miller, A. J. Epstein, *MRS Bull*., **2000**, *25*, 21-28; e) H. Miyasaka, T. Izawa, N. Takahashi, M. Yamashita, K. R. Dunbar, *J. Am. Chem. Soc.,* **2006**, *128*, 11358-11359; f) K. I. Pokhodnya, M. Bonner, J.-H. Her, P. W. Stephens, J. S. Miller, *J. Am. Chem. Soc.* **2006**, *128*, 15592-15593; g) J.-H. Her, P. W. Stephens, K. I. Pokhodnya, M. Bonner, J. S. Miller, *Angew.Chem.,Int.Ed.* **2007**, *46*, 1521-1524; h) N. Motokawa, H. Miyasaka, M. Yamashita, K. R. Dunbar, *Angew Chem. Int. Ed.,* **2008**, *47*, 7760-7763; i) R. Garde, J. M. Herrera, F. Villain, M. Verdaguer, Inorg. Chim. Acta, **2008**, *361*, 3597–3602; j) W. Kosaka, K. Imoto, Y. Tsunobuchi, S.-I. Ohkoshi, *Inorg. Chem.*, **2009**, *48*, 4604–4606; k) J. S. Miller, Polyhedron, **2009**, *28*, 1596-1605.

[40] a) Z. Wang, B. Zhang, M. Kurmoo, M. A. Green, H. Fujiwara, T. Otsuka, H. Kobayashi, *Inorg. Chem.* **2005**, *44*, 1230-1237; b) D. Maspoch, D. Ruiz-Molina, J. Veciana, *Chem. Soc. Rev.*, **2007**, *36*, 770–818; c) S. Galli, N. Masciocchi, G. Tagliabue, A. Sironi, J. A. R. Navarro, J. M. Salas, L. Mendez-Linan, M. Domingo, M. Perez-Mendoza, E. Barea, *Chem. Eur. J.* **2008**, *14*, 9890-9901; d) S. M. Neville, G. J. Halder, K. W. Chapman, M. B. Duriska, P. D. Southon, J. D. Cashion, J.-F. Létard, B. Moubaraki, K. S. Murray, C. J. Kepert, *J. Am. Chem. Soc*., **2008**, *130*, 2869-2876; e) K. Li, D. H. Olson, J. Y. Lee, W. Bi, K. Wu, T. Yuen, Q. Xu, J. Li, *Adv. Funct. Mater.* **2008**, *18*, 2205-2214; f) I. Boldog, A. B. Gaspar, V. Martínez, P.

Pardo-Ibañez, V. Ksenofontov, A. Bhattacharjee, P. Gütlich, J. A. Real, *Angew. Chem. Int. Ed.*, **2008**, *47*, 6433 –6437; g) M. Kurmoo, *Chem. Soc. Rev.*, **2009**, *38*, 1353–1379; h) E. Chelebaeva, J. Larionova, Y. Guari, R. A. S. Ferreira, L. D. Carlos, F. A. Almeida-Paz, A. Trifonov, C. Guérin, *Inorg. Chem.*, **2009**, *48*, 5983-5995; i) A. S. Lytvynenko, S. V. Kolotilov, O. Cador, K. S. Gavrilenko, S. Golhen, L. Ouahab, V. V. Pavlishchuk, *Dalton Trans*. **2009**, *18*, 3503-3509; j) G. Agustí, R. Ohtani, K. Yoneda, A. B. Gaspar, M. Ohba, J. F. Sánchez-Royo, M. C. Muñoz, S. Kitagawa, J. A. Real, *Angew Chem. Int. Ed.,***2009**, DOI: 10.1002/anie.200904379.

[41] a) R. Sessoli, H.-T. Tsai, A. R. Schake, S. Wang, J. B. Vincent, K. Folting, D. Gatteschi, G. Christou, D. N. Hendrickson, *J. Am. Chem. Soc.* **1993**, *115*, 1804-1816; b) R. Sessoli, D. Gatteschi, A. Caneschi, M. A. Novak, *Nature* **1993**, *365*, 141-143; c) J. R. Friedman, M. P. Sarachik, J. Tejada, R. Ziolo, *Phys. Rev. Lett.* **1996**, *76*, 3830-3833; d) L. Thomas, F. Lionti, R. Ballou, D. Gatteschi, R. Sessoli, B. Barbara, *Nature* **1996**, *383*, 145-147; e) J. M. Hernández, X. X. Zhang, F. Luis, J. Bartolomé, J. Tejada, R. Ziolo, *Europhys. Lett.* **1996**, *35*, 301-306; f) G.-Q. Bian, T. Kuroda-Sowa, H. Konaka, M. Hatano, M. Maekawa, M. Munakata, H. Miyasaka, M. Yamashita, *Inorg. Chem*. **2004**, *43*, 4790–4792; g) G. Aromí, E. K. Brechin, in *Single-Molecule Magnets and Related Phenomena, Structure and Bonding, Vol 122* (Ed.: R. Winpenny), Springer, Heidelberg, **2006**, pp. 1-67; h) L. Bogani, W. Wernsdorfer, *Nat. Mater.* **2008**, *7*, 179-186; i) M. Mannini, F. Pineider, P. Sainctavit, C. Danieli, E. Ptero, C. Sciancalepore, A. M. Talarico, M.-A. Arrio, A. Cornia, D. Gatteschi, R. Sessoli, *Nat. Mater*. **2009**, *8*, 194-197.

[42] a) D. B. Chesnut, W. D. Phillips, *J. Chem. Phys*., **1961**, *35*, 1002; b) L. R. Melby, R. J. Harder, W. R. Hertler, W. Mahler, R. E. Benson, W. E., Mochel, *J. Am. Chem. Soc.* **1962**, *84*, 3374.

[43] a) L. Ballester, A. Gutiérrez, M. F. Perpiñán, M. T. Azcondo, A. E. Sánchez, *Synth. Met*. **2001**,*120*, 965-966; b) H. Zhao, R. A. Heintz, K. R. Dunbar, *J. Am. Chem. Soc*. **1996**, *118*, 12844-12845; c) S. Shimomura, S. Horike, R. Matsuda, S. Kitagawa, *J. Am. Chem. Soc*. **2007**, *129*, 10990-10991.

[44] H. Oshio, E. Ino, T. Ito, Y. Maeda, *Bull. Chem. Soc. Jpn.* 1995, **68**, 889.

[45] S. Shimomura, R. Matsuda, T. Tsujino, T. Kawamura, S. Kitagawa, *J. Am. Chem. Soc.* 2006, **128**, 16416.

[46] a) J. S. Miller et al. *J. Phys. Chem.* 1987, **91**, 4344; b) D. A. Dixon, J. C. Calabrese, J. S. Miller, *J. Phys. Chem.* 1989, **93**, 2284.

[47] R. Choukroun, C. Lorber, D. de Caro, L. Vendier, *Organometallics* 2006, **25**, 4243.

[48] a) B. F. Abrahams, T. A. Hudson, R. Robson, *Cryst. Growth & Des.,* **2008**, *8*, 1123-1125; b) T. A. Hudson, R. Robson, *Cryst. Growth & Des.* **2009**, *9*, 1658-1662.

[49] a) J. S. Miller, J. C. Calabrese, A. J. Epstein, R. W. Bigelow, J. H. Zhang, W. M. Reiff, *Chem. Commun.* **1986**, 1026; b) J. S. Miller, A. J. Epstein, W. M. Reiff, *Science*, **1998**, *240*, 40.

[50] J. Zhang, J. Ensling, V. Ksenofontov, P. Gütlich, A. J. Epstein, J. S. Miller, *Angew. Chem. Int. Ed.*, **1998**, *37*, 657-660.

[51] S. A. O'Kane, R. Clérac, H. Zhao, X. Ouyang, J. R. Galán-Mascarós, R. Heintz, K. R. Dunbar, *J. Solid State Chem.* **2000**, *152*, 159.

[52] R. Clérac, S. O'Kane, J. Cowen, X. Ouyang, R. Heintz, H. Zhao, M. J. Jr. Bazile, K. R. Dunbar, *Chem. Mater*. **2003**, *15*, 1840.

[53] E. B. Vickers, I. D. Giles, J. S. Miller, *Chem. Mater.*, **2005**, *17*, 1667–1672.

[54] a) P. J. Kunkeler, P. J. van Koningsbruggen, J. P. Cornelissen, A. N. van der Horst, A. M. van der Kraan, A. L. Spek, J. G. Haasnoot, J. Reedijk, *J. Am. Chem. Soc.* **1996**, *118*, 2190; b) L. Ballester, A. Gutiérrez, M. F. Perpiñán, M. T. Azcondo, *Coord. Chem. Rev.* **1999**, *190*, 447; c) N. Lopez, A. V. Prosvirin, H. Zhao, W. Wernsdorfer, K. R. Dunbar, *Chem. Eur. J*., **2009**, *15*, 11390–11400.

[55] a) C. Campana, K. R. Dunbar, X. Ouyang, *Chem. Commun*. **1996**, 2427; b) H. Miyasaka, T. Madanbashi, K. Sugimoto, Y. Nakazawa, W. Wernsdorfer, K. Sugiura, M. Yamashita, C. Coulon, R. Clérac, *Chem. Eur. J.* **2006**, *12*, 7028; c) N. Motokawa, T. Oyama, S. Matsunaga, H. Miyasaka, K. Sugimoto, M. Yamashita, N. Lopez, Kim R. Dunbar, *Dalton Trans.*, **2008**, 4099–4102.

[56] a) H. Miyasaka, C. S. Campos-Fernández, R. Clérac, K. R. Dunbar, *Angew. Chem. Int. Ed.* **2000**, *39*, 3831; *Angew. Chem.* 2000, **112**, 3989; b) N. Lopez, H. Zhao, A. V. Prosvirin, A. Chouai, M. Shatruk, K. R. Dunbar, *Chem. Commun*., **2007**, *44*, 4611-4613; c) N. Motokawa, T. Oyama, S. Matsunaga, H. Miyasaka, M. Yamashita, K. R. Dunbar, *CrystEngComm*, **2009**, *11*, 2121-2130.

[57] a) Bartley, S. L.; Dunbar, K. R., *Angew. Chem. Int. Ed. Eng.* **1991**, *30*, 448-450; b) Bartley, S. L.; Bazile, Jr. M. J.; Clérac, R.; Zhao, H.; Ouyang, X.; Dunbar K. R., *Dalton Trans.* **2003**, 2937-2944.

[58] a) K. R. Dunbar, R. A. Heintz, *Prog. Inorg. Chem.* **1997**, *45*, 283; b) M. Verdaguer, A. Bleuzen, V. Marvaud, J. Vaissermann, M. Seuleiman, C. Desplanches, A. Scuiller, C. Train, R. Garde, G. Gelly, C. Lomenech, I. Rosenman, P. Veillet, C. Cartier, F. Villain, *Coord. Chem. Rev.* **1999**, *190-192*, 1023-1047; c) M. Verdaguer, G. S. Girolami, *Magn.: Mol. Mater. V* **2005**, 283; d) J. N. Rebilly, T. Mallah, in *Single-Molecule Magnets and Related Phenomena, Structure and Bonding, Vol 122* (Ed.: R. Winpenny), Springer, Heidelberg, **2006**, pp. 103-131; e) P. Day in *Molecules into Materials*, (Ed.: P. Day), World Scientific, Singapore, **2007**, pp. 465-468; f) M. Shatruk, C. Avendaño, K. R. Dunbar, *Prog. Inorg. Chem.* **2009**, *56*, 155–334.

[59] S. Ferlay, T. Mallah, R. Ouahès, P. Veillet, M. Verdaguer, *Nature,* **1995**, *378*, 701-703.

[60] T. Lis, *Acta Crystallogr. B Struct. Sci*. **1980**, *36*, 2042.

[61] D. Gatteschi, R. Sessoli, *Angew. Chem. Int. Ed*., **2003**, *42*, 268-297.

[62] W. Wernsdorfer, *Nat. Mater*., **2007**, *6*, 174-176.

[63] S. A. Wolf, D. D. Awschalom, R. A. Buhrman, J. M. Daughton, S. von Molnár, M. L. Roukes, A. Y. Chtchelkanova, D. M. Treger, *Science* **2001**, *294*, 1488-1495.

[64] D. D. Awshalom, M. M. Flatté, *Nature Phys*., **2007**, *3*, 153-159.

[65] P. Shor, *Proc. 35th Ann. Symp. Foundation of Computer Science* (Ed.: S. Goldwasser) IEEE Computer Society Press Los Alamito, **1994**.

[66] L. K. Grover, *Phys. Rev. Lett*., **1997**, *79*, 4709-4712.

[67] M. N. Leuenberger, D. Loss, *Nature*, **2001**, *410*, 789-793.

[68] F. Meier, J. Levy, D. Loss, *Phys. Rev. Lett*., **2003**, *90*, 0479014.

[69] F. Meier, J. Levy, D. Loss, *Phys. Rev. B* **2003**, *68*, 134417.

[70] F. Troiani, M. Affronte, S. Carretta, P. Santini, G. Amoretti, *Phys. Rev. Lett*., **2005**, *94*, 190501.

[71] a) A. Ardavan, S. J. Blundell, *J. Mater. Chem*., **2009**, *19*, 1754-1760; b) M. Affronte, *J. Mater. Chem.*, **2009**, *19*, 1731-1737.

[72] G. I. Meijer, *Science* **2008**, *319*, 1625.

[73] R. M. Metzger, *Chem. Rev*., **2003**, *103*, 3803-3824.

[74] H. Okamura, M. Matsubara, T. Nanba, T. Tayagaki, S. Mouri, K. Tanaka, Y. Ikemoto, T. Moriwaki, H. Kimura, G. Juhasz, *Phys. Rev. B: Condens. Matter* **2005**, *72*, 073108/1-073108/4.

[75] H. Okamura, M. Matsubara, T. Tayagaki, K. Tanaka, Y. Ikemoto, H. Kimura, T. Moriwaki, T. Nanba, *J. Phys. Soc. Jpn.* **2004**, *73*, 1355-1361.

[76] P. Batail, S. J. LaPlaca, J. J. Mayerle, J. B. Torrance, *J. Am. Chem. Soc.* **1981**, *103*, 951-3.

[77] J. B. Torrance, A. Girlando, J. J. Mayerle, J. L. Crowley, V. Y. Lee, P. Batail, S. J. LaPlaca, *Phys. Rev. Lett.* **1981**, *47*, 1747-50.

[78] R. M. Metzger, J. B. Torrance, *J. Am. Chem. Soc* **1985**, *107*, 117-21.

[79] A. Ota, H. Yamochi, G. Saito, *J. Mater. Chem.* **2002**, *12*, 2600-2602.

[80] M. Chollet, L. Guerin, N. Uchida, S. Fukaya, H. Shimoda, T. Ishikawa, K. Matsuda, T. Hasegawa, A. Ota, H. Yamochi, G. Saito, R. Tazaki, S. Adachi, S. Koshihara, *Science* **2005**, *307*, 86-89.

[81] R. S. Potember, T. O. Poehler, D. O. Cowan, *Appl. Phys. Lett*. **1979**, *34* , 405.

[82] R. S. Potember, T. O. Poehler, R. C. Benson, *Appl. Phys. Lett*. **1982**, *41* , 548.

[83] P. Batail, L. Ouahab, J. B. Torrance, M. L. Pylman, S. S. P. Parkin, *Solid State Commun.* **1985**, *55*, 597.

[84] T. Enoki, J.-I. Yamamura, N. Sugiyasu, K. Suzuki, G. Saito, *Mol. Cryst. Liq. Cryst.* **1993**, *233*, 325.

[85] T. Mallah, C. Hollis, S. Bott, M. Kurmoo, P. Day, *J. Chem. Soc., Dalton Trans.***1990**, 859.

[86] M. Kurmoo, A. W. Graham, P. Day, S. J. Coles, M. B. Hursthouse, J. M. Caulfield, J. Singleton, L. Ducasse, P. Guionneau, *J. Am. Chem. Soc.* **1995**, *117*, 12209.

[87] L. L. Martin, S. S. Turner, P. Day, P. Guionneau, J. A. K. Howard, D. E. Hibbs, M. E. Light, M. B. Hursthouse, M. Uruichi, K. Yakushi, *Inorg. Chem*. **2001**, *40*, 1363.

[88] D. Le Pevelen, S. S. Turner, P. Day, K. Prout, *Synth. Met*. **2001**, *121*, 1842-1843.

[89] F. Setifi, S. Golhen, L. Ouahab, S. S. Turner, P. Day, *CrystEngComm* **2002**, *4*, 1.

[90] S. S. Turner, P. Day, K. M. A. Malik, M. B. Hursthouse, S. J. Tent, E. J. MacLean, L. L. Martin, *Inorg. Chem.* **1999**, *38*, 3543.

[91] S. Rashid, S. S. Turner, D. Le Pevelen, P. Day, M. E. Light, M. B. Hursthouse, S. Firth, R. J. H. Clark, *Inorg. Chem*. **2001**, *40*, 5304.

[92] E. Coronado, S. Curreli, C. Gimenez-Saiz, C. J. Gomez-Garcia, P. Deplano, M. L. Mercuri, A. Serpe, L. Pilia, C. Faulmann, E. Canadell, *Inorg. Chem.* **2007**, *46*, 4446-4457.

[93] L. L. Martin, S. S. Turner, P. Day, F. E. Mabbs, E. J. L. McInnes, *J. Chem. Soc., Chem. Commun.* **1997**, 1367.

[94] R. Kumai, A. Asamitsu, Y. Tokura, *Chem. Lett.* **1996**, 753.

[95] S. S. Turner, D. Le Pevelen, P. Day, K. Prout, *Dalton* **2000**, *16*, 2739-2744.

[96] I. R. Marsden, M. L. Allan, R. H. Friend, M. Kurmoo, D. Kanazawa, P. Day, G. Bravic, D. Chasseau, L. Duchase, W. Hayes, *Phys. Rev.* **1994**, *B50*, 2118.

[97] J. R. Galán-Mascarós, C. Giménez-Saiz, S. Triki, C. J. Gómez-García, E. Coronado, L. Ouahab, *Angew. Chem., Int. Ed. Engl.* **1995**, *34*, 1460.

[98] C. J. Gómez-García, L. Ouahab, C. Giménez-Saiz, S. Triki, E. Coronado, P. Delhaes, *Angew. Chem., Int. Ed. Engl.* **1994**, *33*, 223.

[99] H. Kobayashi, H. Tomita, T. Naito, A. Kobayashi, F. Sakai, T. Watanabe, P. Cassoux, *J. Am. Chem. Soc.* **1996**, *118*, 368.

[100] C. Bourbonnais, R. T. Henriques, P. Wzietek, D. Kongeter, J. Voiron, D. Jerome, *Phys. Rev.* **1991**, *B44*, 641.

[101] V. Gama, M. Almeida, R. T. Henriques, I. C. Santos, A. Domingos, S. Ravy, J. P. Pouget, *J. Phys. Chem.* **1991**, *95*, 4263.

[102] E. Ojima, H. Fujiwara, K. Kato, H. Kobayashi, H. Tanaka, A. Kobayashi, M. Tokumoto, P. Cassoux, *J. Am. Chem. Soc.* **1999**, *121*, 5581.

[103] H. Fujiwara, H. Kobayashi, E. Fujiwara, A. Kobayashi, *J. Am. Chem. Soc.* **2002**, *124*, 6816.

[104] E. Coronado, J. R. Galán-Mascarós, C. J. Gómez-García, V. Laukhin, *Nature* **2000**, *408*, 447.

[105] A. Alberola, E. Coronado, J. R. Galán-Mascarós, C. Giménez-Saiz, C. J. Gómez-García, F. M. Romero, *Synth. Met.* **2003**, *133–134*, 509.

[106] A. Alberola, E. Coronado, J. R. Galán-Mascarós, C. Giménez-Saiz, C. J. Gómez-García, E. Martínez-Ferrero, A. Murcia-Martínez, *Synth. Met.* **2003**, *135–136*, 687.

[107] A. Alberola, E. Coronado, J. R. Galán-Mascarós, C. Giménez-Saiz, C. Gómez-García, *J. Am. Chem. Soc.* **2003**, *125*, 10774.

[108] H. Hiraga, H. Miyasaka, K. Nakata, T. Kajiwara, S. Takaishi, Y. Oshima, H. Nojiri, M. Yamashita, *Inorg. Chem.* **2007**, *46*, 9661.

[109] H. Hiraga, H. Miyasaka, S. Takaishi, T. Kajiwara, M. Yamashita, *Inorg. Chim. Acta* **2008**, *361*, 3863-3872.

[110] W. Kaim, M. Moscherosch, *Coord. Chem. Rev.* 1994, **129**, 157-193.

[111] K. R. Dunbar, *J. Cluster Science* **1994**, *5*, 125-143.

[112] K. R. Dunbar, X. Ouyang, *Mol. Cryst. Liq. Cryst.,* **1995**, *273*, 21-28.

[113] K. R. Dunbar, *Angew. Chem. Int. Ed. Engl.* **1996**, *35*, 1659-1661.

[114] S. DeCurtins, K. R. Dunbar, C. J. Gomez-Garcia, T. Mallah, R. G. Raptis, D. Talham, J. Veciana, in *"Design, Synthesis and Processing of Molecular-Organic and Inorganic-Magnetic Materials."* NATO ASI Series *Molecular Magnetism: From Molecular Assemblies to the Devices*, *Vol. E321* (Eds: Coronado, E.; Delhaès, P.; Gatteschi, D.; Miller, J. S.) Kluwer, **1996**, pp. 571-582.

[115] X. Ouyang, C. Campana, K. R. Dunbar, *Inorg. Chem.* **1996**, *35*, 7188-7189.

[116] H. Zhao, R. A. Heintz, X. Ouyang, G. Grandinetti, J. Cowen, K. R. Dunbar, in *"Insight Into The Behavior Of $M(TCNQ)_n$ (n = 1, 2) Crystalline Solids And Films:*

X-ray, Magnetic And Conducting Properties." NATO ASI: Supramolecular Engineering of Synthetic Metallic Materials: Conductors and Magnets, *Vol 518*, (Ed: J. Veciana), Kluwer, Dordrecht, **1999**, pp. 353-376.

[117] H. Zhao, R. A. Heintz, X. Ouyang, K. R. Dunbar, C. F. Campana, R. D. Rogers, *Chem. Mater*. **1999**, *11*, 736-746.

[118] J. Cowen, R. Clérac, R. A. Heintz, S. O'Kane, X. Ouyang, H. Zhao, K. R. Dunbar, *Mol. Cryst. And Liq. Cryst.* **1999**, *335*, 113-132.

[119] H. Miyasaka, C. S. Campos-Fernández, J. R. Galán-Mascarós, K. R. Dunbar, *Inorg. Chem.* **2000**, *39*, 5870-5873.

[120] H. Miyasaka, R. Clérac, C. S. Campos-Fernández, K. R. Dunbar, *J. Chem. Soc., Dalton Trans.* **2001**, 858-861.

[121] H. Miyasaka, R. Clérac, C. S. Campos-Fernández, K. R. Dunbar, *Inorg. Chem.* **2001**, *40*, 1663-1671.

[122] H. Zhao, M. J. Jr. Bazile, J. R. Galán-Mascarós, K. R. Dunbar, *Angew. Chem. Int. Ed.*, 2003, **42**, 1015.

[123] B. W. Smucker, J. M. Hudson, M. A. Omary, K. R. Dunbar, *Inorg. Chem.* **2003**, *42*, 4714-4723.

[124] F. Conan, B. Le Gall, J.-M. Kerbaol, S. Le Stang, J. Sala-Pala, Y. Le Mest, J. Bacsa, X. Ouyang, K. R. Dunbar, C. F.Campana, *Inorg. Chem.* **2004**, *43*, 3673-3681.

[125] H. Zhao, J. Bacsa, A. V. Prosvirin, N. Lopez, K. R. Dunbar, *Polyhedron* **2005**, *24*, 1907-1912.

[126] N. Motokawa, T. Oyama, S. Matsunaga, H. Miyasaka, K. Sugimoto, M. Yamashita, N. Lopez, K. R. Dunbar, *Dalton Trans.,* **2008**, 4057-4180.

[127] D. S. Acker, R. J. Harder, W. R. Hertler, W. Mahler, L. R. Melby, R. E. Benson, W. E. Mochel, *J. Am. Chem. Soc.* **1960**, *82,* 6408.

[128] J. Ferraris, D. O. Cowan, V., Jr. Walatka, J. H., Perlstein, *J. Am. Chem. Soc.* **1973**, *95*, 948.

[129] A. Hefczyc, L. Beckmann, E. Becker, H.-H. Johannes, W. Kowalsky, *Phys. Stat. Sol. (a)*, **2008**, *205*, 647

[130] J. Billen, S. Steudel, R. Muller, J. Genoe, P. Heremans, *Appl. Phys. Lett.*, **2007**, *91*, 263507

[131] K. Xiao, I. N. Ivanov, A. A. Puretzky, Z. Liu, D. B. Geohegan, *Adv. Mat.*, **2006**, 18, 2184-2188.

[132] Y. Liu, Z. Ji, Q. Tang, L. Jiang, H. Li, M. He, W. Hu, D. Zhang, L. Jiang, X. Wang, C. Wang, Y. Liu, D. Zhu, *Adv. Mater.*, **2005**, *17*, 2953.

[133] Y. Liu, H. Li, D. Tu, Z. Ji, C. Wang, Q. Tang, M. Liu, W. Hu, Y. Liu, D. Zhu, *J. Am. Chem. Soc.*, **2006**, *128*,12917-12922.

[134] H. Liu, Q. Zhao, Y. Li, Y. Liu, F. Lu, J. Zhuang, S. Wang, L. Jiang, D. Zhu, D. Yu, L. Chi, *J. Am. Chem. Soc*. **2005**, *127*, 1120.

[135] K. Xiao, J. Tao, A. A. Puretzky, I. N. Ivanov, S. T. Retterer, S. J. Pennycook, D. B. Geohegan, *Adv. Funct. Mater.* **2008**, *18*, 3043.

[136] a) D. J. Flannigan, V. A. Lobastov, A. H. Zewail, *Angew. Chem. Int. Ed*. **2007**, *46*, 9206. b) H.-X. Ji, J.-S. Hu, Y.-G. Guo, W.-G. Song, L.-J. Wan, Adv. Mater. **2008**, *20*, 4879.

[137] Zhou, Z.; Xiao, K.; Jin, R.; Mandrus, D.; Tao, J.; Geohegan, D. B.; Pennycook, S. *Appl. Phys. Lett*. **2007**, *90* , 193115.

[138] A. P. O'Mullane, N. Fay, A. Nafady, A. M. Bond, *J. Am. Chem. Soc.* **2007**, *129*, 2066.

[139] A. P. O'Mullane, A. K. Neufeld, A. R. Harris, A. M. Bond, *Langmuir*. **2006**, *22*, 10499.

[140] T. Oyamada, H. Tanaka, K. Matsushige, H. Sasabe, C. Adachi, *Appl.Phys. Lett.* **2003**, *83*, 1252.

[141] a) R. S. Potember, T. O. Poehler, A. Rappa, D. O. Cowan, A. N. Bloch, *Synth. Met*. **1982**, *4*, 371. b) R. S. Potember, T. O. Poehler, D. O. Cowan, F. L. Carter, P. Brant, *Molecular Electronic Devices,* Marcel Dekker, New York, **1983**, p 73. c) S. Yamaguchi, R. S. Potember, *Synth. Met.* **1996**, *78*, 117. d) S. Cui, Y. Li, Y Guo, H. Liu, Y. Song, J. Xu, J. Lv, M. Zhu, D. Zhu, *Adv. Mater.* **2008**, *20*, 309.

[142] F. A. Cotton, G. Wilkinson, P. L. Gaus, in *Basic Inorganic Chemistry*, 3rd ed., John Wiley and Sons, New York, **1995**, pp. 60-61.

[143] I. Ikemoto, J. M. Thomas, H. Kuroda, *Bull. Chem. Soc. Jpn.* **1973**, *46,* 2237.

[144] H. Ikegami, C.-H. Chong, H. Yamochi, G. Saito, *Mol. Cryst. Liq. Cryst.* **2002**, *382*, 21.

[145] D. L. Mattern, *J. Org. Chem.* **1984**, *49*, 3051.

[146] *SMART and SAINT*; Siemens Analytical X-ray Instruments Inc.: Madison, WI, 1996.

[147] G. M. Sheldrick, *SADABS*; University of Gottingen: Gottingen, Germany, 1996

[148] G. M. Sheldrick, *SHELXS-97 and SHELXL-97*; University of Gottingen: Gottingen, Germany, 1997.

[149] L. J. Barbour, *J. Supramol. Chem.* **2001**, *1*, 189–191

[150] J. S. Miller *Dalton Trans.* **2006**, 2742

[151] E. B. Vickers, T. D. Selby, M. S. Thorum, M. L. Taliaferro, J. S. Miller, *Inorg. Chem*., **2004**, *43*, 6414–6420.

[152] T. Emge, M. Maxfield, D. Cowand, T. J. Kistenmacher, *Mol. Cryst. Liq. Cryst.* **1981**, *65*, 161.

[153] M. Meneghetti, C. Pecile, *J. Chem. Phys.* **1986**, *84*, 4149.

[154] M. C. Grossel, A. J. Duke, D. B. Hibbert, I. K. Lewis, E. A. Seddon, P. N. Horton, S. C. Weston, *Chem. Mater.* **2000**, *12*, 2319.

[155] a) O. Kahn, J. Larionova, J. V. Yakhmi, *Chem. Eur. J.* **1999**, *5*, 3443; b) G. J. Halder, C. J. Kepert, B. Moubaraki, K. S. Murray, J. D. Cashion, *Science* **2002**, *298*, 1762; c) N. Yanai, W. Kaneko, K. Yoneda, M. Ohba, S. Kitagawa, *J. Am. Chem. Soc.* **2007**, *129*, 3496.

[156] J. A. Mydosh, in *Spin Glasses: An Experimental Introduction,* 1st ed., Taylor and Francis, London, **1993**, ch. 3, pp. 67-71.

[157] a) R. C. Wheland, E. L. Martin, *J. Org. Chem.* **1975**, *40*, 3101.; b) R. A. Heintz, J. A. Smith, P. S. Szalay, A. Weisgerber, K. R. Dunbar, *Inorg. Synth.* **2002**, *33*, 77.

[158] O. Kahn, in *Molecular Magnetism*, WILEY-VCH, New York, **1993**, pp. 3-4.

[159] G. Christou, D. Gatteschi, D. N. Hendrickson, R. Sessoli, *MRS Bull.* **2000**, *25*, 66-71.

[160] a) S. L. Castro, Z. Sun, C. M. Grant, J. C. Bollinger, D. N. Hendrickson, G. Christou, *J. Am. Chem. Soc*. **1998**, *120*, 2365-2375; b) A. L. Barra, D. Gatteschi, R. Sessoli, *Chem. Eur. J*. **2000**, *6*, 1608-1614; c) H. Andres, R. Basler, A. J. Blake, C. Cadiou, G. Chaboussant, C. M. Grant, H.-U. Güdel, M. Murrie, S. Parsons, C. Paulsen, F. Semadini, V. Villlar, W. Wernsdorfer, R. E. P. Winpenny, *Chem. Eur. J.* **2002**, *8*, 4867-4876; d) M. Murrie, S. J. Teat, H. Stoeckli-Evans, H. U. Güdel, *Angew. Chem. Int. Ed.* **2003**, *42*, 4653-4656; *Angew. Chem*. **2003**, *115*, 4801-4804.

[161] C. P. Berlinguette, D. Vaughn, C. Cañada-Vilalta, J. R. Galán-Mascarós, K. R. Dunbar, *Angew. Chem. Int. Ed.* **2003**, *42*, 1523-1526; *Angew. Chem.* **2003**, *115*, 1561-1564.

[162] M. Murugesu, M. Habrych, W. Wernsdorfer, K. A. Abboud, G. Christou, *J. Am. Chem. Soc*. **2004**, *126*, 4766.

[163] T. C. Stamatatos, K. A. Abboud, W. Wernsdorfer, G. Christou, *Angew. Chem., Int. Ed.* **2007**, *46*, 884-888.

[164] a) E. J. Schelter, A. V. Prosvirin, K. R. Dunbar, *J. Am. Chem. Soc.* **2004**, *126*, 15004-15005; b) J. Martínez-Lillo, D. Armentano, G. De Munno, W. Wernsdorfer, M. Julve, F. Lloret, J. Faus, *J. Am. Chem. Soc*. **2006**, *128*, 14218-14219; c) E. J. Schelter, F. Karadas, C. Avendano, A. V. Prosvirin, W. Wernsdorfer, K. R. Dunbar, *J. Am. Chem. Soc.* **2007**, *129*, 8139-8149.

[165] a) J. J. Sokol, A. G. Hee, J. R. Long, *J. Am. Chem. Soc.* **2002**, *124*, 7656-7657; b) S. Wang, J.-L. Zuo, H.-C. Zhou, H. J. Choi, Y. Ke, J. R. Long, X.-Z. You, *Angew.*

Chem. Int. Ed. **2004**, *43*, 5940-5943; *Angew. Chem.* **2004**, *116*, 6066-6069; c) H. J. Choi, J. J. Sokol, J. R. Long, *Inorg. Chem.* **2004**, *43*, 1606-1608.

[166] a) S. Karasawa, G. Zhou, H. Morikawa, N. Koga, *J. Am. Chem. Soc.* **2003**, *125*, 13676; b) D. Yoshihara, S. Karasawa, N. Koga, *J. Am. Chem. Soc.* **2008**, *130*, 10460.

[167] a) S. Osa, T. Kido, N. Matsumoto, N. Re, A. Pochaba, J. Mrozinski, *J. Am. Chem. Soc.* **2004**, *126*, 420-421; b) A. Mishra, W. Wernsdorfer, K. A. Abboud, G. Christou, *J. Am. Chem. Soc.* **2004**, *126*, 15648-15649; c) C. M. Zaleski, E. C. Depperman, J. W. Kampf, M. L. Kirk, V. L. Pecoraro, *Angew. Chem. Int. Ed.* **2004**, *43*, 3912-3914; *Angew. Chem*. **2004**, *116*, 4002-4004; d) A. Mishra, W. Wernsdorfer, S. Parsons, G. Christou, E. K. Brechin, *Chem. Commun*. **2005**, 2086-2088; e) F. Mori, T. Nyui, T. Ishida, T. Nogami, K.-Y. Choi, H. Nojiri, *J. Am. Chem. Soc.* **2006**, *128*, 1440-1441; f) C. Aronica, G. Pilet, G. Chastanet, W. Wernsdorfer, J.-F. Jacquot, D. Luneau, *Angew. Chem. Int. Ed.* **2006**, *45*, 4659-4662; *Angew. Chem.* **2006**, *118*, 4775-4778; g) M. Ferbinteanu, T. Kajiwara, K.-Y. Choi, H. Nojiri, A. Nakamoto, N. Kojima, F. Cimpoesu, Y. Fujimura, S. Takaishi, M. Yamashita, *J. Am. Chem. Soc.* **2006**, *128*, 9008; h) V. M. Mereacre, A. M. Ako, R. Clérac, W. Wernsdorfer, G. Filoti, J. Bartolomé, C. E. Anson, A. K. Powell, *J. Am. Chem. Soc.* **2007**, *129*, 9248; i) V. Chandrasekhar, B. M. Pandian, R. Boomishankar, A. Steiner, J. J. Vittal, A. Houri, R. Clérac, *Inorg. Chem.* **2008**, *47*, 4918-4929; j) T. Kajiwara, M. Nakano, S. Takaishi, M. Yamashita, *Inorg. Chem.* **2008**, *47*, 8604–8606; k) T. C. Stamatatos, S. J. Teat, W. Wernsdorfer, G. Christou, *Angew. Chem. Int. Ed.* **2009**, *48*, 521-524; l)

G. Novitchi, W. Wernsdorfer, L. F. Chibotaru, J.-P. Costes, C. E. Anson, A. K. Powell, *Angew. Chem. Int. Ed.* **2009**, *48*, 1614-1619.

[168] N. Ishikawa, M. Sugita, N. Tanaka, T. Ishikawa, S. Koshihara, Y. Kaizu, *Inorg. Chem.* **2004**, *43*, 5498-5500

[169] a) J. Tang, I. Hewitt, N. T. Madhu, G. Chastenet, W. Wernsdorfer, C. E. Anson, C. Benelli, R. Sessoli, A. K. Powell, *Angew. Chem. Int. Ed.* **2006**, *45*, 1729-1733; *Angew. Chem*. **2006**, *118*, 1761-1765; b) M. T. Gamer, Y. Lan, P. W. Roesky, A. K. Powell, R. Clérac, *Inorg. Chem.* **2008**, *47*, 6581.

[170] a) N. Ishikawa, M. Sugita, T. Ishikawa, S. Koshihara, Y. Kaizu, *J. Am. Chem. Soc.* **2003**, *125*, 8694-8695; b) N. Ishikawa, M. Sugita, T. Ishikawa, S. Koshihara, Y. Kaizu, *J. Phys. Chem. B* **2004**, *108*, 11265-11271; c) N. Ishikawa, M. Sugita, W. Wernsdorfer, *Angew. Chem., Int. Ed.* **2005**, *44*, 2931-2935; *Angew. Chem.* **2005**, *117*, 2991-2995; d) N. Ishikawa, M. Sugita, W. Wernsdorfer, *J. Am. Chem. Soc.* **2005**, *127*, 3650-3651; e) M. A. AlDamen, J. M. Clemente-Juan, E. Coronado, C. Martí-Gastaldo, A. Gaita-Ariño, *J. Amer. Chem Soc.* **2008**, *130*, 8874.; f) M. A. AlDamen, S. Cardona-Serra, J. M. Clemente-Juan, E. Coronado, A. Gaita-Ariño, C. Martí-Gastaldo, F. Luis, O. Montero, Inorg. Chem., **2009**, *48*, 3467–3479.

[171] a) L. Bogani, C. Sangregorio, R. Sessoli, D. Gatteschi, *Angew. Chem. Int. Ed.* **2005**, *44*, 5817-5821; *Angew. Chem.* **2005**, *117*, 5967-5971; b) K. Bernot, L. Bogani, A. Caneschi, D. Gatteschi, R. Sessoli, *J. Am. Chem. Soc.* **2006**, *128*, 7947-7956; c) K. Bernot, L. Bogani, R. Sessoli, D. Gatteschi, Inorg. Chim. Acta **2007**, *360*, 3807-

3812; d) Y.-G. Huang, X.-T. Wang, F.-L. Jiang, S. Gao, M.-Y. Wu, Q. Gao, W. Wei, M.-C. Hong, *Chem. Eur. J.* **2008**, *14*, 10340-10347.

[172] Magnetism and Superconductivity in Low-Dimensional Systems: Utilization in Future Applications, (Ed.: D. Stamopoulos) Nova Science Publishers, New York, **2008**.

[173] D. A. Garanin, *Phys. Rev. B.* **2007**, *75*, 094409.

[174] a) K. Petukhov, S. Bahr, W. Wernsdorfer, A.-L. Barra, V. Mosser, *Phys. Rev. B* **2007**, *75*, 064408/1-064408/12; b) M. Bal, J. R. Friedman, W. Chen, M. T. Tuominen, C. C. Beedle, E. M. Rumberger, D. N. Hendrickson, *EPL* **2008**, *82*, 17005/1-17005/6; c) G. de Loubens, D. A. Garanin, C. C. Beedle, D. N. Hendrickson, A. D. Kent, *EPL* **2008**, *83*, 37006/1-37006/6.

[175] T. Hahn, in *International Tables for Crystallography*, D. Reidel Publishing Company, Dordrecht, **1983**, pp. 177.

[176] K. Bernot, J. Luzon, L. Bogani, M. Etienne, C. Sangregorio, M. Shanmugam, A. Caneschi, R. Sessoli, D. Gatteschi, *J. Am. Chem. Soc.* **2009**, *131*, 5573-5579.

[177] O. Kahn, in *Molecular Magnetism*, WILEY-VCH, New York, **1993**, pp. 251-253.

[178] a) O. Kahn, in *Molecular Magnetism*, WILEY-VCH, New York, **1993**, pp. 11 and 47; b) O. Kahn, in *Molecular Magnetism*, WILEY-VCH, New York, **1993**, pp. 3-4.

[179] K.S. Cole, R.H. Cole, *J. Chem. Phys.* **1941**, *9*, 341-351.

[180] R. J. Glauber, *J. Math. Phys.* **1963**, *4*, 294-307.

[181] a) A. Caneschi, L. Cianchi, F. D. Giallo, D. Gatteschi, P. Moretti, F. Pieralli, G. Spina, *J. Phys.: Condens. Matter* **1999**, 3395-3403; b) D. Li, S. Parkin, G. Wang, G.

T. Yee, R. Clérac, W. Wernsdorfer, S. M. Holmes, *J. Amer. Chem Soc.* **2006**, *128*, 4214-4215.

[182] W. Wernsdorfer, N. E. Chakov, G. Christou, *Phys. Rev. B.* **2004**, *70*, 132413.

[183] a) I. Chiorescu, W. Wernsdorfer, A. Müller, H. Bögge, B. Barbara, *Phys. Rev. Lett.* **2000**, *84*, 3454-3457; b) I. Chiorescu, W. Wernsdorfer, A. Müller, H. Bögge, B. Barbara, *J. Magn. Magn. Mater.* **2000**, *221,* 103-109; c) E. I. Tolis, L. P. Engelhardt, P. V. Mason, G. Rajaraman, K. Kindo, M. Luban, A. Matsuo, H. Nojiri, J. Raftery, C. Schröder, G. A. Timco, F. Tuna, W. Wernsdorfer, R. E. P. Winpenny, *Chem. Eur. J.* **2006**, *12*, 8961-8968.

[184] a) L. F. Jones, E. K. Brechin, D. Collison, M. Helliwell, Talal Mallah, S. Piligkos, G. Rajaraman, W. Wernsdorfer, *Inorg. Chem*. **2003**, *42*, 6601–6603; b)N. Aliaga-Alcalde, R. S. Edwards, S. O. Hill, W. Wernsdorfer, K. Folting, G. Christou, *J. Am. Chem. Soc.* **2004**, *126*, 12503; c) M. Moragues-Cánovas, M. Helliwell, L. Ricard, É. Rivière, W. Wernsdorfer, E. Brechin, T. Mallah, *Eur. J. Inorg. Chem.* **2004**, 2219; d) E.-C. Yang, W. Wernsdorfer, L. N. Zakharov, Y. Karaki, A. Yamaguchi, R. M. Isidro, G.-D. Lu, S. A. Wilson, A. L. Rheingold, H. Ishimoto, D. N. Hendrickson *Inorg. Chem.*, **2006**, *45*, 529–546; e) K. W. Galloway, A. M. Whyte, W. Wernsdorfer, J. Sanchez-Benitez, K. V. Kamenev, A. Parkin, R. D. Peacock, M. Murrie, *Inorg. Chem.* **2008**, *47*, 7438.

[185] L. J. de Jongh, W. D. van Amstel, A. R. Miedema, *Physica* **1972**, *58*, 277.

[186] W. Wernsdorfer, *Adv. Chem. Phys.* **2001**, *118*, 99-190.

[187] a) Benelli, C.; Gatteschi, D. *Chem. Rev.*, **2002**, *102*, 2369; b) D. Luneau, P. Rey, *Coord. Chem. Rev*., **2005**, *249*, 2591-2611.

[188] a) C. Benelli, A. Caneschi, D. Gatteschi, R. Sessoli, *Adv. Mater.*, **1992**, *4,* 504; b) C. Benelli, A. Caneschi, D. Gatteschi, R. Sessoli, *J. Appl. Phys.*, **1993**, *73,* 5333; c) C. Benelli, A. Caneschi, D. Gatteschi, R. Sessoli, *Inorg. Chem.*, **1993**, *32,* 4797.

[189] J. W. Raebiger, J. S. Miller, *Inorg. Chem.*, **2002,** *41*, 3308.

[190] a) C. Benelli, A. Caneschi, D. Gatteschi, L. Pardi, P. Rey, D. P. Shum, R. L. Carlin, *Inorg. Chem.*,**1989**, *28*, 272; b) C. Benelli, A. Caneschi, A. C. Fabretti, D. Gatteschi, L. Pardi, *Inorg. Chem.*, **1990**, *29*, 4153; c) C. Benelli, A. Caneschi, D. Gatteschi, L. Pardi, *Inorg. Chem.*, **1992**, *31*, 741; d) J.-P. Sutter, M. L. Kahn, S. Golhen, L. Ouahab, O. Kahn, *Chem. Eur. J.*, **1998**, *4*, 571; e) C. Lescop, D. Luneau, E. Belorisky, P. Fries, M. Guillot, P. Rey, *Inorg. Chem*., **1999**, *38*, 5472; f) J.-X. Xu, Y. Ma, G.-F. Xu, C. Wang, D.-Z. Liao, Z.-H. Jiang, S.-P. Yan, L.-C. Li, *Inorg. Chem. Commun.*, **2008**, *11*, 1356-1358; g) G. Poneti, K. Bernot, L. Bogani, A. Caneschi, R. Sessoli, W. Wernsdorfer, D. Gatteschi, *Chem. Commun.*, **2007**, *18*, 1807-1809.

[191] a) C. Benelli, A. Caneschi, D. Gatteschi, L. Pardi, P. Rey, *Inorg. Chem.*, **1989**, *28*, 275; b) C. Benelli, A. Caneschi, D. Gatteschi, L. Pardi, P. Rey, *Inorg. Chem.*,**1989**, *28*, 3230; c) C. Benelli, A. Caneschi, D. Gatteschi, P. Rey, *Inorg. Chem.*,**1990**, *29*, 4223.

[192] J.-X. Xu, Y. Ma, D.-Z. Liao, G.-F. Xu, J. Tang, C. Wang, N. Zhou, S.-P. Yan, P. Cheng, L.-C. Li, *Inorg. Chem.*, **2009**, *48*, 8890-8896.

[193] a) F. Pointillart, O. Maury, Y. L. Gal, S. Golhen, O. Cador, L.Ouahab, *Inorg. Chem.*, **2009**, *48*, 7421-7429; b) F. Pointillart, Y. L. Gal, S. Golhen, O. Cador, L. Ouahab, *Chem. Commun.*, **2009**, *25*, 3777-3779; c) F. Pointillart, Y. L. Gal, S. Golhen, O. Cador, L.Ouahab, Inorg. Chem. **2009**, *48*, 4631-4633.

[194] a) A. Dei, D. Gatteschi, C. A. Massa, L. A. Pardi, S. Poussereau, L. Sorace, *Chem. Eur. J.*, **2000**, *6*, 4580; b) T. Nankawa, M. Watanabe, M. Murata, H. Nishihara, *Chem. Lett.*, **2003**, *32*, 286-287; c) A. Caneschi, A. Dei, D. Gatteschi, S. Poussereau and L. Sorace, *Dalton Trans.*, **2004**, 1048.

[195] a) N. Roques, S. Perruchas, D. Maspoch, A. Datcu, K. Wurst, J.-P. Sutter, C. Rovira, J. Veciana, *Inorg. Chim. Acta*, **2007**, *360*, 3861-3869; b) N. Roques, D. Maspoch, I. Imaz, A. Datcu, J.-P. Sutter,C. Rovira, J. Veciana, *Chem. Commun*., **2008**, 3160–3162.

[196] a) T. Tsukuda, T. Suzuki, S.Kaizaki, *Polyhedron*, **2007**, *26*, 3175-3181; b) T. Tsukuda, T. Suzuki, S. Kaizaki, *Inorg. Chim. Acta*, **2005**, *358*, 1253-1257.

[197] G. H. Maunder, A. Sella, M. R. J. Elsegood, *J. Organomet. Chem.*, **2001**, *619*, 152-156.

[198] A. A. Trifonov, I. D. Gudilenkov, G. K. Fukin, A. V.Cherkasov, J. Larionova, *Organometallics*, **2009**, *28*, 3421-3425.

[199] L. Norel, L.-M. Chamoreau, Y. Journaux, O. Oms, G. Chastanet, C. Train, *Chem. Commun.*, **2009**, *17*, 2381-2383.

[200] A. M. Madalan, H. W. Roesky, M. Andruh, M. Noltemeyer, N. Stanica, *Chem. Commun.*, **2002**, 1638.

[201] A. M. Madalan, N. Avarvari, M. Fourmigué, R. Clérac, L. F. Chibotaru, S. Clima, M. Andruh, *Inorg Chem.*, **2008**, *47*, 940-950.

[202] L. Ballester, C. Alonso, M. Fonari, A. Gutiérrez, M. Mitewa, M. F. Perpiñán, K. Suwinska, *J. Alloys Compd.*, **2001**, *323-324*, 138-141.

[203] X. Wang, Z. Tian, Z. Wang, C. Lin, *Chinese Science Bulletin*, **1989**, *34*, 1274-1277.

[204] a) M. J. Rice, L. Pietronero, P. Brüesch, *Solid State Commun.,* **1977**, *21*, 757-760; b) J. S. Chappell, A. N. Bloch, W. A. Bryden, M. Maxfield, T. O. Poehler, D. O. Cowan, *J. Am. Chem. Soc.*, **1981**, *103*, 2442–2443; c) M. T. Azcondo, L. Ballester, S. Golhen, A. Gutiérrez, L. Ouahab, S. Yartsev, P. Delhaes, *J. Mater. Chem.*, **1999**, *9*, 1237–1244; d) F. H. Herbstein, M. Kapon, *Crystallogr. Rev*., **2008**, *14*, 3-74.

[205] O. Kahn, in *Molecular Magnetism*, WILEY-VCH, New York, **1993**, pp. 251-253.

[206] O. Kahn, in *Molecular Magnetism*, WILEY-VCH, New York, **1993**, pp. 48-49.

[207] R. Georges, J. J. Borrás-Almenar, E. Coronado, J. Curély, M. Drillon, in *Magnetism: Molecules to Materials*, ed. J. S. Miller and M. Drillon, Wiley-VCH, Weinheim, **2001**, ch. 1, pp. 14-16.

[208] M. Ohba and H. Okawa, *Coord. Chem. Rev*. **2000**, *198*, 313.

[209] J. Cernák, M. Orendác, I. Potocnák, J. Chomic, A. Orendacová, J. Skorsepa and A. Feher, *Coord. Chem. Rev*. **2002**, *224*, 51.

[210] S. Tanase and J. Reedijk, *Coord. Chem. Rev*. **2006**, *250*, 2501.

[211] C. E. Plecnik, S. Liu and S. G. Shore, *Acc. Chem. Res*. **2003**, *36*, 499.

[212] F. Hulliger, M. Landolt and H. Vetsch, *J. Solid State Chem.* **1976**, *18*, 283.

[213] F. Hulliger, M. Landolt and H. Vetsch, *J. Solid State Chem.* **1976**, *18*, 307.

[214] H.-Z. Kou, S. Gao and X. Jin, *Inorg. Chem.* **2001**, *40*, 6295.

[215] B.-Q. Ma, S. Gao, G. Su and G.-X. Xu, *Angew. Chem., Int. Ed*. **2001**, *40*, 434.

[216] H.-Z. Kou, S. Gao, B.-W. Sun, and J. Zhang, *Chem. Mater*. **2001**, *13*, 1431.

[217] B. Yan, Z. Chen, S. Wang and S. Gao, *Chem. Lett.* **2001**, 350.

[218] B. Yan, H.-D. Wang and Z.-D. Chen, *Polyhedron* **2001**, *20*, 591.

[219] S. Tanase, M. Andruh, A. Müller, M.; C. Schmidtmann, C. Mathonière and G. Rombaut, *Chem. Commun*. **2001**, 1084.

[220] S. Gao, G. Su, T. Yi and B.-Q. Ma, *Phys. Rev. B*, **2001**, *63*, 054431

[221] B. Yan, H.-D. Wang and Z.-D. Chen, Inorg. Chem. Comm. 2000, 3, 653.

[222] B. Yan and Z. Chen, *Helv. Chim. Acta* **2001**, *84*, 817.

[223] H.-Z. Kou, S. Gao, C.-H. Li, D.-Z. Liao, B.-C. Zhou, R.-J. Wang and Y. Li, *Inorg. Chem.* **2002**, *41*, 4756.

[224] A. Figuerola, C. Diaz, M. S. El Fallah, J. Ribas, M. Maestro and J. Mahia, *Chem. Comm*. **2001**, 1204.

[225] A. Figuerola, C. Diaz, J. Ribas, V. Tangoulis, C. Sangregorio, D. Gatteschi, M. Maestro and J. Mahia, *Inorg. Chem*. **2003**, *42*, 5274.

[226] A. Figuerola, C. Diaz, J. Ribas, V. Tangoulis, J. Granell, F. Lloret, J. Mahia and M. Maestro, *Inorg. Chem*. **2003**, *42*, 641.

[227] H.-Z. Kou, B. C. Zhou and R. J. Wang, *Inorg. Chem*. **2003**, *42*, 7658.

[228] A. Figuerola, J. Ribas, D. Casanova, M. Maestro, S. Alvarez and C. Diaz, *Inorg. Chem*. **2005**, *44*, 6949.

[229] A. Figuerola, J. Ribas, X. Solans, M. Font-Bardía, M. Maestro and C. Diaz, *Eur. J. Inorg. Chem*. **2006**, 1846.

[230] B. Du, E. Ding, E. A. Meyers and S. G. Shore, *Inorg. Chem.* **2001**, *40*, 3637.

[231] B. Du, E. Ding, E. A. Meyers and S. G. Shore, *Inorg. Chem*. **2000**, *39*, 4639.

[232] D. W. Knoeppel, J. Liu, E. A. Meyers and S. G. Shore, *Inorg. Chem.* **1998**, *37*, 4828.

[233] D. W. Knoeppel and S. G. Shore, *Inorg. Chem.* **1996**, *35*, 1747.

[234] D. W. Knoeppel and S. G. Shore, *Inorg. Chem*. **1996**, *35*, 5328.

[235] R. Gheorghe, M. Andruh, J.-P. Costes and B. Donnadieu, *Chem. Commun*. **2003**, 2778.

[236] H.-Z. Kou, B. C. Zhou, S. Gao and R.-J. Wang, *Angew. Chem. Int. Ed.* **2003**, *42*, 3288.

[237] B. Yan, Z. Chen and S. X. Wang, *Transition Met. Chem.* **2001**, *26*, 287.

[238] J. A. Kautz, D. F. Mullica, B. P. Cunningham, R. A. Combs and J. M. Farmer, *J. Mol. Struct.* **2000**, *523*, 175.

[239] H.-Z. Kou, G.-M. Yang, D.-Z. Liao, P. Cheng, Z.-H. Jiang, S.-P. Yan, X.-Y. Huang and G.-L. Wang, *J. Chem. Crystallogr*. **1998**, *28*, 303.

[240] D. F. Mullica, J. M. Farmer, B. P. Cunningham and J. A. Kautz, *Coord. Chem*. **2000**, *49*, 239.

[241] G. Li, T. Akitsu, O. Sato and Y. Einaga, *J. Am. Chem. Soc.* **2003**, *125*, 12396.

[242] G. Li, T. Akitsu, O. Sato and Y. Einaga, *Solid State Chem.* **2005**, *178*, 36.

[243] N. Ishikawa, M. Sugita, T. Ishikawa, S. Koshihara and Y. Kaizu, *J. Am. Chem. Soc.* **2003**, *125*, 8694.

[244] N. Ishikawa, M. Sugita and W. Wernsdorfer, *J. Am. Chem. Soc.* **2005**, *127*, 3650.

[245] N. Ishikawa, M. Sugita, T. Ishikawa, S. Koshihara and Y. Kaizu, *J. Phys. Chem. B* **2004**, *108*, 11265.

[246] A. Mishra, W. Wernsdorfer, K. A. Abboud and G. Christou, *J. Am. Chem. Soc.* **2004**, *126*, 15648.

[247] C. M. Zaleski, E. C. Depperman, J. W. Kampf, M. L. Kirk and V. L. Pecoraro, *Angew. Chem. Int. Ed.* **2004**, *43*, 3912.

[248] F. Mori, T. Nyui, T. Ishida, T. Nogami, K.-Y. Choi and H. Nojiri, *J. Am. Chem. Soc.* **2006**, *128*, 1440.

[249] M. Ferbinteanu, T. Kajiwara, K.-Y. Choi, H. Nojiri, A. Nakamoto, N. Kojima, F. Cimpoesu, Y. Fujimura, S. Takaishi and M. Yamashita, *J. Am. Chem. Soc.* **2006**, *128*, 9008.

[250] A. Mishra, W. Wernsdorfer, S. Parsons, G. Christou and E. K. Brechin, *Chem. Commun*. **2005**, 2086.

[251] N. Ishikawa, S. Otsuka, and Y. Kaizu, *Angew. Chem., Int. Ed.* **2005**, *44*, 731.

[252] N. Ishikawa, K. Sugita, and W. Wernsdorfer, *Angew. Chem., Int. Ed.* **2005**, *44*, 2931.

[253] C. Aronica, G. Pilet, G. Chastanet, W. Wernsdorfer, J.-F. Jacquot, and D. Luneau, *Angew. Chem., Int. Ed.* **2006**, *45*, 4659.

[254] J. Tang, I. Hewitt, N. T. Madhu, G. Chastanet, W. Wernsdorfer, C. E. Anson, C. Benelli, R. Sessoli, and A. K. Powell, *Angew. Chem., Int. Ed.* **2006**, *45*, 1729.

[255] J. P. Costes, J. M. Clemente-Juan, F. Dahan and J. Milon, *Inorg. Chem*. **2004**, *43*, 8200.

[256] K. Bernot, L. Bogani, A. Caneschi, D. Gatteschi, and R. Sessoli, *J. Am. Chem. Soc.* **2006**, *128*, 7947.

[257] R. Wietzke, M. Mazzanti, J. M. Latour and J. Pécaut, *Inorg. Chem.* **1999**, *38*, 3581.

[258] C. R. De Silva, J. Wang, M. D. Carducci and S. A. Rajapakshe, *Inorg. Chim. Acta* **2004**, *357*, 630.

[259] G. Y. S. Chan, M. G. B. Drew, M. J. Hudson, N. S. Isaacs and P. Byers, *Polyhedron*, **1996**, *15*, 3385.

[260] M. Estrader, J. Ribas, V. Tangoulis, X. Solans, M. Font-Bardia, M. Maestro and C. Diaz, *Inorg. Chem.* **2006**, *45*, 8239.

[261] a) Y.-B. Dong, Y.-Y. Jiang, J. Li, J.-P. Ma, F.-L. Liu, B. Tang, R.-Q. Huang, S. R. Batten, *J. Am. Chem. Soc.* 2007, *129*, 4520-4521; b) J. Xia, W. Shi, X.-Y. Chen, H.-S. Wang, P. Cheng, D.-Z. Liao, S.-P. Yan, *Dalton Trans.*, **2007**, 2373–2375; c) F. Dai, H. He, D. Sun, *J. Am. Chem. Soc.*, **2008**, *130*, 14064–14065; d) S.-B. Ren, X.-L. Yang, J. Zhang, Y.-Z. Li, Y.-X. Zheng, H.-B. Du, X.-Z. You, *CrystEngComm*, **2009**, *11*, 246–248; e) W.-T. Liu, Y.-C. Ou, Y.-L. Xie, Z. Lin, M.-L. Tong, *Eur. J. Inorg. Chem.* **2009**, 4213–4218; f) F. Dai, H. He, D. Sun, *Inorg. Chem.* **2009**, *48*, 4613–4615; g) K.-L. Huang, X. Liu, X. Chen, D.-Q. Wang, *Cryst. Growth Des.* **2009**, *9*, 1646–1650.

[262] S. K. Ghosh, P. K. Bharadwaj, *Inorg. Chem.* **2005**, *44*, 3156-3161.

[263] C. Ge, H.-Z. Kou, Z.-H. Ni, Y.-F. Jiang, A.-L. Cui and O. Sato, *Chem. Lett.* **2005**, *9*, 1280.

[264] H.-L. Sun, H. Shi, F. Zhao, L. Qi and S. Gao, *Chem. Comm.* **2005**, 4339.

[265] D. Li, L. Zheng, Y. Zhang, J. Huang, S. Gao and W. Tang, *Inorg. Chem*. **2003**, *42*, 6123.

[266] M. Hagiwara, *J. Magn. Magn. Mater.* **1998**, *177*, 89.

[267] S. Sahoo, O. Petracic, W. Kleemann, S. Stappert, G. Dumpich, P. Norblad, S. Cardoso and P. P. Freitas, *Appl. Phys. Lett*. **2003**, *82*, 4116.

[268] T. Mori, and H. Mamiya, *J. Phys. Condens. Mater.* **2004**, *16*, S743.

[269] Theory and Applications of Molecular Paramagnetism, E. A. Boudreaux, L.N. Mulay, Eds; John Wiley & Sons: New York, 1976.

[270] Bruker (2001). SAINT. Version 6.02. Bruker AXS Inc., Madison, Wisconsin, USA.

[271] L. J. Barbour, X-Seed, Graphical interface to SHELX-97 and POV-Ray, 1999, www.x-seed.net.

[272] G. M Sheldrick, (1997) SHELX, Programs for Solving and Refining Crystal Structures, University of Göttingen, Germany.

VITA

Name: Nazario Lopez Cruz

Address: Sitio de Bejar # 560, Colonia Jardines de Santa Isabel, Guadalajara, Jalisco, Mexico C.P. 44300

Email Address: nazariolc@yahoo.com

Education: Ph.D., Chemistry, Texas A&M University, May 2010
M.S., Chemistry, University of Texas at El Paso, August 2004
B.S., Chemical Engineering, Universidad de Guadalajara, May 2002

Publications:

H. Zhao, J. Bacsa, A. V. Prosvirin, N. Lopez, K. R. Dunbar, *Polyhedron* **2005**, *24*, 1907-1912.

N. Lopez, T. E. Vos, A. M. Arif, W. W. Shum, J. C. Noveron, J. S. Miller, *Inorg. Chem*. **2006**, *45*, 4325–4327.

H. Zhao, N. Lopez, A. V. Prosvirin, H. T. Chifotides, K. R. Dunbar, *Dalton Trans*., **2007**, 878-888.

P. S. Mukherjee, N. Lopez, A. M. Arif, F. Cervantes-Lee, J. C. Noveron, *Chem. Commun*., **2007**, 1433-1435.

N. Lopez, H. Zhao, A. V. Prosvirin, A. Chouai, M. Shatruk, K. R. Dunbar, *Chem. Commun*., **2007**, 4611-4613.

N. Motokawa, T. Oyama, S. Matsunaga, H. Miyasaka, K. Sugimoto, M. Yamashita, N. Lopez, K. R. Dunbar, *Dalton Trans*. **2008**, *31*, 4099-4102.

N. Lopez, A. V. Prosvirin, H. Zhao, W. Wernsdorfer, K. R. Dunbar, *Chem. Eur. J*., **2009**, *15*, 11390–11400.

N. Lopez, H. Zhao, A. Ota, A. V. Prosvirin, E. W. Reinheimer, K. R. Dunbar, *Adv. Mater.,* **2010**, *22*, 986-989.

N. Lopez, H. Zhao, A. V. Prosvirin, W. Wernsdorfer, K. R. Dunbar, *Dalton Trans.*, **2010**, *39*, 4341-4352.